

Tesis aprobada por el jurado conformado por los profesores:

Dr. Rolando C. Castillo Caballero. Director de tesis.

Instituto de Física,
Universidad Nacional Autónoma de México.

Dr. José Roberto Zenit Camacho.

Instituto de Investigaciones en Materiales,
Universidad Nacional Autónoma de México.

Dr. Neil Charles Bruce Davidson.

Instituto de Ciencias Aplicadas y Tecnología,
Universidad Nacional Autónoma de México.

Dra. Patricia Goldstein Menache.

Facultad de Ciencias,
Universidad Nacional Autónoma de México.

Dr. Ramón Castañeda Priego.

División de Ciencias e Ingenierías,
Universidad de Guanajuato, Campus León.

Universidad Nacional Autónoma de México
2019

For my beloved parents, sister and Choco,
who always give me the strength to
continue along the journey.

Para mis amados padres, mi hermana y
Choco, quienes siempre me dan la fortaleza
para continuar a lo largo del viaje.

“Se asentó y ha quedado por costumbre, que los que se graduasen de doctores y maestros en cualquier facultad, envíen las conclusiones a todos los doctores y maestros a sus casas con los bedeles o persona de calidad, con música de trompetas, pompa y aparato y que se diese vejamen en los grados de doctor; y acabados los grados, en el teatro se den guantes a los señores doctores y maestros, un par a cada uno, y por cada cosa que faltase, fuese multado con 30 pesos.”

**Crónica de la Real y Pontificia
Universidad de México**

Cristóbal Bernardo de la Paz y Jaén

Acknowledgments

This work is the result of the effort and dedication exerted during the years of my graduate studies at the National University of Mexico. Without the support and knowledge provided for many people, the research could not have been carried out.

I want to thank to my principal advisor, Dr. Rolando C. Castillo Caballero, who has oriented me in moments of doubts and has taught me how to develop a scientific research project. In the same way, I thank to my advisory committee, Dr. Denis Boyer and Dr. Héctor Domínguez Castro, who were always interested in discussing and evaluating my academic performance.

Many thanks to all members of the Complex Fluids Group at IFUNAM: M.S. Salvador Ramos Solórzano, M.S. Cristina Garza Lozano, and Erick Guzmán Gómez, for all the help they gave me in the lab. Thanks to the former students of the group, and to the ones who are still there, Paloma Vilchis León, Raziel Garza Melchor, Virginia Carrasco Fadanelli, Natalia Rincón Londoño, Ricky Frank López Santiago, Diego Colín Taboada, specially to Erick Sarmiento Gómez, Danaí Montalván Sorrosa and Brisa Arenas Gómez, who always were available to help me with my questions and ideas. Also, my gratitude to Marko Vinceković and Atiđa Selmani, former postdoctoral researchers of the group. To all members and friends of the Complex Fluids community I met in Mexico and abroad.

My gratitude to the members of the committee for the evaluation of the thesis, Dr. Patricia Goldstein Menache, Dr. Roberto Zenit Camacho, Dr. Neil Charles Bruce Davidson and Dr. Ramón Castañeda Priego. And many thanks to all the professors that have been involved in the different evaluations of my performance along my graduate studies, Dr. Raúl Esquivel Sirvent, Dr. Jorge Delgado García, Dr. Carlos Ignacio Mendoza Ruiz, Dr. Anna Kozina, Dr. Pedro Díaz Leyva and Dr. Francisco Javier Sevilla Pérez, as well.

Special thanks to Dr. María Ester Brandan Siqués, who always trusted me since I started the master program. Thanks to Dr. Rafael Pérez Pascual, former director of the physics graduate studies program, who supported me to start the master program in physics, and also thanks to the current director Dr. Alejandro Reyes Esqueda, who always heeded my concerns when I was a member of the Academic Committee.

Thanks to the Academic Technicians of the IFUNAM, Jorge I. Cruz Morales, Rodrigo Gutiérrez Arenas and Alberto García Ramírez. Without their help I could not have finished my experiments. To the administrative workers at the physics program, especially to Isabel Mendoza Romero, Martha Tinoco González and Yanalté Herrero Quezadas, former chief at the graduate studies in physics office. Also, thanks to Guillermina Moreno Moreno, Catalina García García and Ma. de la Luz Vela Rosales, who are personnel of the IFUNAM library.

I want to thank also to Dr. Karen Volke Sepúlveda, Dr. Libertad Barrón Palos and Dr. Saúl Ramos Sánchez, who always supported the Student's Seminar project which I carried out with my colleagues

ACKNOWLEDGMENTS

since 2012. Thanks to María Guadalupe Sánchez Rojas and Pedro Zaldívar Sánchez for their support in the diffusion of the seminar. Also, thanks to all the former and current organizers of the seminar. My gratefulness to Aleida Rueda Rodríguez, on charge of the IFUNAM science communication office, Luis Novoa Rodríguez, and Dulce Aguilar Téllez, current and former graphic designers at the IFUNAM respectively.

Thanks to the friends with whom I have shared my experiences studying at the National University and living in Mexico City, but particularly to Deydreth Martínez Álvarez who always has supported and motivated me even during the most complicated moments. She always has trusted in my capacity. Also, many thanks to Nayheli Iraís Estrada Nava, for her invaluable support.

My family deserves all my gratefulness, especially my mother Alejandra, and my sister Lucy, who have never stop to encourage me to keep going on. I want to give the most special thanks to my father, Antonio, that although I know I will never reach his steps, he will always be my role model.

And finally, thanks for the financial support to the National Council of Science and Technology (CONACyT) under the program “Padrón Nacional de Posgrados de Calidad” and the support with the fellowship for SNI III. Thanks to DGAPA-UNAM under PAPIIT-2018 project.

Agradecimientos

Este trabajo ha sido el resultado del esfuerzo empleado y dedicación que he tenido durante los años de maestría y doctorado en el Posgrado en Ciencias Físicas de la UNAM. Sin el apoyo y conocimiento brindado por muchas personas no habría podido llevar a cabo mi investigación.

Agradezco a mi tutor, el Dr. Rolando C. Castillo Caballero, quien me ha orientado en los momentos de dudas y me enseñó a desarrollar proyectos de investigación científica. De igual manera me apoyó siempre en los momentos más complicados durante el posgrado. A los profesores miembros de mi comité tutor, Dr. Denis Boyer y Dr. Héctor Domínguez Castro, por estar interesados en discutir y evaluar mi desempeño académico. Siempre aportaron sus valiosos puntos de vista para ayudar a mejorar mi investigación.

A todos los miembros del Grupo de Fluidos Complejos del IFUNAM: al M. en C. Salvador Ramos Solórzano, a la M. en C. Cristina Garza Lozano y a Erick Guzmán Gómez por sus enseñanzas y ayuda brindada en el laboratorio. A los colegas que se formaron antes de mí en el laboratorio y a los que continúan en él, por su ayuda y amistad; Paloma Vilchis León, Raziel Garza Melchor, Virginia Carrasco Fadanelli, Natalia Rincón Londoño, Ricky Frank López Santiago, Diego Colín Taboada, y en especial a Erick Sarmiento Gómez, Danaí Montalván Sorrosa y Brisa Arenas Gómez, quienes siempre estuvieron dispuestos a discutir mis dudas y me ayudaron con sus magníficas ideas y experiencia. También, mi agradecimiento a Marko Vinceković y Atiða Selmani, que en su momento fueron investigadores posdoctorales miembros del Grupo de Fluidos Complejos, quienes colaboraron en mi trabajo de investigación. A todos los colegas del área de Fluidos Complejos que he conocido en los congresos en México y fuera del país.

A los profesores miembros del jurado que evaluaron la tesis, Dra. Patricia Goldstein Menache, Dr. Roberto Zenit Camacho, Dr. Neil Charles Bruce Davidson y Dr. Ramón Castañeda Priego, por la revisión y valiosa aportación para la conclusión del documento. De igual manera agradezco a los profesores que estuvieron involucrados en la revisión del protocolo de investigación para el ingreso al doctorado, y a los profesores que me evaluaron en el examen de candidatura, Dr. Raúl Esquivel Sirvent, Dr. Jorge Delgado García, Dr. Carlos Ignacio Mendoza Ruiz, Dra. Anna Kozina, Dr. Pedro Díaz Leyva y Dr. Francisco Javier Sevilla Pérez.

De manera especial agradezco a la Dra. María Ester Brandan Siqués, quien siempre confió en mi desempeño académico desde el ingreso a la maestría. También al Dr. Rafael Pérez Pascual, anterior coordinador del posgrado por su apoyo para mi ingreso a la maestría en Física y al actual coordinador Dr. Alejandro Reyes Esqueda, quien siempre ha escuchado mis inquietudes y ha apoyado las ideas que he tenido como representante de los estudiantes en el Comité Académico del posgrado.

También, a los Técnicos Académicos del IFUNAM ya que sin su ayuda los experimentos y presentaciones no podrían haber salido adelante: Jorge I. Cruz Morales, Rodrigo Gutiérrez Arenas y Alberto García Ramírez. A todos los trabajadores administrativos del posgrado que de manera atenta estuvieron al pendiente de lo necesario, en especial a Isabel Mendoza Romero, Martha Tinoco González y Yanalté Herrero Quezadas, anterior encargada administrativa del posgrado. También agradezco la amabilidad y apoyo del personal de la biblioteca del IFUNAM, sobre todo a Guillermina Moreno Moreno, Catalina García García y Ma. de la Luz Vela Rosales.

A los profesores, Dra. Karen Volke Sepúlveda, Dra. Libertad Barrón Palos y Dr. Saúl Ramos Sánchez, que en su gestión como coordinadores docentes del IFUNAM han impulsado el proyecto del Seminario de Estudiantes llevado a cabo desde el 2012, con valioso aprendizaje y extraordinarias pláticas. Gracias al apoyo administrativo de María Guadalupe Sánchez Rojas y fotografías de Pedro Zaldívar Sánchez. También a los colegas que han pasado a través de la organización del seminario a quienes reconozco toda su dedicación. A Aleida Rueda Rodríguez, comunicadora de la ciencia del IFUNAM por sus enseñanzas. A Luis Novoa Sandoval y a Dulce Aguilar Téllez, actual y anterior diseñadores gráficos del IFUNAM, por la creación de grandiosos diseños para el seminario.

A todos los amigos con los que he compartido mi experiencia estudiando el posgrado en la UNAM y las vivencias en la Ciudad de México, pero de manera particular y muy especial a Deydreth Martínez Álvarez, quien me ha apoyado y motivado hasta en los momentos más complicados y siempre ha confiado en mí y en mis capacidades. Muchas gracias también a Nayheli Iraís Estrada Nava por el invaluable apoyo que me brindó.

A toda mi familia en especial a mi mamá Alejandra y mi hermana Lucy, de quienes no dejo de recibir ánimos y apoyo incondicional. Quiero dar el agradecimiento más especial a mi papá Antonio, que aunque sé que nunca alcanzaré sus pasos, siempre será mi modelo a seguir.

Finalmente, gracias por el apoyo económico a CONACyT bajo el programa de “Padrón Nacional de Posgrados de Calidad” y la beca otorgada de ayudante de investigador SNI III. Gracias a DGAPA-UNAM bajo el proyecto PAPIIT-2018.

Abstract

Complex fluids with embedded thread-like morphologies are interesting systems to study. These complex liquids with anisotropic particles are present widespread in nature rather than spherical ideal systems, and are widely used in the industry of food, pharmacy, cosmetics, and composite material. The advantage of their applications is due to the self-assembly mechanisms in which these liquids are involved at a mesoscopic scale. The cylindrical shapes lead to interconnections between the components of the liquid suspensions, giving an increase in the rigidity of the systems even when the compounds are soft, or stiff which work as a ladder giving rise to a connected network. The assembly processes remind us the dynamically arrested states such as colloidal and polymeric gels. Experimentally, obtaining the rheological properties of soft materials and their study with scattering techniques help us to understand their self-organization processes. Three model systems have been studied to understand the mechanisms that increase the rheological responses of interconnected thread-like morphologies.

1) A diblock copolymer (1,4 poly(1,3-butadiene)–polyethylene oxide), with degree of polymerization $m = 37$ for the polybutadiene block and $n = 57$ for the polyethylene oxide block (PBPEO57), was characterized in aqueous solution at different weight percentage concentration. The diblock copolymer self-assembles in water as worm-like micelles determined by small angle neutron scattering (SANS). Rheological experiments found an uncommon non Maxwellian relaxation behavior, rather than the worm-like micelles formed with surfactants. Performing microrheology experiments by diffusing wave spectroscopy (DWS), the mean square displacement of probe particles in the micellar solution was obtained. From the unilateral Fourier transform of the mean square displacement and applying a numerical inversion of the generalized Stokes-Einstein equation, the viscoelastic moduli at high frequencies was computed. $|G^*|$ exhibits a power law behavior showing that the stress relaxation changes as frequency increases, first dominated by the Rouse-Zimm modes and then by the bending modes of the Kuhn segments. This allowed the estimation of worm-like micelles persistence lengths that depend on the copolymer concentration, in agreement with the results obtained by SANS. As a comparison model, the same diblock copolymer was analyzed, but with a difference in size of the polyethylene oxide block, with a degree of polymerization of $n = 45$ (PBPEO45). The size modification of the polyethylene block produced different changes in aqueous solutions. The maximum possible concentration before phase separation for PBPEO45 was roughly one third of the maximum achievable for PBPEO57. The mechanical rheology results were quite different from PBPEO57, but with a better agreement with microrheology results. Structural analysis with SANS revealed a significant change just in the persistence length of the worm-like micelles, being stiffer the PBPEO57 worm-like micelles than the PBPEO45 micelles. Additionally, the inverse adding doubling method (IAD) was implemented for a first time in a complex fluid suspension in order to get the necessary optical parameters to perform DWS experiments. The IAD method quantifies the reduced scattering coefficient (inverse of the transport mean free path), the absorption coefficient (inverse of the absorption length), and the anisotropy factor of the sample at the same time. Several previous tests were done with water, spherical particle suspensions, and PEBPEO45 with the addition of an agent with absorption of light. These tests guaranteed good final experimental results.

2) Aqueous solutions of worm-like micelle aggregates done with the cationic surfactant cetyltrimethylammonium bromide with the counterion sodium salicylate (CTAB-NaSal) were studied. An extra feature presented in this system is the structural modification of the micelles after addition of the photo-responsive molecule 4-phenylazo benzoic acid (AzoCOOH, when deprotonated we call it AzoCOO). This molecule performs conformational structural changes (trans-cis isomerization) when light beams of certain wavelength strike the molecule. DWS microrheology experiments were performed and compared directly with mechanical rheology results. The IAD method was used to estimate the optical parameters of the samples which is primarily necessary because the photo-responsive molecule presents absorption of light. It turned out that the addition of AzoCOO reinforce the Maxwellian behavior of the systems when the molecule is maintained in trans state, and with no particular changes when it is stabilized in cis state. Hence, it was possible to obtain a set of values for the characteristic lengths of worm-like micelles.

3) Nanocomposite suspensions of single wall carbon nanotubes (SWCNTs) were prepared. Nevertheless, the poor solubility of carbon nanotubes and the fact that they are not prone to form dispersions lead to their potential applications difficult to be reached. Some polymers have been used effectively as exfoliation agents of nanotube bundles making possible the incorporation of the nanotubes as individual entities or as very thin bundles. Polyelectrolyte suspensions of poly(acrylic) acid (PAA) were chosen as dispersing medium candidate for the SWCNTs, with successful results. PAA presents a globular conformation in acidic aqueous state, and an almost elongated shape in basic aqueous state. Rheological experiments were performed to analyze the mechanical response of PAA suspensions at low concentrations, much lower before a gel state is encounter. The suspensions presented a viscoelastic regime with an increase in strength as the pH increase. When a small amount of SWCNTs is added to the PAA suspensions ($C_{\text{SWCNTs}} = 0.5, 1, \text{ and } 2 \text{ mg/mL}$), there is a huge change in the rheological response, and with the pH as a parameter to go from viscoelasticity to the gel regime. Under certain combination of PAA and SWCNT concentrations, the critical gel was found for suspensions at $\text{pH} = 7$ and 9 . To characterize the gel point, a critical gel model developed by F. Chambon and H. H. Winter was applied. This model assumes a power law behavior of the elastic and viscous moduli in the Fourier domain, and the same power law for the relaxation modulus in the time domain. The power law exponent found in the studied cases (always below 1), has a value in good agreement to the ones got for physical gels. A comparison with the values of the exponent for different systems allows to formulate that the exponent is a fingerprint of the studied gel, with achievable values below 0.5 for physical gels, and above 0.5 for chemically interconnected gels. Also, speculations of the hierarchical structure sizes of the formed gels was done, based on the exponent values found.

Resumen

Entre los fluidos complejos se consideran una gran variedad de sistemas, como soluciones poliméricas, coloides, cristales líquidos, surfactantes, soluciones de macromoléculas como materia biológica: proteínas, membranas celulares, ADN o virus. Todos los fluidos complejos se encuentran en la categoría de *Materia blanda*. Este tipo de materia suele construirse a partir de moléculas aisladas que se auto-ensamblan debido a fuerzas electrostáticas (van der Waals), interacciones entrópicas o interacciones estéricas, para dar origen a estructuras más complejas a escala mesoscópica. La entropía juega un papel vital para obtener estructuras que se organizan autónoma y espontáneamente en morfologías ordenadas y funcionales a escala supramolecular. Las escalas de longitud involucradas en la auto-organización de estos materiales se extienden desde aproximadamente 100 nm hasta 1.5 μm , donde los fluidos complejos comparten propiedades intrínsecas de distribución, orden y transporte que determinan la física del sistema, como la alta reacción a los campos externos, el tipo de transferencia de energía, la difusividad, las propiedades viscoelásticas y los fenómenos interfásicos. Por lo tanto, existe una fuerte relación entre los bloques de construcción moleculares, su orden a un nivel mesoscópico y su comportamiento macroscópico [1] [2] [3]. Además, el comportamiento físico de los fluidos complejos ocurre a una escala energética del orden de la energía térmica, por lo tanto, los procesos dinámicos y la activación pueden analizarse en condiciones ambientales [3] [4].

Existe una relación jerárquica entre estructuras a diferentes escalas de longitud. Estas escalas incluyen diferentes niveles, desde el microscópico donde las uniones químicas forman moléculas. Sus tamaños abarcan órdenes atómicos y moleculares hasta ~ 5 nm. La escala mesoscópica a la que se produce el auto-ensamblaje de las moléculas, que abarca tamaños desde ~ 50 nm hasta ~ 1.5 μm . Y finalmente, la escala macroscópica que alcanza tamaños por arriba de ~ 2 μm . A esta escala se puede observar experimentalmente la mayoría de las respuestas en los fluidos complejos. En casos particulares los nano compuestos desarrollan una conectividad entre ellos debido a las interacciones energéticas y entrópicas, generando una red interconectada que se extiende hasta los tamaños mesoscópicos, formando materiales viscoelásticos fuertes. Existe la posibilidad de traspasar los límites de equilibrio termodinámico que dan lugar a la formación de geles físicos y químicos, e incluso vidrios cuando las interacciones de volumen excluido se vuelven relevantes. Los pilares básicos de ensamblaje para estos diferentes materiales nano estructurados pueden ser partículas esféricas coloidales, o partículas anisotrópicas como varillas rígidas; pero también, elementos más alargados y sistemas semiflexibles como cadenas poliméricas, que en principio son suaves pero dinámicas y resistentes al mismo tiempo. Una revisión con perspectivas futuras en el campo de los materiales poliméricos interconectados, con el objetivo de identificar y unificar los principios que controlan los mecanismos de endurecimiento y el comportamiento mecánico de autocuración se puede encontrar en [5]. Se presume que la anisotropía de las partículas filiformes y sus interacciones atractivas de corto alcance pueden afectar significativamente la competencia entre estados cinéticamente arrestados, equilibrio de fases, microestructuras auto-ensambladas y propiedades reológicas macroscópicas. El proyecto que se detalla en esta tesis tiene la intención de entender y apreciar diversas formas y funciones de objetos anisotrópicos que la naturaleza genera a nivel microscópico y macroscópico.

Por otro lado, los fluidos complejos han tomado gran importancia en las aplicaciones tecnológicas. Los coloides son elementos base en la industria de los polímeros, las pinturas y los adhesivos. También se utilizan para la elaboración de cosméticos y alimentos, o incluso como fluidos geológicos. Los cristales líquidos son comúnmente utilizados en el diseño de pantallas y biosensores; los fosfolípidos son los bloques elementales para la creación membranas celulares y diferentes tipos de jabones. Incluso existe el desarrollo de la tecnología robótica suave. Científicos se inspiran en la aparente simplicidad y la verdadera complejidad de la naturaleza, soñando para imitarla, lo que da pie para desarrollar ingeniería de materia blanda. Hoy en día se emplean toda clase de materiales con una amplia gama de propiedades mecánicas, físicas y químicas, desde líquidos y geles hasta sólidos orgánicos e inorgánicos. Una buena revisión de las aplicaciones actuales se puede encontrar en [6].

Los procesos de auto-ensamblaje pueden dividirse en estáticos o dinámicos. Las diferencias entre ellos radican en la descripción termodinámica de los sistemas resultantes. Los primeros son estructuras que se acercan al equilibrio a medida que se organizan, reduciendo su energía libre hasta alcanzar la estabilidad termodinámica. En cambio, los sistemas resultantes de procesos dinámicos son estructuras estables con menos entropía, formados fuera de equilibrio. Estas estructuras se obtienen como resultado del suministro constante de energía que posteriormente se disipa durante un estado cuasi estacionario [7]. Este tipo de auto-ensamblaje se inspira en los sistemas biológicos, que son difíciles de estudiar desde el punto de vista físico debido a su complejidad. En general, el estudio de sistemas auto-ensamblados se ha convertido en un trabajo cooperativo entre físicos, químicos, ingenieros, biólogos y médicos. Una revisión extensa de las diferentes áreas de estudio de la materia blanda se puede encontrar en [8], la cual incluye coloides, materiales granulares, espumas, emulsiones, cristales líquidos, polímeros, sistemas activos, materia adaptativa, simulaciones y macrodatos, con énfasis en la constante cooperación entre el científico experimental, computacional y teórico, para obtener grandes resultados.

Existe la posibilidad de adaptar las funcionalidades de los materiales suaves de manera no covalente, para construir materiales inteligentes. Explotando las propiedades intrínsecas de la capacidad de respuesta a distinto tipo de interacciones, se han desarrollado diferentes mecanismos de auto-organización de la materia, como sensores, materiales auto-curables, dispositivos piezoeléctricos, dispositivos sensibles a estímulos externos o materiales capaces de controlar la entrega de sustancias químicas en organismos vivos. La idea general para la construcción de estructuras adaptativas es el diseño ingenioso de los bloques base para que respondan a estímulos externos. Los bloques de construcción y sus interacciones no covalentes permiten que todo el sistema responda a diferentes tipos de estímulos externos, abordados en tres clases de adaptabilidad diferentes: (1) adaptabilidad al medio ambiente, incluyendo auto-ensamblajes inteligentes adaptables a cambios de pH, temperatura, presión y humedad; (2) adaptación química especial, incluidas las nanoestructuras adaptables a enzimas, CO_2 , iones metálicos, agentes de óxido-reducción, explosivos, biomoléculas, entre otras; (3) adaptación a campos externos incluyendo el auto-ensamblado de materiales que son capaces de adaptarse a campos magnéticos o eléctricos, irradiación de luz y fuerzas de cizallamiento. Se puede encontrar una revisión detallada de los sistemas adaptativos en [9].

La investigación que se resume en este documento incluye la búsqueda de las propiedades mecánicas y la estructura mesoscópica de tres sistemas adaptativos que incluyen estructuras filiformes:

adaptación a los cambios de grado de polimerización en cadenas de polímeros, cambios conformacionales bajo exposición a la luz, y cambios cuando se modifica el pH. Los objetivos se centran en la comprensión de los mecanismos que aumentan la respuesta reológica de las estructuras filiformes para cada sistema. Estos sistemas son:

1) Un copolímero de dos bloques (1, 4 poli (1, 3-butadieno)–polióxido de etileno), con grado de polimerización $m = 37$ para el bloque de polibutadieno y $n = 57$ para el bloque de polióxido de etileno (PBPEO57), caracterizado en solución acuosa a diferente concentración porcentual en peso. El copolímero se auto-ensambla en agua en forma de micelas tubulares. Esta estructura ha sido determinada con experimentos de dispersión de neutrones de ángulo bajo (SANS, en inglés). También se realizó un estudio comparativo con el mismo PBPEO pero con un número diferente de bloques para el polióxido de etileno ($n = 45$) llamado PBPEO45.

2) Resultados preliminares obtenidos en el estudio de soluciones acuosas de agregados de micelas tubulares realizadas con el surfactante catiónico bromuro de cetiltrimetilamonio y con el contraión salicilato de sodio (CTAB-NaSal). Varios estudios previos han sido realizados con este sistema, sin embargo, el sistema estudiado en el proyecto doctoral se modifica con la adición de una molécula fotosensible, 4-(fenilazo) ácido benzoico (AzoCOOH, cuando se desprotona lo hemos llamado AzoCOO). Esta molécula realiza cambios estructurales conformacionales, de isomerización trans a isomerización cis cuando luz de cierta longitud de onda irradia a la molécula. Se ha encontrado que la adición de esta molécula, en el estado trans, refuerza el comportamiento Maxwelliano de los sistemas micelares de CTAB-NaSal, y no se encontró un cambio sustancial una vez que la molécula migra al estado cis. También se estudiaron micelas tubulares auto-ensambladas a partir del surfactante zwitteriónico, NtetradecilN,N-dimetil-3-amonio-1-propanosulfonato, con el co-surfactante aniónico sulfato dodecil de sodio (TDPS-SDS). A estas micelas también se les añadió AzoCOOH, sin embargo, los resultados no se presentan en la tesis. De esta manera, el estudio de dos sistemas diferentes con afinidades iónicas diferentes ha ayudado a incrementar nuestro conocimiento sobre agregados macromoleculares fotosensibles con morfologías anisotrópicas alargadas.

3) Suspensiones de nanocompuestos de nanotubos de carbono de pared simple (SWCNTs, en inglés) fueron preparadas. Sin embargo, la escasa solubilidad de los nanotubos de carbono y el hecho de que no son propensos a formar dispersiones provoca que sea complicado alcanzar varias de sus potenciales aplicaciones. Algunos polímeros se han utilizado efectivamente como agentes de exfoliación de los paquetes de nanotubos haciendo posible la incorporación de éstos como entidades individuales o como paquetes muy delgados. Suspensiones de ácido poliacrílico (PAA, en inglés) fueron elegidas como medio dispersor para los SWCNTs, con resultados acertados.

Antes de presentar los resultados experimentales, en el capítulo II se muestra una introducción a la teoría de los polímeros semiflexibles. Aquí se hace una revisión del movimiento de partículas Brownianas (sección II.2). Luego, tomando las ecuaciones de Smoluchowski y Langevin como elementos teóricos fundamentales, se revisitan los modelos de Rouse-Zimm en el régimen diluido (sección II.3). A continuación se muestra una breve introducción a la viscoelasticidad en suspensiones poliméricas diluidas (sección II.4). En la sección II.5 se discute el modelo de reptación de los polímeros en régimen semidiluido, dando lugar más adelante a la presentación de las características de los

polímeros vivos (sección II.6). El modelo común de los sistemas de polímeros vivos es el de micelas tubulares, que se introducen en la sección II.7. Al final del Capítulo II se presenta una breve discusión sobre la formación de geles (sección II.8) y se dan algunas características de los nanotubos de carbono y los polielectrolitos (sección II.9).

En el capítulo III se presentan las técnicas experimentales utilizadas durante la investigación. En las secciones III.1 y III.2 se muestra el formalismo de reología y el fondo teórico de reometría respectivamente. La sección III.3 está dedicada a introducir los diferentes experimentos de dispersión de luz utilizados. Se presenta una introducción a dispersión dinámica de luz (DLS, en inglés) incluyendo la espectroscopía de onda difusa (DWS, en inglés) para obtener información microreológica. Al final de la sección, se presenta el formalismo de dispersión estática de luz (SLS, en inglés), con énfasis en las similitudes entre las diferentes fuentes de luz que se pueden utilizar. En la sección III.4 se presentan pruebas y resultados preliminares para los experimentos de dispersión de luz, las cuales es necesario realizar antes de llevar a cabo los experimentos finales.

En el capítulo IV se muestra el desarrollo experimental y los resultados. Primero el desarrollo de la investigación de las micelas tubulares de copolímeros de bloque (PBPEO) (sección IV.1). Son presentados los resultados de los experimentos de reología mecánica. Estas micelas presentan un comportamiento de relajación no Maxwelliano, a diferencia de las micelas tubulares comunes formadas con surfactantes. También se muestran los resultados de DWS con información microreológica, donde se obtuvo el desplazamiento cuadrado medio de partículas trazadoras embebidas en la solución micelar. Con los espectros viscoelásticos complejos fue posible extraer información estructural de los agregados de micelas tubulares. También fue posible estimar la longitud de persistencia de las micelas tubulares mediante la búsqueda de cambios en los mecanismos de relajación, desde relajación por modos de Rouse-Zimm a ciertas frecuencias, hasta los modos de oscilación de plegado de los segmentos de Kuhn a frecuencias más altas. Estas longitudes de persistencia resultaron dependientes de la concentración de copolímero. Las longitudes de persistencia encontradas concuerdan satisfactoriamente con los resultados obtenidos por SANS. El análisis estructural con SANS reveló un cambio significativo sólo en la longitud de persistencia de las micelas tubulares, siendo más rígidas las micelas de PBPEO57 que las micelas de PBPEO45. Adicionalmente, el método de duplicación inversa (IAD, Inverse Adding Doubling en inglés) se implementó por primera vez en una suspensión compleja para obtener los parámetros ópticos necesarios para realizar los experimentos de DWS.

En la sección IV.2 se introducen los resultados preliminares obtenidos en el estudio de soluciones acuosas de agregados de micelas tubulares de CTAB-NaSal con la adición de la molécula fotosensible AzoCOO (estabilizada en medio básico). Aquí se muestran los resultados de microreología por DWS, y se comparan directamente con los resultados de reología mecánica. También se presenta un conjunto de valores calculados para las longitudes características de las micelas. Se enfatiza el hecho de que la molécula fotosensible absorbe la luz, por lo cual, el uso del método IAD se vuelve totalmente necesario para evitar interpretaciones erróneas de los resultados de DWS debidas a las pérdidas por absorción de luz. Se muestran los valores obtenidos de los parámetros ópticos de las muestras estudiadas. El estudio completo es parte del proyecto doctoral de Natalia Rincón Londoño.

En la sección IV.3 se presentan los resultados relacionados con el sistema de SWCNTs y PAA. El ácido poliacrílico presenta una conformación globular en estado acuoso a pH ácido, y una forma casi alargada en estado acuoso a pH básico. Los experimentos reológicos de las suspensiones de PAA se realizaron a concentraciones mucho más bajas que las necesarias para alcanzar un estado de gel. Las suspensiones presentaron un régimen viscoelástico con un aumento en la respuesta de los módulos al aumentar el pH. Cuando se añade una pequeña cantidad de SWCNTs a las suspensiones de PAA ($C_{\text{SWCNTs}} = 0.5, 1, \text{ and } 2 \text{ mg/mL}$), hay un cambio considerable en la respuesta reológica, donde el pH juega el papel de parámetro sintonizable para lograr una transición de viscoelasticidad a gel. Bajo cierta combinación de las concentraciones de PAA y de SWCNTs, el gel crítico fue encontrado para las suspensiones a $\text{pH} = 7$ y 9 . Se aplicó el modelo de ley de potencia para geles críticos desarrollado por F. Chambon y H. H. Winter. Los resultados muestran que el exponente de la ley de potencias que se encuentra en los casos estudiados (siempre por debajo de 1), tiene un valor que concuerda con los valores encontrados para geles físicos antes estudiados. Una comparación con los valores del exponente para diferentes sistemas permite inferir que el exponente es una huella digital del gel estudiado. Al final, se hicieron especulaciones de los tamaños jerárquicos de la estructura de los geles formados, basados en los valores de los exponentes encontrados.

Por último, se presentan las conclusiones finales en el capítulo V y en el capítulo VI las carátulas de los artículos publicados como resultado de las investigaciones.

General Goals

- To study the structure and mechanical properties of thread-like morphologies embedded in complex fluids.
- To understand the self-assembly dynamics of these systems, how they aggregate, and how the aggregation and dynamics have an effect at mesoscopic level.
- Obtaining the optical properties of these complex fluids, when they scatter and present absorption of light, to then perform microrheology experiments with light scattering.

Contents

| | |
|--|-----------|
| ACKNOWLEDGMENTS..... | vii |
| AGRADECIMIENTOS..... | viii |
| ABSTRACT..... | xi |
| RESUMEN..... | xiii |
| GENERAL GOALS..... | xix |
| I. INTRODUCTION..... | 1 |
| 1. MICROSCOPIC AND MESOSCOPIC APPROACH..... | 3 |
| 2. OUTLINE OF THESIS..... | 3 |
| II. THEORY OF POLYMERS..... | 7 |
| 1. INTRODUCTION..... | 7 |
| 1.1. Polymer concentrations..... | 8 |
| 2. BROWNIAN MOTION: SMOLUCHOWSKI AND LANGEVIN EQUATIONS..... | 9 |
| 2.1. Smoluchowski equation..... | 9 |
| 2.2. Langevin equation..... | 12 |
| 2.3. Interacting particles..... | 13 |
| 3. CLASSICAL THEORY OF FLEXIBLE POLYMERS: DILUTED REGIME..... | 15 |
| 3.1. The Rouse model..... | 17 |
| 3.2. The Zimm model..... | 19 |
| 4. VISCOELASTICITY IN DILUTED POLYMERIC SUSPENSIONS..... | 20 |
| 5. REPTATION MODEL: SEMIDILUTE REGIME..... | 22 |
| 6. LIVING POLYMERS..... | 26 |
| 7. WORM-LIKE MICELLES..... | 27 |
| 7.1. Surfactant worm-like micelles..... | 28 |
| 7.2. Block copolymer worm-like micelles..... | 32 |
| 8. GELS..... | 34 |
| 8.1. Model for critical gels..... | 37 |
| 9. SINGLE WALL CARBON NANOTUBES AND POLYELECTROLYTES..... | 38 |
| III. EXPERIMENTAL TECHNIQUES..... | 43 |
| 1. RHEOLOGY..... | 43 |
| 1.1. Maxwell model..... | 44 |
| 1.2. Linear response: the Boltzmann superposition principle..... | 45 |
| 1.3. Oscillatory shear..... | 47 |
| 2. RHEOMETRY..... | 49 |

| | |
|---|------------|
| 3. LIGHT SCATTERING | 53 |
| 3.1. Dynamic Light Scattering (DLS) | 54 |
| 3.2. Diffusing Wave Spectroscopy (DWS)..... | 57 |
| 3.3. DWS for media with light absorption | 62 |
| 3.4. Microrheology | 64 |
| 3.5. Static Light Scattering (SLS) | 68 |
| 4. EXPERIMENTAL DETAILS AND PROCEDURE..... | 77 |
| 4.1. Diffusing Wave Spectroscopy (DWS)..... | 77 |
| 4.2. Small Angle Neutron Scattering (SANS) | 88 |
| | |
| IV. EXPERIMENTAL RESULTS..... | 91 |
| 1. PBPEO WORM-LIKE MICELLES | 91 |
| 1.1. Motivation and purpose..... | 91 |
| 1.2. Specific goals..... | 91 |
| 1.3. Materials and sample preparation | 92 |
| 1.4. Structure of the PBPEO aggregates..... | 93 |
| 1.5. Rheology results..... | 100 |
| 1.6. Microrheology results..... | 103 |
| 1.7. An attempt to connect microrheology with mechanical rheology | 107 |
| 1.8. Microrheology and structure..... | 111 |
| 1.9. PBPEO worm-like micelles' conclusions..... | 113 |
| 2. PHOTORESPONSIVE WORM-LIKE MICELLES..... | 115 |
| 2.1. Motivation and purpose..... | 115 |
| 2.2. Specific goals..... | 116 |
| 2.3. Materials and sample preparation | 116 |
| 2.4. Microrheology results..... | 117 |
| 2.5. Photoresponsive worm-like micelles' conclusions..... | 124 |
| 3. SUSPENSIONS OF SWCNTs IN A POLYELECTROLYTE | 125 |
| 3.1. Motivation and purpose..... | 125 |
| 3.2. Specific goals..... | 125 |
| 3.3. Materials and sample preparation | 126 |
| 3.4. Rheology results for PAA..... | 127 |
| 3.5. Mesoscale structure of SWCNTs/PAA suspensions | 131 |
| 3.6. Rheology results for SWCNTs/PAA | 134 |
| 3.7. Rheological model for the SWCNTs/PAA suspensions..... | 138 |
| 3.8. Suspensions of SWCNTs in a polyelectrolyte conclusions..... | 142 |
| | |
| V. SUMMARY AND CONCLUSIONS..... | 145 |
| 1. PBPEO WORM-LIKE MICELLES | 145 |
| 2. PHOTORESPONSIVE WORM-LIKE MICELLES..... | 146 |
| 3. SUSPENSIONS OF SWCNTs IN A POLYELECTROLYTE | 147 |
| 4. CONCLUDING REMARKS AND FUTURE PERSPECTIVES..... | 148 |
| | |
| VI. PUBLISHED WORKS | 151 |
| REFERENCES..... | 153 |

I. Introduction

The developing of techniques for treating materials has influenced human history. The main necessities for human survival were changing in each era of history accompanied by the evolution of the different applications of a variety of materials discovered at every moment. Humans have used naturally occurred complex materials, much more common than simple ones, without realizing that they were dealing with *macromolecules*. Nowadays, particularly during the 20th century, the develop of new techniques try to enhance the quality of life of communities with the use of new theoretical approaches and computer simulations. Understanding the basic structures of materials has come with the development of never before imaged technologies. In particular, the study of materials in the liquid state is now a significant multidisciplinary area of research which combines the knowledge of physicist, chemist, engineers, biologists, and experts in medical disciplines. These sort of soft systems are commonly called *Complex Fluids*.

Complex fluids consider a great variety of systems, like polymer solutions, colloids, liquid crystals, surfactants, macromolecules solutions like biological matter: proteins, cellular membranes, DNA or viruses. All complex fluids lie in the category of *Soft Matter* which is built up from isolated molecules that self-assemble due to electrostatic forces (van der Waals), entropic interactions or steric interactions, to give born to more complex structures, already mentioned, at a mesoscopic scale. The entropy plays a vital role to get structures that organize autonomously and spontaneously in ordered and functional morphologies at a supramolecular scale. These length scales span over from approximately 100 nm to 1.5 μm , where complex fluids share peculiar intrinsic properties of distribution, order, and transport which determine the physics of the system as the high reaction to external fields, energy transfer, diffusivity, viscoelastic properties, and interphase phenomena. Therefore, there is a strong relationship among the molecular building blocks, their order at a mesoscopic level and their macroscopic behavior [1] [2] [3]. Also, the physical behavior of complex fluids occurs at an energy scale of the order of thermal energy. Hence the dynamical processes and activation could be analyzed at ambient conditions [3] [4]. Figure I.1 shows the *triangle of Soft Condensed Matter*, taken from the European Journal of Physics E editorial [10] which presents a unified vision of different systems studied continuously in the field of soft matter, and emphasizes the relationship between their building blocks.

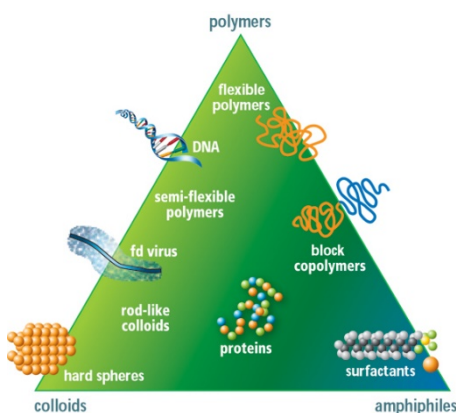


Figure I.1 Soft condensed matter triangle. It unifies different systems where their amphiphilic character, surface responses, electrostatic interactions and flexibility are enlightened [10].

It is worth to further mention the importance of complex fluids in technological applications. In polymer industry, paints and adhesives, colloids are base elements. They are also used for the elaboration of cosmetics and food, or are contained within geological fluids. Liquid crystals are commonly used in the design of electronic screens and biosensors; phospholipids are base building blocks for cellular membranes and different sort of soaps for cleaning necessities; and there is even a development of soft robotic technology. Scientists are inspired by the apparent simplicity and true complexity of nature, dreaming to mimic nature to create a world of engineered soft matter devices. All conceivable classes of materials with a wide range of mechanical, physical and chemical properties are employed, from liquids and gels to organic and inorganic solids. Functionalities never seen before are achieved. A nice review of current applications can be found in [6].

The self-assembly processes can be divided into static or dynamic. The differences among them lie in the thermodynamic description of the resulting systems. The former are structures which approach to equilibrium as they are organized, reducing their free energy until reach thermodynamic stability. The latter are stable structures with less entropy, formed out of equilibrium. These structures are obtained as a result of the constant supply of energy which subsequently is dissipated during a quasi-stationary state [7]. This sort of self-assembly is inspired by biological systems, which are hard to study from the point of view of physicists due to their complexity. In general, the study of self-assembled systems has become a cooperative job among physicists, chemists, engineers, biologists, and physicians. An extended review of different areas of study of soft matter (colloids, granular materials, foams and emulsions, liquid crystals, polymers, active and adaptive matter, simulations and big data), with an emphasis in the constant needed cooperation between experimental, computational and theoretical scientist, to obtain great results can be found in [8].

Among all systems with valuable applications that have been mentioned, there exists the possibility to adapt their functionalities in a non-covalent manner, to construct smart materials in various fields. Exploiting the intrinsic properties of responsiveness of non-covalent interactions, a great number of fancy self-assemblies have been achieved such as controlled-delivery, sensors, self-healing materials, piezoelectric devices, mechanochromism, or stimuli responsive devices. The general idea for the construction of adaptive architectures is to ingeniously design building blocks which may respond to external stimuli, and to produce self-assembly of these building blocks through multiple noncovalent interactions. The building blocks and the non-covalent interactions run together to allow the whole system to respond to different types of external stimuli, addressed in three different adaptiveness classes: (1) environmental adaptiveness, including smart self-assemblies adaptive to pH, temperature, pressure, and moisture; (2) special chemical adaptiveness, including nanostructures adaptive to important chemicals, such as enzymes, CO₂, metal ions, redox agents, explosives, biomolecules; (3) field adaptiveness, including self-assembled materials that are capable of adapting to external fields such as magnetic field, electric field, light irradiation, and shear forces. A better detailed review for adaptive systems can be found elsewhere [9].

1. Microscopic and mesoscopic approach

There exists a hierarchical relation between structures at different length scales for complex fluids. These scales include different levels, from the microscopic at the molecular level, where the chemical unions form molecules. Their sizes span over atomic and molecular order up to ~ 5 nm. The mesoscopic scale at which the self-assembly of molecules occurs, span over ~ 50 nm up to ~ 1.5 μm . And finally, the macroscopic scale which reaches sizes above ~ 2 μm . At this scale, we can observe experimentally most of the complex fluids responses. In particular cases, the nano-compounds develop a connectivity among them due to energetic and entropic interactions, generating an interconnected network which extend up to mesoscopic sizes, forming strong viscoelastic materials, and even stronger materials as rubbers. There exists the possibility to trespass the thermodynamic equilibrium boundaries giving place to the formation of physical and chemical gels, and when the excluded volume interactions become stronger, glasses can be formed. The basic building blocks for these different nano-structured materials can be colloidal spherical particles, or anisotropic particles like rigid rods; but also, more elongated elements and semiflexible systems as polymeric chains, which in principle are soft but dynamic and tough at the same time. A review with future perspectives in the field of connected polymeric materials, with the aims to identify and unify the underlying principles of controlling toughening mechanisms and mechanical self-healing behavior can be found in [5]. It is hypothesized that the anisotropy of rod-like particles with short-range attractions can significantly affect the competition between kinetically arrested states, equilibrium phases, self-assembled microstructures, and macroscopic rheological properties. Hopefully one can appreciate the diverse forms and functions of anisotropic objects that nature generates on a microscopic and a macroscopic level.

2. Outline of thesis

The research includes seeking on the mechanical properties and mesoscopic structure of three adaptive systems: adaptiveness to polymerization size changes in polymer chains, conformational changes under light exposure, and changes when pH is modified, respectively. The aims are focused in understanding the mechanisms that increase the rheological responses of the interconnected thread-like morphologies within each system. These systems are:

1) A diblock copolymer (1,4 poly(1,3-butadiene)–polyethylene oxide), with degree of polymerization $m = 37$ for the polybutadiene block and $n = 57$ for the polyethylene oxide block (PBPEO57), characterized in aqueous solution at different weight percentage concentration. The diblock copolymer self-assembles in water as worm-like micelles determined by small angle neutron scattering (SANS). A comparison study with the same PBPEO but with different number of blocks for the polyethylene ($n = 45$, called PBPEO45) was performed.

2) Preliminary results obtained in the study of aqueous solutions of worm-like micelle aggregates done with the cationic surfactant cetyltrimethylammonium bromide with the counterion sodium salicylate (CTAB-NaSal). Previous studies have been largely made with this system, however, our

system is modified with the addition of a photo-responsive molecule 4-(phenylazo) benzoic acid (AzoCOOH, when deprotonated we call it AzoCOO⁻) which perform conformational structural changes (trans-cis isomerization) when light beams of certain wavelength strike the molecule. The addition of this photo-responsive molecule, even at trans configuration, reinforce the Maxwellian behavior of the systems. When the molecule is stabilized at cis state, no particular changes were observed. Also worm-like micelle macromolecules of zwitterionic surfactant, N-tetradecyl-N,N-dimethyl-3-ammonio-1-propanesulfonate with the anionic cosurfactant sodium dodecyl sulfate (TDPS-SDS) were studied, with the addition of AzoCOOH as well, however results are not presented. Nonetheless, the study of two different systems with different ionic affinities works to increment our knowledge in photo-responsive macromolecular aggregates with thread-like morphologies.

3) Nanocomposite suspensions of single wall carbon nanotubes (SWCNT) were prepared. Nevertheless, the poor solubility of carbon nanotubes and the fact that they are not prone to form dispersions lead to their potential applications difficult to be reached. Some polymers have been used effectively as exfoliation agents of nanotube bundles making possible the incorporation of the nanotubes as individual entities or as very thin bundles. Polyelectrolyte suspensions of poly(acrylic acid) (PAA) were chosen as dispersed medium candidate for the SWCNT, with successful results.

Before presenting the experimental results, an introduction to the theory of semiflexible polymers is shown in Chapter II. Here, there is a review of particle Brownian motion (section II.2). Then, taking Smoluchowski and Langevin equations as the basic formalisms for Brownian dynamics in polymeric chain components, the Rouse-Zimm models in diluted regime are revisited (section II.3). Next, a brief introduction to viscoelasticity in diluted polymeric suspensions is shown (section II.4). In section II.5 the reptation model for polymers in semidilute regime is discussed, giving place later to the presentation of the characteristics of living polymers (section II.6). The common model of living polymers systems is worm-like micelles, which are introduced in section II.7. At the end of Chapter II, a brief discussion about formation of gels is presented (section II.8) and some characteristics of carbon nanotubes and polyelectrolytes are given (section II.9).

In Chapter III the experimental techniques used during the research are presented. In sections III.1 and III.2 the rheology formalism is shown and the theoretical background for rheometry as well respectively. Section III.3 is devoted to introducing the different light scattering experiments used. An introduction to dynamic light scattering (DLS) including diffusing wave spectroscopy (DWS) to get microrheology information is revisited. At the end of the section, the formalism of static light scattering (SLS) is reviewed, with an emphasis in the similarities among the different sources of light that can be used. In section III.4 tests and preliminary results for light scattering experiments necessary to get before performing the final experimental research are presented.

In Chapter IV the experimental development and results are shown. First the concerning to both PBPEO diblock copolymers worm-like micelles (section IV.1). Results for rheological experiments are shown, which present an uncommon non Maxwellian relaxation behavior, rather than the common worm-like micelles formed with surfactants. Additionally, DWS results show microrheological information, where the mean square displacement of probe particles in the micellar

solution was obtained. With the complex viscoelastic spectra was possible to extract valuable structural information of the worm-like micelle aggregates. Estimation of worm-like micelles persistence lengths was possible through finding relaxation mechanisms changes, from Rouse-Zimm modes to bending modes of the Kuhn segments. These persistence lengths are copolymer concentration depended, and sizes results to be in agreement with the results obtained by SANS. Structural analysis with SANS revealed a significant change just in the persistence length of the worm-like micelles, being stiffer the PBPEO57 worm-like micelles than the PBPEO45 micelles. Additionally, the inverse adding doubling method (IAD) was implemented for a first time in a complex fluid suspension in order to get the necessary optical parameters to perform DWS experiments.

In section IV.2 we introduce the preliminary results obtained in the study of aqueous solutions of worm-like micelle aggregates done with CTAB-NaSal with the addition of the photo-responsive molecule AzoCOO (stabilized in basic medium). Here there are shown some DWS microrheology results which are compared directly with the mechanical rheology results. A set of calculated values for the characteristic lengths of micelles is also presented. It is emphasized the fact that the photo-responsive molecule absorbs light, then the use of the IAD method is primarily necessary to avoid misinterpretations of DWS results. Measured values of the obtained optical parameters are shown. The complete study is under development of Natalia Rincón-Londoño, as her doctoral project.

In section IV.3 the results related with the system of SWCNT and PAA are presented. Poly(acrylic) acid presents a globular conformation in acidic aqueous state, and an almost elongated shape in basic aqueous state. Rheological results of PAA suspensions are shown at low concentrations, much lower before a gel state is encounter. The suspensions presented a viscoelastic regime with an increase in strength as the pH increase. When a small amount of SWCNT is added to the PAA suspensions ($C_{\text{SWCNTs}} = 0.5, 1, \text{ and } 2 \text{ mg/mL}$), rheology experiments were performed, and the results are also presented. There is a huge change in the rheological response, and with the pH as a parameter to go from viscoelasticity to the gel regime. Under certain combination of PAA and SWCNT concentrations, the critical gel was found for suspensions at $\text{pH} = 7$ and 9 . We applied the power law model for critical gels developed by F. Chambon and H. H. Winter. Presented results show that the power law exponent found in the studied cases (always below 1), has a value in good agreement to the ones got for physical gels. A comparison with the values of the exponent for different systems allows to formulate that the exponent is a fingerprint of the studied gel. At the end, speculations of the hierarchical structure sizes of the formed gels was done, based on the exponent values found.

Finally, the concluding remarks are presented in Chapter V, and the cover headings of the published articles are presented in Chapter VI.

II. Theory of polymers

1. Introduction

As has been mentioned in the last chapter, complex fluids are materials built up from basic macromolecular blocks which are assembled in the mesoscopic scale, giving rise to peculiar macroscopic behaviors. Depending on the sizes and interactions among the building blocks, the resulting mesoscopic structures can present different macroscopical responses: viscoelasticity, gelation, vitrification, solidification, etc. The resulting response is also altered by the thermodynamic state of the system; in some cases, in equilibrium, and in many other interesting cases, out of equilibrium; as well as when the system is subjected to deformation.

This work focuses on the viscoelastic response of certain complex fluids, and in a particular case of gelation. To understand the viscoelastic and gel behavior, it is essential to describe the dynamics of these macromolecules in liquid state. The most convenient approach is the theory of polymers, which is possible to be applied for understanding different thread-like systems like: worm-like micelles and carbon nanotubes embedded in a polyelectrolyte matrix; always forming liquid solutions or suspensions. One can find in the literature different approaches and explanations for polymer dynamics. Here is presented the classic formalism used by M. Doi and S. F. Edwards [11], and M. Rubinstein and R. H. Colby [12]. In the case of classic polymers, there exist two limits: (a) highly flexible polymers, where, on a sufficiently large scale, the polymer appears as a random walk with a step length much smaller than the length of the whole polymer (Figure II.1a), and (b) rigid polymer rods (Figure II.1b) with a persistence length larger than the polymer chain length. At ambient temperature, these polymers are in thermal agitation, and as individual entities (in diluted regime), we are allowed to study them in a Langevin (or Smoluchowski) approximation, figuring out that the constituent components of the chains are subjected to a constant interaction with the particles of solvent (much smaller than the basic blocks of the polymers). At higher concentrations, (semi-dilute and concentrated regimes) as shown in Figure II.1c and d; there must be considered the impeded dynamics of a single polymer chain due to the interactions between different polymer chains. Here, to understand the relaxation mechanism of polymeric chains, it is useful the concept of *tube* where the polymer is engaged until the moment where the stress relaxes completely. We will come back to this concept when the reptation model is described.

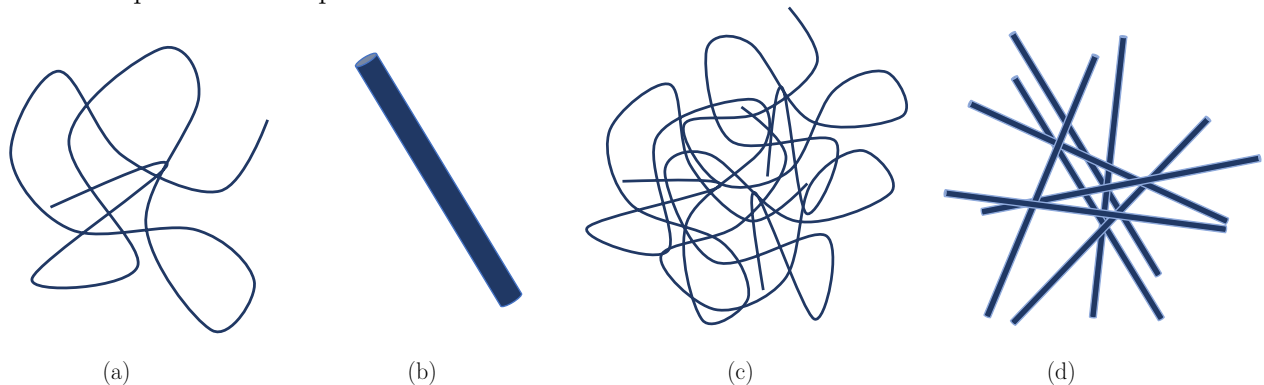


Figure II.1 (a) Flexible polymer, (b) rod-like polymer, (c), (d) their concentrated solutions.

1.1. Polymer concentrations

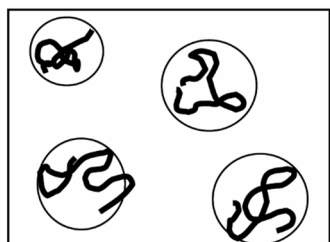
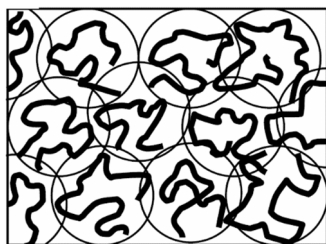
(a) Dilute ($c < c^*$)(b) Overlap ($c = c^*$)(c) Overlap ($c > c^*$)

Figure II.2 Solution regimes of flexible polymers. Taken from [12].

For ideal polymeric chains, there are no interactions between monomers that are far along the chain, even if they approach each other in space. Ideal chains are good models for polymer melts, concentrated solutions, and solutions at θ -temperature. This section and subsequent are restricted to the study of ideal chains of polymers in good solvent solutions.

Polymer solutions are classified as dilute or semidilute (sometimes also concentrated) depending on the polymer mass concentration c , the ratio of the total mass of polymer dissolved in a solution, and the volume of the solution. An alternative measure of concentration is the volume fraction ϕ , the ratio of occupied volume of the polymer in the solution and the volume of the solution. These two concentrations are related through ρ , the polymer density; $c = \phi\rho$. The pervaded volume V is the volume of solution spanned by the polymer chain, $V \approx R^3$, where in this case R is the size of the chain. This volume is typically orders of magnitude larger than the occupied volume of the chain, which is the sum of the volume occupied by each monomer. The volume fraction of a single molecule inside its pervaded volume is called the *overlap volume fraction* ϕ^* or in terms of concentration it is known as the *overlap concentration* c^* .

If the concentration of the polymer solution is equal to the overlap concentration, the pervaded volumes of macromolecules densely fill space and chains are just at overlap ($c = c^*$) (see Figure II.2b). If the polymer concentration is below the overlap concentration, the solution is diluted ($c < c^*$) and therefore, the average distance between chains is larger than their size (see Figure II.2a). In this case most properties of diluted solutions are very similar to the pure solvent. At polymer concentrations above the overlap ($c > c^*$), the solution is in the semidilute regime (see Figure II.2c). The actual values of volume fractions in these solutions is very small, and most of the volume is occupied by the solvent. However, polymer chains overlap and dominate most of the different physical properties, rather than the solvent, such as viscosity and viscoelasticity.

It is worth to mention here, that depending on the nature of the solvent, polymers will behave different due to interactions with the solvent molecules. In general, we classify the solvents as poor solvents, when the polymer chains have a coil-like conformation and do not disperse well with a probable sedimentation. Theta solvents, when polymer chains are exactly neutrally interacting with the solvent with an elongated conformation. And good solvents, when polymeric chains swell and prefer to stay totally dispersed an elongated. Flory developed a theory of polymers in good solvent, and a good introduction to this can be found in the book of M. Rubinstein and R. H. Colby [12].

The next two sections treat with the classical theory of flexible polymers in dilute regime. This theory consists of well-known models which describes the relaxation mechanisms of individual polymer chains. These approaches are also well applied for the case of thread-like systems in solution under deformation, in semidilute regime at very short times of stress relaxation response, compared to their typical relaxation times, or in the Fourier domain, at high frequencies beyond the frequencies achievable by rheometers. Before starting with the models, it is necessary to introduce the movement of individual particles due to thermal agitation. The random motion of particles is the mechanism for displacements of all constituents of polymeric chains by the constant interaction with the solvent molecules. The Smoluchowski and Langevin equations contain the information regarding the displacement of particles immersed in a fluctuating thermal system.

2. Brownian motion: Smoluchowski and Langevin equations

Brownian motion dominates various time-dependent phenomena in polymer solutions such as viscoelasticity, diffusion, birefringence, or dynamic light scattering. In this section, the discussion will be limited to the aspects useful in the application to polymer solutions and suspensions. Here we take a phenomenological approach, regarding Brownian motion as a kind of stochastic process described with known macroscopic laws, according to the proposed model by A. Einstein [13] [14]. This approach is limited to time scales and length scales much longer than those characteristic of solvent molecules.

The Smoluchowski equation is derived from a diffusion equation which generalize the changes in concentration as a distribution function which depends on time and position. The Smoluchowski equation has a clear relevance in the thermodynamics of stochastic processes. The Langevin equation, on the other hand, analyzes the movement of particles from the stochastic forces of the medium that give rise to the process of diffusion, which permits obtaining a direct relation between fluctuations in the system at thermal equilibrium and the response of the system to perturbations [11] [15]. In general, the Brownian motion of particles is a functional prototype to provide valuable insights about the mechanisms responsible for the existence of fluctuations and energy dissipation. Figure II.3 sketches this random motion of particles within a liquid.

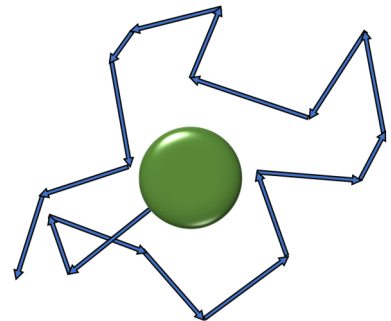


Figure II.3 Motion of a particle in a liquid is a random walk that results from random collisions with molecules in the liquid.

2.1. Smoluchowski equation

The diffusion process is phenomenologically described by Fick's law, which says that if the concentration of particles in an erratic movement is not uniform, there exists a net flux $\mathbf{J}(\mathbf{r}, t)$, which varies from regions at high concentrations to others with less concentration

$$\mathbf{J}(\mathbf{r}, t) = -D\nabla c(\mathbf{r}, t), \quad (\text{II.2.1})$$

where D is the diffusion coefficient. The microscopic origin of the flux is the random motion of the particles; if the concentration is not uniform, the flux comes entirely from fluctuations in the velocity of individual particles. If we have a delimited volume V , by a surface S , the quantity of matter that goes through the surface is described by a Gauss integral

$$\int_S \mathbf{J} \cdot d\mathbf{a} = \int_V \nabla \cdot \mathbf{J} dV. \quad (\text{II.2.2})$$

On the other hand, the flux of particles through the volume is compensated with a change in concentration

$$-\frac{d}{dt} \int_V c dV = -\int \frac{\partial c}{\partial t} dV, \quad (\text{II.2.3})$$

which leads to the familiar continuity equation

$$\nabla \cdot \mathbf{J} = -\frac{\partial c}{\partial t}. \quad (\text{II.2.4})$$

Using Fick's law (equation (II.2.1)), we obtain the diffusion equation

$$\frac{\partial c(\mathbf{r}, t)}{\partial t} = D\nabla^2 c(\mathbf{r}, t). \quad (\text{II.2.5})$$

The diffusion equation allows to calculate the concentration of particles at a site \mathbf{r} , and time t , under certain initial and boundary condition. For the case of $t = 0$, centered at $\mathbf{r} = 0$, with a Dirac delta shape, the solution of the diffusion equation is

$$c(\mathbf{r}, t) = \frac{N}{(4\pi Dt)^{3/2}} \exp\left(-\frac{\mathbf{r}^2}{4Dt}\right), \quad (\text{II.2.6})$$

moreover, renormalizing it to one, for identical particles, this quantity is understood as the probability of finding a particle at a position \mathbf{r} and time t , that we call $\Psi(\mathbf{r}, t)$. In the last equation N is the total number of particles immersed in the fluid. In this approach, it is considered the motion of an *ensemble* of N Brownian particles, placed under equivalent physical conditions, rather than considering the motion of a single particle over a length of time. This treatment is known as the Einstein-Smoluchowski theory. Using the distribution function, it is possible to calculate its second moment, which is

$$\langle \Delta \mathbf{r}^2(t) \rangle = \frac{4\pi}{N} \int_0^\infty c(\mathbf{r}, t) r^4 dr = 6Dt. \quad (\text{II.2.7})$$

This equation is the mean square displacement of Brownian diffusive particles at sufficiently long times. The equation represents the average traveled distance by each particle at time t , starting at time $t = 0$.

Generalizing the Einstein-Smoluchowski treatment including an external potential $U(\mathbf{r})$, which exerts a conservative force $\mathbf{F} = -\nabla U(\mathbf{r})$, Fick's law must be modified. Whether this is a weak force, the potential gives rise to an average velocity linear in \mathbf{F} , so that

$$\mathbf{v} = -\frac{1}{\zeta} \nabla U(\mathbf{r}). \quad (\text{II.2.8})$$

The term ζ is a friction constant. When the particles are sufficiently large, spherical with radius a , and are immersed in a solvent with viscosity η , the friction constant can be obtained from hydrodynamics, known as the Stokes friction term

$$\zeta = 6\pi\eta a. \quad (\text{II.2.9})$$

The Fick's law with an additional flux $c\mathbf{v}$ is now

$$\mathbf{J}(\mathbf{r}, t) = -D\nabla c(\mathbf{r}, t) - \frac{c(\mathbf{r}, t)}{\zeta} \nabla U(\mathbf{r}). \quad (\text{II.2.10})$$

We notice that the diffusion coefficient, in the equilibrium state is none other than the Stokes-Einstein equation

$$D = \frac{k_B T}{6\pi\eta a}. \quad (\text{II.2.11})$$

Using the Stokes-Einstein equation and the continuity equation (II.2.4) to rewrite the modified Fick's law (II.2.10), we obtain a generalized diffusion equation

$$\frac{\partial c}{\partial t} = \frac{\partial}{\partial x} \frac{1}{\zeta} \left(k_B T \frac{\partial c}{\partial x} + c \frac{\partial U}{\partial x} \right), \quad (\text{II.2.12})$$

which is called the Smoluchowski equation. This equation was obtained in one dimension for simplicity. If a flux velocity is defined by $v_f \equiv J/c$ (equation (II.2.10) in one dimension), that is

$$v_f = -\frac{1}{\zeta} \frac{\partial}{\partial x} (k_B T \ln c + U), \quad (\text{II.2.13})$$

we can rewrite the Smoluchowski equation as

$$\frac{\partial c}{\partial t} = -\frac{\partial}{\partial x}(cv_f), \quad (\text{II.2.14})$$

which is the equivalent continuity equation with an external potential. The term $U(x) + k_B T \ln c$ is the chemical potential of noninteracting particles of concentration c . It establishes that what must be constant in the equilibrium state is not concentration, but the chemical potential. This results in a generalization of the Fick's law. In a more standardized way, it is more appropriate to use the normalized probability distribution function $\Psi(\mathbf{r}, t)$, rather than the concentration term $c(\mathbf{r}, t)$.

2.2. Langevin equation

An equivalent treatment to Smoluchowski's consist in analyzing the case of just a Brownian particle using the Newton's-like equation

$$m \frac{d\mathbf{v}}{dt} = \mathcal{F}(t). \quad (\text{II.2.15})$$

where \mathbf{v} is the velocity of the center of mass of the particle with mass m . Langevin described the interaction of the colloidal particle with the particles of the solvent assuming that colloidal particles are significantly larger than the molecules in the liquid but small enough that collisions with molecules noticeable move the particle. He separated the force $\mathcal{F}(t)$ in two terms: one term of friction (slow and systematic) which accounts for the viscosity of the solvent; and one term of fluctuating motion due to the constant collisions with the molecules of the solvent (fast and stochastic),

$$m \frac{d\mathbf{v}}{dt} = -\zeta \mathbf{v} + \mathbf{F}'(t). \quad (\text{II.2.16})$$

$-\zeta \mathbf{v}$ is a drag force which coefficient is the Stokes friction parameter and $\mathbf{F}'(t)$ has a white noise behavior due to its stochastic nature, that means that $\mathbf{F}'(t)$ is a Gaussian force with $\langle \mathbf{F}'(t) \rangle = 0$, but $\langle \mathbf{F}'(t) \mathbf{F}'(t') \rangle = 2\zeta k_B T \delta(t - t')$. Taking the vectoral product of equation (II.2.16) with \mathbf{r} , and averaging on the ensemble, we obtain

$$\frac{d^2}{dt^2} \langle \mathbf{r}^2 \rangle + \frac{\zeta}{m} \frac{d}{dt} \langle \mathbf{r}^2 \rangle = 2 \langle \mathbf{v}^2 \rangle. \quad (\text{II.2.17})$$

If the particle is in thermal equilibrium with the molecules of the liquid, the energy equipartition theorem give us that $\langle \mathbf{v}^2 \rangle = 3k_B T/m$, and solving the equation, we obtain two results for different time approximations: for $t \ll m/\zeta$, at early times it is known as a ballistic regime

$$\langle \Delta \mathbf{r}^2(t) \rangle \approx \frac{3k_B T}{m} t^2. \quad (\text{II.2.18})$$

For $t \gg m/\zeta$, the mean square displacement is

$$\langle \Delta \mathbf{r}^2(t) \rangle \approx \frac{6k_B T}{\zeta} t = 6Dt. \quad (\text{II.2.19})$$

This last equation is the same obtained with the Smoluchowski formalism. Both formalisms are equivalent but with clear differences between them. Smoluchowski deals with a probability distribution function, derived from the diffusion equation when it considers indistinguishable particles for the calculus of different moments of the distribution. On the other hand, Langevin approximation is centered in one particle, and it is just capable of calculating averages on the ensemble, given the properties of the stochastic forces.

2.3. Interacting particles

So far, all the derived equations have considered the displacement of particles in one or three dimensions. However, it is useful to consider a system with many degrees of freedom. Furthermore, a more realistic situation includes interactions between each one of the colloidal particles suspended in a fluid, all having equal size. The study of this system is the basis for the general theory of polymer solutions and suspensions. To construct the Smoluchowski and Langevin equations, we have to know the relation between the average velocity \mathbf{V}_n and the external forces given for the Smoluchowski equation or the drag forces given for the Langevin equation. Let $\{\mathbf{R}_n\} \equiv (\mathbf{R}_0, \dots, \mathbf{R}_N)$ be the position of the particles. The sought relation is written as

$$\mathbf{V}_n = \sum_m \mathbf{H}_{nm} \cdot \mathbf{F}_m, \quad (\text{II.2.20})$$

which defines the mobility tensor \mathbf{H}_{nm} . Here, \mathbf{F}_m is the force acting on particle m . This force creates a velocity field and alters the velocity of particle n due to hydrodynamic interactions between them. To understand the relaxation mechanisms of polymers which are treated in the next section, it is necessary to know a proper expression for the mobility tensor. For this, we follow the calculations to get the fluid velocity $\mathbf{v}(\mathbf{r})$, created by external forces [11]. In the usual condition of Brownian motion, the relevant hydrodynamic equation of motion is that of the low Reynolds number hydrodynamics which assumes:

- The fluid is incompressible

$$\frac{\partial}{\partial r_\alpha} v_\alpha = 0, \quad (\text{II.2.21})$$

where the tensor notation is used.

- The inertia force of the fluid is negligibly small, so that if $\sigma_{\alpha\beta}(\mathbf{r})$ and $g_\alpha(\mathbf{r})$ represent the stress tensor and the external force per unit volume, respectively, then

$$\frac{\partial}{\partial r_\beta} \sigma_{\alpha\beta} = -g_\alpha(\mathbf{r}). \quad (\text{II.2.22})$$

When a strain is applied to the system, assuming this as the constitutive equation, the components of the stress tensor are [16]

$$\sigma_{\alpha\beta} = \eta \left(\frac{\partial v_\beta}{\partial r_\alpha} + \frac{\partial v_\alpha}{\partial r_\beta} \right) + P \delta_{\alpha\beta}, \quad (\text{II.2.23})$$

where P is the pressure. From the last equations, it follows that

$$\eta \frac{\partial^2}{\partial r_\beta^2} v_\alpha + \frac{\partial}{\partial r_\alpha} P = -g_\alpha. \quad (\text{II.2.24})$$

Equations (II.2.21) and (II.2.24) are called *the Stokes approximation* and are the basis of the hydrodynamic interactions in colloidal suspensions and polymer solutions. Calculating the force field created by the external forces acting on the particles, one finds that the particles move with the same velocity as the fluid [11], and the mobility tensor has the analytical form

$$\mathbf{H}(\mathbf{r}) = \frac{1}{8\pi\eta r} (\mathbb{I} + \hat{\mathbf{r}}\hat{\mathbf{r}}). \quad (\text{II.2.25})$$

This equation is the so-called *Oseen tensor*. \mathbb{I} is the unitary matrix and $\hat{\mathbf{r}}$ is a unitary vector in the direction of vector \mathbf{r} . A simple approximation is adopted in the theory of polymer solutions to avoid the failure in which $\mathbf{H}_{nn} = \mathbf{H}(0)$ has infinite value, because so far we have considered that the particles are regarded as point. Starting from a collection of particles with finite size, this difficulty does not arise. However, for finite size particles the solution of Stokes equation is obtained only in the form of a perturbation expansion. The approximation is

$$\mathbf{H}_{nn} = \frac{\mathbb{I}}{\zeta}; \quad \mathbf{H}_{nm} = \mathbf{H}(\mathbf{R}_n - \mathbf{R}_m), \quad n \neq m. \quad (\text{II.2.26})$$

With this formalism, we obtain the generalization for the Smoluchowski and Langevin equation for interacting particles subjected to an external field

$$\frac{\partial \Psi}{\partial t} = \sum_{n,m} \frac{\partial}{\partial \mathbf{R}_n} \cdot \mathbf{H}_{nm} \cdot \left(k_B T \frac{\partial \Psi}{\partial \mathbf{R}_m} + \frac{\partial U}{\partial \mathbf{R}_m} \Psi \right), \quad (\text{II.2.27})$$

$$\frac{\partial}{\partial t} \mathbf{R}_n(t) = \sum_m \mathbf{H}_{nm} \cdot \left(-\frac{\partial U}{\partial \mathbf{R}_m} + \mathbf{F}'_m(t) \right) + \frac{1}{2} k_B T \sum_m \frac{\partial}{\partial \mathbf{R}_m} \cdot \mathbf{H}_{nm}, \quad (\text{II.2.28})$$

respectively. These equations join up the interaction between particles, using the Oseen tensor as a result of the hydrodynamic interactions. The external potential U is regarded as the interaction potential between particles.

3. Classical theory of flexible polymers: diluted regime

Having seen the general background of Brownian motion, now we have the analytical tools to discuss the dynamics of a polymer in solution. Before that, in this section is pointed out that the static properties of a polymer can be represented by a set of beads connected along a chain. Flexible polymers are allowed to take a considerable number of different configurations due to the rotation of their chemical monomer-monomer connections. For this reason, the static properties of polymers are more adequately described statistically. Here we consider the simple case of the *freely jointed model*. This model consists of a chain with N links, each of length b_0 , able to point in any direction independently of each other (see Figure II.4). The spatial conformation of the complete chain is specified by the set of $N + 1$ position vectors $\{\mathbf{R}_n\} \equiv (\mathbf{R}_0, \dots, \mathbf{R}_N)$ of the joints, or alternatively by the set of joint vectors $\{\mathbf{r}_n\} \equiv (\mathbf{r}_1, \dots, \mathbf{r}_N)$, where $\mathbf{r}_n = \mathbf{R}_n - \mathbf{R}_{n-1}$ for $n = 1, 2, \dots, N$. Because the joint vectors are independent of each other, the distribution function for the spatial conformation of the polymer is described by

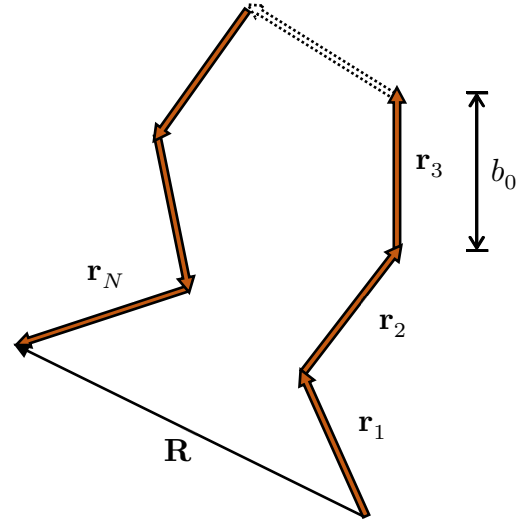


Figure II.4 Freely jointed chain for flexible polymers.

$$\Psi(\{\mathbf{r}_n\}) = \prod_{n=1}^N \psi(\mathbf{r}_n), \quad (\text{II.3.1})$$

where $\psi(\mathbf{r}_n)$ is the random distribution of a vector with constant length b_0 ,

$$\psi(\mathbf{r}) = \frac{1}{4\pi b_0^2} \delta(|\mathbf{r}| - b_0), \quad (\text{II.3.2})$$

which is normalized to one. There is a way to estimate the size of a polymer, considering the end-to-end vector \mathbf{R} of the chain

$$\mathbf{R} = \mathbf{R}_N - \mathbf{R}_0 = \sum_{n=1}^N \mathbf{r}_n. \quad (\text{II.3.3})$$

The freely jointed polymer chain resembles the displacement of a random walker, known as a random coil; hence $\langle \mathbf{r}_n \rangle = 0$ and $\langle \mathbf{R} \rangle = 0$, but $\langle \mathbf{R}^2 \rangle$ has a finite value, which can be used as a characteristic length of the chain. The value is

$$\langle \mathbf{R}^2 \rangle = \sum_{n,m=1}^N \langle \mathbf{r}_n \cdot \mathbf{r}_m \rangle = \sum_{n=1}^N \langle \mathbf{r}_n \rangle^2 + 2 \sum_{n>m} \langle \mathbf{r}_n \cdot \mathbf{r}_m \rangle = Nb_0^2. \quad (\text{II.3.4})$$

Using $\bar{R} = \sqrt{\langle \mathbf{R}^2 \rangle}$, the characteristic size of the chain is then

$$\bar{R} = \sqrt{Nb_0}. \quad (\text{II.3.5})$$

More general models also preserve the proportionality with the number of joints $\langle \mathbf{R}^2 \rangle \propto N$ and its length b_0 . Another value which is essential to estimate is the Kuhn statistical segment length

$$b_k \equiv \frac{\langle \mathbf{R}^2 \rangle}{R_{max}}, \quad (\text{II.3.6})$$

with R_{max} the maximum length of the end-to-end vector \mathbf{R} . In most cases, an effective bond length b (in the simplest cases it is the constant value b_0) is assumed as the Kuhn length. This value permits us to elucidate the stiffness of the polymer, and also the persistence length of worm-like chains as will be mentioned further in this document.

It is also important to mention the statistic distribution of the end-to-end vector of a polymeric chain. Consider $\Phi(\mathbf{R}, N)$, as the distribution function with the probability \mathbf{R} that the end-to-end vector of the chain consists of N links. Given the conformational distribution for $\Psi(\{\mathbf{r}_n\})$, $\Phi(\mathbf{R}, N)$ is calculated by

$$\Phi(\mathbf{R}, N) = \int d\mathbf{x}_1 \int d\mathbf{x}_2 \dots \int d\mathbf{x}_N \delta \left(\mathbf{R} - \sum_{n=1}^N \mathbf{r}_n \right) \Psi(\{\mathbf{r}_n\}). \quad (\text{II.3.7})$$

For the freely jointed model with large N , the result is

$$\Phi(\mathbf{R}, N) = \left(\frac{3}{2\pi Nb^2} \right)^{3/2} \exp \left(-\frac{3\mathbf{R}^2}{2Nb^2} \right). \quad (\text{II.3.8})$$

The distribution function is Gaussian. The same kind of distribution appears for \bar{R} and the same N in more general polymer chain models. A Gaussian distribution is a widespread used distribution for the calculation of the end-to-end vector as well.

3.1. The Rouse model

As it has been seen in this chapter, the static properties of a polymer can be represented by a set of beads connected along a chain. A typical procedure to model the dynamics of the polymer is assuming a Brownian motion of such beads [11]. Here, we consider a Gauss chain mechanical model with the beads connected by harmonic springs. Such a model was first proposed by P. E. Rouse [17] and has been the basic formulation for the dynamics of dilute polymer solutions. Consider $\{\mathbf{R}_n\}$ as the positions of the beads mentioned already in the last section, here starting from the subscript 1 (Figure II.5). The equation of motion is described by either the Smoluchowski equation (II.2.27) or the Langevin equation (II.2.28).

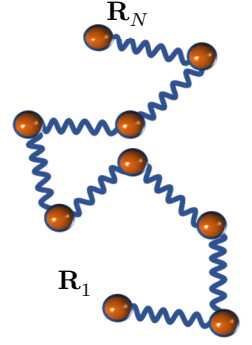


Figure II.5 Rouse model with beads connected by harmonic springs.

In the Rouse model, for simplicity the excluded volume and hydrodynamic interactions are neglected. Thus the mobility tensor and the interaction potential are written as

$$\mathbf{H}_{nm} = \frac{\mathbb{I}}{\zeta} \delta_{nm}, \quad (\text{II.3.9})$$

$$U = \frac{3k_B T}{2b^2} \sum_{n=2}^N (\mathbf{R}_n - \mathbf{R}_{n-1})^2, \quad (\text{II.3.10})$$

which is the potential of a harmonic oscillator. It includes a phenomenological thermodynamic counterpart proportional to the thermal energy $k_B T$ as the “spring constant”, chosen using the equipartition of energy principle. In this model, the Langevin equation (II.2.28) is a linear equation for \mathbf{R}_n

$$\begin{aligned} \zeta \frac{d\mathbf{R}_n}{dt} &= -k(2\mathbf{R}_n - \mathbf{R}_{n+1} - \mathbf{R}_{n-1}) + \mathbf{F}'_n, \quad \text{for } n = 2, 3, \dots, N-1, \\ \zeta \frac{d\mathbf{R}_1}{dt} &= -k(\mathbf{R}_1 - \mathbf{R}_2) + \mathbf{F}'_1, \quad \text{for } n = 1, \\ \zeta \frac{d\mathbf{R}_N}{dt} &= -k(\mathbf{R}_N - \mathbf{R}_{N-1}) + \mathbf{F}'_N, \quad \text{for } n = N. \end{aligned} \quad (\text{II.3.11})$$

As previously mentioned, \mathbf{F}'_n is a Gaussian random force. The suffix n can be regarded as a continuous variable. Hence, in the continuous limit, equations (II.3.11) are rewritten as a set of nonlinear differential equations with boundary conditions. The essence of the Rouse model is in the spirit of modeling the dynamics of connected objects, in this case, beads with Brownian motion connected by springs. A way of treating such a system is to find the normal coordinates which uncouple the motion of the beads, reducing the system of nonlinear equations into a system of linear

equations in the new coordinates \mathbf{X}_p [11]. The motion of the system in these normal coordinates is called Rouse modes. The transformation rule to get the normal coordinates is

$$\mathbf{X}_p \equiv \frac{1}{N} \int_0^N \cos\left(\frac{p\pi n}{N}\right) \mathbf{R}_N(t), \quad \text{with} \quad p = 0, 1, 2, \dots \quad (\text{II.3.12})$$

Theses normal coordinates have a physical significance, which is evident when one obtains the inverse transform to get the spatial coordinates

$$\mathbf{R}_n = \mathbf{X}_0 + 2 \sum_{p=1}^{\infty} \mathbf{X}_p \cos\left(\frac{p\pi n}{N}\right). \quad (\text{II.3.13})$$

\mathbf{X}_0 represents the position of the center of mass with a mean square displacement $6 \frac{k_B T}{N\zeta} t$, that means a diffusive behavior with a definite diffusion coefficient. \mathbf{X}_p with $p > 0$ represents the internal conformation of the polymer, that is, the normal coordinates generate the local motion of the chain which includes N/p segments and corresponds to the motion with the length scale of the order $(Nb^2/p)^{1/2}$, for instance, when $p = 1$, the corresponding Rouse mode includes all N segments of the polymer, and $(Nb^2)^{1/2}$ is the length of the end-to-end vector (equation (II.3.5)).

Using the transformation (II.3.12), it is possible to construct the correlation function of normal coordinates. With $p > 0$, it is

$$X_{p\alpha}(t) X_{q\beta}(0) = \delta_{pq} \delta_{\alpha\beta} \frac{Nb^2}{6\pi^2 p^2} \exp(-t / \tau_p), \quad (\text{II.3.14})$$

where the decaying time τ_p is

$$\tau_p = \frac{\zeta N^2 b^2}{3\pi^2 k_B T p^2} = \tau_1 p^{-2}, \quad (\text{II.3.15})$$

from where we can conclude that the lower the Rouse mode (the ones with longer chains in collective motion), the slower the Rouse mode. $\tau_1 = \tau_R$ is the slowest mode, known as the Rouse time.

On the other hand, using the inverse transformation, (II.3.13), it is possible to calculate the time correlation function of the end-to-end vector. Renaming the end-to-end vector as $\mathbf{P}(t) \equiv \mathbf{R}_N(t) - \mathbf{R}_0(t)$, to avoid confusion with the parameter \mathbf{R} which will be used later, the correlation function is

$$\langle \mathbf{P}(t) \cdot \mathbf{P}(0) \rangle = Nb^2 \sum_{p=1,3,\dots} \frac{8}{p^2 \pi^2} \exp(-p^2 t / \tau_R), \quad (\text{II.3.16})$$

which behaves as a sum of relaxation mechanisms, with a common relaxation Rouse time.

Even when the Rouse model is useful to understand the dynamics of polymers in dilute solutions, it does not consider the hydrodynamic interactions between beads, neither the excluded volume interactions. B. H. Zimm introduces the generalization when only the hydrodynamic interactions are accounted for and later, including also the excluded volume. The role of solvent becomes important and allows to extent the usefulness of the model to systems at high densities, as the worm-like micellar systems that are introduced later in this text.

3.2. The Zimm model

The polymeric suspension presents Θ conditions when the hydrodynamic interactions are taking into account. In this model the mobility tensor change and the Oseen tensor has to be used (equation (II.2.25)), in this case with $r = |\mathbf{r}_{nm}|$, and $\mathbf{r}_{nm} \equiv \mathbf{R}_n - \mathbf{R}_m$, the difference between any two vector positions of the beads. With the Oseen tensor, the Langevin equation in the continuous limit, and considering the same harmonic potential between particles as previously, is now

$$\frac{\partial}{\partial t} \mathbf{R}_n(t) = \sum_m \mathbf{H}_{nm} \cdot \left(\frac{3k_B T}{b^2} \frac{\partial^2}{\partial m^2} \mathbf{R}_m + \mathbf{F}'_m(t) \right). \quad (\text{II.3.17})$$

Since \mathbf{H}_{nm} is a nonlinear function of \mathbf{r}_{nm} , the last equation is quite tricky to handle. To simplify it, Zimm proposed an average of the Oseen tensor [18]. After applying it, it is possible to obtain again a set of normal coordinates, which are uncoupled under certain approximations. The difference with the Rouse model is in the coefficients of the decaying times associated with the correlation functions calculated from the transformation rules between coordinates and normal coordinates. Here the decaying times are

$$\tau_p = \tau_R p^{-3/2}, \quad (\text{II.3.18})$$

with the corresponding Rouse time (Rouse-Zimm time)

$$\tau_R = \frac{\eta (Nb^2)^{3/2}}{(3\pi)^{1/2} k_B T} = 0.325 \frac{\eta (Nb^2)^{3/2}}{k_B T}. \quad (\text{II.3.19})$$

If not just the hydrodynamic interactions are considered, but also the excluded volume interaction (volume v), the polymer is assumed to be diluted in a good solvent. There is then an addition of a new potential

$$U_1 = \frac{1}{2} v k_B T \sum_{n,m} \delta(\mathbf{R}_n - \mathbf{R}_m). \quad (\text{II.3.20})$$

As previously, with this model the Langevin equation is nonlinear, but using the normal coordinates and using certain approximations, it is possible to find the correct set of linear equations for the

normal coordinates. This model is called Rouse-Zimm with excluded volume interactions. Now, the decaying times for the correlation functions of the normal coordinates are

$$\tau_p = \tau_R p^{-3\nu}, \quad (\text{II.3.21})$$

and

$$\tau_R = \frac{\eta(N^\nu b)^3}{k_B T}, \quad (\text{II.3.22})$$

where ν is the exponent of Flory theory for polymeric solutions. For the case of a good solvent, the exponent has the value $\nu = 3/5$. Finally, even when the relaxation times are different, they could be summarized in the following manner

$$\tau_p \propto p^{-\mu}, \quad (\text{II.3.23})$$

with $\mu = 2$ for the Rouse model, $\mu = 3/2$ for the Rouse-Zimm model with hydrodynamic interactions, and $\mu = 9/5$ for the Rouse-Zimm model when excluded volume interactions are added.

4. Viscoelasticity in diluted polymeric suspensions

Colloidal suspensions and polymer solutions have interesting mechanical properties. In general, these materials have a viscoelastic response. The introduction to the study of the rheological properties of viscoelastic materials is devoted to Chapter III, but here is given an introduction to the microscopic fundamentals of viscoelasticity. For a system under strain, we need a proper expression for the macroscopic stress tensor $\sigma_{\alpha\beta}$, which represents the force per unit area exerted on a surface defined by vector β , in the direction of vector α . The stress tensor can be expressed as the sum of an isotropic tensor $\bar{\sigma}\delta_{\alpha\beta}$ and an anisotropic tensor $\sigma_{\alpha\beta}^{(a)}$ [11]. In an incompressible fluid, the isotropic part is determined by the external conditions and is irrelevant in our discussion. The anisotropic tensor, which is a constitutive equation, from now just called $\sigma_{\alpha\beta}$ is conformed by two parts

$$\sigma_{\alpha\beta} = \eta(\kappa_{\alpha\beta} + \kappa_{\beta\alpha}) + \langle P \rangle \delta_{\alpha\beta} - \frac{c}{N} \sum_{m=1}^N \langle F_{m\alpha} R_{m\beta} \rangle. \quad (\text{II.4.1})$$

The terms $\eta(\kappa_{\alpha\beta} + \kappa_{\beta\alpha}) + \langle P \rangle \delta_{\alpha\beta}$ represent the stress due to the solvent molecules, which include information about its viscosity η , the local velocity gradient $\kappa_{\alpha\beta}$ (macroscopically is the shear rate

$\kappa = \dot{\gamma}$), and pressure P . The term $-\frac{c}{N} \sum_{m=1}^N \langle F_{m\alpha} R_{m\beta} \rangle = \sigma_{\alpha\beta}^{(p)}$ is the contribution of the beads

conforming the polymer chain. This last part is the one that concerns us to obtain the viscoelasticity of the polymer. $\sigma_{\alpha\beta}^{(p)}$ contains the contribution of the component of the joint vector between particles

R_m , mediated by force $F_m = -\frac{\partial}{\partial R_m}(k_B T \ln \Psi + U)$, which has the form of a chemical potential, with Ψ the probability distribution function which reminds us the distribution function considered in the Smoluchowski equation. Rewritten regarding the corresponding potential

$$\sigma_{\alpha\beta}^{(p)} = \frac{c}{N} \sum_m \left\langle \frac{\partial U}{\partial R_{m\alpha}} R_{m\beta} \right\rangle. \quad (\text{II.4.2})$$

The factor c/N accounts for the number of polymers in the unit volume. Passing to the continuous limit and transforming to normal coordinates, the equation (II.4.2) is transformed to

$$\sigma_{\alpha\beta}^{(p)} = \frac{c}{N} \sum_m k_p \langle X_{p\alpha} X_{p\beta} \rangle, \quad (\text{II.4.3})$$

where it was considered the same potential used for the Rouse model. Here $k_p = \frac{6\pi^2 k_B T}{Nb^2} p^2$. The strain imposed on the material induce a velocity gradient in the fluid, and consequently in the polymer beads. This velocity gradient changes the distribution function of the polymer particles. Hence the Smoluchowski and Langevin equations are modified, adding an extra term. Through the Smoluchowski equation, in normal coordinates, it is possible to obtain a result for $\langle X_{p\alpha} X_{p\beta} \rangle$ in the case of a no constant velocity gradient

$$\langle X_{p\alpha} X_{p\beta} \rangle = \frac{k_B T}{k_p} \int_{-\infty}^t dt' \exp[-(t-t')/\tau_p] \kappa(t'), \quad (\text{II.4.4})$$

with τ_p the relaxation times for different p values, in the Rouse model. Substituting the equation (II.4.4) into the equation (II.4.3), and comparing with the equation of linear response for the stress tensor (equation (III.1.10) introduced in Chapter III), with the velocity gradient equal to the shear rate, $\kappa = \dot{\gamma}$, it is possible to obtain the relaxation modulus $G(t)$, for the polymer beds,

$$G(t) = \frac{c}{N} k_B T \sum_p \exp(-t/\tau_p). \quad (\text{II.4.5})$$

The relaxation modulus includes the contribution for each τ_p relaxation time, from Rouse modes, which considers all polymer segments. From the relaxation modulus, it is possible to calculate the storage (elastic) and loss (viscous) moduli, according to the equation (III.1.18)

$$\begin{aligned} G'(\omega) &= \int_0^\infty dt \omega \sin(\omega t) \sum_p \exp(-t/\tau_p) = \sum_{p=1}^\infty \frac{(\omega\tau_p)^2}{1 + (\omega\tau_p)^2}, \\ G''(\omega) &= \int_0^\infty dt \omega \cos(\omega t) \sum_p \exp(-t/\tau_p) = \sum_{p=1}^\infty \frac{\omega\tau_p}{1 + (\omega\tau_p)^2}. \end{aligned} \quad (\text{II.4.6})$$

Further analyses of these equations permit us to realize the contribution of viscoelasticity in the system at different time scales. We can divide the time scales in two regimes:

1) For $\omega\tau_R \ll 1$. In this case, the elastic and viscous moduli are approximated as

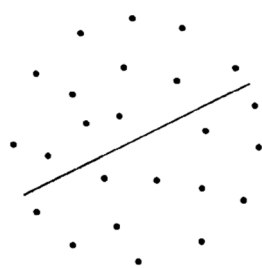
$$G'(\omega) = (\omega\tau_R)^2 \sum_{p=1}^{\infty} p^{-2\mu}, \tag{II.4.7}$$

$$G''(\omega) = \omega\tau_R \sum_{p=1}^{\infty} p^{-\mu}.$$

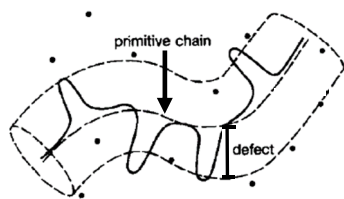
The elastic and viscous moduli are proportional to ω^2 and ω respectively.

- 2) For $\omega\tau_R \gg 1$. Here the sum over p can be replaced by an integral, thus
- For the Rouse model, $\mu = 2$, the moduli are proportional to $\omega^{1/2}$.
 - For the Rouse-Zimm model with hydrodynamic interactions, $\mu = 3/2$, the moduli are proportional to $\omega^{2/3}$.
 - For the Rouse-Zimm model with hydrodynamic and excluded volume interactions, $\mu = 9/5$, the moduli are proportional to $\omega^{5/9}$.

5. Reptation model: semidilute regime



(a) Tube for a rigid polymer.



(b) Tube for a flexible polymer. It includes the primitive chain and defects.

So far, we have been considering polymeric solutions in the dilute regime, with isolated polymeric chains. That was useful to understand the fast relaxation mechanisms of the systems or their response at high frequencies. Now, in this section, our concern is the relaxation mechanism when the polymer chains overlap with others. The relaxation response is now a process which involves topological constraints on a single chain, due to all the other chains at the surroundings. The study presented here is restricted to the case when the systems are uncrosslinked, based in the formalism of M. Doi and S. F. Edwards [11].

In the case of semidilute and concentrated solutions, the key concept which helps us to understand the relation between a polymer chain and its neighbors is the *tube model*. This tube can be imaged easily for a rod-like polymer as in Figure II.6a. In this case, the concept of a tube is defined when the free movement of the rigid rod is considered on a plane. In the same plane, other polymers are represented by dots, and equally rods perpendicular to the plane. Suppose that other rods are frozen, and the rod we are interested in is free to move along itself but any other movements with perpendicular displacements, are

Figure II.6 Tube model for different polymer shapes. Taken from [11].

forbidden. The tube is formed by the frozen rods, so the displacement of the rod-like polymer is suppressed by the topological constrictions. In the case of flexible polymers, the tube model is more complicated (Figure II.6b). De Gennes introduced this concept who discussed the Brownian motion of an unattached chain moving through a fixed network. The motion of the chain is almost confined in a tube-like region denoted by dotted lines in Figure II.6b. Since the chain is rather longer than the tube, the slack will constitute a series of defects, which can flow up and down the tube. De Gennes visualized this as a gas of non-interacting defects running along a *primitive chain* [19]. This motion was called *reptation*. As a result of this motion, the tube itself changes with time; part of the original tube maintains the polymer chain within, but the new topological restrictions on the polymer, generates a new tube. Even though this picture is clear, the time evolution of the polymer, at short time scale is regarded as wriggling around the primitive chain. However, we are interested in the large-scale motion of the chains so that we may disregard small-scale fluctuations. Our problem consists in determining the dynamics of the primitive chain during the reptation process, within its tube [11]. To denote a point, the segment s of the primitive chain represents the segment of length s , measured from the chain end. $\mathbf{R}(s, t)$ is the position at time t and $\mathbf{u}(s, t) = \frac{\partial}{\partial s} \mathbf{R}(s, t)$ is the unit tangent vector to the primitive chain. The dynamics of the primitive chain is characterized by

- The primitive chain has constant contour length L_c .
- The primitive chain is allowed to move back and forth only along itself with a diffusion constant D_c , which is the center of mass diffusion constant of Rouse model.
- The correlation of the tangent vectors at positions s and s' , decreases quickly with $|s - s'|$.

The three assumptions correspond to neglecting the fluctuations of the contour length, the reptating motility, the Gaussian conformation of the chain on a large length-scale respectively. The last assumption introduces a new parameter into the problem: the length a , called the step length of the primitive chain. Therefore, the mean square distance of the end-to-end vector of the chain is $L_c a$. Then, the primitive chain is characterized by three parameters, L_c , D_c and a , which can be represented by the parameters of the Rouse model. We find that $D_c = k_B T / N \zeta$ and $L_c = N b^2 / a$. The dynamics of the primitive chain is characterized by certain time correlation functions, as in the previous case of the Rouse model. Consider again the time correlation function of the end-to-end vector, previously calculated for the Rouse model in the equation (II.3.16), $\mathbf{P}(t) \equiv \mathbf{R}_N(L, t) - \mathbf{R}_0(0, t)$.

Figure II.7 explains the evolution of the primitive chain within the tube. The images explain the principle of calculating the correlation function. The conformation of the tube is defined at time $t = 0$ (Figure II.7a). As time passes, the chain reptates to the left or right, so some sections of

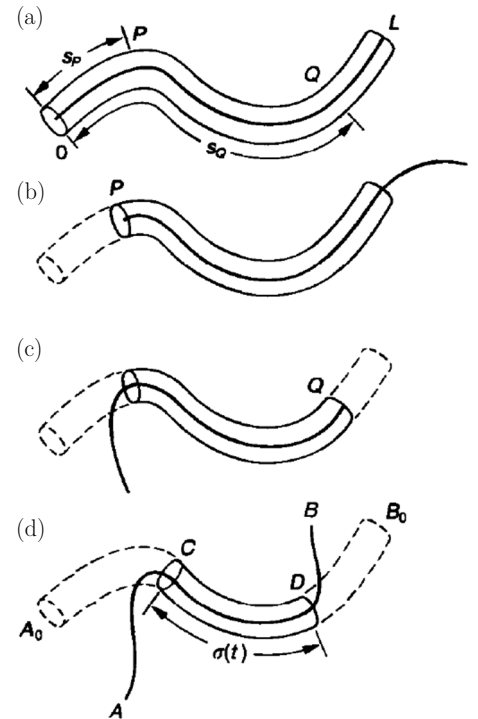


Figure II.7 Successive situations of a reptating chain. Each step shows the evolution of the primitive chain within the tube. Taken from [11].

the primitive chain leave the original tube (Figure II.7b and c). At some time, there is only one segment CD remaining in the tube, while the parts AC and DB define a new tube (Figure II.7d).

As $\mathbf{P}(0) = \overrightarrow{A_0C} + \overrightarrow{CD} + \overrightarrow{DB_0}$ and $\mathbf{P}(t) = \overrightarrow{AC} + \overrightarrow{CD} + \overrightarrow{DB}$, the correlation function is

$$\langle \mathbf{P}(t) \cdot \mathbf{P}(0) \rangle = \langle \overrightarrow{CD}^2 \rangle = a \langle \sigma(t) \rangle, \quad (\text{II.5.1})$$

where $\sigma(t)$ is the contour length of the remaining original tube. Here it was considered that \overrightarrow{AC} and \overrightarrow{DB} are uncorrelated with $\mathbf{P}(0)$. To calculate $\langle \sigma(t) \rangle$, we select a segment s of the original tube. This segment disappears when it is reached by either end of the primitive chain. Let $\psi(s, t)$ be the probability that this tube remains on time t . $\langle \sigma(t) \rangle$ is then

$$\langle \sigma(t) \rangle = \int_0^{L_c} ds \psi(s, t). \quad (\text{II.5.2})$$

Now, let $\Psi(\xi, t; s)$ be the probability that the primitive chain moves the distance ξ while the end has not reached the segment s of the original tube. This probability satisfies the one-dimensional diffusion equation for D_c . Solving the equation with the corresponding initial and boundary conditions, it is possible to calculate $\Psi(\xi, t; s)$, and with its result, $\psi(s, t)$

$$\psi(s, t) = \int_{s-L_c}^s d\xi \Psi(\xi, t; s) = \sum_{p:\text{odd}} \frac{4}{p\pi} \sin\left(\frac{p\pi s}{L_c}\right) \exp\left(-p^2 t / \tau_d\right), \quad (\text{II.5.3})$$

where $\tau_d = L_c^2 / D_c \pi^2$. With this result, we can obtain

$$\langle \mathbf{P}(t) \cdot \mathbf{P}(0) \rangle = Nb^2 \psi(t) = \frac{Nb^2}{L_c} \int_0^{L_c} ds \psi(s, t) = Nb^2 \sum_{p:\text{odd}} \frac{8}{p^2 \pi^2} \exp\left(-p^2 t / \tau_d\right). \quad (\text{II.5.4})$$

As it is evident, the longest relaxation time for the correlation function is given by τ_d . This is called the *reptation time* because is the time the primitive chain takes to disengage from the tube it was confined to at $t = 0$. If we check the correlation function obtained for the Rouse model (equation (II.3.16)) and rewriting τ_d with the values of D_c and L_c , we note that τ_d is proportional to N^3 , so τ_d is much larger than τ_R (depends on N^2) for large N . This demonstrates the crucial effect of topological constraints on the conformational change of polymers.

In all the current section it was considered that the system of polymer chains prefers to relax by reptation mechanisms, in the semidilute regime (even at concentrated regime or melt states). However, the statement for the correlation function of the end-to-end chain makes clear that the relaxation mechanisms are influenced by the length and time scales involved in the problem. There must be a particular characteristic length which distinguishes between the case of Rouse (or Rouse-Zimm) relaxation, and the case of reptation relaxation. This length is represented by the step length

of the primitive chain (parameter a), settled in context already; which approximately represents the diameter of the constrained tube. Within this framework, one can draw a somewhat simplified picture of the dynamics of the polymer in the entangled state. (1) If the length scale of a motion is smaller than a , the entanglement effect is not important, and the dynamics is well described by the Rouse-Zimm model. (2) On the other hand, if the length scale of the motion is more extensive than a , the dynamics is governed by reptation. To illustrate both cases regarding time scales, consider the mean square displacement of a Rouse segment, $\langle \Delta \mathbf{R}^2(t) \rangle$ (the whole development can be followed in [11]).

(1) For very short times, $t < \tau_c \ll \tau_R$, the segment does not feel the constraints of the network and $\langle \Delta \mathbf{R}^2(t) \rangle$ is the same as for the Rouse model in free space, $\langle \Delta \mathbf{R}^2(t) \rangle \sim (t/\tau_R)^{1/2}$. Here we defined a characteristic time τ_c at which the segmental displacement becomes comparable to a . Under strain, the viscoelastic response characterized by the relaxation modulus is $G(t) \sim \sum_p \exp(-t/\tau_p)$, as previously denoted (equation (II.4.5)).

(2) For $t > \tau_c$, the motion of the Rouse segment perpendicular to the primitive path is restricted, but the motion along the primitive path is free. For $\tau_c < t < \tau_R$, the mean square displacement behaves as $\langle \Delta \mathbf{R}^2(t) \rangle \sim (ta^2/L_c^2\tau_R)^{1/4}$. For $\tau_R < t < \tau_d$, the behavior goes as $\langle \Delta \mathbf{R}^2(t) \rangle \sim (t/\tau_d)^{1/2}$. Nevertheless, in the linear regime of deformation, the process of relaxation of the contour length (by Rouse-Zimm modes) can be neglected to first order, since the change in the contour length by the shear strain is an even function of the strain value. Thus, strictly speaking, the relaxation for $t > \tau_c$ is only due to the disengagement mechanism. This can be evaluated as follows. At $t \approx \tau_c$ the polymer is still within the tube, and as time evolves, the polymer reptates and the central segments are the only ones staying in the tube. These are the only segments that contribute to the remaining stress. Then, the stress is proportional to the fraction $\psi(t)$ of the polymer within the tube,

$$G(t) = G_0\psi(t) = G_0 \sum_{p:\text{odd}} \frac{8}{p^2\pi^2} \exp(-p^2t/\tau_d). \quad (\text{II.5.5})$$

M. E. Cates [20] found that a steepest descents analysis suggests a good approximation of $\psi(t)$, which can be replaced, giving a relaxation modulus

$$G(t) \sim \exp\left[-\left(t/\tau_d\right)^{1/4}\right]. \quad (\text{II.5.6})$$

In this approximation, all different τ_d/p^2 times have collapsed to just one characteristic reptation time. In summary, we can say that at short times (or high frequencies), the polymer dynamics follows the Rouse-Zimm model for relaxation. At longer times, (of low frequencies), the dynamics are dominated by the reptation relaxation mechanisms.

So far, we have been reviewed the relaxation mechanisms for conventional polymers under stress. There are other kinds of polymeric systems which present a different relaxation mechanism, involved at different time scales. These polymers are called *living polymers* since the individual chains break

and recombine in addition to the already mentioned dynamics. These systems are treated in the next section.

6. Living polymers

Living polymers are linear chain polymers that can break and recombine on experimental time scales. The first formal theoretical studies in these systems were done by M. E. Cates [20], and later in collaboration with S. J. Candau [21], M. S. Turner [22] and R. Granek [23]. Cates and Candau introduced a model to understand the processes of scission and recombination. It is worth to mention that these reactions do not avoid the fact of occurrence of reptation relaxation; it will be present, but its importance will depend on the time scales where the measurements are carried on. In this model, it is assumed that [21]

- Scission of a chain is a unimolecular process, which occurs with equal probability per unit time per unit length on all chains. The rate of this reaction is constant and is inversely proportional to the lifetime τ_b , of a chain of mean length \overline{L}_c , before breaking into two pieces.
- Recombination occurs as a bimolecular process, with a rate that is independent of the molecular weights of the two reacting subchains. There are sufficient ends in the system that a chain is unlikely to recombine with its former partner. Thus, the lifetime of a free chain before recombination is also τ_b .

Even with these restrictions, they allow the coupled reaction/reptation equations to be cast as a one-dimensional stochastic process, whose statistics can be worked out numerically. Here it was defined the breaking/recombination characteristic relaxation time τ_b .

Additionally, Cates mentioned some experimental results as motivations to develop the theoretical framework. In particular, some studies of surfactant organization in micellar systems demonstrated that under special conditions, the equilibrium structure consists of a concentrated solution of tubular micelles that are very much longer than an appropriately defined Kuhn length; that can be treated theoretically as polymers [24]. Theoretical work on micellization [24] [25] suggest that, under certain conditions, there may be no upper limit to the length of the micelles in equilibrium. Presumably, therefore, there exists a regime of parameters in which the reptation times of the micelles is so long that it exceeds the time scale characterizing the dynamic equilibrium of their breakage and recombination. In the next section, it is specified more about the conformation of these cylindrical micelles, that we called *worm-like micelles*, and there will be mentioned some experiments with conclusive results.

For the theory of breaking and recombination kinetics, it is necessary to calculate the fraction of polymer that remains at a time t in the definite original tube, as in the case of reptation, since this fraction will be proportional to the relaxation modulus. The remaining stress in the system is precisely the probability of a section of the polymer that stays still within the tube. Cates estimated this fraction considering a section of the original tube as a particle with diffusion D_c which starts its motion with equal probability on the line segment $[0, L_c]$ with absorbing walls at either end. Due to

the processes of breaking and recombination of the living polymer, the absorbing walls are allowed to make jumps, increasing or decreasing the size of the original polymer segment. This stochastic process was solved numerically by Cates, and he found two limiting cases.

In the first case, in the limit where $\tau_b \gg \tau_d$, the fraction of polymer, $\psi(t)$, remaining at a time t within the tube (or the stress relaxation function), has the same form as in the case of reptation (equation (II.5.5)). On the other hand, for the case where the breaking and recombination time is shorter than the reptation, $\tau_b \lesssim \tau_d$, the stress relaxation (or the relaxation modulus) behaves as a monoexponential

$$G(t) \sim \exp(-t/\tau), \quad (\text{II.6.1})$$

therefore, in the frequency domain, the elastic and viscous moduli get the form

$$G'(\omega) = G_0 \frac{(\omega\tau)^2}{1 + (\omega\tau)^2}, \quad (\text{II.6.2})$$

$$G''(\omega) = \frac{\omega\tau}{1 + (\omega\tau)^2}.$$

In this case there is only one characteristic relaxation time, which is

$$\tau \simeq (\tau_b \cdot \tau_d)^{1/2}. \quad (\text{II.6.3})$$

For $\omega \ll 1/\tau$ the approximation for the viscoelastic moduli is $G'(\omega) \sim \omega^2$ and $G''(\omega) \sim \omega$, the same values as obtained in the case of the Rouse-Zimm modes. The form of the relaxation time emphasizes that the dominant relaxation process involves cooperation between the breaking and reptation mechanisms. For times shorter than τ it is expected that the processes of breaking and recombination be frozen, and the preferred dynamics at these time scales will be Rouse like.

The equation (II.6.1) reminds the response of Maxwellian fluids, characterized for one relaxation time, applied to viscoelastic systems. An extended introduction to this model is presented in Chapter III. In addition, a Cole-Cole plot produces a typical semicircle in Maxwell fluids [23] [22] [26], observed in worm-like micelle systems, made of surfactants.

7. Worm-like micelles

It was mentioned earlier that there is a vast variety of systems formed by self-assembled molecules (Chapter I). A particular and widespread subject to study is amphiphilic molecules characterized for having two sections with opposite affinities to the solvent where they are dissolved. In the case of a polar solvent, the common amphiphiles known as surfactants, have a hydrocarbon chain

(hydrophobic) and a polar head (hydrophilic). The contact with the polar solvent with the hydrocarbon chain, and an entropic-energetic interplay of the system, incite the self-organization of these molecules in aggregates with diverse structures, as spherical micelles, inverted spherical micelles (for nonpolar solvents), cylindrical micelles (worm-like), lamellae, bilipid layers or vesicles. Some of the possible morphologies can self-assemble at a higher level as occur with lyotropic liquid crystals formed with surfactants or with amphiphilic block copolymers, colloidal amphiphilic cumulus, soft nano-engines and even living organisms.

7.1. Surfactant worm-like micelles

Size and shape of micelles at a mesoscopic scale depend on the surfactant geometry, charge, concentration in suspension, temperature, pH, ionic force, among other characteristics. Nonetheless, the morphology of these micelles could be explained using a geometric model, despite it does not include shape and size changes directly, modifying the already mentioned parameters. Even so, the geometric model is a good approximation for visualizing the micelles shape. In this model, the relevant parameter is called *packing parameter* after J. N. Israelachvili [27], $p = v/a_0l_c$, with v the occupied volume by a molecule, a_0 the effective area corresponding to the polar head and, l_c the hydrocarbon chain length. For $p < 1/2$ it is predicted that the molecules will form a sphere; for $1/3 \leq p \leq 1/2$ the aggregates will have a tubular or worm-like shape. Other values correspond to other geometries. Figure II.8 shows the way amphiphilic molecules arrange to form a micelle. There is also a computer simulated worm-like micelle which shows a possible self-assembly of surfactants [28].

The preferred morphology will be fixed by the spontaneous curvature of the assembly that is determined by the most efficient packing of the involved aggregates [2] [27] [29]. The spontaneous curvature optimizes the system energetically. However, it does not account for the effects of entropy that also can stabilize some structures and defects. The quantity of surfactant in solution determines the formation of worm-like micelles when a *critical micelle concentration* (CMC) is reached, defined as the concentration at which each new molecule added to the solution has an equal probability to go in a micelle or to stay as a disperse monomer. Below the CMC, entropy favors a uniform dissolution of the amphiphile in the solvent, and aggregation is negligible. Above the CMC, interaction dominates and entropy effects are reduced. Consequently, the number of aggregates usually for a spherical form sharply increases. Subsequently, cylindrical micelles are formed when the amphiphiles have a moderate spontaneous curvature, lower than spherical micelles but larger than vesicles or bilayers. Here, energy is optimized when the curvature is uniform everywhere, forming worm-like micelles (WLMs). Nevertheless, entropy introduces in the system a degree of randomness through bending of cylindrical micelles, which adds conformational entropy like the configurational entropy of polymeric chains, and through topological defects, in the form of end-caps and branch junction points. When these two defects appear, regions with different local curvatures are formed but incurring in different energetic penalties. The overall entropic gain associated with end-caps is higher than that of branch points. Although the appearance of topological defects introduces an entropy gain, the type of defect that dominates is set by the amphiphile spontaneous

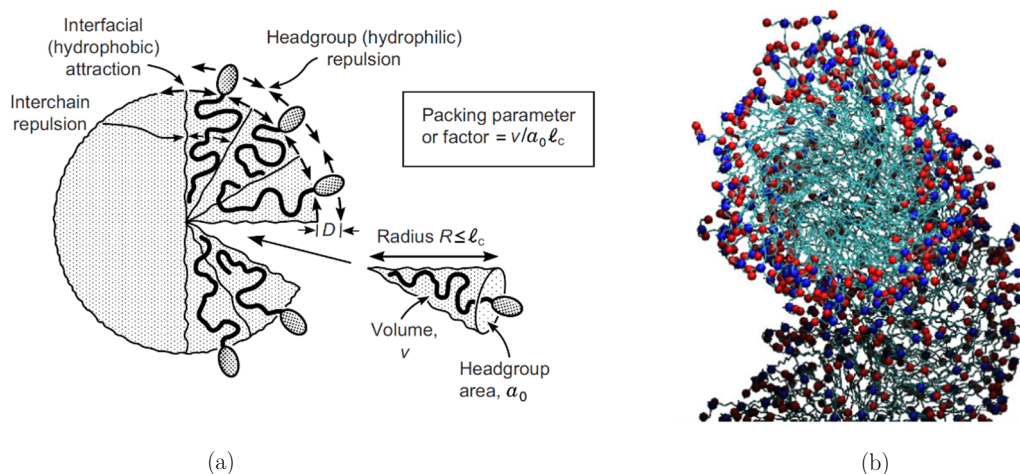


Figure II.8 (a) Micelle formation considering the geometric model. The sizes of the amphiphiles are shown to make clear each element of the packing parameter [27]. (b) Computer simulation of a worm-like micelle. Here we are not making any difference between colors [28].

curvature. If the scission energy of a WLM (the energy required for creating two end-caps from an infinite cylinder) is large enough, then the semi-flexible linear micelles may become very long and entangled. End-caps increase entropy by increasing the number of micelles in the system. Thus, lowering the scission energy shortens the total contour length of the linear micelles.

On the other hand, branch junction points increase the number of possible configurations, enabling percolation, and the formation of extended micellar networks, which lead to a multi-connected rather than an entangled network of cylindrical micelles. A review about junctions and end-caps formation can be found elsewhere [30]. The final structure is an interplay between minimization of total energy reducing the formation of end-caps, against the increment of entropy decreasing the contour length of WLMs. The thermodynamic equilibrium is reached with stable WLMs in solution but with constant breaking and recombination processes in addition to the reptation mechanisms, typical of polymer chains.

The aggregation and self-organization of WLMs in thermodynamic equilibrium, at mesoscopic level influences directly the behavior we can observe at macroscopic scale, as viscosity or viscoelastic properties under applied stress. WLMs self-assembly strongly depends on the concentration in solution, in the same way as polymer concentration affects the behavior of polymeric solutions. This dependence can be described as follows: just above the CMC concentration, the fluid with embedded WLMs is in a so-called diluted regime, where each micelle is isolated. The WLM solutions also present a low viscosity. Once the micellar concentration increases, the system reaches an entanglement concentration c^* (as the overlap concentration), from which WLMs start to entangle with each other, forming a mesh of size ξ , which inversely depends on the micellar concentration. At this point, the solution has reached the semidiluted regime, where viscosity has considerably increased, and arrangement of WLMs is isotropic. When the cylindrical micelles are long enough, it is probably that the bending energy of the micelles overcome the thermal energy of the solvent. The straight segments length that micelles possess before the bending energy exceeds the thermal energy is called *persistence length*, l_p . The persistence length of WLMs affects the entanglement between

them and the mesh size directly. When $\xi < l_p$ the system has reached a concentrated regime. When the system has just reached the concentrated regime, the viscosity of the system has not changed considerably. Figure II.10 presents the self-organization of surfactants with the steps that form micelles and WLMs depending on concentration [31].

In the concentrated regime, orientational correlations start to appear. At high surfactant concentration there has been found nematic phases due to the arrangement of WLMs and hexagonal ordering even at higher concentrations [32]. Figure II.9 presents a typical diagram where there are shown different transitions a system of WLMs experiment when the concentration of these structures is increased [33].

In semidilute and concentrated regimes, under a deformation WLM solutions present viscoelasticity and the stress decays with just one characteristic relaxation time due to the faster scission and recombination times rather than the reptation mechanism. For this reason, WLMs made of surfactants are living polymers, and a robust approximation to a Maxwellian fluid at long times

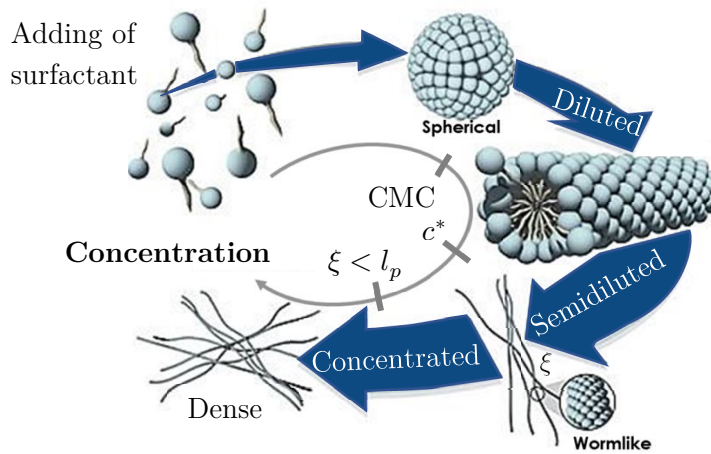


Figure II.10 WLMs organization under the dependence of surfactant concentration. There can be appreciated the different regimes reached by the WLM solutions. Taken from [31].

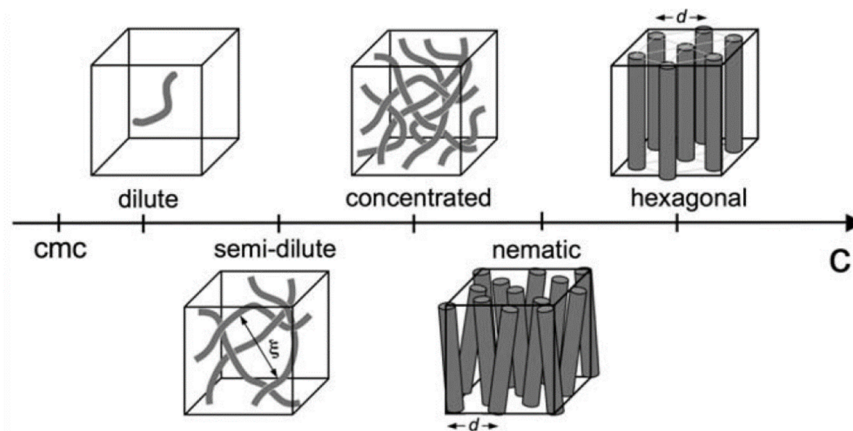


Figure II.9 Different concentrations regimes encountered in wormlike micellar solutions with increasing concentration. ξ is the mesh size of the entangled network and d denotes the average distance between colinear micelles in the concentrated isotropic, nematic and hexagonal phases [33].

(10 – 1000 ms) or low and intermediate frequencies ($\omega < 100 \text{ s}^{-1}$), within the linear regime. At high frequencies, when time scales are shorter than those of WLMs breakage time, the Maxwellian stress relaxation processes are essentially frozen, and the micelles can be regarded as semiflexible polymer chains, as mentioned in the last section. Stress relaxes via intramicellar processes: first, it is dominated by the Rouse-Zimm modes and then by the internal relaxation of individual Kuhn segments [34]. At this frequency range, G^* exhibits a power-law behavior, $G^* \sim \omega^\nu$, with the exponent $\nu \sim 5/9$ in the Rouse-Zimm regime mentioned previously, which changes to $\nu \sim 3/4$, where the internal bending modes of Kuhn segments dominate. This change occurs at a critical frequency, ω^* , corresponding to the shortest relaxation time in the Rouse-Zimm spectrum [35].

There exist other characteristic lengths involved at the mesoscopic level of WLMs, although these lengths can be generalized to polymeric solutions. Figure II.11 presents the structural arrangement of these systems where the polymeric shape structures maintain an isotropic organization [36]. The contour length, the persistence length and the mesh size have been mentioned earlier. In addition to these lengths there exist the *entanglement length* l_e which is the contour length between two consecutive crossing points with other polymer chains; and the thick d of the polymer (or diameter of the micelle). When the structures under study are living polymers (or WLMs made of surfactant), it is possible to estimate some of the polymeric network characteristic lengths through their rheological properties. The mesh size is obtained from the elastic modulus value at intermediate frequencies, that is, knowing G_0 which is the value where $G'(\omega)$ and $G''(\omega)$ overlap and cross each other. The equation with this relation is [11] [37]

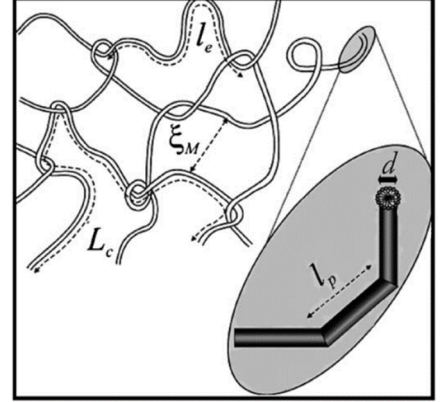


Figure II.11 Mesoscopic polymeric structure. The different characteristic lengths are shown. Taken from [36].

$$\xi = \left(\frac{k_B T}{G_0} \right)^{1/3}. \quad (\text{II.7.1})$$

With the already mentioned critical frequency ω^* , where a change of relaxation modes takes place, it can be found the associated parameter for the stiffness of the WLMs (or polymeric chains). So, the persistence length is obtained with the expression [35]

$$\omega^* = \frac{k_B T}{8\eta l_p^3}, \quad (\text{II.7.2})$$

with η the solvent viscosity. With the persistence length and the mesh size, it is possible to calculate the entanglement length [23]

$$l_e = \frac{\xi^{5/3}}{l_p^{2/3}}, \quad (\text{II.7.3})$$

equation which is obtained from a Poisson renewal model for living polymers. From the same treatment, the contour length can be computed

$$\frac{G''_{\min}}{G_0} \approx \frac{l_e}{L_c}, \quad (\text{II.7.4})$$

where G''_{\min} is the minimum of $G''(\omega)$ after the first crossing between $G''(\omega)$ and $G'(\omega)$, at intermediate frequencies, where the relaxation mechanisms are led by reptation.

Several investigations have been developed where the design and understanding of worm-like micellar systems made of surfactant is the main topic. In addition to the already mentioned references, here are quoted some other works: [38] [39] [40] [41].

7.2. Block copolymer worm-like micelles

At the beginning of this section it has been pointed out that some of the possible morphologies which self-assembled at high level to form worm-like micelles are surfactant molecules or amphiphilic block copolymers. Even when the affinities with different sort of solvents are very similar for both kind of building blocks, however, block copolymers assemble into worm-like micelle morphologies with certain different mechanical properties rather than the ones built up by surfactants, that complicates the understanding. F. S. Bates and G. H. Fredrickson made a nice introduction to the design of soft materials with block copolymers as building blocks [42].

In diblock copolymers, recent advances have shown that stability of different morphologies can be tuned by varying the solvent composition [43] [44], because of the free energy contribution from the interfacial tension between the solvent and the insoluble block. Therefore, a complex interplay between molecular geometry and the amphiphilic character of the diblock copolymer determines the organization of supramolecular structures. This interplay leads to taking into account the micellar core that could be partially swollen by poor solvent, the surface free energy per chain associated to the core-shell interface, and the structure of the shell; the latter is determined from a balance among the elastic stretching of their constitutive blocks, and the repulsive interaction among their monomers. The long morphology of each copolymer can provoke a peculiar structural conformation of the WLMs which causes different rheological properties of the micellar solutions, as has been studied in some cases.

We are interested in the study of diblock copolymers of the type polybutadiene-polyethylene oxide, due to their amphiphilic behavior. The polybutadiene is extremely hydrophobic while the polyethylene oxide is hydrophilic. In a polar solvent, water in particular, these copolymers can form WLMs. The most extensively studied diblock copolymers of the type polybutadiene-polyethylene oxide in water solution are those rich in the 1, 2-microstructure (IUPAC name: poly1-vinylethylene) [45] [46] [47] [48] [49] [50] (see Figure II.12). They will be referred to as P(1,2)B-PEO from now on. Morphology of the supramolecular structures of these copolymers depends on the weight fraction (w_{PEO}) of polyethylene oxide (PEO) in the copolymer, which is related to the hydrophilic block

length, and on the degree of polymerization of the hydrophobic block, polybutadiene P(1,2)B. Even though the full phase diagram of these systems is not known, the weight fraction where the different structures (micelles, WLMs, lamellas, etc.) are located is approximately known. Aggregation in dilute aqueous solutions leads to spherical micelles approximately at $w_{\text{PEO}} > 0.6$, WLMs approximately in the range of $0.47 < w_{\text{PEO}} < 0.59$, and bilayers at $w_{\text{PEO}} < 0.47$ [47] [51]. One important difference between small non-ionic surfactants and diblock copolymers dispersed in a polar solvent, such as water, is the value of the CMC. For the former ones, the CMC is not too low; molecular exchange and equilibration are relatively rapid. On the contrary for the latter ones, molecular exchange is extremely slow due to the very small CMC ($\leq 10^{-6} \text{Mol L}^{-1}$) and decreases as temperature increases; the presence of free chains in solution is practically negligible. This impediment of micellar rearrangement has its origin on the extremely high hydrophobicity of the P(1,2)B block. Therefore, observed aggregates are not necessarily at equilibrium.

A more recent work done by B. Arenas-Gómez and coworkers [52], treats the case of the self-assembled aggregates made of 1,4 poly(1,3-butadiene)-polyethylene oxide diblock copolymer (from now on: P(1,4)B-PEO; IUPAC name: poly(but-2-ene-1,4-diyl)-block-polyoxyethylene) in water. The hydrophobic block, P(1,4)B (polybutadiene, PB) is rich in 1,4 microstructure, (see Figure II.12). The degree of polymerization of the P(1,4)B and PEO blocks used here are $m = 37$ and $n = 45$, respectively, so the system will be called PBPEO45 from now on. This system is similar the those made with P(1,2)B-PEO [48], which self-assembles in spheres, cylinders or bilayers, when the polymer blocks have a degree of polymerization ($m = 46$, and $n = 35, 39, 42, 44, 56$) relatively close to those of the blocks used in this work. The solution concentration was limited to $C_{\text{PBPEO45}} \leq 2.5 \text{ wt\%}$, to avoid phase separation. First, B. Arenas-Gómez and collaborators obtained the morphology of the self-assembled structures with small angle X-ray scattering (SAXS, explained in Chapter III) experiments, from where it was determined a cylindrical shape and a core-shell cross-section structure with a diameter of $\sim 12 \text{nm}$ (Figure II.13i). Also, rheological experiments were developed in which the main results show a deviation from the Maxwellian behavior, according to oscillatory experiments at low and intermediate frequencies, and Cole-Cole plots (Figure II.13ii), which is atypical in a WLM solution. This uncommon behavior for a WLM system is explained by the slow dynamics of the self-assemble; there is an impediment of any micellar rearrangement through water, due to the extremely high hydrophobicity of the PB block [52], and the system is dynamically arrested. This feature has been observed in similar diblock copolymers of the type P(1,2)B-PEO in other circumstances, already mentioned above [53] [48].

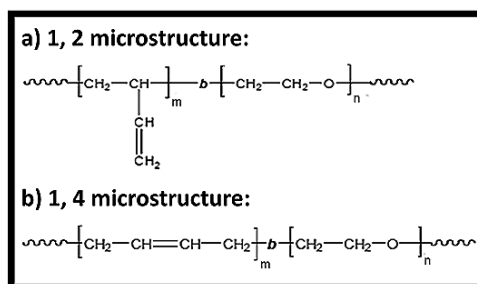


Figure II.12 Diblock copolymers of the type polybutadiene-polyethylene oxide showing two different polybutadiene microstructures: (a) P(1,2)B; source name: 1,2-poly(1,3-butadiene); IUPAC name: poly 1-vinylethylene. (b) P(1,4)B; source name: 1,4 poly(1,3-butadiene); IUPAC name: poly(but-2-ene-1,4-diyl). At the very end, both terminal groups end up with hydrogen. Taken from [52].

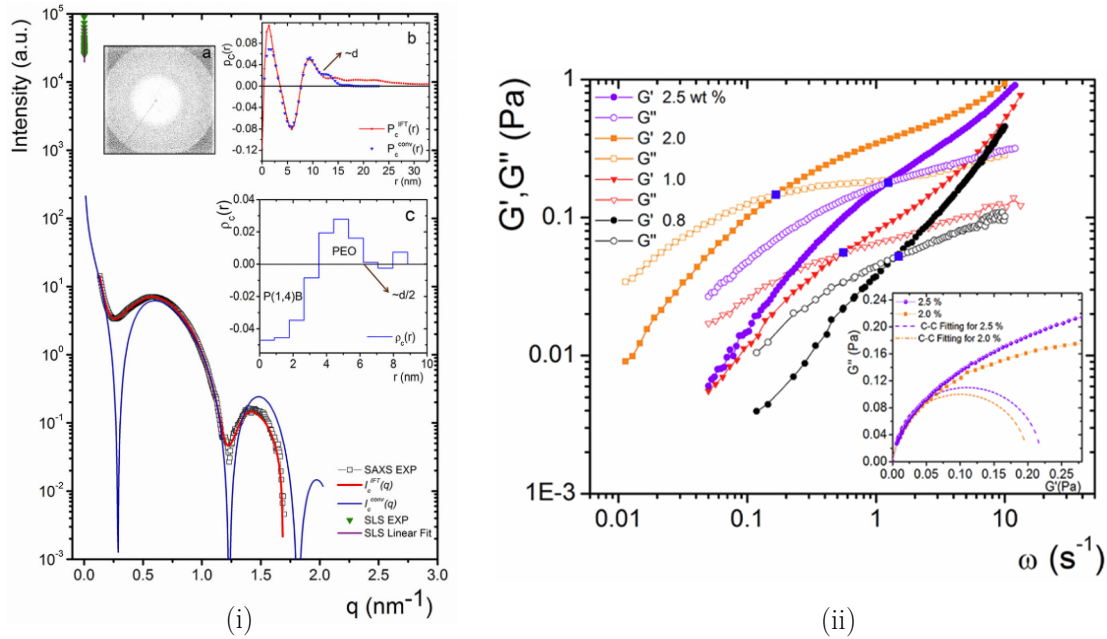


Figure II.13 (i) SAXS intensity vs. q for the solution of PBPEO45 in water. Experimental data (\square) for SAXS at $C_{\text{PBPEO45}} = 2$ wt%. Experimental data for SLS (\blacktriangledown) at $C_{\text{PBPEO45}} = 1$ wt%. $I_c^{\text{IFT}}(q)$ (red line) is the cross-section scattering function computed with the Fourier transform method, and $I_c^{\text{conv}}(q)$ is the cross-section scattering function obtained with the deconvolution method (blue line). Both scattering functions correspond to cylindrical geometries. Insets: a) X-ray scattering intensities in a 2-dimensional multi-wire proportional counter. b) $p_c(r)$ is the cross-section pair distance distribution function, $p_c^{\text{IFT}}(r)$ computed with the Fourier transform method (in red) and $p_c^{\text{conv}}(r)$ computed with the deconvolution method (in blue). c) $\rho_c(r)$ is the radial electron density distribution function. (ii) Viscoelastic spectra for the PBPEO45 in water at different concentrations. Inset: G'' vs. G' for $C_{\text{PBPEO45}} = 2$ wt% and 2.5 wt%, with fittings (Cole-Cole plots). All plots taken from [52]. Details are found in the same reference.

8. Gels

So far, we have been established some models to understand the dynamics of polymers in liquid state, in dilute and semidilute regime. Also, we have seen briefly the behavior of living polymers which reptate as polymers to liberate energy, but also break and recombine to maintain thermodynamic equilibrium. In special cases when the living polymers have Maxwellian behavior, it is also possible to extract structural information on the systems. Now, I introduce the case when polymer chains possess crosslinks with other chains, phenomenon present in many materials in transition from liquid to solid states. This behavior is called gelation. Here I summarize important aspects of polymer gelation that are well explained as introductory level by M. Rubinstein and R. H. Colby [12]. Although in general, polymer gelation processes are different from colloidal gelation processes and furthermore, different among colloidal particles with different shapes (anisotropic), some fundamental concepts are the same, hence here there are included some ideas for colloidal gelation, taken mainly from E. Zaccarelli review [54].

Linking chains together leads to progressively larger branching polymers (Figure II.14a). The polydisperse mixture of branched polymers obtained as the result of such a process is called the *sol*, since the molecules are soluble. As the linking process continues, still larger branched polymers are obtained (Figure II.14b). At a certain extent of reaction, a molecule spanning the whole system

appears. Such a huge molecule will not dissolve but may only swell in a solvent. This “infinite polymer” is called the *gel* or *network* and is permeated with finite branched polymers (Figure II.14c). The transition from a system with exclusively sol, to a system containing also a gel is called the *sol-gel transition* or gelation and the critical point where gel first appears is called the *gel point*. Later in the text we introduce a model to know where the critical gel is found with rheology experiments. For the case of colloids, a more general definition follows. A coherent mass consisting of a liquid in which particles are either dispersed or arranged in a low density disordered arrested state, which does not flow but possess solid-like properties such as a yield stress is commonly named a gel. Similarly to glasses, the gel structure does not show any significant order, and in this respect, it is similar to that of a liquid. However, for dilute systems, a gel often displays a large length scale signal associated with the fractal properties of its structure [54].

Different types of gelation transitions are summarized in Table II.1. Here, gelation is divided in two main groups: physical gelation and chemical gelation. The chemical gelation involves formation of covalent bonds and always results in a strong gel. There are three main chemical gelation processes: condensation, vulcanization (crosslinking polymers), and addition polymerization, whose gelation transition was associated with the formation of an infinite network with finite shear modulus and infinite zero-shear viscosity (this feature was also found in our experiments for single wall carbon nanotubes within poly(acrylic) acid matrix, which presumably reaches the weak physical gelation). A more extended explanation of these gels can be found in [12]. For further understanding the chemical gelation process, refer to the work of E. Zaccarelli [54], in which a distinction between gelation and vitrification is shown, in terms of the polymerization process that interconnects monomers. A length scale dependent analysis of the chemical gel and glassy states should be able to discriminate between the two cases. Indeed, while the glass is nonergodic at all relevant length-scales, the gel only has a correlation, dictated by the infinite network, strictly at large length scales, while all other length scales retain a quasi-ergodicity [54]. Examples of computational and experimental studies on chemical gels are mentioned in [54].

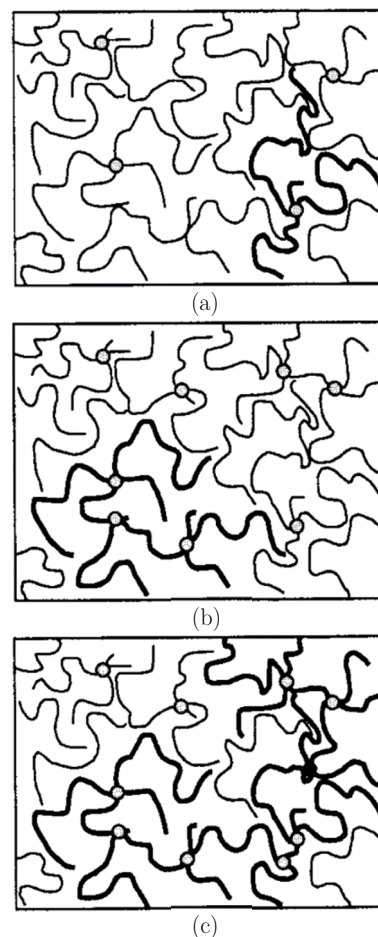


Figure II.14 Crosslinking of linear chains. (a) Four crosslinks, (b) eight crosslinks, (c) ten crosslinks. The largest branched polymer is highlighted and the 10th crosslink (dark) formed an incipient gel. Taken from [12].

| Physical | | Chemical | | | |
|----------|--------|-------------------|----------|-----------------------|----------------------|
| Weak | Strong | Reacting monomers | | Crosslinking polymers | |
| | | Condensation | Addition | End-linking | Random cross linking |

Table II.1 Classification of gelation transition. Taken from [12].

The physical gel can be strong or weak. Strong physical gels have strong bonds between polymer chains that are effectively permanent at a given set of experimental conditions. These gels are solids and can only melt and flow when the external conditions change. Strong physical gels are kind of analogous to chemical gels. Weak physical gels have reversible links formed from temporary associations between chains, which bonds originate from physical interactions of the order of $k_B T$. These associations have finite lifetimes, breaking and reforming continuously. Among this sort of gels, we can find bonds as hydrogen bonds, block copolymer micelles above their glass transitions, ionic associations, or hydrophobic interactions. Such reversible gels are never truly solids but if the association lifetime is sufficiently long they can appear to be solids on certain time scales. Hence, whether a reversible gel is weak or strong depends on the time scale over which it is observed.

A formal definition of gelation refers that it is a connectivity transition, or percolation transition. The mean-field theory of percolation was developed by P. J. Flory [55] and W. H. Stockmayer [56] [57], under the following two assumptions: independent bonds and absence of bonding loops. Percolation describes a process by which sites or links on a (potentially random) graph or lattice can be connected. In the context of material physics, the theory of percolation has three obvious applications: understanding the flow of fluid through a disordered porous medium, in the conductivity of random networks, and involved in the formation and physical properties of gels, formed when a minimum *percolation threshold* fraction of bonds has been formed between the clusters making up the gel. Gelation can be described by a bond percolation model. Imaging a container fill of monomers, which occupy the sites of a lattice. In simple bond percolation model, all sites of the lattice are assumed to be occupied by monomers. The crosslinking reaction between monomers is modeled by randomly connecting monomers on adjacent sites by bonds. The fraction of all possible bonds that are formed at any point in the reaction is called *the extent of reaction* p , which increases from zero to unity as the reaction proceeds. In this model, a polymer is represented by a cluster of monomers (sites) connected by bonds. When all possible bonds are formed, the reaction is completed ($p = 1$) and the polymer is a fully developed network. At the percolation threshold or gel point, the system undergoes a connectivity transition. Slightly below the gel point, the system is a polydisperse mixture of branched polymers, but one structure percolates through the entire system. This morphology is a tenuous structure which is quite different from the fully developed network that exists far above the gel point. This connectivity transition from a sol below the gel point, to a gel permeated with sol above the gel point is called the gelation transition. The *gel fraction* is defined as the fraction of all monomers belonging to the gel. Every monomer must be either part of the sol or part of the gel, so the sum of the sol and gel fractions is unity. Below the gel point, all monomers are either unreacted or belong to finite sized polymers and therefore the sol fraction is unity and the gel fraction is zero. Above the gel point, the gel fraction is non-zero and the sol fraction is less than unity. Therefore, the gel fraction is the probability that a randomly selected monomer belongs to the gel, and it is the order parameter for gelation. The order parameter indicates the gel fraction, when the reaction has passed the gel point. The order parameter is continuous through the sol-gel transition, which means that gelation is analogous to a continuous phase transition. For a further review of gelation models, refers to [12].

In standard percolation studies, the bond lifetime, and hence the lifetime of the spanning cluster, is not taken into account. For chemical gels, the bond lifetime is infinite and thus percolation theory

has been the theoretical framework for describing the gel transition. In the case of chemical bonds, where bond formation and bond duration are coupled, the percolation concept is connected to the dynamics and thus it can describe the chemical gelation transition. For colloidal gels, and polymeric physical gels, bonds are transient. Clusters break and reform continuously. Percolation theory can thus be applied only to describe static connectivity properties [54]. It turns out that percolation is not a sufficient condition for physical gelation. However, it should be at least a necessary condition, if one follows the idea that a gel arises from a stable percolating network. Within this picture, attraction should be a necessary ingredient for gel formation. However, some systems may form arrested states at extremely low densities, and their properties be not at all related to percolation. This happens primarily in systems with sufficiently long-range repulsion, that in the end acts as the stabilizing mechanism for arrest. The question that naturally arises is whether these states should be considered gels or glasses in general terms. According to [54], it is proposed that a gel should necessarily have attraction as the leading mechanism for gelation, while a glass can be driven either by repulsion (hard-sphere or Wigner glass), or by attraction just in the high-density region (attractive glass).

More recent computational studies for colloidal spheres, developed by P. D. Godfrin and coworkers [58], have established a general phase behavior view on systems with an excluded volume with short-range attraction (SA) and long-range repulsion (LR), or SALR potentials. The investigation in [58] is motivated by previous experimental and simulation results that obtained structural information of particle aggregates (small angle neutron scattering and small angle x-ray scattering), which have provided direct evidence that low- q peaks in the scattering patterns are not necessarily a consequence of clustering as envisioned in the earlier sense, but rather, are a general representation of the presence of intermediate range order (IRO) in the fluid. Hence, a low- q peak in the structure factor is not an accurate indication of cluster formation and is more accurately termed an IRO peak. Using the so-called extended law of corresponding states, and after surveying different interaction potentials (with different relative strengths of repulsion to attraction), they found four different phase states in terms of a critical temperature and particle fill fractions: dispersed fluid, clustered fluid, random percolated and cluster percolated. One of the asseverations is that gel or glass formation must be preceded by the formation of a cluster percolated network. Further studies are necessary to include interactions between anisotropic particles with high aspect ratios and different persistence lengths, as the single wall carbon nanotubes systems in which we have worked. For rods, bond orientation can significantly affect the surface attraction strength, which can vary significantly depending on the Hamaker constant, angle of alignment, aspect ratio, and surface separation distance. Hence, the percolation process is quite different from the spherical isotropic case [27]. An extended rheological and structural study of rod-like systems with different short-range interactions and not so long aspect ratios can be found in [59].

8.1. Model for critical gels

H. H. Winter and co-workers have characterized critical gels where dynamic arrest leads to gelation due to attractive interactions [60]. Sometimes it is possible to extract information about the gelation point of a system when rheology experiments are applied. In this sense, a critical gel exhibits an

unusually simple and regular relaxation behavior, which expresses itself in a self-similar relaxation modulus $G(t) = St^{-n}$, where $G(t)$ is the real relaxation modulus [60] where S and n are the two fitting material parameters that characterize the gel. S is the "strength" of the network, and n reflects the nature of the size distribution of the mesoscale superstructure. A higher value of n means a broader aggregate size distribution, consistent with a slightly more open structure [61] The values of n range between 0 and 1, and provide structural information.

Close to the gel point in the frequency domain, performing oscillatory rheology experiments and if the resulting plots allow us, it is easy to fit a power law function as

$$\begin{aligned} G'(\omega) &= G'_c \omega^n, \\ G''(\omega) &= G'_c \omega^m, \end{aligned} \tag{II.8.1}$$

where G'_c and G''_c represent two material constants. F. Chambon and H. H. Winter [62] using the Kramers-Kronig relation (III.1.24), found out that both exponents must be equal, and within the range $0 < n < 1$. The elastic moduli is

$$G'(\omega) = S\Gamma(1-n)\cos\left(n\pi/2\right)\omega^n, \tag{II.8.2}$$

with $G'(\omega) = G''(\omega)/(\tan n\pi/2)$, $0 < \omega < \infty$, and

$$S = \frac{2\Gamma(n)}{\pi}\sin\left(n\pi/2\right)G'_c, \tag{II.8.3}$$

where $\Gamma(n)$ is the gamma function, and clearly $G''(\omega) > G'(\omega)$ for $n > 1/2$, $G'(\omega) > G''(\omega)$ for $n < 1/2$, and $G'(\omega) = G''(\omega)$ for $n = 1/2$. To assure that a system is around the gel point, using Flory's principles ($\eta_0 \rightarrow \infty$, and $G_\infty = 0$) [63] is experimentally difficult [61] [62]. A more general method to find the gel point in a system consists in the calculation of the tangent of the phase angle between the dynamical moduli, $\tan \delta = G''(\omega)/G'(\omega)$. When the tangent of the phase δ is independent of the frequency, we can assure that the system is in the gel point, and the value of n can be estimated directly, for $0 < n < 1$,

$$\tan \delta = \tan\left(n\pi/2\right). \tag{II.8.4}$$

9. Single wall carbon nanotubes and polyelectrolytes

Liquids with dispersed rod-like particles present different microstructural orderings that exhibit different rheological responses [64]. For applications, it is essential to foresee the rheological response of these suspensions from the underlying properties of the rods and the dispersant agent, as well as other features that affect their response as percolation, phase stability, aggregation, flexibility,

polydispersity, etc. It is not uncommon that rod-like colloidal suspensions in highly viscous polymers flow at low shear stress with quiescently formed rod networks which rapidly break down and then re-gel upon cessation of flow. Single-wall carbon nanotubes (SWCNTs) dispersed in a polymer are a clear model example of this case. It is stated that when the rod length is such that the suspension is in the colloidal domain, four properties control the microstructure, dynamics, and rheology of rod-containing materials [64]: interparticle forces, aspect ratio, particle number density, and flexibility. The principal way to generate a significant level of elasticity in colloidal suspensions is to arrest particle dynamics at the microscopic level, although dynamic arrest can lead to gelation with slow dynamics due mainly to attractive interactions and bonding, or to vitrification with slow dynamics due primarily to excluded volume interactions and packing. However, the microstructures linked to these two kinds of slow dynamics are different [64], heterogeneous fractal clusters of rods for the former and homogeneous rod network for the latter. The volume fraction range for the transition between these two limiting cases is strongly aspect ratio dependent.

The poor solubility of carbon nanotubes (CNTs) is a direct consequence of their strong van der Waals interactions that produce the formation of large nanotube bundles. Here, the attraction is directly proportional to the diameter of the nanotubes and inversely related to the inter-tube distance [27]. Therefore, even at a modest concentration, the inter-tube attraction yields the formation of aggregates or bundles constituting this attraction the most significant challenge towards the dispersion of SWCNTs in a polymer matrix. However, some polymers have been used effectively as exfoliation agents of nanotube bundles making possible the incorporation of the nanotubes as individual entities or as very thin bundles. Many mechanisms have been mentioned for explaining why they are so effective [65] [66]. Some examples of polymers dispersing SWCNTs can be found in the literature [67] [68] [69] [70]. To improve the dispersion, CNTs can be modified noncovalently [71], covalently [72] [73] [74] [75], using surfactants [76] [77] [78], DNA [79] or proteins [80]. These chemical and physical approaches can be successful at low and intermediate CNTs concentrations. Nonetheless, the dispersion of CNTs is still a challenging problem at high concentration.

The behavior of CNTs dispersed in a polymer matrix can be characterized into three regimes according to its concentration and their orientational or structural correlation [81]. In the dilute regime, dispersed nanotubes or completely exfoliated behave as individual tubes or as thin dispersed bundles. In this regime, short-range intertube interactions are present, but long-range interactions are negligible. The transition from dilute to semidilute regime coincides with a percolation event. As exfoliation is improved, the percolation transition occurs at a lower concentration. In the semidilute regime, the extent of exfoliation of the nanotubes, or their small bundles, and their interaction with each other control the overall rheological behavior of the nanocomposite. Close to this percolation threshold, dramatic changes in the rheological properties are observed that arise supposedly from the inter-tube interaction. Incorporation of CNTs in the polymer gradually transforms the liquid-like behavior to solid-like behavior where the storage and loss modulus are almost frequency independent at low frequencies and $G'(\omega) > G''(\omega)$ [81]. The percolation threshold decreases with an increase in CNTs aspect ratio suggesting the formation of a matrix spanning path at a low or modest nanotube loading. At concentrations significantly larger than the percolation concentration, the excluded-volume interactions lead to an isotropic-nematic transition as occurring in CNTs dispersed in acid, [82] where the concentrated regime starts, and the rheological properties tend to

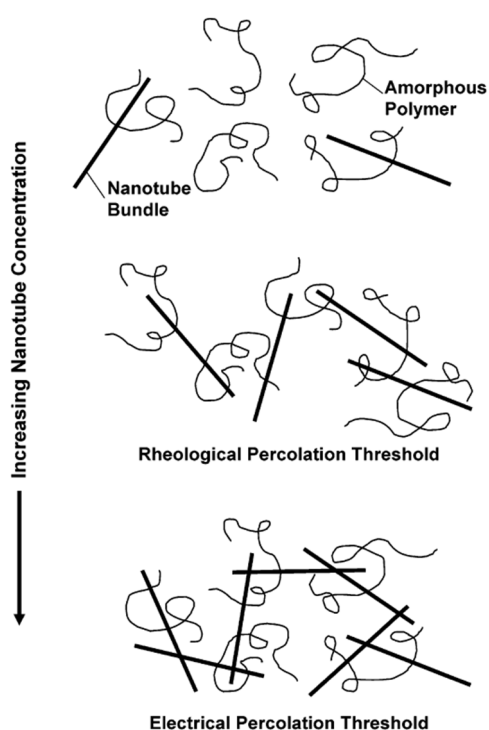


Figure II.15 Schematic of SWNT/polymer nanocomposites in which the nanotube bundles have isotropic orientation. (top) At low nanotube concentrations, the rheological and electrical properties of the composite are comparable to those of the host polymer. (middle) The onset of solid-like viscoelastic behavior occurs when the size of the polymer chain is somewhat large to the separation between the nanotube bundles. (bottom) The onset of electrical conductivity is observed when the nanotube bundles are sufficiently close to one another to form a percolating conductive path along the nanotubes. Taken from [83].

reach asymptotic values. More about the rheological behavior of CNTs in a polymer matrix can be found elsewhere [81]. A very illustrative image which coincides with the transition from dilute to semidilute regime and the percolation threshold, is the one introduced by K. I. Winey and coworkers [83]. The system they used is a mixture of SWCNTs embedded in a polymer matrix of poly(methyl methacrylate) (PMMA), in dimethylformamide (DMF) suspension (Figure II.15). In this image they propose a so-called *rheological percolation threshold* (or mechanical percolation threshold) at the semidilute regime, where the polymer chains are connected with the help of nanotubes bundles, and as a consequence the whole system presents a typical gel rheological behavior. When SWCNTs concentration increases, but the system is still in the semidilute regime, the system gets the *electrical percolation threshold*, which means that the suspension in gel state has formed a percolating conductive path along the nanotubes that are now in touch. They conclude that the required tube-tube distance has to be less than ~ 5 nm for the nanocomposites to be electrically conductive. However, as long as the tube-tube distance is comparable to the diameter of random coils of PMMA chains, the nanotube network can effectively restrain polymer motion. Thus, the required tube-tube distance for electrical conductivity percolation is smaller than that for the rheological percolation, so that more nanotubes are required to reach the electrical conductivity threshold. Furthermore, note that the nonmetallic tubes do not contribute significantly to the electrical conductivity, although they can restrict polymer motion. The same idea is applicable to the system we have

studied, but with the difference that we decided to disperse SWCNTs in a polyelectrolyte matrix, which possesses an extra degree of freedom to get adapted under certain external conditions.

Some polyelectrolytes are stimuli-responsive polymers that show significant reversible structural changes in response to small changes in their environment, such as pH [84]. The environmental adaptiveness of polyelectrolytes leads to smart self-assembly processes with intriguing results. Polar solvents can dissociate polymers with ionizable groups leaving charges on the polymer chains and releasing counterions into the solution [85]. Electrostatic interactions between charges in the polymer lead to a rich behavior different from those of uncharged polymers, for example: the crossover from dilute to semidilute solution regime occurs at much lower polymer concentrations than that in solutions of neutral chains, polyelectrolyte chains in semidilute regime follow unentangled dynamics in a much wider concentration range and the crossover to the entangled dynamics occurs further

away from the chain overlap concentration than in solutions of uncharged polymers, among other characteristics [85].

One example is the poly(acrylic) acid (PAA) [86]. The carboxyl groups of polyacid polymers in aqueous solution are protonated at low pH and neutrally charged; thus, hydrophobic interactions promote a relatively compact polymer structure. Electrostatic repulsion between some charged, not protonated carboxyl groups, leads to the formation of extended polymer structures; a sort of loose coil. This pH-responsive conformational change just occurs in relatively high molar mass PAA (> 16.5 kDa) [86]. PAA is protonated in an aqueous medium at $\text{pH} < 3$, as the pH increases, carboxylic groups are deprotonated, forming a polyelectrolyte that becomes highly charged ($\text{pH} \sim 5$), and its backbone becomes stretched, forming a 3D interacting network of polymer chains. As a consequence, the size of the PAA and the regular polymer-polymer interactions both lead to a significant change in the rheological behavior of this polymer in water solution with different H^+ content.

III. Experimental techniques

1. Rheology

Flow constraint and deformation of materials are subjects that rheology studies. In practice, it is normal to restrict the rheological experiments to the study of the constitutive relations between stress and strain (typically under the application of a shear: σ and γ are shear stress and shear strain respectively). The way a material flows is determined by its mesoscopic structure which is an intrinsic characteristic of its physical state. A solid corresponds to a material with strong attractive interactions between molecules, instead of the behavior in gas, with its constitutive molecules almost without interactions. Among these structures, we can find a liquid with short ranged repulsive interactions and long ranged attractive interactions. Of course, these physical states are subjected to the surrounding thermodynamic conditions, which determine the final rheological properties of the system. The classical theory of elasticity considers the mechanical properties of elastic solids by the Hooke's law, where the strain is proportional to the applied stress, $\sigma(t) = G\gamma(t)$, with G the relaxation modulus. On the other hand, theory of hydrodynamics deals with the properties of viscous liquids according to Newton's law, where the response of the stress is proportional to the rate of deformation (or shear rate), but independent of the applied strain, as occur in a damped system, $\sigma(t) = \eta\dot{\gamma}(t)$, where η is the instantaneous viscosity of the system [87] [88]. The SI unit of stress is Pascal (Pa), the strain is dimensionless, so the relaxation modulus has units of Pascal as well, and because the shear rate has units of the inverse of a second, the IS viscosity unit is Pa s.

Figure III.1 clarifies the mechanical behavior of a system under a shear strain. If the system is a Hookean solid, its response will endure as long as the strain persists, unlike Newtonian liquids which response decays instantaneously. A system with an intermediate mechanical response is called *viscoelastic* which response at short times is similar to a solid, but after some time it relaxes like a liquid. The time it takes to relax is called *relaxation time*, and the decaying shape depends on the structure at different mesoscopic length scales.

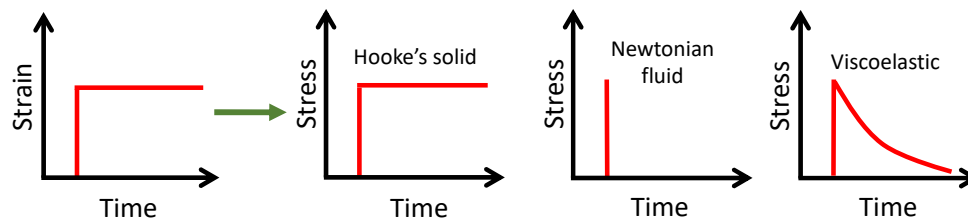


Figure III.1 Different stress responses when a square-like pulse strain is applied. The solid response is proportional to the strain applied, unlike the Newtonian fluid response. The viscoelastic system contains mechanical response similar to a solid at earlier times and a liquid at longer times.

1.1. Maxwell model

Polymers are viscoelastic, but generally under stress, they have different relaxation mechanisms as is outlined in Chapter II (Theory of polymers). These mechanisms depend on the regime of concentration of the polymers in liquid solutions, and in the sort of interactions with the solvent. Other systems of interest are the living-polymers in solution, which present a particular relaxation mechanism above the semi-dilute regime as pointed out in Chapter II. This is the simplest model of viscoelasticity called Maxwell model after J. C. Maxwell [16] [12], which combines a perfectly elastic element with a perfectly viscous element in series. The total shear strain γ is the sum of the shear strains in each element

$$\gamma = \gamma_e(t) + \gamma_v(t), \quad (\text{III.1.1})$$

where $\gamma_e(t)$ is the shear strain in the elastic element and $\gamma_v(t)$ is the corresponding viscous element. Consequently, each part must possess the same stress

$$\sigma(t) = G_M \gamma_e(t) = \eta_M \dot{\gamma}_v(t). \quad (\text{III.1.2})$$

Here, the M subscripts specify the Maxwellian relaxation modulus and viscosity. The ratio between the viscosity and the modulus defines a characteristic relaxation time, $\tau_M \equiv \eta_M / G_M$. If we assume a strain step experiment, where the total strain γ is constant, the combination of equations (III.1.1) and (III.1.2) gives a first order differential equation for the time-dependent strain in the viscous element

$$\tau_M \frac{d\gamma_v(t)}{dt} = \gamma - \gamma_v(t). \quad (\text{III.1.3})$$

With an initial condition of $\gamma_v(0) = 0$, it is possible to solve the differential equation

$$\ln[\gamma - \gamma_v(t)] = \frac{-t}{\tau_M} + C, \quad (\text{III.1.4})$$

with the constant of integration $C = \ln \gamma$. This last equation leads us to rewrite the equation (III.1.1) as,

$$\gamma_e(t) = \gamma - \gamma_v(t) = \gamma \exp(-t / \tau_M). \quad (\text{III.1.5})$$

Using equation (III.1.2), we can see that the stress relaxes exponentially towards zero on the time scale τ_M , for a viscoelastic Maxwellian system,

$$\sigma(t) = G_M \gamma_e = G_M \gamma \exp(-t / \tau_M). \quad (\text{III.1.6})$$

or rewriting it, the stress relaxation modulus has a simple exponential decay

$$G(t) \equiv \frac{\sigma(t)}{\gamma} = G_M \exp(-t / \tau_M). \quad (\text{III.1.7})$$

The relaxation modulus depends explicitly on time for a viscoelastic system. Analyzing the equation (III.1.5), it is easy to observe two characteristic regimes in a viscoelastic Maxwellian fluid. If $t \ll \tau_M$, the strain is due just for the elastic element. On the other hand, if $t \gg \tau_M$, the viscous contribution of the strain is much more significant. We can be sure that the relaxation time τ_M is a fundamental dynamic property of all viscoelastic liquids.

In practice there exist two different viscoelastic materials, the so-called *viscoelastic solid* and the *viscoelastic liquid*. For a viscoelastic solid, the equation (III.1.7) is not a good approximation for long times. In this case the relaxation modulus tends to a constant, $\lim_{t \rightarrow \infty} G(t) = G_{eq}$, due to the original shape the solid possesses before the applied strain, in contrast to a viscoelastic liquid, where the behavior at long times agrees with the equation (III.1.7). This equation decays up to zero when time goes to infinity. At short times, $t \ll \tau_M$, both viscoelastic specimens tend to an initial value G_M .

In general, polymer liquids have multiple relaxation times, described as power laws with an exponent that is a fingerprint of the mechanical properties of the polymeric solution. Any stress relaxation modulus of this kind can be described by a series of Maxwell elements. There exist several models depending on the degree of complexity of the problem. There is even a mathematical formalism which includes fractional calculus to obtain the viscoelastic response of the systems [89] [90] [91] [92].

1.2. Linear response: the Boltzmann superposition principle

All materials have a region of *linear response* at sufficiently small values, where the relaxation modulus is independent of strain. For longer deformations, the relaxation modulus is not anymore independent of strain, what is called *nonlinear viscoelasticity*. Boltzmann suggested that small strain values correspond to small stress response [93],

$$\delta\sigma_i(t) = G(t)\delta\gamma_i(t_i) = G(t)\dot{\gamma}_i\delta t_i. \quad (\text{III.1.8})$$

The stresses resulting from any linear combination of small step strains, $\delta\gamma_i$, applied at a time t_i is the total stress detected at time t ,

$$\sigma(t) = \sum_i G(t - t_i)\delta\gamma_i = \sum_i G(t - t_i)\dot{\gamma}_i\delta t_i, \quad (\text{III.1.9})$$

where the summation increment on the right side of the equation was transformed into time. This equation states that for linear response, the stress resulting from each step is independent of all other steps. The relaxation modulus tells how much stress remains at a time t from each past deformation

$\delta\gamma_i$ through the elapsed time $t - t_i$ that has passed since that deformation was applied at the time t_i . The sum of smooth strains can be changed for an integral over the strain history,

$$\sigma(t) = \int_{-\infty}^t G(t - t') \dot{\gamma}(t') dt'. \quad (\text{III.1.10})$$

The integration is over all past times, up to the time of stress response, to ensure that all deformations are taken into account. The equation (III.1.10) is the constitutive model for the linear viscoelastic behavior which is algebraically identical to the fundamental linear response equations, like the ones developed by R. Kubo [94]. Identically to the linear response theory, the integral of the last equation consists of two terms: one characteristic from the material, and the other inherent to the process of deformation.

A change of variables in the equation (III.1.10) provides a better suitable way for integration

$$\sigma(t) = \int_0^{\infty} G(s) \dot{\gamma}(t - s) ds. \quad (\text{III.1.11})$$

In the case of simple steady shear, the shear rate is a time-independent constant, and it can be pulled out of the last equation. The relaxation modulus $G(t)$ eventually decays to zero for any liquid. Thus, the last equation is nothing more than the equation for a Newtonian fluid, with a viscosity equal to the time integral of the relaxation modulus, constant during time,

$$\eta = \int_0^{\infty} G(t) dt. \quad (\text{III.1.12})$$

The viscosity for a viscoelastic Maxwellian fluid, using the equation (III.1.7), under a steady shear, takes the simple form

$$\eta = G_M \int_0^{\infty} \exp(-t / \tau_M) dt = G_M \tau_M = \eta_M. \quad (\text{III.1.13})$$

Reminding that $\lim_{t \rightarrow \infty} G(t) = G_{eq}$ for a viscoelastic solid, the viscosity tends to infinity at very long times, in accordance with Flory's principle. On the other hand, for most viscoelastic liquids the stress decays to zero in a nearly exponential fashion on time scales longer than the relaxation time τ .

If the applied shear rate is too large for linear response, an apparent viscosity (or instantaneous viscosity) is defined as the ratio between shear stress and shear rate, or what is the same, the slope of a plot of shear stress against shear rate. For a viscoelastic material, this slope changes with time, so this viscosity should not be taken as the same as the zero shear rate viscosity. Most viscoelastic materials exhibit *shear thinning* of the apparent viscosity at large shear rates. The instantaneous viscosity has also been observed to increase with shear rate for some colloidal suspensions and worm-

like micelles, what is called *shear thickening*. For instance, a system of colloids studied by N. J. Wagner and J. F. Brady can be found in [95].

1.3. Oscillatory shear

Under the linear regime, there exist several different experimental procedures to obtain the viscoelastic spectrum of the system. These are experiments which allow us to obtain the basic information from the mechanical response of the system. In typical oscillatory experiments the applied shear strain and the shear rate change in a sinusoidal way,

$$\gamma(t) = \gamma_0 \sin(\omega t), \quad (\text{III.1.14})$$

$$\dot{\gamma}(t) = \gamma_0 \omega \cos(\omega t). \quad (\text{III.1.15})$$

The linear response of the stress for a viscoelastic material oscillates at the same frequency as the applied strain, but generally out of phase, because the response is not instantaneous as has been pointed out in Figure III.1,

$$\sigma(t) = \sigma_0 \sin(\omega t + \delta). \quad (\text{III.1.16})$$

In general, $0 \leq \delta \leq \pi/2$ and can be frequency dependent. There are two special extreme cases: when $\delta = 0$, the system is in phase with the strain, so it has a response of a solid; on the other case, when $\delta = \pi/2$, the system is in phase with the shear rate. Thus, it corresponds to a Newtonian liquid. Substituting the equation (III.1.15) in the equation of the Boltzmann superposition principle (equation (III.1.11)), we find that

$$\sigma(t) = \int_0^{\infty} G(s) \gamma_0 \omega [\cos(\omega t) \cos(\omega s) + \sin(\omega t) \sin(\omega s)] ds. \quad (\text{III.1.17})$$

The viscoelastic moduli are defined in this equation in the manner

$$G'(\omega) = \omega \int_0^{\infty} G(s) \sin(\omega s) ds, \quad (\text{III.1.18})$$

$$G''(\omega) = \omega \int_0^{\infty} G(s) \cos(\omega s) ds.$$

$G'(\omega)$ is defined as the *storage modulus* or elastic modulus, and $G''(\omega)$ is defined as the *loss modulus* or viscous modulus. If one observes the equation (III.1.16), it is possible to relate δ with the moduli,

$$\tan \delta = \frac{G''}{G'}. \quad (\text{III.1.19})$$

The magnitudes of the moduli with respect to ω are known as *viscoelastic spectrum* and are related to the complex modulus

$$G^*(\omega) = G'(\omega) + iG''(\omega). \quad (\text{III.1.20})$$

Substituting the equations (III.1.18) in the viscoelastic spectrum, we obtain,

$$G^*(\omega) = \omega \left\{ \int_0^{\infty} G(s) [\sin(\omega s) + i \cos(\omega s)] ds \right\} = \omega \int_0^{\infty} G(s) \exp(i\omega s) ds, \quad (\text{III.1.21})$$

hence [16],

$$G^*(\omega) = i\omega \Im \{ G(t) \}. \quad (\text{III.1.22})$$

The complex modulus is the unilateral Fourier transform of the relaxation modulus. All the mechanical information of relaxation of a system under stress is contained in the viscoelastic spectrum. Experimental obtaining of the moduli to study viscoelastic fluids, is the most relevant procedure in rheology. For Maxwellian fluids with one characteristic stress relaxation time (equation (III.1.7)), after substituting $G(t)$ in the equations (III.1.18), the form of the viscoelastic spectrum is

$$G'(\omega) = \int_0^{\infty} dt \omega \sin(\omega t) \exp(-t/\tau_M) = \frac{(\omega\tau_M)^2}{1 + (\omega\tau_M)^2}, \quad (\text{III.1.23})$$

$$G''(\omega) = \int_0^{\infty} dt \omega \cos(\omega t) \exp(-t/\tau_M) = \frac{\omega\tau_M}{1 + (\omega\tau_M)^2},$$

which are exactly the same expressions found for polymer beads bonded with harmonic springs, presenting Rouse modes (equation (II.4.6)) but with only one relaxation time $\tau_p = \tau_M$.

Also, according to the equation of linear response, where the relaxation modulus behavior is a causal effect of past events, and considering the relation between moduli in the complex space, the Kramers-Kronig relations are a natural way to relate the viscoelastic moduli [96] [97],

$$G'(\omega) = \frac{2\omega^2}{\pi} P \int_0^{\infty} \frac{G''(\omega) / \omega}{\omega^2 - y^2} dy, \tag{III.1.24}$$

$$G''(\omega) = -\frac{2\omega^2}{\pi} P \int_0^{\infty} \frac{G'(\omega)}{\omega^2 - y^2} dy,$$

where y is an integration variable and P denotes the principal value of the integrals.

2. Rheometry

Now that we developed an introduction to the rheology principles, here it is presented a brief introduction to the theoretical framework behind the operation of a rheometer. A rheometer measures the stress and strain history of a material. The results exposed here follow the same ideas shown by C. W. Macosko [16].

The goal is to determine the relation between deformation and responsive stress within a fluid. In Chapter II it was included the analysis of a continue flux under concentration gradients. We started with the Fick's law, and at the end we obtained a description of diffusive particles with the Smoluchowski and Langevin equations. In the middle, the continuity equation (II.2.4) was found which explains that changes of concentration in time induce a divergence in the flux of particles. The same idea is applicable to the case of variation of mass within a certain volume, V . Temporal changes of the mass density are directly related with the divergence of a flux of mass $\rho \mathbf{v}$, through the boundary surface of the volume,

$$\frac{\partial \rho}{\partial t} = -\nabla \cdot \rho \mathbf{v}, \tag{III.2.1}$$

with ρ the mass density of the material, and \mathbf{v} the flux velocity. On the other hand, the momentum associated to a volume element within the material is

$$m\mathbf{v} = \int_V \rho \mathbf{v} dV. \tag{III.2.2}$$

It is possible to transfer momentum to V by different processes: mass convection through the surface, contact forces acting on the surface from out the volume, and provoked by external fields.

Convection: this contribution to changes in momentum within V is due to a flux traveling through the surface and is $-(\hat{\mathbf{n}} \cdot \mathbf{v})\rho \mathbf{v} dS$.

Contact: the three-component vector \mathbf{t}_n is the stress acting on the surface, which is written as

$$\mathbf{t}_n = \hat{\mathbf{n}}\sigma_{nn} + \hat{\mathbf{m}}\sigma_{nm} + \hat{\mathbf{o}}\sigma_{no} = \hat{\mathbf{n}} \cdot \tilde{\sigma}, \quad (\text{III.2.3})$$

with the first term normal to the surface and the other two tangent to it. The first subscript in the stress magnitude deals with the plane where the force is acting, and the second subscript gives the direction the force takes on the plane. The last term is the tensor notation, where $\tilde{\sigma}$ is the stress tensor.

External fields: the unique contribution that is accounted here is the gravity force. The force per unit volume is $\rho\mathbf{g}$.

The total changes of momentum in time within the volume, are described as

$$\frac{d}{dt} \int_V \rho \mathbf{v} dV = - \int_S (\hat{\mathbf{n}} \cdot \mathbf{v}) \rho \mathbf{v} dS + \int_S \hat{\mathbf{n}} \cdot \tilde{\sigma} dS + \int_V \rho \mathbf{g} dV, \quad (\text{III.2.4})$$

and using the divergence theorem it is rewritten as

$$\frac{\partial \rho \mathbf{v}}{\partial t} = -(\nabla \cdot \rho \mathbf{v}) \mathbf{v} + \nabla \cdot \sigma + \rho \mathbf{g}. \quad (\text{III.2.5})$$

The equations (III.2.1) and (III.2.5) are the fundamental equations for conservation of mass and momentum and are the equations of motion of the current problem. It is now required to obtain a relation between the flow velocities, the shear rate and the stress response, which is sensed by the rheometer. In general, the velocity in the fluid is a function of position and time, $\mathbf{v}(\mathbf{x}, t)$. The relative rate of separation of two points within the material, can be calculated using the velocity gradient function, which is

$$\Delta \mathbf{v} = \frac{\partial \mathbf{v}}{\partial \mathbf{x}} \cdot \Delta \mathbf{x} = \mathbf{L} \cdot \Delta \mathbf{x}, \quad (\text{III.2.6})$$

where the velocity gradient tensor \mathbf{L} , was defined. $\Delta \mathbf{x}$ is the separation distance between the two points. The velocity gradient tensor has two directions: one the direction of the velocity and the other of the gradient. Also, the velocity gradient \mathbf{L} is often written out as the dyad product of the gradient vector and the velocity vector, which are related as

$$\mathbf{L} = (\nabla \mathbf{v})^T. \quad (\text{III.2.7})$$

It is easy to see that the index order of $\nabla \mathbf{v}$ is the reverse of that for \mathbf{L} . Moreover, after using a deformation gradient tensor in terms of stretch and rotation tensors, we can define the *rate of deformation tensor* $2\mathbf{D}$ (which we called $\dot{\gamma}$ in vector form), and the *vorticity tensor* $2\mathbf{W}$ written as

$$2\mathbf{D} = (\nabla \mathbf{v})^T + \nabla \mathbf{v}, \quad (\text{III.2.8})$$

which is a symmetric tensor, and the antisymmetric counterpart

$$2\mathbf{W} = (\nabla\mathbf{v})^T - \nabla\mathbf{v}. \quad (\text{III.2.9})$$

These two last equations condense in one by the velocity gradient tensor,

$$\mathbf{L} = \mathbf{D} + \mathbf{W}. \quad (\text{III.2.10})$$

It is worth to mention that the tensor $2\mathbf{D}$ is associated with the rate as the constituents of a fluid are separated during time (rate of squared length change). To this, note that

$$\frac{d|\Delta\mathbf{x}|^2}{dt} = \frac{d(\Delta\mathbf{x} \cdot \Delta\mathbf{x})}{dt} = 2\Delta\mathbf{x} \cdot \frac{d(\Delta\mathbf{x})}{dt}. \quad (\text{III.2.11})$$

Using the equation (III.2.6), the equation (III.2.11) gives

$$\frac{d|\Delta\mathbf{x}|^2}{dt} = \Delta\mathbf{x} \cdot 2\mathbf{L} \cdot \Delta\mathbf{x} = \Delta\mathbf{x} \cdot 2\mathbf{D} \cdot \Delta\mathbf{x} + \Delta\mathbf{x} \cdot 2\mathbf{W} \cdot \Delta\mathbf{x}. \quad (\text{III.2.12})$$

In each of the right-hand terms the tensor is operating on two $\Delta\mathbf{x}$ vectors. Because these vectors are identical, we can reverse the operations, operating on the other one first. However, changing the operation order requires the tensor to be symmetric. Thus, the last term is 0 and we have

$$\frac{d|\Delta\mathbf{x}|^2}{dt} = \Delta\mathbf{x} \cdot 2\mathbf{D} \cdot \Delta\mathbf{x}, \quad (\text{III.2.13})$$

which is the expected result. Now, with all necessary equations, we can use the relation for conservation of momentum applied to a cone-plate geometry, to evaluate the relation between deformations and stress.

Consider Figure III.2, which shows the geometry. Between the cone and plate the sample is settled. The plate has a radius R , and the cone possesses an angle β with the horizontal. The cone rotates with an angular velocity Ω . Spherical coordinates are used, therefore θ is measured from the cone surface to the plate surface, and the flow velocity is V_ϕ in the direction of cone rotation. Isothermal, laminar and stationary flow is assumed. The flow velocity is only a function r and θ , hence $V_\phi(r, \theta)$, $V_r = V_\theta = 0$. Also, the angle β is enough small ($< 6^\circ$). Note that under this flow, the stress tensor component applied to a surface normal to θ in the direction of ϕ is the shear stress $\sigma_{\theta\phi}$, and the shear rate is in the same direction. The boundary conditions assume that there is not slip of fluid at the surfaces, and

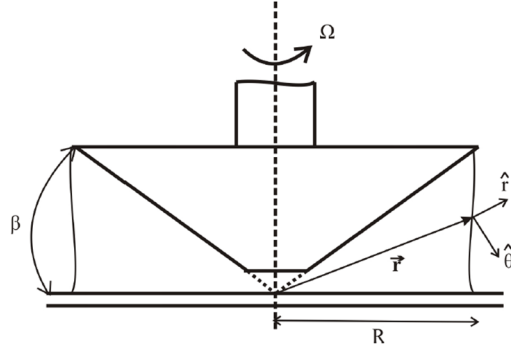


Figure III.2 Cone-plate geometry for a rheometer. The sizes are not in scale. The aperture angle is overdone just to make it clear.

$$V_{\phi} \left(\frac{\pi}{2} \right) = 0, \quad (III.2.14)$$

$$V_{\phi} \left(\frac{\pi}{2} - \beta \right) = \Omega r.$$

Solving the equation (III.2.5) in spherical coordinates, considering the equations (III.2.8) and (III.2.10), and the boundary conditions (III.2.14), we found out that the only concerning expression in the equation (III.2.5), is the component in the direction of ϕ ,

$$0 = \frac{1}{r} \frac{\partial \sigma_{\theta\phi}}{\partial \theta} + \frac{2}{r} \sigma_{\theta\phi} \cot \theta. \quad (III.2.15)$$

Integrating gives

$$\sigma_{\theta\phi} = \frac{C}{\sin^2 \theta}, \quad (III.2.16)$$

where C is a constant of integration that does not depend on θ . Now the torque \mathbf{M} is computed, which is exerted on the plate. Note that $d\mathbf{F} = \sigma_{\theta\phi} da$, therefore $|d\mathbf{M}| = |\mathbf{r} \times d\mathbf{F}| = r \sigma_{\theta\phi} |_{\theta=\pi/2} r dr d\phi$. Integrating this expression

$$M = \int_0^{2\pi} \int_0^R r^2 \sigma_{\theta\phi} |_{\theta=\pi/2} dr d\phi = \frac{2\pi}{3} R^3 \sigma_{\theta\phi} |_{\theta=\pi/2}. \quad (III.2.17)$$

Using equation (III.2.16), the expression for the shear stress is

$$\sigma_{\theta\phi} = \frac{3M}{2\pi R^3 \sin^2 \theta} \approx \frac{3M}{2\pi R^3}. \quad (III.2.18)$$

In the last equation it was considered that $\sin(\pi/2 - \beta) \approx 1$. The equation (III.2.18) relates the torque that the sample applies on the plate, with the shear stress.

Now, computing the shear rate for a small angle β , evaluating the velocity gradient tensor we found

$$\dot{\gamma} = 2D_{\theta\phi} \approx \frac{1}{r} \frac{\Delta V\phi}{\Delta\theta} = \frac{1}{r} \frac{V_\phi(\pi/2 - \beta) - V_\phi(\pi/2)}{\beta} = \frac{\Omega}{\beta}, \quad (\text{III.2.19})$$

where the boundary conditions were used. One advantage for using the cone-plate geometry is the independence of r in the shear rate, therefore the sample is always under a constant shear rate whatever the position between the geometry. Another advantage is the no dependence of shear stress in the shear rate. As can be seen from equations (III.2.18) and (III.2.19), a rheometer in cone-plate geometry, obtains the shear stress component with measuring the torque sensed by the geometry, and computes the shear rate after measuring the angular velocity of the geometry.

3. Light Scattering

The nature of light has played a vital role in our understanding of the physical world. The discovery of the dual nature of light has been essential which permitted the development of technological advances during the last century and with even more promising achieves in future years. For particular interests in Condensed Matter Physics, light serves as a nonperturbative probe that can be used to obtain information about the structure and dynamics of macromolecules. For that reason, the study of transport and localization of light through matter has to become a cornerstone in the physical and chemical sciences [98] [99].

A totally homogeneous medium does not scatter radiation away from the incident direction. Scattering is caused by fluctuations in the medium. Usually these fluctuations are associated with variations in the *density of scattering material* within the medium. It is well known that for a specific sort of radiation the interaction with matter is different. In Soft Matter it is a standard procedure to analyze systems with visible light, where the interaction is governed via changes in the dielectric constant of the medium (or index of refraction); X-rays that interact according to variations in the electronic density of the material and neutron beams which detects a contrast of the nucleons of the atoms of the sample under study.

When the energy of the photon is preserved during the scattering mechanism, the mechanism is called elastic scattering for an ideal situation (quasi-elastic in the laboratory). There exist different regimes of elastic scattering depending on the size of the macromolecules involved in the process (Table III.1), which differ with each other by the preferred direction of the scattered light.

| Approximation | Regime | Preferred scattering direction |
|----------------|---|--|
| Rayleigh | Spherical particles, $a < \lambda/10$ | Isotropic |
| Rayleigh-Debye | Arbitrary shape particles, $a \geq \lambda$ | Forward |
| Mie | Arbitrary shape particles, $a \gg \lambda$ | Forward, high dependence on scattering angle |

Table III.1 Different scattering regimes. a is the radius of spherical particles and λ the wavelength of light.

In addition, the intensity of the scattered light is dependent upon the spatial arrangement of the scattering centers at any instant in time. In fact, in a liquid solution, the macromolecules are undergoing constant motion because of the collisions with the solvent molecules. When the analysis of the scattered light is carried out considering the fluctuations of macromolecule displacements, the convention is to call it Dynamic Light Scattering (DLS), otherwise when an average of the dynamics of the macromolecules is analyzed, independent of the time evolution of the system, the process is called Static Light Scattering (SLS). It is usual to perform DLS experiments in the visible range of the light spectrum, and for SLS it is common to do it also in the range of visible light, X-rays and with neutrons.

DLS experiments are performed when dynamic properties are likely to be obtained as the diffusion coefficient of colloidal particles, their mean square displacement (MSD), their hydrodynamic radius and their size distribution. On the other hand, SLS experiments recover information resulting from the average fluctuations of the complex system as the radius of gyration, the molecular weight in some cases, the second virial coefficient, the form factors for diluted suspensions and the structure factors in concentrated ones. In the next section the DLS formalism will be mentioned, restricted to our convenient approach, and at the end of the chapter, Small Angle Neutron Scattering (SANS) will be pointed out to obtain the structure of different systems in water suspensions.

3.1. Dynamic Light Scattering (DLS)

In this kind of experiments [100] [101] [102], laser light (coherent source of light) with an incident wave vector \mathbf{k}_0 strikes on to a sample of colloidal spheres embedded in a complex fluid transparent to the incident light. If the concentration of the particles is dilute enough, there will be just one scattering event for each wave passing along the sample. The scattering is due to the difference in polarizability (dielectric constant) between the particles and the solvent. The electromagnetic wave then induces a dipolar moment which irradiates in all directions. This scattered light is detected at a particular angle θ in the direction of the wave vector \mathbf{k}_s , in the far field. If the scattered field at the detector from a single particle is \mathbf{E}_0 , then the total field \mathbf{E} is a superposition of scattered fields from all N particles in the scattering volume

$$\mathbf{E}(t) = \sum_{i=1}^N \mathbf{E}_0 \exp[i\mathbf{q} \cdot \mathbf{r}_i(t)], \quad (\text{III.3.1})$$

where $\mathbf{q} = \mathbf{k}_s - \mathbf{k}_0$ is the scattering wave vector, $\mathbf{r}_i(t)$ is the position of the i th particle, and the amplitude of the wave contents all information related with the polarizability of the molecules. The argument of the exponential represents a phase shift introduced by the differences in the optical pathway each wave will take after the scattering event. This shift for each scattered wave will induce an interference pattern at the plane of detection. This pattern is called *speckle* that is not other than the fluctuation of the intensity of the light directly related with the motion of the particles. These fluctuations can be characterized by their temporal autocorrelation function

$$g^{(1)}(t) = \frac{\langle \mathbf{E}(0)\mathbf{E}^*(t) \rangle}{\langle |\mathbf{E}|^2 \rangle}, \quad (\text{III.3.2})$$

which is related through the Siegert relation to the time-averaged light intensity autocorrelation function $g^{(2)}(t)$, measured experimentally,

$$g^{(2)}(t) = 1 + \beta |g^{(1)}(t)|^2, \quad (\text{III.3.3})$$

where β is an instrumental factor determined by the collection optics, related with the coherence area, $A_{coh} \sim \lambda^2 R^2 / \pi a^2$ (R is the distance from the scattering volume to the detector), that accounts for the number of speckles observed on the detector of area a at the same time. Its value varies from 0 to 1; in our experiments, the value is very close to 1. $\mathbf{E}^*(t)$ is the complex conjugate of the electric field.

In general, in the Rayleigh regime for spherical particles, the field autocorrelation function is given by [103]

$$g^{(1)}(t) = A \frac{\sum_{i,j=1}^N \langle e^{i\mathbf{q}[\mathbf{r}_i(0) - \mathbf{r}_j(t)]} \rangle}{\sum_{i,j=1}^N \langle e^{i\mathbf{q}[\mathbf{r}_i(0) - \mathbf{r}_j(0)]} \rangle}, \quad (\text{III.3.4})$$

with A a constant which depends on the refraction index of the medium, the intensity of scattered light, the wavelength of the light and the distance from the scattering volume to the detector. For non-interacting particles, the cross-terms vanish, then

$$g^{(1)}(t) = A \langle \exp[-i\mathbf{q} \cdot \Delta\mathbf{r}(t)] \rangle, \quad (\text{III.3.5})$$

with $\Delta\mathbf{r}(t) \equiv \mathbf{r}(t) - \mathbf{r}(0)$. If $\Delta\mathbf{r}(t)$ is a Gaussian variable, then

$$g^{(1)}(t) = A e^{-q^2 D t} = A \exp\left[-\frac{1}{6} q^2 \langle \Delta r^2(t) \rangle\right], \quad (\text{III.3.6})$$

where q is the magnitude of the scattering vector, $q = \frac{4\pi m_0}{\lambda} \sin(\frac{\theta}{2})$ (m_0 is the refraction index of the medium), and D is the diffusion coefficient of the scattering particles. In the expression of the right, it was assumed a diffusive motion of the probe particles.

In the laboratory, the experiments are not limited to be developed with small scatterers; in fact, it is usual to perform measurements with particles in the Rayleigh-Debye regime, with not necessarily spherical shape. A detailed discussion of the formalism of DLS for large anisotropic particles is found in the work of S. R. Arag3n and R. Pecora [104]. In the Rayleigh-Debye approximation, it is assumed

that every portion of the scatterer captures the same incident radiation. Its validity is assured when the condition $2k_0L(m - m_0) \ll 1$ is satisfied, where m is the refraction index of the probe particle and L is a characteristic size of the particle. The main problem is that one particle possesses several scattering centers which contribute to the speckle pattern at the detector. For monodisperse dispersions of a single type of particle and in a dilute or ideal solution, the correlation function is considerably simplified since there are no correlations between different particles for nonzero scattering vector. Even, if we consider a molecule composed just by isotropic segments, the associated polarizability tensors are scalars, resulting in a simplified autocorrelation function

$$g^{(1)}(t) = NAe^{-q^2Dt} |\hat{\epsilon} \cdot \hat{\epsilon}_0|^2 \alpha^2 S(\mathbf{q}, t), \quad (\text{III.3.7})$$

where e^{-q^2Dt} is the contribution due to the translation of the center of mass of the particles, $\hat{\epsilon}_0$ and $\hat{\epsilon}$ are the directions of polarization of the incident wave and the scattered one respectively, α is the spatial Fourier transform of the whole particle, and $S(\mathbf{q}, t)$ is the internal correlation function with the form

$$S(\mathbf{q}, t) = \left(\frac{1}{n^2} \right) \sum_{j,k} \langle \exp \{ i\mathbf{q} \cdot [\rho_k(t) - \rho_j(0)] \} \rangle, \quad (\text{III.3.8})$$

where n is the number of scattering centers in the particle and ρ_j represents the position of the j th segment within the particle. The zero-time value of the internal correlation function is the form factor, $S(\mathbf{q}, t) = P(qL)$. The last equation could be solved in cylindrical coordinates, which takes the form

$$S(\mathbf{q}, t) = \sum_l (2l + 1) d_l^2(\mathbf{q}L) \exp[-l(l + 1)\Theta_{\perp} t], \quad (\text{III.3.9})$$

with Θ_{\perp} representing the rotations of the molecular symmetry axis and $d_l = \frac{1}{v} \int_v d^3\rho J_l(\cos\theta)$, where J_l is a spherical Bessel function and v the total volume of the molecule. For a particle with spherical shape, the only accountable value is $l = 0$, and integrating over the whole angular space, the result is

$$d_l(\mathbf{q}L) = \frac{3\delta_{l0}}{(qL)^3} (\sin qL - qL \cos qL). \quad (\text{III.3.10})$$

For this geometry, the internal correlation function is equal to the form factor, and it does not depend on the distance between different scattering centers. For this reason, it is possible to use DLS experiments for spherical particles in the Rayleigh-Debye regime connecting the autocorrelation function for the contribution of different segments. Hence, the autocorrelation function for the particles in this regime is

$$g^{(1)}(t) = Ce^{-q^2Dt} \left[\frac{3}{(qL)^3} (\sin qL - qL \cos qL) \right]^2, \quad (\text{III.3.11})$$

where C is a constant amplitude value. With this autocorrelation function, we are able to correct the results obtained in the experiment. Moreover, there are specific angles at which the autocorrelation function is maximum, depending on the size of the particles. Monitoring these sites, we can obtain a better estimation of the diffusion coefficient of the particles.

However, DLS has the power to analyze just the large quadratic displacements of particles to assure at least an out of phase of π in the wavelength of different scattered beams, due to the difference in the optical paths of light. If we are interested in the estimation of shorter length and time scales of the dynamics of the probe particles, an affordable experiment is DWS.

3.2. Diffusing Wave Spectroscopy (DWS)

DWS is a light scattering technique that extends the analytical power of DLS to the limit of multiple scattering events. Due to this, it is possible to examine opaque samples such as concentrated suspensions, obviating the need to dilute or index-match. For typical experiments in complex fluids, a turbid suspension is prepared with adding colloidal probe particles at a certain concentration to assure multiple scattered light but at the same time to avoid interparticle interactions. A time autocorrelation function of the intensity of the scattered light is obtained which is related to the mean square displacement of the tracers. We will follow the formalism developed by D. J. Pine and D. A. Weitz towards the late eighties [105] [106].

Obtaining of a speckle pattern at the detector and hence a temporal autocorrelation function in DWS, imply two fundamental approaches: *diffusion approximation* of the light intensity along each path taken by the photons through the medium and an *average of scattering events* instead of considering individual events, where each one plays a less critical role. Unlike DLS, the angle between the incident and detected light is not crucial in DWS, and although it does not yield explicit information of the so-called dynamic structure factor of the particles, it can provide unique information on particle motion on very short time scales. However, since light is scattered from a large number of particles, each particle must move only a small fraction of a wavelength for a cumulative change in the path length to be a full wavelength so that DWS can probe motion on very short length scales, from ~ 1 nm up to ~ 1 μm [107]. As a consequence, there are different allowed experimental geometries, where the most suitable are total transmission and backscattering. Therefore, the multiply scattered light loses information of its origin and the direction of propagation after traveling a distance called *transport mean free path*, l^* , where the light starts to take a random direction. The transport mean free path is related to the *mean free path* l , which is the distance traveled among every scattering event, according to

$$l = \frac{1}{\rho\sigma}, \quad (\text{III.3.12})$$

$$l^* = \frac{l}{\langle 1 - \cos\theta \rangle}, \quad (\text{III.3.13})$$

with ρ the particle density, σ the scattering cross section, θ is the scattering angle and $\langle \dots \rangle$ represents an ensemble average upon plenty scattering events. For small particles, near the Rayleigh scattering limit, when $k_0 a \ll 1$ ($k_0 = 2\pi/\lambda$ is the wave vector and a is the radius of the particles), the single particle scattering is isotropic, and the direction of light is randomized after one scattering event ($l^* = l$). In the case of larger particles, in the Mie scattering limit, they reach their maximum point in the forward direction, so that, there are necessary several scattering events, on average, to randomize the direction of propagation ($l^* > l$). Also, the transport mean free path is a parameter that has to be calculated independently from the DWS experiment. In our laboratory we established the *Inverse Adding Doubling* method to get the optical parameters of the studied systems; it will be mention in detail in the next section once we introduce the problem of light absorption in suspensions.

For calculation of the electric fields autocorrelation function, consider a total transmission geometry measurement. A laser beam is impinging towards the sample with a thickness $L \gg l^*$, where every incident photon is emerging in the opposite site after been scattered N times, with a phase that depends on its total path length s . Figure III.3 shows a sketch of this phenomenon.

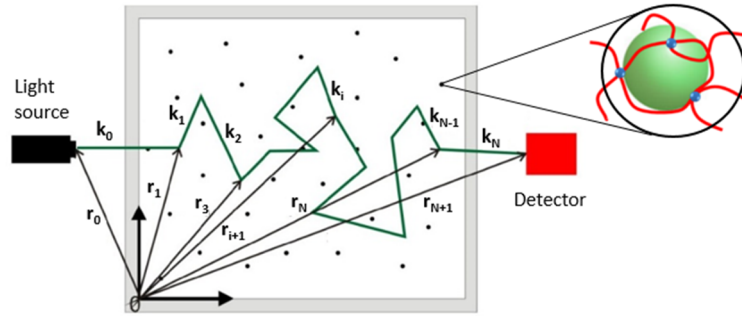


Figure III.3 Sketch of the path followed by a multiply scattered photon through a sample. Each point represents a particle embedded in the fluid. The small blue spheres represent the unions between macromolecules within the complex fluid. The green sphere is a probe particle. Modified from [108].

The total pathway of the photon will be

$$s = \sum_{i=0}^N |\mathbf{r}_{i+1} - \mathbf{r}_i| = \sum_{i=0}^N \left(\frac{\mathbf{k}_i}{|\mathbf{k}_i|} \right) \cdot (\mathbf{r}_{i+1} - \mathbf{r}_i), \quad (\text{III.3.14})$$

where \mathbf{k}_i is the wave vector after i scattering events, \mathbf{r}_i is the position of the particle i , \mathbf{r}_0 is the position of the light source and \mathbf{r}_N is the position of the detector (photomultiplier). If we assume

quasi-static scattering, all wave vectors have the same magnitude, then the total phase shift $\phi(t)$ for each photon is

$$\phi(t) = k_0 s(t) = \sum_{i=0}^N \mathbf{k}_i(t) [\mathbf{r}_{i+1}(t) - \mathbf{r}_i(t)]. \quad (\text{III.3.15})$$

On the other hand, we note that the total amplitude of the scattered electric field is the superposition of all the fields due to all the different pathways of light through the sample,

$$E(t) = \sum_p E_p e^{i\phi_p(t)}, \quad (\text{III.3.16})$$

with p representing each one of the different trajectories of light and E_p is the total electric field amplitude for trajectory p . Notice that this sum is over each path the light is allowed to take and not over each scattering element. The equation (III.3.16) involves two sums, one over light paths and another over the particles in each path. Similar to the equation (III.3.2), the autocorrelation function is given by

$$g^{(1)}(t) = \frac{\langle \mathbf{E}(0) \mathbf{E}^*(t) \rangle}{\langle |\mathbf{E}|^2 \rangle} = \frac{1}{\langle I \rangle} \left\langle \left(\sum_p E_p e^{i\phi_p(0)} \right) \left(\sum_{p'} E_{p'}^* e^{-i\phi_{p'}(t)} \right) \right\rangle, \quad (\text{III.3.17})$$

where I is the total average scattered intensity at the detector. This field autocorrelation function is related to the time-averaged light intensity autocorrelation function $g^{(2)}(t)$ through the Siegert relation as in DLS (equation (III.3.3)).

For independent particles, the field from different trajectories are to an excellent approximation uncorrelated, thus in the equation (III.3.17) the terms with $p \neq p'$ do not contribute, and we obtain

$$g^{(1)}(t) = \sum_p \frac{\langle I_p \rangle}{I} \left\langle e^{i[\phi_p(0) - \phi_p(t)]} \right\rangle, \quad (\text{III.3.18})$$

with $I_p \equiv \langle |E_p|^2 \rangle$ the average intensity from path p . Here we assumed the independence of phase and field amplitude E_p at the detector. After some treatment of the equations, we can obtain an expression for the phase shift $\Delta\phi_p(t) = \phi_p(t) - \phi_p(0)$, as

$$\Delta\phi_p(t) = \sum_{i=1}^N \mathbf{q}_i \cdot \Delta\mathbf{r}_i(t), \quad (\text{III.3.19})$$

where $\mathbf{q}_i \equiv \mathbf{k}_i(0) - \mathbf{k}_{i-1}(0)$, is equivalent to the scattering vector defined for DLS but this time for each particle i , and $\Delta\mathbf{r}_i(t) \equiv \mathbf{r}_i(t) - \mathbf{r}_i(0)$. It is possible to evaluate the phase shift in the equation

(III.3.18), noting that $\Delta\phi_p(t)$ is a Gaussian variable for large N and using the central limit theorem, we have

$$\left\langle e^{-i[\Delta\phi_p(t)]} \right\rangle = e^{-\frac{\langle \Delta\phi_p^2(t) \rangle}{2}}. \quad (\text{III.3.20})$$

Using the equation (III.3.19) we obtain

$$\Delta\phi_p^2(t) = \sum_{i=1}^N \sum_{j=1}^N \left\langle [\mathbf{q}_i \cdot \Delta\mathbf{r}_i(t)][\mathbf{q}_j \cdot \Delta\mathbf{r}_j(t)] \right\rangle = \sum_{i=1}^N \left\langle [\mathbf{q}_i \cdot \Delta\mathbf{r}_i(t)]^2 \right\rangle = \frac{1}{3} N \langle q^2 \rangle \langle \Delta r^2(t) \rangle, \quad (\text{III.3.21})$$

where we have assumed the independence of successive phase factors and that the scattering vector \mathbf{q}_i and displacement vector $\Delta\mathbf{r}_i(t)$ are independent. If we relate the average over q^2 with the mean free paths, we get

$$\left\langle \Delta\phi_p^2(t) \right\rangle = \frac{2}{3} k_0^2 \left\langle \Delta r^2(t) \right\rangle \frac{s}{l^*}, \quad (\text{III.3.22})$$

equation in which we consider that $s = Nl$ for $N \gg 1$ scattering events. Notice that the average of the squared phase shift depends only on the parameter s so that, we can change the sum over paths for a sum over path lengths, provided that we replace the fraction of scattered intensity I_p/I in path p , with the fraction of scattered intensity $P(s) = I_s/I$, in paths of length s . Furthermore, passing to the continuum limit and applying the equations (III.3.19) and (III.3.22) on (III.3.18), we obtain

$$g^{(1)}(t) = \int_0^\infty P(s) \exp \left[-\frac{1}{3} k_0^2 \left\langle \Delta r^2(t) \right\rangle \frac{s}{l^*} \right] ds. \quad (\text{III.3.23})$$

The equation (III.3.23) is the basis of the calculation of autocorrelation functions in DWS. It states that a light trajectory of length s corresponds to a random walk of s/l^* steps and that such a path contributes on average $\exp[-\frac{1}{3} k_0^2 \langle \Delta r^2(t) \rangle]$ per step to the decay of the autocorrelation function. Seeing forward for further analysis, we rewrite the equation (III.3.23) as

$$g^{(1)}(t) = \int_0^\infty P(s) e^{-\frac{\left(\frac{2t}{\tau}\right)^s}{l^*}} ds, \quad (\text{III.3.24})$$

where $\tau = (k_0^2 \langle \Delta r^2(t) \rangle / 6t)^{-1}$. For diffusive particle motion, it is possible to write $\langle \Delta r^2(t) \rangle = 6Dt$ (thermal motion as previously mentioned in Chapter II, for the Smoluchowski and Langevin equations), with D the diffusion coefficient of the particles. From here it is easy to convince ourselves that equation (III.3.23) is the Laplace transform of the path length distribution,

$$g^{(1)}(t) = \mathcal{L}\{P(s)\}(t). \quad (\text{III.3.25})$$

The calculation of $P(s)$ is highly dependent on the geometry of the setup for obtaining the scattered light. It is not complicated to imagine that larger paths will be involved in a total transmission experiment rather than the shorter paths occurring for a backscattering setup. However, the main feature to get $P(s)$ is the accurate modeling of the transport of light by a diffusion equation for scales greater than the transport mean free path.

Consider a thought experiment: an instantaneous pulse of light is incident to the sample. The scattered light executes a random motion until it escapes. Thus, there is some delay between the light reaching the detector and the incident pulse due to the scattering events. The light that reaches the detector a time t after the pulse was emitted, has been traveled a distance $s = ct$, where c is the average velocity of light inside the sample. Thus, the flux of photons $\mathbf{J}_{out}(\mathbf{r}_{out}, t)$ arriving at the point \mathbf{r}_{out} will be directly proportional to $P(s)$. Then, as mentioned earlier, a diffusion equation describes the transport of light, deduced from the Fick's law as pointed out in Chapter II (equation (II.2.1)),

$$\frac{\partial U}{\partial t} = D_l \nabla^2 U, \quad (\text{III.3.26})$$

with U the energy density of light or the number of photons per unit volume in the sample, and $D_l = cl^*/3$ is the diffusion coefficient of light. To solve equation (III.3.26) we consider that the light path becomes random at a distance close to l^* ; for that reason, the source of diffuse light should be an instantaneous pulse at a distance $z = z_0$ inside the illuminated face of the sample. In accordance, $z_0 \sim l^*$ and the initial condition is

$$U(z, t = 0) = U_0 \delta(z - z_0, t). \quad (\text{III.3.27})$$

Additionally, the boundary conditions ensure that there is no net flux of diffusive photons entering the sample (from the boundary), hence if we consider a sample with thickness L , the inflow and outflow must be zero, $J_+(z < 0) = 0$ and $J_-(z > L) = 0$, or equivalently

$$U + \frac{2}{3} l^* \hat{n} \cdot \nabla U = 0. \quad (\text{III.3.28})$$

Considering the Fick's Law and equation (III.3.28), we get the relation

$$P(s) \propto \mathbf{J}_{out}(\mathbf{r}, t) \Big|_{\mathbf{r}_{out}} = \frac{Uc}{4} - \frac{cl^*}{6} \hat{n} \cdot \nabla U \Big|_{\mathbf{r}_{out}} = \frac{Uc}{2} \Big|_{\mathbf{r}_{out}}. \quad (\text{III.3.29})$$

Exploiting the fact already stated in the equation (III.3.25), instead of solving the diffusion equation for light to obtain $P(s)$, we can solve the Laplace transform of the diffusion equation and obtain

$g^{(1)}(t)$ directly without explicit calculation of $P(s)$. We introduce a change of variables into the diffusion equation ($t = s/c$), and multiplying both sides of the equation (III.3.26) by \exp^{-ps} ; we obtain the Laplace transform of the diffusion equation after integration,

$$\nabla^2 \bar{U} - \frac{3p}{l^*} \bar{U} = -\frac{3}{l^*} U_{00}(\mathbf{r}), \quad (\text{III.3.30})$$

where $\bar{U}(\mathbf{r}, p)$ is the Laplace transform of $U(\mathbf{r}, s)$, and $U_{00}(\mathbf{r}) = \lim_{t \rightarrow 0} U_0 \delta(z - z_0, t)$. It is also necessary to consider the Laplace transform of the boundary conditions (equation (III.3.28)). Taking the Laplace transform of the equation (III.3.29), we can relate this solution, $\bar{U}(\mathbf{r}, p)$, to the Laplace transform of $P(s)$, which is precisely the expression of the equation (III.3.24) for $g^{(1)}(t)$. Thus, we obtain

$$g^{(1)}(t) = \frac{\bar{U}(\mathbf{r}, p)|_{\mathbf{r}_{out}}}{\bar{U}(\mathbf{r}, 0)|_{\mathbf{r}_{out}}}, \quad (\text{III.3.31})$$

where $\bar{U}(\mathbf{r}, p)$ has been normalized so that $g^{(1)}(0) = 1$.

These equations can then be solved using Green's function techniques to obtain $\bar{U}(\mathbf{r}, p)$, as discussed by H. S. Carslaw and J. C. Jaeger [109]. The most used geometry in the laboratory is the transmission one due that it allows one to probe motion over length scales much shorter than the wavelength of light. For the case of a sample with thickness L and parallel plane faces, and with uniform illumination (a circular spot of around 1.5 cm) of a plane wave beam, the autocorrelation function is solved as

$$g^{(1)}(t) = \frac{\frac{L/l^* + 4/3}{\alpha^* + 2/3} \left[\sinh(\alpha^* x) + \frac{2}{3} x \cosh(\alpha^* x) \right]}{\left(1 + \frac{4}{9} x^2 \right) \sinh\left(\frac{L}{l^*} x\right) + \frac{4}{3} x \cosh\left(\frac{L}{l^*} x\right)}, \quad (\text{III.3.32})$$

with $x \equiv \sqrt{k_0^2 \langle \Delta r^2(t) \rangle}$ and $\alpha^* \equiv z_0/l^*$. As it is evident, the only free parameter is l^* , which as has been mentioned earlier, it is calculated experimentally in an independent way, with the Inverse Adding Doubling experimental formalism. On the other hand, $z_0 \sim l^*$, but numerical values are insensitive to the exact choice of z_0 , since $L \gg z_0$. A different choice of z_0 would affect only the first few steps in a random walk that consists of a large number of steps. There is a way to calculate the exact experimental value according to [110], with a backscattering geometry.

3.3.DWS for media with light absorption

The classical formalism of DWS does not allow to study liquid systems that absorbs or scatters light prior to the incorporation of probe particles. However, many systems with biological interests,

magnetic fluids, photo-responsive liquid materials, suspensions with metal nanoparticles, carbon-based suspensions, among others, are not able to be studied if absorption effects are not evaluated and corrected theoretically. Recently, E. Sarmiento-Gómez, B. Morales-Cruzado and R. Castillo [111] applied a technique never used before in complex fluids, to circumvent absorption issues. They corrected the theory, first discussed by D. A. Weitz and D. J. Pine [105] [106], pointing out that absorption exponentially attenuates light paths according to their path length, cutting off the longest paths; however, Weitz and Pine did not derive analytical results.

Whether $P(s)$ is the path length distribution in the absence of absorption, the path length distribution in the presence of absorption will be $P(s)\exp(-s/l_a)$, where l_a is the absorption length of the sample; $\mu_a \equiv 1/l_a$ where μ_a is the absorption coefficient. Therefore, the field autocorrelation function (equation (III.3.24)) is rewritten as

$$g^{(1)}(t) = \int_0^{\infty} P(s) \exp\left[-\left(\frac{2t}{\tau} + \frac{l^*}{l_a}\right)\frac{s}{l^*}\right] ds. \quad (\text{III.3.33})$$

Here it is evident that the effect of absorption is mathematically just a shift in the time axis. As for conventional DWS, a diffusion equation for the energy density is necessary to get an analytical relation for $g^{(1)}(t)$, but in this case, it has to be included an absorption term to get the correct path distribution function of scattered photons. Monte Carlo simulations have revealed that a useful model considers an absorption independent diffusion coefficient D_l for light [112]. Thus, the diffusion equation must be written as

$$\frac{\partial U}{\partial t} = D_l \nabla^2 U - \mu_a c U. \quad (\text{III.3.34})$$

It is possible to derive this diffusion equation from the radiative transfer equation, by considering a nearly isotropic light distribution and assuming that $l_a \gg l^*$ [113] [114]. Before get the diffusion equation solution with the absorption correction, it is necessary to follow the same reasoning used earlier in the absence of absorption. For transmission geometry, the procedure can be followed in [111]. After some algebraic calculations, the equation for the field autocorrelation function is obtained,

$$g^{(1)}(t) = \frac{\left(1 + \frac{4}{9}\eta^2\right) \sinh\left(\frac{L}{l^*}\eta\right) + \frac{4}{3}\eta \cosh\left(\frac{L}{l^*}\eta\right) \left[\sinh(\alpha^* x_a) + \frac{2}{3}x_a \cosh(\alpha^* x_a) \right]}{\sinh(\alpha^* \eta) + \frac{2}{3}\eta \cosh(\alpha^* \eta)} \frac{1}{\left(1 + \frac{4}{9}x_a^2\right) \sinh\left(\frac{L}{l^*}x_a\right) + \frac{4}{3}x_a \cosh\left(\frac{L}{l^*}x_a\right)}, \quad (\text{III.3.35})$$

where $\eta \equiv \sqrt{3l^*/l_a}$ and $x_a \equiv \sqrt{k_0^2 \langle \Delta r^2(t) \rangle + \eta^2}$. This equation seems more complicated than its counterpart with no absorption. Nevertheless, when $l_a \rightarrow \infty$, we recover the equation (III.3.32). It is not sufficient to estimate the value of l^* ; it is necessary the calculation of l_a as well, with an independent experiment. For this purpose, E. Sarmiento-Gómez, et al., have established the use of

the Inverse Adding Doubling method (IAD), developed by S. A. Prahl for biomedical applications [115] [116] [117]. The IAD is a method for generating the optical parameters of materials with scattering and absorption of light. It consists on the experimental measurement of the total reflectance, total transmittance and collimated transmittance of incident light to the sample. All these measurements are performed using an integrating sphere. The obtained optical parameters are the scattering coefficient $\mu'_s = 1/l^*$, the absorption coefficient $\mu_a = 1/l_a$, and the anisotropy factor g . In technical terms, in the IAD method a general numerical solution for a radiative transport equation is given through the following steps: (1) A guess for a set of the optical parameters is given. (2) The reflection and transmission of the samples are evaluated using the Adding Doubling method developed by H. C. van de Hulst [118] [119]. (3) Transmittance and reflectance are compared with the experimental measurements. (4) If the match is not good enough, the set of optical parameters is modified using a minimization algorithm. This process is iteratively followed until a match with the experimental measurements at some specific level is made. IAD also takes into account several features experimentally challenging to assess, such as light lost out the edges of the sample cell and non-linear effects in the integrating sphere measurements.

Forward in subsequent sections, there will be visible the importance of applying this numerical method to perform the DWS experiments. In the experimental results section, there are mentioned the details of the experimental arrangement in order to get the optical parameters and the measurements of light scattering.

3.4. Microrheology

In previous sections, an introduction to rheometry was presented. It was pointed out that a mechanical rheometer can perform oscillatory experiments to deform the material under study and measure the relaxation after the application of stress. However, the frequency achievable by the mechanical engine is limited to work below $\omega \sim 10^2 \text{ s}^{-1}$. Furthermore, it is necessary to be sure that the measurements are maintained in the linear regime, otherwise the deformation of the material with this mechanism can provoke destruction and reorganization of the structures within the sample, leading to an erroneous measurement. During the last three decades, the microrheological techniques have boomed for their advantageous application to extract information at smaller length and time scales, only possible with the minimization of the probing device, as for the use of force microscopy through the sensitivity of a microcantilever [120] [121] [122]. There also exists the implementation of colloidal particles as mentioned in the DWS section, as probes to extract mechanical information of the system under study. This kind of microrheology is what concerns to us [123] [124]. Due to the almost negligible inertia of the probe particles, the frequency interval that could be reached is considerably extended (up to $\omega \sim 10^6 \text{ s}^{-1}$) [39].

Here we will detail the microrheological technique we implement for colloidal particles. It relates the mean square displacement of the particles in the Laplace or equivalently, in the Fourier domain, with the viscoelastic spectrum of the complex fluid. T. G. Mason et al., developed a generalized Stokes-Einstein equation, which takes into account the thermal fluctuation of the particles due to the presence of a surrounding complex fluid. If we consider a stochastic displacement of the particles,

statistical physics theory approaches the dynamics of these systems more simply. A modified Langevin equation is used which includes a causal memory function to consider the viscoelasticity response of the medium. The equation has the following form,

$$m \frac{d\mathbf{v}}{dt} = \mathbf{f}_R(t) + \int_0^t \zeta(t-t') \mathbf{v}(t') dt', \quad (\text{III.3.36})$$

where the hydrodynamic resistance is $\zeta(t-t')$, which satisfy the fluctuation-dissipation theorem. This term includes the energy storage due to the elasticity of the fluid. m is the particle's mass and $\mathbf{v}(t)$ its velocity; and $\mathbf{f}_R(t)$ is a Gaussian random force, that incorporates both instantaneous and reactive stochastic forces of the solvent particles against the probe spheres, and therefore differs from the white spectrum of a viscous fluid.

$\zeta(t)$ is causal, meaning $\zeta(t) = 0$ for $t < 0+$, therefore, the limits of integration for the convolution term can be changed to $(0, \infty)$. Then, applying the unilateral Fourier transform to the equation (III.3.36), and retaining the initial conditions for the velocity, we get

$$\mathbf{v}^*(\omega) = \frac{\mathbf{f}_R^*(\omega) + m\mathbf{v}(0)}{\zeta^*(\omega) + i\omega m}. \quad (\text{III.3.37})$$

Here we have to assume for an arbitrary function that the unilateral Fourier transform is

$$g^*(\omega) = \int_0^{\infty} g(t) e^{-i\omega t} dt = \mathfrak{S}_u \{g(t)\}(\omega). \quad (\text{III.3.38})$$

Now, to calculate the transform of the velocity autocorrelation function, we multiply the equation (III.3.37) by $\mathbf{v}(0)$, and ensemble average,

$$\langle \mathbf{v}^*(\omega) \cdot \mathbf{v}(0) \rangle = \frac{\langle \mathbf{f}_R^*(\omega) \cdot \mathbf{v}(0) \rangle + m \langle \mathbf{v}(0) \cdot \mathbf{v}(0) \rangle}{\zeta^*(\omega) + i\omega m}. \quad (\text{III.3.39})$$

Causality guarantees that the distribution of random forces is decoupled from the distribution of velocities at $t = 0$, $\langle \mathbf{f}_R(t) \cdot \mathbf{v}(0) \rangle = 0$, then formally in the frequency domain, the first term on the right side of the equation (III.3.39) has the same result. On the other hand, equipartition energy sets the value of the instantaneous average square velocity, $m \langle \mathbf{v}(t) \cdot \mathbf{v}(t) \rangle = k_B T$, so the second term on the right of the equation (III.3.39) is equivalent to this. Also, the term $i\omega m$ represents inertia of the colloidal particle. This term is only significant at high frequencies ($> 10^6 \text{ s}^{-1}$) for latex particles of micron diameter sizes. The achievable limit for DWS and this microrheological technique coincides with this limit frequency so that we can neglect the inertial term in a good approximation. Using these considerations and solving for the local memory function, we find

$$\zeta^*(\omega) = \frac{k_B T}{\langle \mathbf{v}^*(\omega) \cdot \mathbf{v}(0) \rangle}. \quad (\text{III.3.40})$$

For $\omega > 0$ and using the identity $\mathfrak{S}_u \{ \Delta r^2(t) \} = \left[6 / (i\omega)^2 \right] \mathfrak{S}_u \{ \langle \mathbf{v}(0) \cdot \mathbf{v}(t) \rangle \}$, the equation (III.3.40) is rewritten as

$$\zeta^*(\omega) = \frac{6k_B T}{(i\omega)^2 \mathfrak{S}_u \{ \Delta r^2(t) \}}. \quad (\text{III.3.41})$$

This equation is also consistent with the fluctuation-dissipation theorem. The generalized Stokes-Einstein equation, as the classical one, assumes that the complex fluid is treated as a continuum around the spherical particle. This argument is valid when the length scales of the structures giving rise to the elasticity are much smaller than the particle's radius. We also assume that the Stokes relation for the drag of a purely viscous fluid can be used to determine the complex viscosity ($\zeta^*(\omega) = 6\pi a \eta^*(\omega)$) over all frequencies and the relation with the complex modulus, $\eta^*(\omega) = G^*(\omega)/i\omega$, as well. With these relations, we obtain

$$G^*(\omega) = \frac{k_B T}{\pi a (i\omega) \mathfrak{S}_u \{ \langle \Delta r^2(t) \rangle \}}, \quad (\text{III.3.42})$$

valid for $\omega > 0$, with a the radius of the spherical particle. This equation is the generalized Stokes-Einstein equation which relates the complex modulus of a viscoelastic fluid with the unilateral Fourier transform of the mean square displacement of the tracer particles; consistent with the conventions of mechanical rheology. As mentioned above, there is an equivalent result in the Laplace domain, but the development in the frequency domain permit us to compare directly with mechanical experiments.

3.4.1. Evaluation of experimental data

Even when it is possible to use the generalized Stokes-Einstein equation to obtain the mechanical information of the system under study from a DWS experiment, there are technical complications for using MSD experimental data. In experiments, each measurement occurs at discrete times over a limited temporal range, i.e., we do not have a well behaving mean square displacement function for input in equation the (III.3.42). Computation of transforms into the frequency domain may introduce errors in the moduli. To overcome this problem, we followed two procedures:

Bellour's equation

First, we adjusted a functional form to the experimental data of the MSD, proposed by M. Bellour, et al., [125]. They introduce a master function that describes the MSD of the particles in the entire time range. This function was developed primarily for Maxwellian fluids and a straightforward interpretation of the relaxation mechanism and relaxation times was given for a system of wormlike micelles made of surfactants. Nevertheless, the application of Bellour's fitting equation is not limited to Maxwellian fluids when we are not seeking a significant physical interpretation to each term in the equation, but instead we just need a continuous well-behaved MSD, mainly at low and high times where there is a lack of data, to be able to manage it numerically.

The equation proposed by M. Bellour and coworkers is

$$\Delta r^2(t) = 6\delta^2 \left(1 - e^{-\left(t \frac{D_0}{\delta^2}\right)^\gamma} \right)^{1/\gamma} \left(1 + \frac{D_m}{\delta^2} t \right). \quad (\text{III.3.43})$$

For the time window achievable for the MSD in DWS experiments, it is possible to distinguish three different regimes for the motion of particles, each one represented with the different terms in the equation (III.3.43). At short times the dynamics is Brownian, where D_0 is the local diffusion coefficient; at intermediate times, the MSD remains constant for a certain time, where $6\delta^2$ is the value of the MSD at the inflection point; at longer times, the motion is diffusive again, with D_m the long-time diffusion coefficient corresponding to the macroscopic viscosity of the solution [125]. The first term in brackets times $6\delta^2$ represents the MSD of a particle harmonically bounded and executing a Brownian motion around a stationary mean position. Notwithstanding, the system of WLMs is viscous at long times, and the cages in which particles are trapped fluctuate due to the breaking/recombination – reptation mechanisms, hence, the MSD displays the longer times behavior with the second term in brackets. Finally, to fit Bellour's equation to the characteristic MSD at the plateau onset, it is necessary to include the parameter γ , which accounts for the broad spectrum of relaxation times at this site. $\gamma = 1$ corresponds to a monoexponential relaxation and a decrease in the value corresponds to a larger relaxation spectrum. For a detailed explanation for understanding the meaning of equation (III.3.43), it worth it to check reference [125].

Logarithmic derivative of the MSD

To overcome the problem at the edges of the MSD, T. G. Mason introduced the second procedure [124]. Usually to implement the Laplace transform numerically, people use the classical trapezoid rule as an integration method; or for calculating the Fourier transform numerically, the Fast Fourier Transform (FFT) is the most common procedure. Both of them introduces errors near the frequency extremes due to the truncation of the data set. Mason estimate the transforms algebraically by

expanding the MSD locally around the frequency of interest, s (or ω), using a power law and retaining the leading term, we get

$$\Delta r^2(t) \approx \left| \langle \Delta r^2(1/\omega) \rangle \right| (\omega t)^{\varrho(\omega)}, \quad (\text{III.3.44})$$

where $|\langle \Delta r^2(1/\omega) \rangle|$ is the magnitude of $\langle \Delta r^2(t) \rangle$ at $t = 1/\omega$ and $\varrho(\omega) \equiv \left. \frac{d \ln \Delta r^2(t)}{d \ln t} \right|_{t=1/\omega}$ is the

power law exponent describing the logarithmic slope of the MSD. For Brownian particles, this slope lies between zero for elastic confinement and one for viscous diffusivity. Evaluation of the Fourier transform leads to the relation

$$i\omega \mathfrak{S}_u \left\{ \langle \Delta r^2(t) \rangle \right\} \approx \left| \langle \Delta r^2(1/\omega) \rangle \right| \Gamma[1 + \varrho(\omega)] i^{-\varrho(\omega)}. \quad (\text{III.3.45})$$

Substituting in the generalized Stokes-Einstein equation (III.3.42), and using the Euler's equation to separate real and imaginary parts, we obtain

$$\begin{aligned} G'(\omega) &= \left| G^*(\omega) \right| \cos(\pi\varrho(\omega)/2), \\ G''(\omega) &= \left| G^*(\omega) \right| \sin(\pi\varrho(\omega)/2), \end{aligned} \quad (\text{III.3.46})$$

where

$$\left| G^*(\omega) \right| \approx \frac{k_B T}{\pi a \left| \langle \Delta r^2(1/\omega) \rangle \right| \Gamma[1 + \varrho(\omega)]}, \quad (\text{III.3.47})$$

and Γ is the gamma function. This algebraic estimation method provides much better values for the moduli at the frequency extremes, at the cost of small errors introduced where the logarithmic slope of the MSD varies rapidly. It also can be implemented when time-sampled data are logarithmically spaced, and finally, the method is also faster than the FFT.

3.5. Static Light Scattering (SLS)

Now that DLS techniques are explained, including the limit of multiple scattering events, here the introduction of light scattering techniques is extended to the static cases, where an average of the dynamics of the macromolecules is analyzed, independent of the time evolution of the system, with the aims to obtain structural information. Scattering measurements are performed in the Fourier (also called reciprocal) space, not real space like microscopy. For this, scattering data have to be either inverted back to real space or fitted to models describing structures in reciprocal space.

In the equation (III.3.1) we saw a simplified version of the electric field of a scattered wave by a sample, where each term of the sum corresponds to the contribution of each particle to the total scattered electric field. If we consider relative big particles, which possess more than one scattering center, we have to deal with the phenomenon in the Rayleigh-Debye approximation. It was already expressed that the main problem is that one particle has several scattering centers which contribute to the total scattered light at the detector. For dispersions of a single type of particle with isotropic segments and in an ideal solution, the DLS autocorrelation function was considerably simplified since there are no correlations between different particles for nonzero scattering vector (see the equation (III.3.7)), where the $S(\mathbf{q}, t)$ is the internal correlation function of the scattering particles. Also, it was mentioned that the zero-time value of the internal correlation function is the form factor, $S(\mathbf{q}, t) = P(qL)$, which contains structural information.

A more general expression for the amplitude $E_s(\mathbf{R}, t)$, of the electric field of the radiation scattered to a point detector at position \mathbf{R} in the far field, due to *discrete scatterers* (with more than one scattering center, see Figure III.4) is given by

$$E_s(\mathbf{R}, t) = -\frac{k^2 E_0}{4\pi} \frac{\exp[i(kR - \omega t)]}{R} \times \sum_j \left\{ \int_{V_j} \left[\frac{\varepsilon_P(\mathbf{r}_j, t) - \varepsilon_L}{\varepsilon_0} \right] \exp(-i\mathbf{q} \cdot \mathbf{r}_j) d^3r_j \right\} \exp[-i\mathbf{q} \cdot \mathbf{R}_j(t)]. \quad (\text{III.3.48})$$

Here we consider N particles in the scattering volume V , whose centers of mass at time t are described by position vectors $\{\mathbf{R}_j(t)\}$. $\mathbf{r}_j(t)$ is the position of volume element $dV_j (= d^3r_j)$ in particle j relative to its center of mass. $\varepsilon_P(\mathbf{r}, t)$ is the local dielectric constant at position \mathbf{r}_j in particle j , ε_L is the average dielectric constant of the liquid, and ε_0 is the average dielectric constant of the whole suspension. The term with the inverse of R describes a spherical wave of scattered radiation emanating from the origin; the final term $\exp[-i\mathbf{q} \cdot \mathbf{R}_j(t)]$ takes account of the shifted in phase by the radiation scattered by the volume element at the center of mass (at \mathbf{R}_j relative to the origin O , and time t), as explained for DLS; and the central element in the equation (III.3.48) integrates the contribution per particle, for the phase shift but now due to the scattering centers at positions \mathbf{r}_j , relative to the center of mass for each particle, modulated by the difference in dielectric constant within each particle, and summed up for the N particles. We define the term

$$\Delta\rho(\mathbf{r}_j, t) = \frac{k^2}{4\pi} \left[\frac{\varepsilon_P(\mathbf{r}_j, t) - \varepsilon_L}{\varepsilon_0} \right], \quad (\text{III.3.49})$$

that can be regarded as a *local density of scattering material*. With the appropriate identification of $\Delta\rho(\mathbf{r}_j, t)$, the henceforth results will apply also to X-ray and neutron scattering. The physical principles are the same for all scattering cases, with the proper change of dielectric constant to

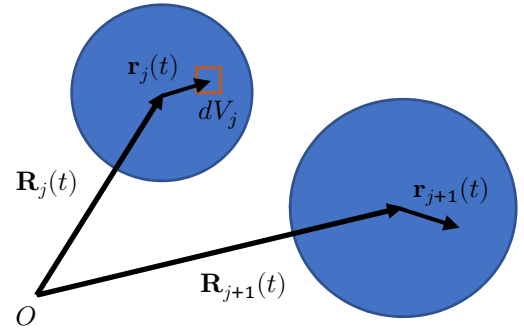


Figure III.4 Coordinates for discrete scatterers, relative to an origin O .

electronic density, or contrast of nucleon density of the atoms, for X-rays and neutron scattering respectively. Another definition is done to the integral in the equation (III.3.48), as follows

$$b_j(\mathbf{q}, t) = \int_{V_j} \Delta\rho(\mathbf{r}_j, t) \exp(-i\mathbf{q} \cdot \mathbf{r}_j) d^3r_j, \quad (\text{III.3.50})$$

called the *scattering length* of particle j . Experimentally one measures the scattered intensity $I(\mathbf{q}, t) = |E_s(\mathbf{q}, t)|^2$, as function of the scattering vector, rather than the position of the detector. The two are equivalent, but now it is analyzed in the reciprocal space. For structural information the ensemble average is required, so the intensity has the form (equivalent to a time average when we are dealing with ergodic samples)

$$\langle I(q) \rangle = \frac{E_0^2}{R^2} \left\langle \sum_{j=1}^N \sum_{k=1}^N b_j(\mathbf{q}) b_k^*(\mathbf{q}) \exp[-i\mathbf{q} \cdot (\mathbf{R}_j - \mathbf{R}_k)] \right\rangle. \quad (\text{III.3.51})$$

For diluted systems, there is a simplification of the last equation. In this case the individual particles are, on average, widely separated spatially so that their behaviors are uncorrelated. Omitting for simplicity the prefactors, the equation (III.3.51) is rewritten as

$$\langle I(q) \rangle = \sum_{j=1}^N \langle |b_j(\mathbf{q})|^2 \rangle + \sum_{j \neq k=1}^N \langle b_j(\mathbf{q}) \exp(-i\mathbf{q} \cdot \mathbf{R}_j) \rangle \langle b_k^*(\mathbf{q}) \exp(i\mathbf{q} \cdot \mathbf{R}_k) \rangle = \sum_{j=1}^N \langle |b_j(\mathbf{q})|^2 \rangle, \quad (\text{III.3.52})$$

where we have considered that in the average, the exponential terms are randomly distributed about zero, thus, their ensemble average is zero. For identical particles,

$$\langle I(q) \rangle = N \langle |b(0)|^2 \rangle P(q), \quad (\text{III.3.53})$$

where we have introduced the form factor $P(q) = \langle |b(\mathbf{q})|^2 \rangle / \langle |b(0)|^2 \rangle$, which is defined so that $P(q) \rightarrow 1$ as $q \rightarrow 0$, and provides information on the structure of the individual particles. For spherical particles, it was computed already and it is shown in the equation (III.3.10).

An extended data analysis treatment is out of the scope of the thesis, but here it is introduced the possibility for obtaining structural information within a particle, about the different sizes in spatial space. This treatment was developed by O. Glatter and can be found elsewhere [126] [127] [99].

For dilute suspensions, consider the equation (III.3.53). Various approaches to data analysis can be taken. One can try comparing data spanning a wider range of q with specific models for the form factor $P(q)$, as will be introduced later; however, if a good fit of the data cannot be obtained in this way, one is forced to a more general inversion approach from the reciprocal space.

After some algebraic considerations, one finds that

$$\frac{\langle I(q) \rangle}{N} = \langle |b(\mathbf{q})|^2 \rangle = 4\pi \int dR p(R) \frac{\sin qR}{qR}, \quad (\text{III.3.54})$$

where

$$p(R) = \overline{R^2 \Delta\rho^2(\mathbf{R})} \quad (\text{III.3.55})$$

is known as the *pair-distance distribution function*, with $\overline{\Delta\rho^2(\mathbf{R})} = \int d^3r \Delta\rho(\mathbf{r}) \Delta\rho(\mathbf{r} - \mathbf{R})$.

Finally, Fourier inversion of the equation (III.3.54) gives

$$p(R) = \frac{1}{2\pi^2} \int_0^\infty \langle |b(\mathbf{q})|^2 \rangle qR \sin qR dq. \quad (\text{III.3.56})$$

Thus, the pair-distance distribution function for the particles can be obtained by numerical Fourier transformation of scattering data, using the equations (III.3.53) and (III.3.56). It can be seen from $\overline{\Delta\rho^2(\mathbf{R})}$ and the equation (III.3.55), that $p(R)$ essentially describes the number of ways in which one can choose a vector length $|\mathbf{R}|$ which connects scattering material within the particle, and contains information of the particle structure. Figure III.5 sketches the relation between the typical functional shape of $p(R)$, with the particle shape. An emphasis is done here; $p(R)$ depends totally on the local density of scattering material which in turn depends on the kind of incident radiation and the molecular and atomic components of the sample to analyze. It is completely different to use light, X-rays or neutrons, and the resolution to resolve the different curves in Figure III.5 depends on these considerations.

For concentrated systems the exponential terms in the equation (III.3.52) are not annulated. For simplicity we consider identical homogeneous spheres, so that all $b_j(\mathbf{q}) = b(q)$, then at the end the scattered intensity has the general form

$$\langle I(q) \rangle = b^2(q) \sum_{j=1}^N \sum_{k=1}^N \langle \exp[-i\mathbf{q} \cdot (\mathbf{R}_j - \mathbf{R}_k)] \rangle = Nb^2(0)P(q)S(q), \quad (\text{III.3.57})$$

where $S(q)$ is the *static structure factor* defined by

$$S(q) \equiv \frac{1}{N} \sum_{j=1}^N \sum_{k=1}^N \langle \exp[-i\mathbf{q} \cdot (\mathbf{R}_j - \mathbf{R}_k)] \rangle. \quad (\text{III.3.58})$$

The structure factor represents the modification of the intensity due to the spatial correlation of the particles, as is clear in the equation (III.3.57), where $Nb^2(0)P(q)$ describes the scattering by N uncorrelated particles. In a dilute system, $S(q) = 1$.

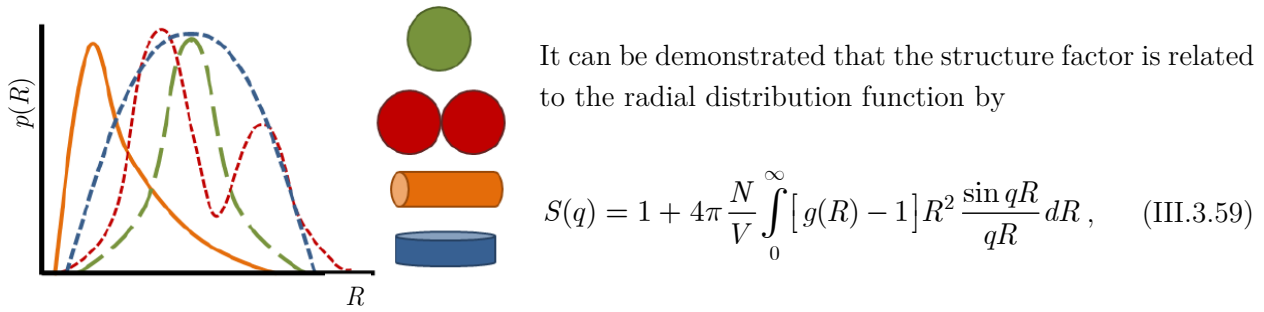


Figure III.5 Different shapes associated with a different $p(R)$ function. The colors of plots determine the different structural shape of particles.

It can be demonstrated that the structure factor is related to the radial distribution function by

$$S(q) = 1 + 4\pi \frac{N}{V} \int_0^\infty [g(R) - 1] R^2 \frac{\sin qR}{qR} dR, \quad (\text{III.3.59})$$

which Fourier inversion gives the radial distribution function

$$g(R) = 1 + \frac{1}{2\pi^2} \frac{V}{N} \int_0^\infty [S(q) - 1] q^2 \frac{\sin qR}{qR} dq. \quad (\text{III.3.60})$$

Figure III.6 shows sketches of a typical radial distribution function, for instance for a concentrated suspension of hard-sphere colloids, and the corresponding structure factor. Since two particles cannot occupy the same space, $g(R)$ is zero for center-to-center interparticle separations smaller than the particle diameter. The main peak in $g(R)$ describes the nearest neighbour shell of particles around any given particle. At large interparticle separations $g(R) \rightarrow 1$ implying that spatial correlations are usually short-ranged (but not in a crystal). The peak in $S(q)$ can be considered, approximately, to be a *Bragg refraction* from planes of particles separated by distances equal to the mean nearest neighbour separation. Thus, one finds that the positions R_{max} and q_{max} of the main peaks in $g(R)$ and $S(q)$ are related by an approximate *Bragg condition* $q_{max} R_{max} \approx 2\pi$. For this reason, we say that a scattering experiment, operating at scattering vector q , measures structure on a spatial scale $2\pi/q$. Nevertheless, this rule should not be taken literally, because the value $S(q)$ at a particular scattering vector q , is determined by the values of $g(R)$ at all R [99].

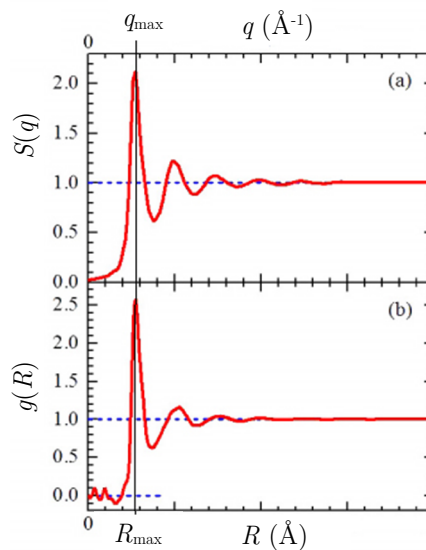


Figure III.6 (a) $S(q)$ and (b) $g(R)$ for a suspension of concentrated colloidal suspensions.

3.5.1. Small Angle X-ray Scattering (SAXS) and Small Angle Neutron Scattering (SANS)

Aside from the different mechanisms by which the radiation is scattered, a major difference between light, X-rays and neutrons is their wavelengths; $\sim 400 - 600$ nm for light, ~ 0.1 nm for X-rays and neutrons. For various scattering angles, Table III.2, taken from [99], shows approximate values of the scattering vector \mathbf{q} , and the spatial scale $2\pi/q$ probed by scattering.

| X-rays, neutrons ($\lambda = 0.1$ nm) | | | Light ($\lambda = 400 - 600$ nm) | | |
|--|--------------------------|---------------|-----------------------------------|--------------------------|-----------------|
| θ (degrees) | q (nm^{-1}) | $2\pi/q$ (nm) | θ (degrees) | q (nm^{-1}) | $2\pi/q$ (nm) |
| 0.01 | 0.01 | 600 | 1 | 3×10^{-4} | 2×10^4 |
| 0.1 | 0.1 | 60 | 10 | 3×10^{-3} | 2000 |
| 1 | 1 | 6 | 100 | 2.4×10^{-2} | 300 |
| 10 | 10 | 0.6 | | | |

Table III.2 Approximate magnitudes of the scattering vector and its reciprocal for X-rays, neutrons and light at various scattering angles. Reproduced from [99].

To reach scales of interest, > 10 nm in much of soft matter, scattering angles smaller than 1° must be used (that is the reason of the names SAXS and SANS). The minimum scale probed by light scattering at large angles overlaps the maximum scale of very small-angle X-ray and neutron scattering. While the X-ray scattering lengths of atoms are simply proportional to the atomic number, neutron scattering lengths vary irregularly with the type of nucleus and can be negative as well as positive. Furthermore, different isotopes of the same atom can have very different scattering lengths. Neutron scattering in general is sensitive to fluctuations in the density of nuclei in the sample. X-ray scattering is sensitive to inhomogeneities in electron densities [128].

The advantage of SANS over other small-angle scattering methods is the deuteration method. This consists in using deuterium labeled components in the sample in order to enhance their contrast. This is reminiscent of contrast variation in microscopy whereby the level of light incident upon a sample is varied using a diaphragm. Labeling is difficult to achieve with SAXS since this involves heavy atom labels that change the sample drastically. SANS can measure density fluctuations and composition (or concentration) fluctuations. SAXS can measure only density fluctuations. The deuteration method allows this bonus. SANS is disadvantaged over SAXS by the intrinsically low flux of neutron sources (nuclear reactors or spallation sources using cold source moderators) compared to the higher orders of magnitude of fluxes for X-ray sources (rotating anode or synchrotrons).

Microscopy has the advantage that data are acquired in direct (real) space whereas static scattering methods measure in reciprocal space. Although electron microscopy (EM) and SANS are complementary methods, EM is applied on very thin samples only and it cannot measure samples at different concentrations and temperatures directly. Also, the observed images are a 2D projection. SANS can do all these things but cannot produce an image in real space [128].

SANS data analysis is performed at many levels. The initial level consists of *follow the trends* type of approach using standard plot methods. These are linear plots of functions of the scattered intensity

$I(q)$ plotted against functions of the scattering variable q . The next level uses nonlinear least squares fits to realistic models. The final trend makes use of sophisticated ab-initio or *shape reconstruction* methods in order to obtain insight into the structure and morphology within the investigated sample [128]. Note that the absolute intensity $I(q)$ is a short hand notation for the macroscopic scattering cross section $d\Sigma(q)/d\Omega$ (explained in the next section).

In the following, a few standard plots are mentioned to understand the basic information the scattering patterns could offer. However, in most cases, these plots fall short to get all the structural information, hence it is necessary to use more sophisticated functions to fit the scattering patterns.

The Guinier plot

When the scattering vector tends to zero there is an analytical approximation to the total scattered intensity

$$I(q) = I_0 \exp\left(-\frac{q^2 R_g^2}{3}\right). \quad (\text{III.3.61})$$

Rewriting it in a linear approximation, to plot $\ln[I(q)]$ vs. q^2 ,

$$\ln[I(q)] = \ln[I_0] - \frac{q^2 R_g^2}{3}, \quad (\text{III.3.62})$$

where R_g^2 is the radius of gyration of the scattering object which is contained in the slope of the last equation. It represents the effective size of the scattering particle whether it is a polymer chain, part of a protein, a micelle, or a domain in a multiphase system. The first term gives information in the regime of q^{-0} (independent of q values), at the intercept I_0 , related with the volume of the particle, and then gives an estimation of the total size of the structures. The range of a Guinier plot corresponds to $qR_g < \sqrt{3}$, that is obtained when the probed range $2\pi/q$ is larger than the particle size.

There is a modification to the Guinier plot when we are treating elongated objects. For a cylinder of length L (the contour length L_c , in the case of worm-like micelles or semiflexible polymers) and radius R , the low- q Guinier approximation remains as in the equation (III.3.61), but this time with

$$R_g^2 = \frac{L^2}{12} + \frac{R^2}{2}. \quad (\text{III.3.63})$$

The intermediate- q Guinier approximation is different,

$$I(q) = \frac{I(0)}{q} \exp\left(-\frac{q^2 R_{g-cs}^2}{2}\right), \quad (\text{III.3.64})$$

where $R_{g-cs}^2 = R^2/2$, the cross-sectional radius of gyration. Then, the intermediate linear plot becomes $\ln[qI(q)]$ vs. q^2 .

The Porod plot

The Porod region corresponds to a probed range smaller than the scattering objects (at large- q) so that the scattering radiation is probing the local structure. The Porod plot, $\log[I(q)]$ vs. $\log[q]$, yields information about the fractal dimension of the scattering objects. At large- q one can approximate

$$I(q) = \frac{A}{q^n} + B \quad \text{or} \quad \log[I(q) - B] = \log(A) - n \log(q). \quad (\text{III.3.65})$$

A Porod slope $n = 1$ is obtained for scattering from rigid rods; a slope $n = 4$ represents a smooth surface for the scattering particle; whereas a slope n between 3 and 4 characterizes rough interfaces of fractal dimension D with $n = 6 - D$. This is called a surface fractal. Moreover, in the case of polymer coils, the Porod slope n is related to the excluded volume parameter as its inverse $n = 1/\nu$. A slope $n = 2$ is a signature of Gaussian chains in a dilute environment, a slope $n = 5/3$ is for fully swollen coils, and a slope $n = 3$ is for collapsed polymer coils. A slope between 2 and 3 is for mass fractals such as branched systems (gels) or networks.

The Zimm plot

A plot of $1/I(q)$ vs. q^2 which found wide use in light scattering from dilute polymer solutions where extrapolation to zero q and zero concentration yields the molecular weight, the radius of gyration and the second virial coefficient. The Zimm plot is also useful in polymer blends [128]. For this plot, there is an assumption of a Lorentzian form for the q -dependence of the scattering intensity

$$I(q) = \frac{I_0}{1 + q^2 \xi^2}, \quad (\text{III.3.66})$$

with ξ the correlation length, related to the radius of gyration in the low- q region assuming an expansion of the equation (III.3.66). Low- q departure from the linear behavior of the Zimm plot is a signature of non-homogeneity in the sample or of chain-branching. Also, a negative value of the intercept I_0 is a sign of phase separation. It is also possible to consider an expansion of the equation (III.3.66) at high- q , with the extra consideration of excluded volume interactions.

The Kratky plot

This plot emphasizes a deviation from the high- q behavior of the scattering intensity. For polymer chains, the Kratky plot ($q^2 I(q)$ vs. q) emphasizes the Gaussian chain nature or departure from it. Since the form factor for Gaussian chains varies like $I(q) \sim 1/q^2$ at high- q , this plot tends to a horizontal asymptote. Deviation from a horizontal asymptotic behavior indicates a non-Gaussian characteristic for the scattering chains. For rigid rods this plot would go to a linearly increasing asymptote because the form factor for a rod varies like $I(q) \sim 1/q$ at high- q . And also, for branched systems (or mass fractals), the plot would behave as $\sim q^{-1}$, because the form factor at high- q goes like $I(q) \sim 1/q^3$.

Figure III.7a presents a scattering pattern used for SANS and SAXS. Different regimes are depicted, each one with a power law fingerprint in the scattering vector. In each achievable regime it is possible to estimate different shapes and geometry of the studied particles within the sample. Figure III.7b clarifies the Guinier regimes, in a pattern for a system with cylindrical shape.

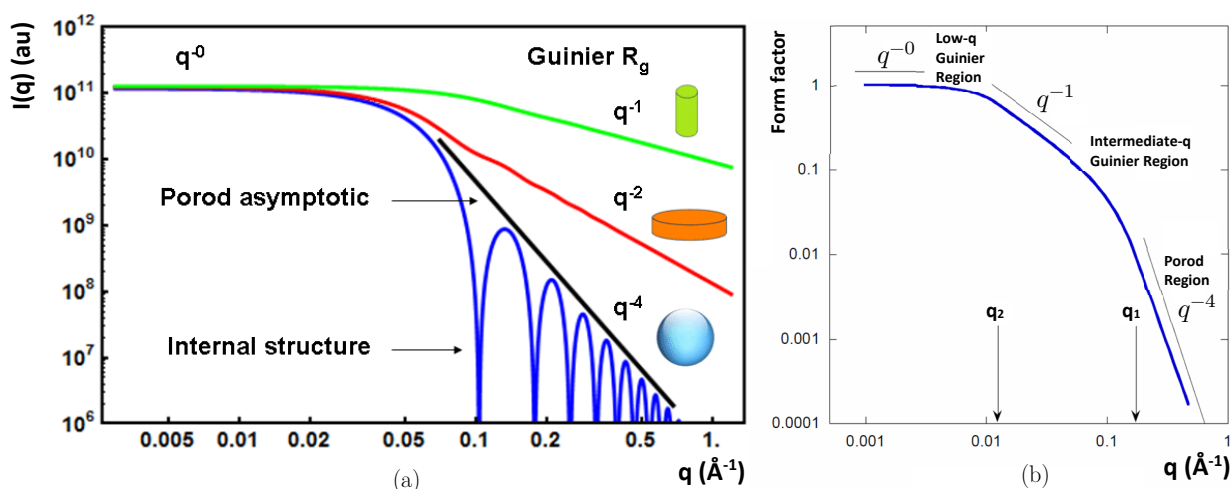


Figure III.7 (a) Scattering patterns where different q dependent regimes are shown. Depending on the power law followed by the scattering vector, it is possible to estimate the shape of the elements studied. (b) Form factor for a cylinder showing the low- q Guinier region, the intermediate- q Guinier region and the high- q Porod region. Taken and modified from [128].

The presentation of more complex functions to reproduce the scattering SANS patterns is out of the scope of the thesis. Further information can be found in [99] [128]. In Chapter IV, section of PBPEO worm-like micelles, where the experimental results of the research are shown, we present the SANS pattern analysis of PBPEO diblock copolymers, where we used the standard intermediate- q Guinier plot to obtain the cross-sectional radius of gyration of the aggregates, R_{g-cs} . Additionally it was necessary to use two more sophisticated functions: a core-shell cylinder model to extract useful information from the intermediate and large- q regions, which makes possible to know that the PBPEO aggregates have elongated morphologies with internal cross-sectional structure; and at the low- q region, we used a flexible cylinder model with a circular cross-section and a uniform scattering

length density to fit the data, which permit us to get some approximate values of the persistence lengths in these cylindrical systems.

4. Experimental details and procedure

Every project starts with a planification of the procedures and steps to be followed, to get the proposed goals. In particular experimental cases, it is necessary to make a plan considering the facilities to which we have access, and to perform organized experiments. Occasionally it is also necessary to book and schedule the pertinent dates and consuming time to obtain the results in a desirable time. The most critical tests before DWS experiments start are mentioned in this section, and the technical information about DWS and SANS facilities used as well.

4.1. Diffusing Wave Spectroscopy (DWS)

Our DWS setup is a homemade instrument, assembled several years ago in the group. It has been used for studying many different systems. For its construction there were considered the respective technical details, tested formerly for other scientific groups [110] [129] [130]. With the pass of time, the DWS set up has been improved. Figure III.8 shows the current set up. In a typical DWS experiment, we use special optical glass cuvettes where the liquid sample is verted. The path length of the cells is 1, 2, 2.5, 4 or 5 mm, depending on the sample, the fill fraction of probe particles added, and the amount of light absorption of the sample. In a standard experiment, light travels several tens of meters within the sample, due to the multi-scattering events, for that reason the source of light has to be coherent enough to be able to produce an interference pattern (speckle) at the detector. We used an argon laser which produces a beam of wavelength of 514.5 nm. The first step the light pass is a spatial filter to eliminate the internal spurious structure of the beam (to make it completely Gaussian), and then to expand it (BE). Here, a set of two convex lenses is used with a pinhole in the middle of a 2 μm aperture. After that, the beam passes through a shutter (P1) which eliminates the external parts of the Gaussian beam and approximate it to a plane wave. Next, the laser beam strikes a slab formed by a turbid suspension made of the liquid under study and probe colloidal particles (the sample, S). The sample (S) is thermally stabilized in a bath (TB). The scattered light passes through an achromatic doublet (AD) which forms an image of scale 1:1 of the back side of the sample, on the plane of the iris (I), along the CCD camera detection branch. Next to the achromatic doubled there is a beam splitter (BS) which separates the scattered light in two directions: the CCD camera detection branch, and the photomultipliers (PMT) detection branch. If the system to analyze is ergodic, a mirror is set instead of the beam splitter. In the PMT detection branch, the scattered light is collected by an optic fiber. Then, the light within the fiber is divided 50/50 to reach two PMT detectors. After the increment of electric signal inside the PMT, the signal is converted to TTL pulses and the autocorrelation function is processed by a correlator card, in cross correlation mode, to extend the initial sampling time (12.4 ns) [106], and to eliminate the correlation due to the after pulsing (electronic noise). The correlator card is controlled by a computer. In the CCD camera detection branch, the iris acts as an incoherent source of light, hence, when the iris aperture is changed and also the distance to the camera, the detection at the camera is optimized,

since the size of the speckle pattern is modified with respect to the size of a pixel. The detection with the CCD camera is almost instantaneously, with each pixel representing an individual system of a set of systems in an ensemble. A Matlab software controls every pixel of the camera, making a direct ensemble average to generate a time autocorrelation function. The camera can be used directly to analyze non-ergodic samples, but the CCD camera response is as fast as ~ 11 ms, taking into account the frame rate and the acquisition time. For short lag times, the non-ergodicity problem can be avoided by remixing the scattered light coming from the sample by the use of a slowly rotating diffuser disk (DD) placed before the collection optics of the PMT (2-cell technique [131] [132]). This procedure provides a true ensemble-averaged time correlation function over $\sim 7 - 8$ decades of time. Multi-scattered light is depolarized; if the autocorrelation function is processed directly, the contrast (β factor) is reduced by half. To avoid this decrement, two polarizers (A1 and A2) are set at the entrance of the detectors, with cross polarization compared to polarization of the incident beam (linear polarization).

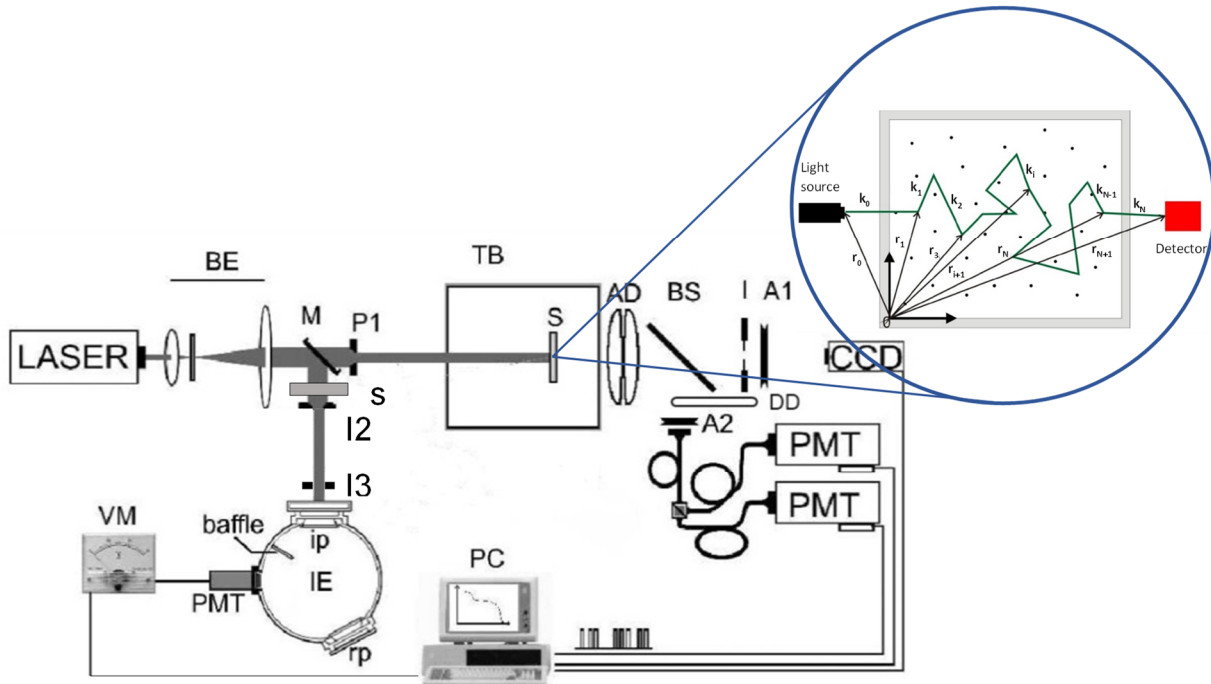


Figure III.8 DWS experimental setup. All components are shown.

For determining the values of l^* and l_a , a mirror (M) is set next to the spatial filter. We make use of an integrating sphere (IE) [133]. Between the mirror and the integrating sphere, we set two iris (I2 and I3), separated a fixed distance, to obtain three measurement values: reflectance, transmittance and collimated transmittance (or unscattered transmittance), which are the input parameters for the Inverse Adding Doubling method (IAD). After a numerical inversion procedure in the IAD method, the values of l^* , l_a and the anisotropy factor g , are obtained [111] [115] [134]. Each one of these last measurements have a precise experimental setup, if not followed, it could lead to erroneous readings on the sample.

4.1.1. Reflectance and transmittance

In order to measure the total reflectance and total transmittance of light on and through the sample respectively, with the integrating sphere, it is necessary to consider the next equations

$$M_R \equiv r_{std} \frac{R(r_s^{direct}, r_s) - R(0,0)}{R(r_{std}, r_{std}) - R(0,0)}, \quad (III.4.1)$$

$$M_T \equiv \frac{T(t_s^{direct}, r_s) - T_{dark}}{T(0,0) - T_{dark}}. \quad (III.4.2)$$

Each term of the equations is measured independently, according to Figure III.9. The values M_R and M_T are the total reflectance and total transmittance respectively. Standard usage is that reflection is the light being reflected by the sample, while the reflectance is the light being reflected by the sample normalized by the incoming light. Reflectance has no units. The same idea applies to transmission and transmittance; the transmission has units while the transmittance is normalized to the incident power. For reflectance, r_{std} is the reflectance value of the integrating sphere walls, $R(r_{std}, r_{std})$ is the reflection measurement for a standard sample (we used the same value of reflection obtained for the walls), $R(r_s^{direct}, r_s)$ is the reflection measurement for the sample, and $R(0,0)$ is the measurement of the intensity of light without sample and light is allowed to go out of the sphere. For transmittance the back wall of the sphere is never open (light that does not interact with the sample bounces around in the sphere). $T(0,0)$ is the measurement of the intensity of light when the light strikes inside the sphere without sample, $T(r_s^{direct}, r_s)$ is the transmission measurement through the sample, and T_{dark} is the measurement of the intensity of light with the entrance port blocked.

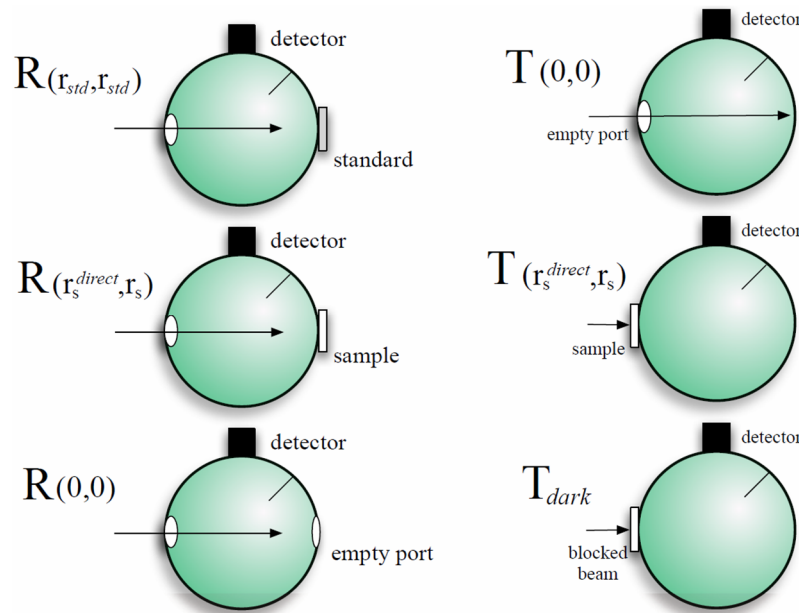


Figure III.9 Setup of the integrating sphere to obtain M_R and M_T . Taken from [117].

4.1.2. Collimated transmittance

It was necessary to follow the research carried out by B. Morales-Cruzado and coworkers [134], in which a computational development is described, where the propagation of photons is simulated through an optical system composed by a biological tissue, to estimate the amount of light that is not scattered by the sample, and the amount of light scattered in the same direction as the incident beam of light. The analysis of photons through the sample is determined with a multilayer Monte Carlo simulation, which considers a Gaussian beam as the source of light. Several tests were done, to compare with the expected theoretical results, for different optical parameters in turbid media. The parameters used in [134] were: 5×10^5 photons, for samples with scattering coefficient $\mu_s < 100$, and 1×10^6 photons, for samples with $\mu_s > 100$ or when the expected collimated transmitted value drops down 1×10^{-5} . To have enough data, they performed 25 simulations.

The experimental setup is shown in Figure III.10, which is the first branch shown in Figure III.8, when the mirror is set next to the spatial filter.

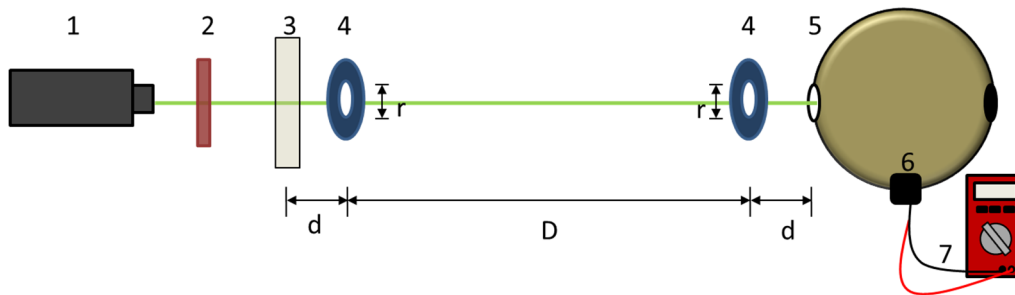


Figure III.10 Experimental setup for collimated transmittance. For simplicity, the spatial filter is not shown. Each element is set in strategic way to obtain favorable results according to [134].

The elements in Figure III.10 can be identified as follows: 1. Argon laser with wavelength of 514.5 nm, 2. Filter with neutral optical density, 3. Sample, 4. Two iris, 5. Integrating sphere, 6. Detector, 7. Voltmeter. The distances and iris apertures were chosen according to tests in [134]. Ideally, $D \rightarrow \infty$ to assure a clean light scattering just in the direction of incidence. If D is too short, scattered light in all other directions would have more possibilities to reach the detector. Results showed that above a distance $D \approx 25$ cm, the results are good enough. In the laboratory, the chosen configuration was with $D = 68$ cm. The iris apertures were chosen taking into account simulations which considers an incident Gaussian beam, and a scattered Gaussian beam with a wider profile waist, than for the incident beam. The aperture should be approximated the same size as the profile waist. Thus, the chosen value was $r = 0.15$ cm. Ideally, both iris must be as close as possible to the sample, and to the integrating sphere. Due to technical limitations, the chosen separation was $d = 5$ cm.

Collimated transmittance is related theoretically with the Beer-Lambert law, which relates the light attenuation with the optical properties of the sample traversed by the light. The law determines a

logarithmic dependence between the transmittance T of light through the sample, and the attenuation coefficient times the traveled distance by the light within the sample

$$T = \frac{I_i}{I_0} = e^{-\mu l}. \quad (\text{III.4.3})$$

In the last equation, the coefficient of attenuation considers the attenuation due to scattering and due to absorption of light, namely $\mu = \mu_s + \mu_a = \mu_s + 1/l_a$, with $\mu_s = \mu'_s/(1-g) = 1/l^*(1-g)$. The term μ'_s is properly named the reduced scattering coefficient, which is a lumped property incorporating the scattering coefficient μ_s and the anisotropy factor g . The purpose of μ'_s is to describe the diffusion of photons in a random walk step size (the transport mean free path, l^*), where each step involves isotropic scattering (considered in the term $1-g$). This equation is the same mentioned in the DWS section, which relates the mean free path of light with the transport mean free path (equation (III.3.13)). So, $g = \langle \cos \theta \rangle$, with θ the deflection angle due to each scattering event.

We made two tests to corroborate the proper operation of the collimated transmittance experiment. The first test comprises deionized water filling a cuvette made of optical glass, with a wall thickness of 1.5 mm, an optical path of 1 mm, and index of refraction of 1.523. The second test comprises an experimental proof of Beer-Lambert law. For this, we used a suspension of spherical particles made of polystyrene in water, with a diameter of 800 nm and a fill fraction of $\phi = 0.00021$. In both cases, we used an optical filter which absorbs 88.1 % of light, settled just outside the laser, with a beam light power of 50 mW. This help us to have a stable beam and at the same time, low intensity of light to avoid saturation in the detector.

In the case of water, the measured collimated transmittance was $M_U = I_i/I_0 = 40.2 \text{ mV}/44.4 \text{ mV} = 0.905 \rightarrow 90.5 \%$, where I_i is the intensity of the laser beam with the sample, and I_0 is the intensity of the laser beam without sample, both measured in terms of volts. This result was compared theoretically considering the Fresnel coefficients of the sample [135]. Figure III.11 shows a sketch of the cuvette with the index of refraction of the glass, the internal and external media. The result, applying the coefficients is

$$M_U = \frac{4^4 n_{\text{glass}}^4 n_{\text{water}}^2 n_{\text{air}}^2}{(n_{\text{glass}} + n_{\text{air}})^4 (n_{\text{glass}} + n_{\text{water}})^4} = 0.908 \rightarrow 90.8 \%.$$

There exists just a percentage difference of 0.33 %, as a reason of the theoretical result with the experimental one. Then, there is a good agreement between both, and the first test is consistent.

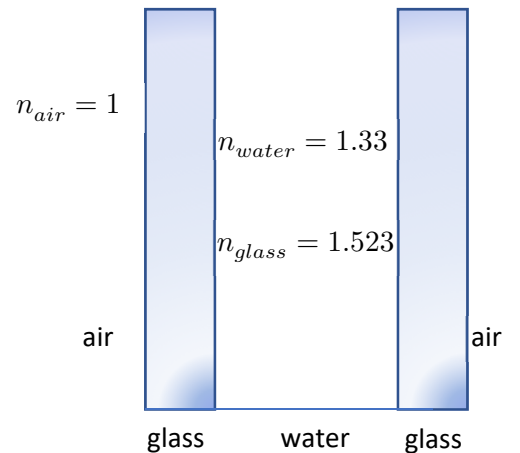


Figure III.11 The bars are the walls of a cuvette, filled with water and immersed in air. The respective index or refraction are indicated.

In the case of the spherical particles, we varied the optical path length, from 1 mm to 5 mm. We made the proper corrections due to the reflection of light onto the cuvettes walls and the water, using the results of the former test. The results are shown in Figure III.12. The exponential fit in the plot is perfect, with a correlation factor of $R^2 = 0.9967$, and an exponential decay coefficient of $1/\mu = 0.9799$ mm. With these results, with a decaying exponential behavior, we conclude that the collimated transmittance setup is well settle.

After the tests for collimated transmittance, we performed reliability measurements for IAD method. We used the same system of spherical particles as before, with the same parameters. The results of the optical parameters computed by the IAD method were compared with theoretical results for Mie scattering [136] [113]. Table III.3 shows all obtained results. To get the value of M_U we used the exponential fit from plot in Figure III.12, and the IAD values of μ'_s , μ_a and g . This result proves the auto-consistency of the method. We got a good adjustment between theory and experiments. The percentage deviation among them is 9.2 % (Mie-IAD), and 6 % (Mie- M_U).

The tests have proven that the experimental setup in combination with the IAD method, are reliable to get the optical parameters of the liquid samples we are interested on, to perform DWS.

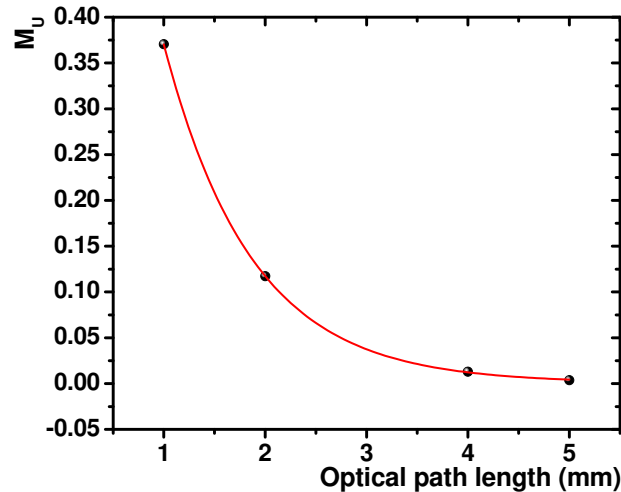


Figure III.12 Collimated transmittance plot for different optical path length in the cuvettes. A suspension of polystyrene spherical particles (800 nm) was used. The line represents an exponential fit.

| Microspheres | l^* (mm) | l_a (mm) | g |
|--------------|------------|------------|--------|
| IAD | 10.8120 | 75.2445 | 0.9116 |
| Mie theory | 11.9492 | | 0.9166 |
| M_U (fit) | 11.2311 | | |

Table III.3 IAD tests results in comparison with Mie theory and collimated transmittance (Beer-Lambert law) which proves auto-consistency of all measurements.

4.1.3. Light absorption

Other experimental tests with samples with absorption of light are necessary to corroborate the validity of IAD. We tried with different suspensions of spherical polystyrene particles (diameter = 2 μm) at a fill fraction of $\phi = 0.030$, and with solutions of PBPEO45 diblock copolymer (1,4 poly(1,3-butadiene)–polyethylene oxide), prepared at concentrations of 1 wt%, 1.5 wt%, 1.7 wt% and 2 wt%. Above 2.5 wt% phase separation was found. The followed procedure was the same followed in [111]. Indian ink is added (previous tests confirm that at high dilution, indian ink do not scatters light, but just has absorption effects) diluted up to a 1 vol% of the original concentration when purchased. The ink was added in 3 ml suspension of the corresponding sample, in aliquots of 5 μl for each measurement, up to 45 μl , to ensure on the one hand that $l_a/l^* \geq 30$, and on other hand that $9 \leq L/l^* \leq 25$. Both values permit the applicability of the theory of diffusion of light within the sample. The first value refers whether the quantity of absorption agent is too much. In that case the light paths can be attenuated more than sufficient, provoking a lack of scattering events and consequently a lack of diffusing light beams. The second relation refers to the number of scattering events. Whether the relation L/l^* is too small, the possibility for diffusing light beams decreases a lot, and if L/l^* is too long, the possibility of colloidal particles interacting with each other increases. In the same way, the addition of ink should not affect the value of l^* because the transport mean free path is linked just to a leakage of light by scattering events, and not to absorption.

The results for the polymer particles are shown in Figure III.13. The autocorrelation function (Figure III.13a) shows a shift to longer times due to the addition of ink. This displacement could lead to a misinterpretation of the results. Also, in Figure III.13b and c, the MSD is shown first for the case when the equation (III.3.32) is used. Once the correction for absorption is implemented (equation (III.3.35)), all MSD plots fall on the same line. A good correction is notorious because all plots lie where the MSD of the original particle suspension lies. In Figure III.13c there is a small deviation in the case of 35 μl of ink added to the sample; this is associated to the more diluted suspension due to the addition of more water (we did not take care to recalculate the final particle concentration). Even though, the agreement is satisfactory.

Before addition of ink to the PBPEO45 samples, optical parameters were obtained with the IAD method. For this system (and for PBPEO57 mentioned later) it is crucial to know the amount of light scattered by the sample before addition of probe particles. Even at very low concentration the PBPEO45 samples are opaque which is a signal of scattered light (see Figure III.14). The results after application of IAD method are shown in Table III.4 for a sample at concentration of 1.2 wt%. A cuvette of optical path length of 5 mm was used, due to the low light scattering compared to the case when particles are added.

| PBPEO45 | l^* (mm) | l_a (mm) | g |
|----------------|------------|------------|--------|
| IAD | 109.5 | 59.2 | 0.8954 |
| M_U | 91.17 | | |

Table III.4 Optical parameters for PBPEO45 obtained with the IAD method and collimated transmittance.

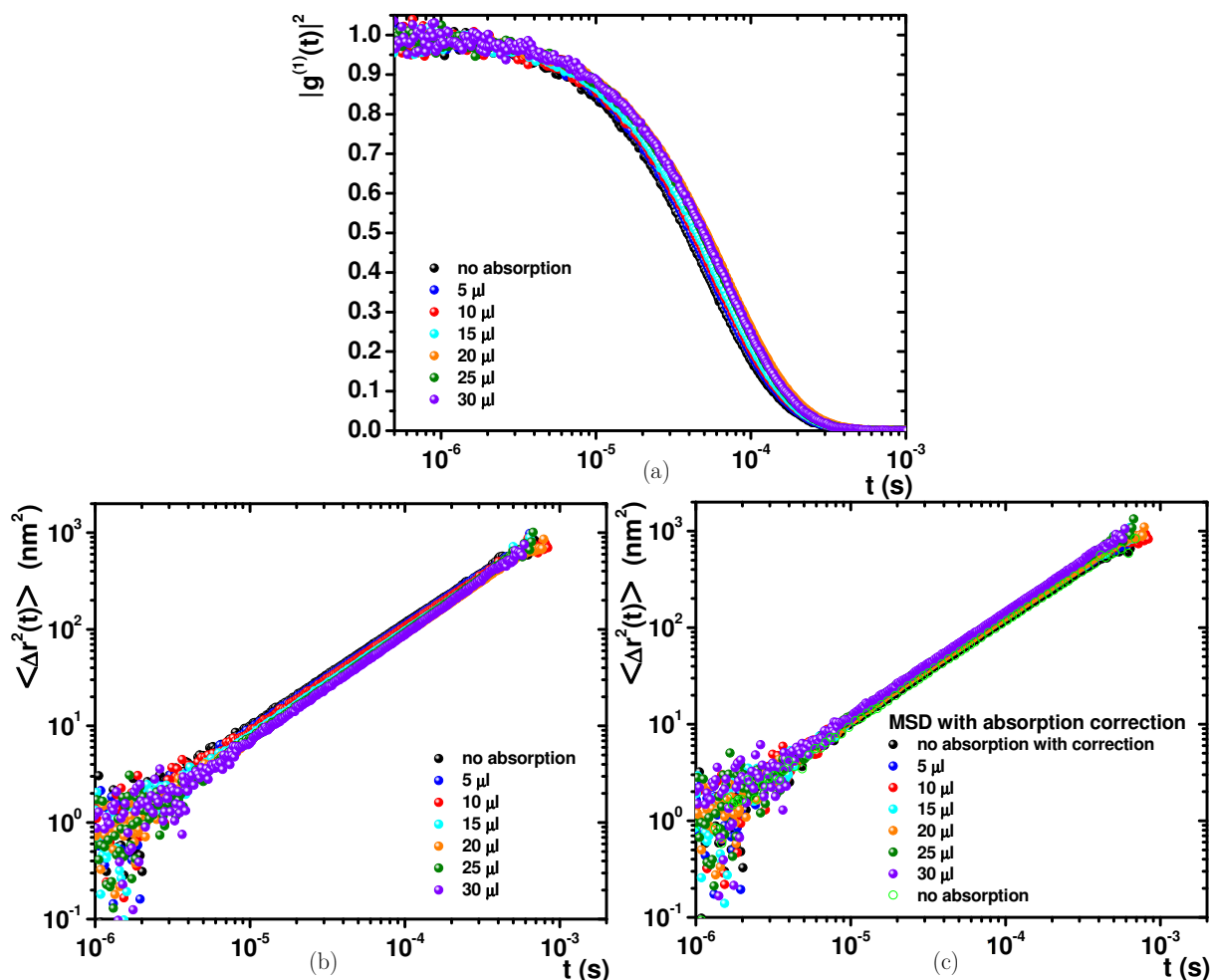


Figure III.13 (a) Autocorrelation functions, adding an agent with absorption every time. It is evident a small shift to the right side. (b) Mean square displacement for different concentration of added absorbent agent. The shift to longer times is more evident at short times. (c) Mean square displacement corrected for absorption. All plots overlap on the plot with no absorption. For comparison it was added a corrected plot with no ink added.

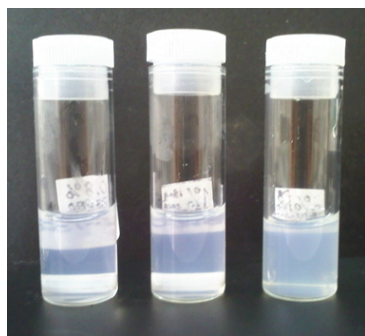


Figure III.14 PBPEO45 samples at concentrations of 1 wt%.

According to the results, the sample presents more absorption of light rather than scattering. Also, the transport mean free path is three orders of magnitude longer than the transport mean free path values of typical particle concentrations used in DWS. Therefore, it is possible to make DWS experiments with a neglected contribution of scattered light by the PBPEO45.

After IAD measurements for PBPEO45, probe particles are added (diameter = 2 μm , $\phi = 0.030$), and indian ink as well. The results for PBPEO45 concentrations of 1.5 wt% and 2 wt% are shown in Figure III.15 and Figure III.16 respectively. In all cases, including the ones not shown for concentrations of 1 wt% and 1.7 wt%, the correction for absorption is well enough. The results are satisfactory compared to the case shown in [111], where ~ 100 nm particles were

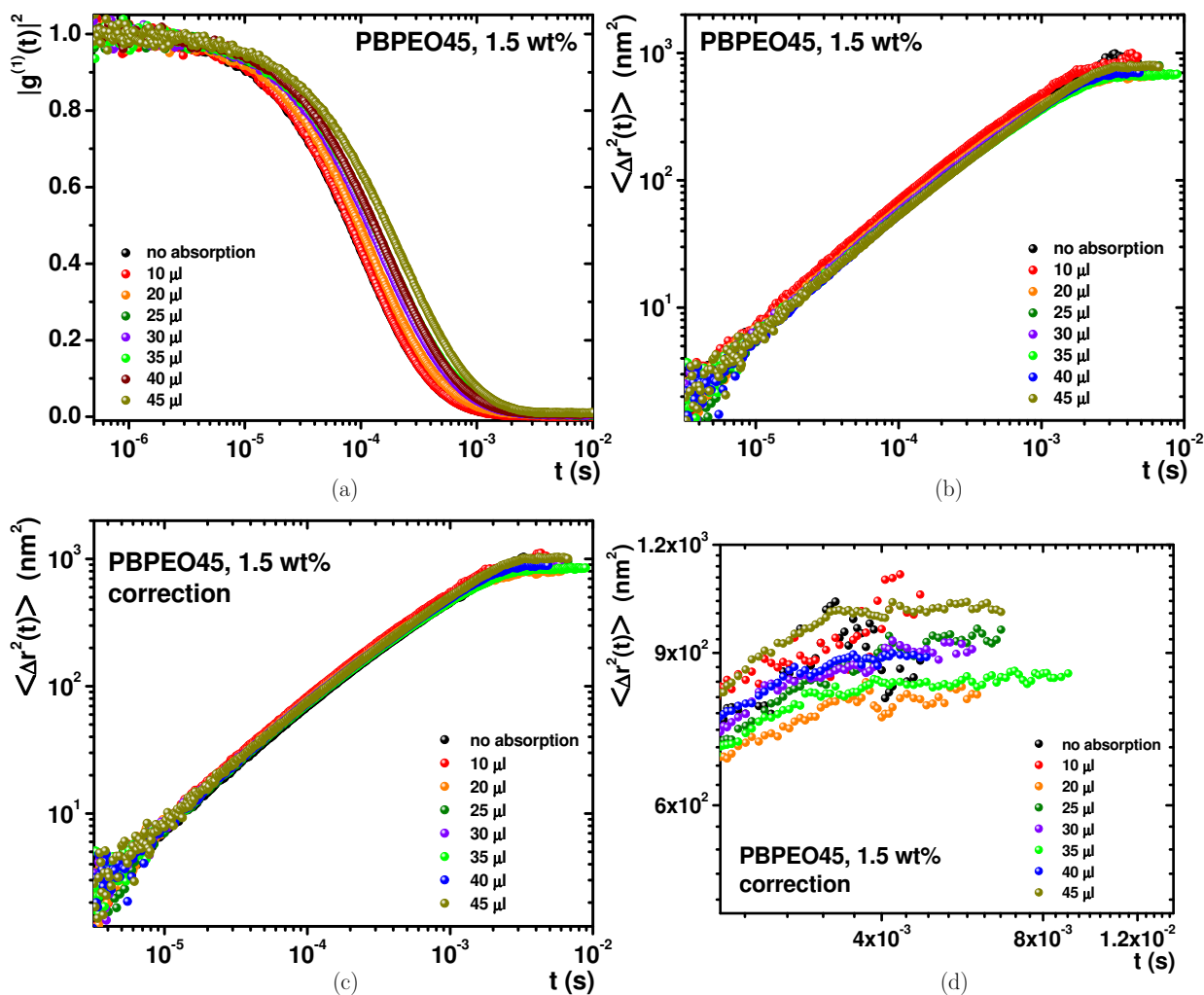


Figure III.15 Results for PBPEO45 at 1.5 wt%, adding indian ink. (a) Autocorrelation function where each curve is for a different ink concentration. (b) MSD for different ink concentrations with no absorption correction. (c) MSD with absorption correction for all different ink concentrations. (d) A zoom in at longer times found in the MSD corrected for absorption. Here it is notorious a longer curve when 35 μl of ink are added.

used. In that case, the shift to longer times with the addition of ink is more pronounced, probably due to the isotropic scattering of light by particles of those sizes (Rayleigh regime). Figure III.15d and Figure III.16d also show plots where an extension of the MSD is obtained to longer times, when the plots have been corrected. This is an effect of the attenuation of longer paths of light within the sample. In the case of ~ 100 nm the extension to longer times is more evident, reaching an extension of almost an order of magnitude. Thus, the preferred scattering direction of light contributes to this phenomenon. Further research in this direction is underway.

Figure III.17 presents the variation of l^* in terms of l_a for the four PBPEO45 analyzed concentrations. l^* values are almost constant in all cases, but with a tendency to increase towards the addition of more ink. This behavior is normal because we always used the same sample with each addition of ink, and we did not recalculate and correct the real fill fraction of particles. The dashed line refers to the theoretical value of $l^* = 150 \mu\text{m}$, which varies from experimental values because sedimentation of particles is fast in this low viscous samples. Error bars represent the maximum and minimum l^* measured values before and after DWS experiments.

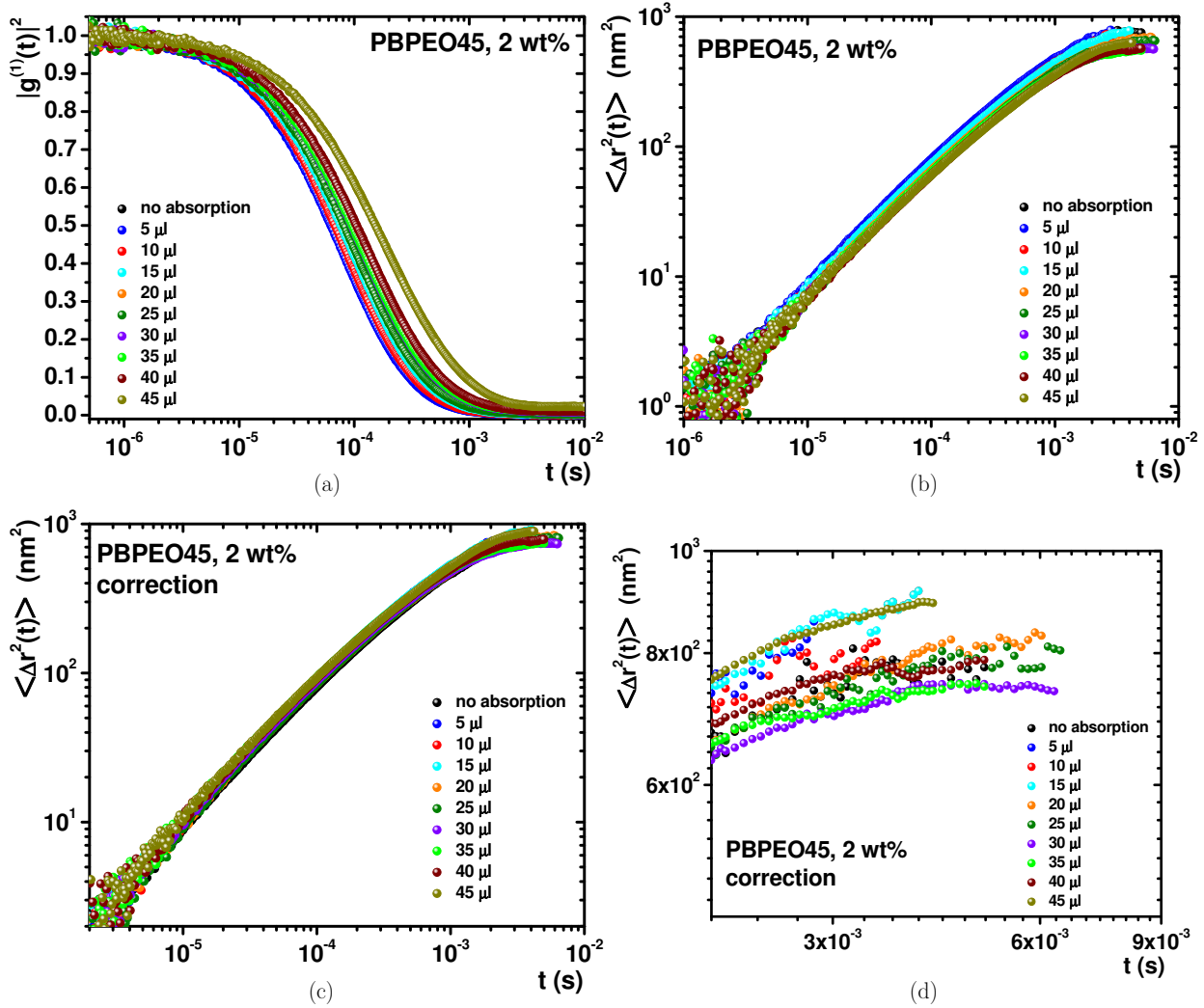


Figure III.16 Results for PBPEO45 at 2 wt%, adding indian ink. (a) Autocorrelation function where each curve is for a different ink concentration. (b) MSD for different ink concentrations with no absorption correction. (c) MSD with absorption correction for all different ink concentrations. (d) A zoom in at longer times found in the MSD corrected for absorption. Here it is notorious a longer curve when 25 and 30 μl of ink are added.

Figure III.18 shows the variation of L/l^* as a function of l_a/l^* . The fact of being within the valid range for the diffusion of light approach was always taken care of. The shadowed region is the allowed to keep $\sim 9 \leq L/l^* \leq 25$. Above the vertical line we keep $l_a/l^* \geq 30$.

All successful results presented are as expected, in accordance with [111]. These allowed us to continue with other DWS experiments after applying the IAD method.

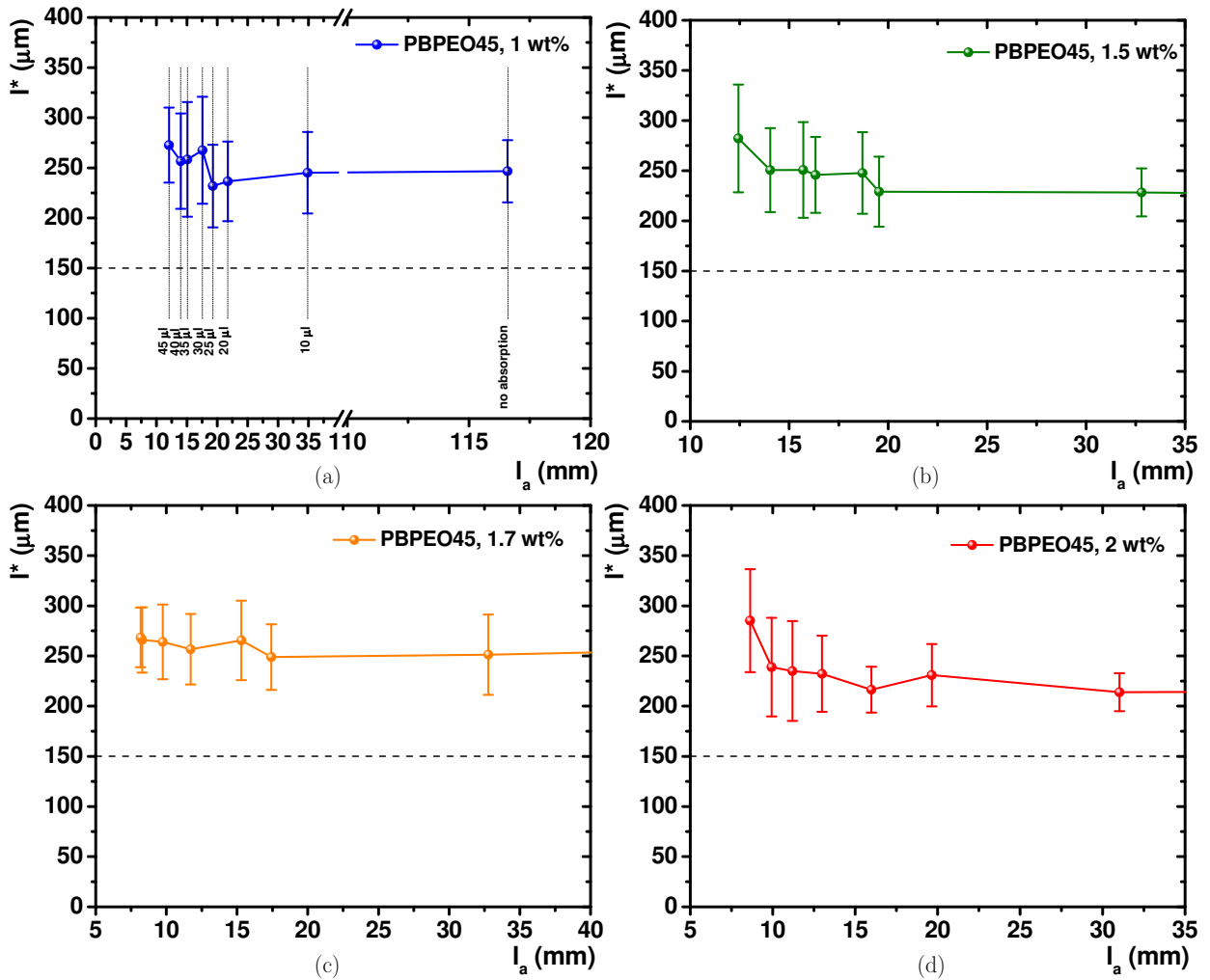


Figure III.17 Variation of l^* in terms of l_a for the four PBPEO45 analyzed concentrations. (a) Shows concentration of 1 wt% and indicates the quantities of ink added. All other plots emphasize the l_a values with just added ink, in correspondence to the ink added values indicated in (a). (b) Concentration of 1.5 wt%, (c) concentration of 1.7 wt%, and (d) concentration of 2 wt%. Dashed lines refer the theoretical value of $l^* = 150 \mu\text{m}$. Error bars include the maximum and minimum value of measured l^* .

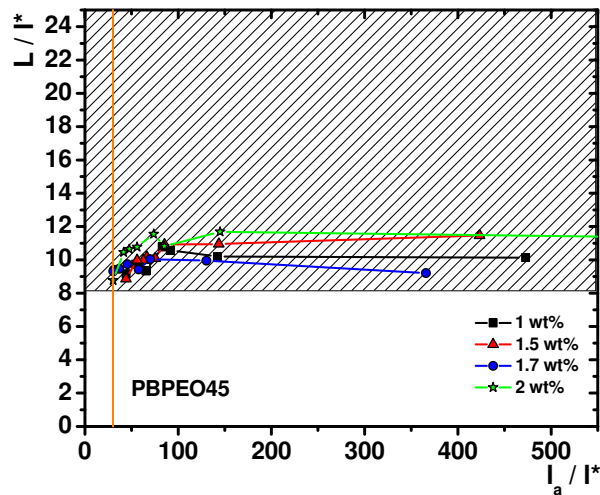


Figure III.18 Variation of L/l^* as a function of l_a/l^* . The shadowed region comprises the valid values for L/l^* . The vertical line is the minimum limit for allowed values of l_a/l^* in order to maintain the experiment within the diffusion approximation.

4.2. Small Angle Neutron Scattering (SANS)

SANS involves the basic four steps used in all scattering techniques: monochromatization, collimation, scattering and detection. Monochromatization is performed mostly using a velocity selector. Collimation is performed through the use of two apertures (a source aperture and a sample aperture) placed far (meters) apart. Scattering is performed from either liquid or solid samples. Detection is performed using a neutron area detector inside an evacuated scattering vessel.

A general scheme of the experiment is shown in Figure III.19, taken from [128]. The large collimation and scattering distances make SANS instruments very large (typically 30 m long) compared to other scattering instruments [128]. SANS facilities could have a distance of ~ 15 m from the source to the sample, and an additional distance of ~ 13 m from the sample to the detector; while for SAXS experiments, if the experimental line is not a synchrotron, distances could be ~ 3 m, from source to detector, limiting the achievable low- q values. Every SANS experiment begins with the choice of one (or more) instrument configurations to be measured. Decisions are made based on the characteristic features of the investigated system (characteristic sizes and scattering level). A program is used to simulate configurations by choosing a neutron wavelength and wavelength spread, source and sample aperture sizes, source-to-sample and sample-to-detector distances. The q range, neutron beam current and beamstop size are obtained for each configuration.

For our research, SANS measurements were performed within the NG7 SANS beamline at the NIST Center for Neutron Research (NCNR) at the National Institute of Standards and Technology (Gaithersburg, MD, USA). A broad scattering vector range was set at various neutron wavelengths with three sample-detector distances: 1 m, 4 m and 13 m with eight, four, and one beam guides, respectively; $\Delta\lambda/\lambda = 0.12$, where λ is the neutron wavelength. The PBPEO samples (which will be detailed in Chapter IV) were measured in titanium cells (2 nm path length with quartz windows) at a constant temperature of 20 °C. The scattering data were averaged over 2000 s.

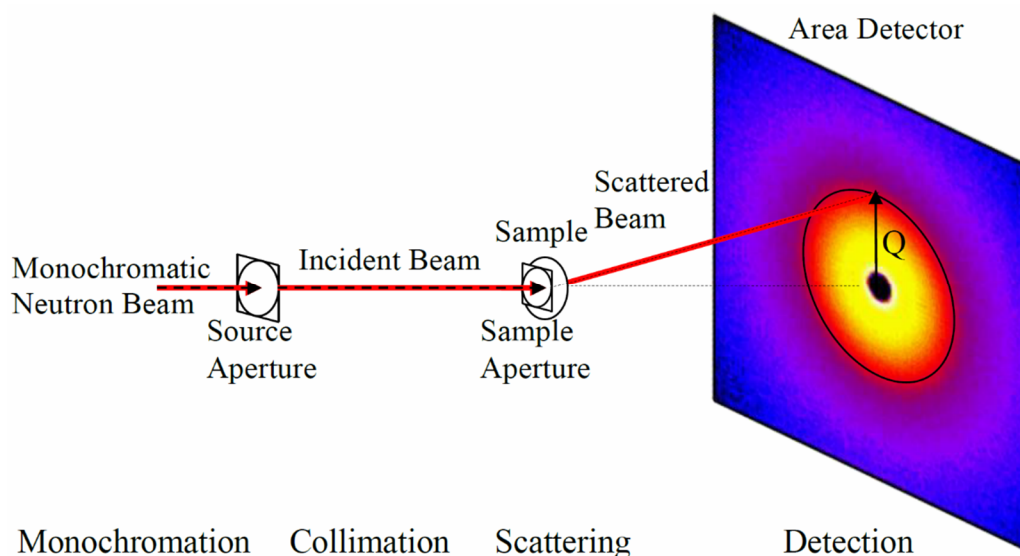


Figure III.19 Schematics of the SANS technique. It is not to scale with vertical sizes in centimeters whereas horizontal distances are in meters. Taken from [128].

Raw data is obtained in a 2D detector (as is shown in Figure III.19, with the circular scattering pattern), collecting all scattered neutrons subtending a solid angle. This 2D information is reduced to a 1D typical $I(q)$ vs. q pattern. Using the neutron beam counts $I_0(\lambda)$ (empty beam transmission), the scattering intensity is scaled to an absolute cross section (units of cm^{-1}) as $d \sum(q)/d\Omega = I(q)/(I_0(\lambda)T(\lambda)d\Delta\Omega)$, where T , d and $\Delta\Omega$ are the sample transmission, thickness and solid angle subtending one detector cell, respectively. SANS data in peripheral detector cells and those close to the beamstop are masked out in order to keep only the reliable data. Then the 2D corrected and scaled data are radially averaged to produce the 1D data. Circular binning is the norm for isotropic scattering. Sector or rectangular averaging is used for scattering with anisotropic features [128].

Data is reduced and then analyzed using the Igor Pro SANS software according to standard methods [137]. Finally, all data were corrected for detector response characteristics before their analysis.

IV. Experimental results

1. PBPEO worm-like micelles

1.1. Motivation and purpose

It was mentioned in Chapter II, in the section devoted to block copolymer worm-like micelles, a recent study of the PBPEO45 (1,4 poly(1,3-butadiene)–polyethylene oxide diblock copolymer) in water, with a degree of polymerization $m = 37$ for the PB block and $n = 45$ for the PEO block. Still, there are some open questions related to the structure and rheological behavior of this system. This former work was limited to low concentrations of diblock copolymer in solution to avoid a phase separation, and microrheology was never performed to analyze the possibility of a Maxwellian behavior. Also, the form factor obtained with SAXS was limited to not so small values of q , so only information about the cross section of the WLMs was obtained, and an insight of cylindrical structures was extracted. Additionally, a comparison with a common surfactant made WLMs, and with another 1,4 poly(1,3-butadiene)–polyethylene oxide copolymer with a different degree of polymerization is needed to understand the self-assembly processes involved in the formation of this kind of WLMs.

The main purpose is to present: (1) the rheology and microrheology of water solutions embedded with self-assembly aggregates of a PBPEO diblock copolymer, where the PB block is rich in 1,4-microstructure, and with the same degree of polymerization of the PB block in the PBPEO45, but with the PEO block larger, i.e., with a degree of polymerization $n = 57$. This will be called PBPEO57, and as seen below, this system also self-assembles in WLMs; (2) the microrheology of the micellar solution of PBPEO45; and (3) a comparison for the first time of the rheological behavior at a high frequency of both micellar solutions with those of conventional surfactants. The concentration of PBPEO57 (C_{PBPEO57} in wt%) was limited in this study to $C_{\text{PBPEO57}} \leq 9$ wt% to avoid a phase separation. The rheology of the aqueous solution of PBPEO57 in water was determined, i.e., flow curves and the viscoelastic spectra at different polymer concentrations. To apply local rheological measurements (microrheology), the mean square displacement (MSD) of particles embedded in the micellar solutions under study was determined using diffusive wave spectroscopy (DWS). From the MSD, the high-frequency complex modulus $G^*(\omega)$ was obtained.

1.2. Specific goals

The questions that we would like to answer in this study are: can we obtain structural information about the systems of interest here from the microrheology results? Moreover, is the stress relaxation observed by the rheology and microrheology notably modified when PEO size is increased? Before making these measurements, there is a need to determine the morphology of the self-assembled structures in the PBPEO57 solution. We used small angle neutron scattering (SANS), and we observed them with negative staining using a low energy transmission electron microscope in a

scanning microscope (STEM-in-SEM). To complete this report, we included the SANS scattering for the PBPEO45 micellar solution.

The work was recently published in *Soft Matter* [138]: A. Tavera-Vázquez, B. Arenas-Gómez, C. Garza, Y. Liu and R. Castillo, "Structure, rheology, and microrheology of wormlike micelles made of PB-PEO diblock copolymers," *Soft Matter*, vol. 14, pp. 7264-7276, 2018. B. Arenas-Gómez performed the SANS experiments and C. Garza prepared the samples for SEM images.

1.3. Materials and sample preparation

PBPEO57 and PBPEO45 were purchased from Polymer Source (Canada); they were used as received. Data given by the manufacturer for PBPEO57: $m = 37$, $n = 57$, $M_w = 4500 \text{ g Mol}^{-1}$, 2000-*b*-2500, PB block rich in 1,4 microstructure $> 85 \text{ wt}\%$, $M_w/M_n = 1.08$, *trans/cis* ratio $\sim 40/60$. For PBPEO45: $m = 37$, $n = 45$, $M_w = 4000 \text{ g Mol}^{-1}$, 2000-*b*-2000, PB block rich in 1,4 microstructure $> 93 \text{ wt}\%$, $M_w/M_n = 1.08$, *trans/cis* ratio $\sim 27/68$, and 1,2 microstructure $\sim 5 \text{ wt}\%$. Water was deionized (Nanopure-UV, USA; resistivity $\sim 18.3 \text{ M}\Omega \text{ cm}$). $2 \mu\text{m}$ tracer microspheres for DWS experiments are made of plain polystyrene (Bangs Laboratories, Inc.); they are negatively charged in pure water due to the negatively-charged sulfate groups that populate the surface of the plain polystyrene beads.

Sample preparation. PBPEO stock water solutions were prepared by weight and stirred for 14 days at $40 \text{ }^\circ\text{C}$ before use. No phase separation was observed for both systems; up to $C_{\text{PBPEO57}} = 9 \text{ wt}\%$ and up to $C_{\text{PBPEO45}} = 2.5 \text{ wt}\%$. Above these limits, phase coexistence appeared with one birefringent phase at rest, presumably a lamellar phase. For that reason, we studied samples of PBPEO57 at $C_{\text{PBPEO57}} = 1, 1.7, 2, 3, 4, 5, 6$ and $7 \text{ wt}\%$, and for PBPEO45 at $C_{\text{PBPEO45}} = 1, 1.5, 1.7$ and $2 \text{ wt}\%$.

Rheology. Measurements were carried out in a MCR 702-TwinDrive rheometer (Anton Paar, Austria). Flow curves and oscillatory measurements were performed using a cone-plate geometry (2° ; diameter = 40 mm). Samples were allowed to relax before measurements. Experiments were performed at $20 \text{ }^\circ\text{C}$.

DWS. Solutions with a polymer concentration slightly above the desired concentration to be measured were prepared. Then, $2 \mu\text{m}$ polystyrene microspheres in water suspension ($10.17 \text{ wt}\%$) were added while the samples were stirred; the final particle volume fraction was $\phi = 0.03$. Stirring was maintained for 20 min to ensure a homogeneous dispersion. Sample sonication must be avoided to prevent breaking of the polymer chains. Final studied diblock copolymer concentrations were the same as for mechanical rheology, for both copolymers. Samples were allowed to relax and thermalize at $20 \text{ }^\circ\text{C}$ in rectangular cuvettes of a light path thickness of 2.5 mm , for 10 min, because the samples have low viscosity and they are prone to particle sedimentation. Typical acquiring times are around 600 s to 900 s , enough sampling time due to the fast relaxation of the systems under study.

Electron microscopy (SEM). We used an extreme resolution analytical field-emission scanning electron microscope (SEM; JSM-7800F JEOL Ltd. Japan) working at low electron acceleration voltages [139] on negatively stained samples of the systems under study. Low energy STEM (Scanned Transmission Electron Microscopy)-in-SEM was also employed in addition to the backscattered electrons to survey the samples. This is a powerful technique that permits imaging soft material samples with lower accelerating voltages (less than 30 kV) and larger fields of view. Standard TEM grids covered first with a collodion layer and then covered with a layer of carbon were used to deposit the specimens of the systems under study. The grid is placed over a piece of filter paper, and a few microliters drop of the diblock copolymer solution is deposited on it ($\sim 5 \mu\text{l}$). After 2 or 3 min, a drop of phosphotungstic acid (3 wt%) is subsequently added to the sample. The filter paper absorbs the excess of deposits on the grid, and the sample is dried under ambient conditions. Before placing it on the microscope, the sample was covered with a thin carbon layer to ensure that the sample on the grid is conductive.

1.4. Structure of the PBPEO aggregates

Determining the aggregate structure in a system is critical for understanding its rheological behavior. Therefore, in this section, we describe our results using SANS and SEM.

1.4.1. Small Angle Neutron Scattering

We measured the static SANS pattern for the diblock copolymer micellar solution made of PBPEO57 at $C_{\text{PBPEO57}} = 0.5 \text{ wt\%}$, dissolved in deuterated water in the dilute regime. It is presented in Figure IV.1 as a function of q (\mathbf{q} = scattering vector); for comparison, we also included the measurements for the WLM system made of PBPEO45. The scattering curves cover q values from 0.0008 to 0.2 \AA^{-1} which correspond to length scales of $2\pi/q \sim 20 - 6000 \text{ \AA}$ corresponding to systems made of small structures. In Figure IV.1a, the scattering patterns display a $\sim q^{-1}$ dependence at low q values, although a slight deviation between the scattering functions for both diblock copolymers can be observed. For PBPEO45 pattern there is observed a slight change of curvature at the very low q values, that permits a specific estimation of the persistence length of the WLMs. However, this inflection point is not observable for the case of PBPEO57, so just a lowest possible value of the persistence length can be estimated. Meanwhile, at intermediate and high q there is no significant difference. These patterns are typical of extended cylindrical structures, as previously observed with SAXS in the case of the PBPEO45 that self assembles in a core-shell cylinder [52] (see Figure II.13i). Consequently, the mean radius for both tubular structures is quite similar. The scattering window for flexible cylindrical structures usually includes the analysis of three different regions (Figure IV.1b): at low q and at intermediate q in the Guinier regions, and at high q in the Porod region [140] [141] [38]. Here, the low q Guinier region is not accessible with the present instrument configuration. At high q (Porod region), the scattering arises from the local cross section of the rod-like aggregates and the scattering patterns commonly present oscillations.

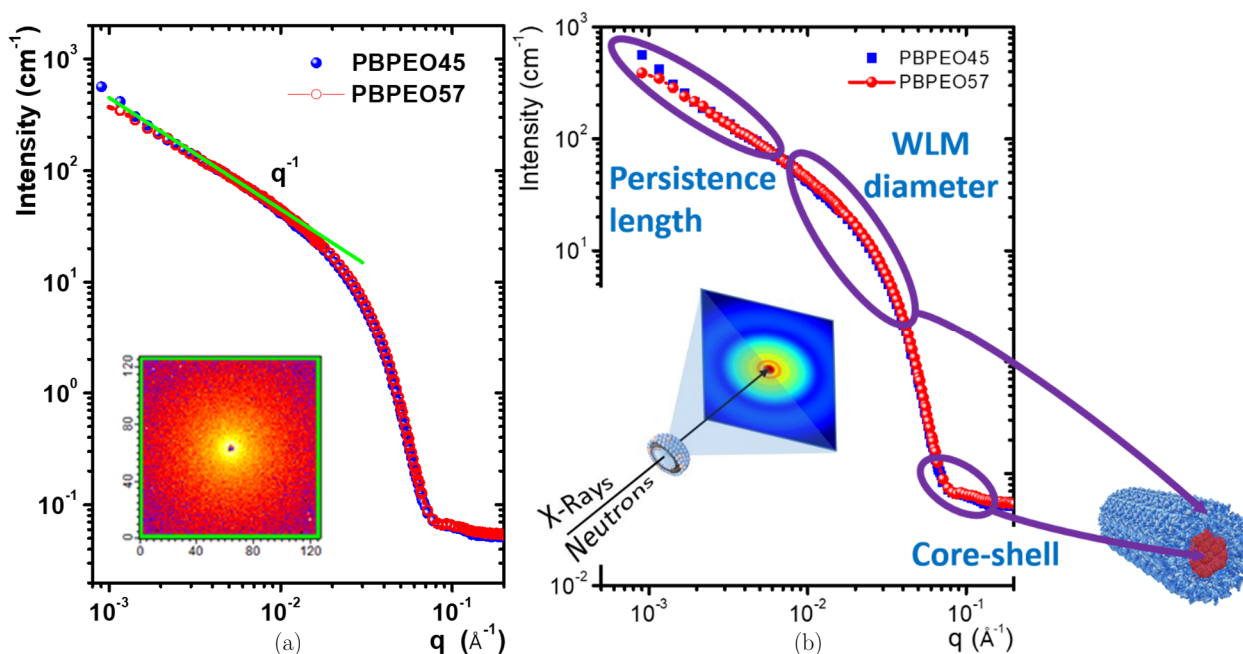


Figure IV.1 Static SANS patterns for both diblock copolymers PBPEO57 and PBPEO45 dissolved in deuterated water at 0.5 wt%. Circles, spheres and squares represent experimental data. Both plots are the same. (a) The green line is a guide to the eye which shows a power law behavior of q^{-1} , representative of a cylindrical structure. Within the plot, appears the 2D scattering pattern at the detector. (b) Different regions of the SANS pattern are shown. Each region is used to extract different structure information of the WLMs. SANS and SAXS work to extract the same information, the difference is just the achievable length scales due to the scattering angle, the contrast of material and the wavelength of the radiation.

Cross-sectional size. For cylinders at intermediate q , the scattering function can be described by $I(q)q = K\chi\exp(-q^2R_{g-cs}^2/2)$, where χ is a constant related to the size of the cylindrical aggregates, and R_{g-cs} is the cross-sectional radius of gyration. The contrast factor K is given by $K = (b_m - V_m\rho_s)^2$, where b_m is the sum of neutron scattering lengths, V_m is the volume per surfactant monomer in the micelle, and ρ_s is the scattering length density of the solvent [140] [141]. When the cross-section is circular, the cylinder radius is $R_{cs} = \sqrt{2}R_{g-cs}$ [140] [141]. Intermediate Guinier fits of our diblock copolymer systems are shown in Figure IV.2. The linearity of data indicates the extended cylindrical nature of the micelles. The fitting reveals a total cross-sectional diameter of 12.77 nm and 12.70 nm for PBPEO45 (Figure IV.2a) and PBPEO57 (Figure IV.2b), respectively. These values are summarized in Table IV.1 as all the other extracted structural values. There is no significant difference between the cross-section of both diblock copolymer WLMs. The diameter of the PBPEO45 WLMs is similar to the previous value obtained using SAXS (~ 12.4 nm) [52] (see Figure II.13i).

Core-shell structure. A core-shell cylinder model is used to fit the data for both copolymer systems to extract useful information from the intermediate and large q regions; best fits are obtained when polydispersity in the core radius is included [142]. Therefore, the resulting scattering of each particle is the scattering intensity with a specific size weighted by the polydispersity of a cylinder core, modeled with a normalized log-normal distribution.

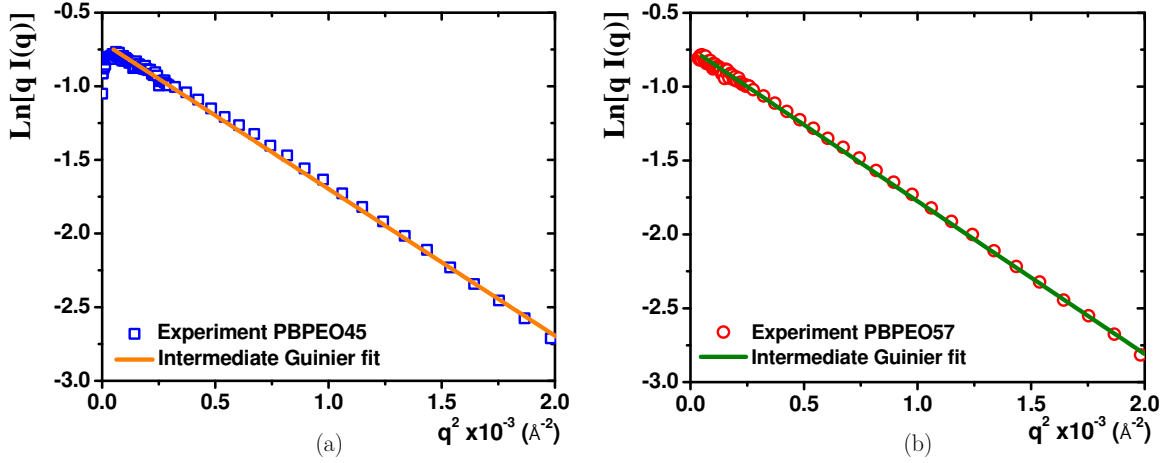


Figure IV.2 Intermediate Guinier plots for (a) PBPEO45, and (b) PBPEO57.

The fittings to the SANS patterns are presented in Figure IV.3a and b, and the calculated model parameters are in Table IV.1.

The overall intensity of the core-shell model is given by

$$I(q) = background + \frac{scale}{V_p} \sum_{R_p} n(R_p, \sigma_p) P(q, R_p, R_l, H_p, H_l, \rho_p, \rho_l, \rho_{solv}), \quad (IV.1.1)$$

where the normalized log-normal function is given by

$$n(R_p) = \frac{\exp\left[-\frac{1}{2} \left(\frac{\ln(R_p / R_o)}{\sigma_p}\right)^2\right]}{\sqrt{2\pi\sigma_p} R_p}, \quad (IV.1.2)$$

and

$$P(q) = \int_0^{\pi/2} \sin \theta \cdot d\theta \left[V_l (\rho_l - \rho_{solv}) \frac{\sin\left(\frac{qH_l \cos \theta}{2}\right)}{\frac{qH_l \cos \theta}{2}} \frac{2J_1(qH_l \sin \theta)}{qH_l \sin \theta} + V_p (\rho_p - \rho_l) \frac{\sin\left(\frac{qH_p \cos \theta}{2}\right)}{\frac{qH_p \cos \theta}{2}} \frac{2J_1(qH_p \sin \theta)}{qH_p \sin \theta} \right]^2. \quad (IV.1.3)$$

Here, $J_1(x)$ is the first order Bessel function, θ is the angle between the cylinder axis and \mathbf{q} . V_i and ρ_i refer to volumes and densities, where the subscripts $i = p, l$ and $solv$ represents parameters for core, corona and solvent, respectively. H_l is the full cylinder contour length, R_l is the full cylinder radius, H_p is the core contour length, R_p is the core radius, and R_o is the mean core radius. These variables incorporate the dimension of the bare particle, taking into account the radial thickness ($R_l = R_p + \text{radial thickness}$) and the face thickness, x , given by $2x = H_l - H_p$. σ_p is the standard

deviation of the log-normal distribution. Upon setting the scattering length density of D₂O ($\rho_{D_2O} = 6.4 \times 10^{10} \text{ cm}^{-2}$) and a relatively large polydispersity ($\sigma_p/\text{mean size value} = 0.28$), the fits show a good agreement with the SANS data (Figure IV.3a and b), although the fitting is not so good at low q , because this model does not consider cylinder flexibility. The contour length is outside the experimental resolution ($L_c \gg 1/q_{\text{min}}$) and it was set at $\sim 1 \mu\text{m}$. The data show a poor contrast at high q compared with SAXS [52]. For both systems, L_c seems to be larger than 600 nm; therefore, the aggregates are WLMs. The total diameter obtained from this fitting model differs from that deduced from the linear decrease in the intermediate Guinier fits (see Table IV.1).

| | Model | | | | |
|---------|----------------------|----------------------------------|------------------|-----------------|---------------------------------------|
| | Intermediate Guinier | Polydisperse core-shell cylinder | | | Polydisperse radius flexible cylinder |
| | Diameter | Diameter | Mean core radius | Shell thickness | Persistence length |
| PBPEO57 | 12.70 ± 0.01 | 11.42 ± 0.08 | 2.69 ± 0.01 | 3.02 ± 0.03 | > 225 |
| PBPEO45 | 12.77 ± 0.02 | 11.52 ± 0.1 | 2.64 ± 0.02 | 3.12 ± 0.03 | 141 |

Table IV.1 WLM parameters obtained with the different fitting models and errors between experimental data and models. All reported values have dimensions of nanometers.

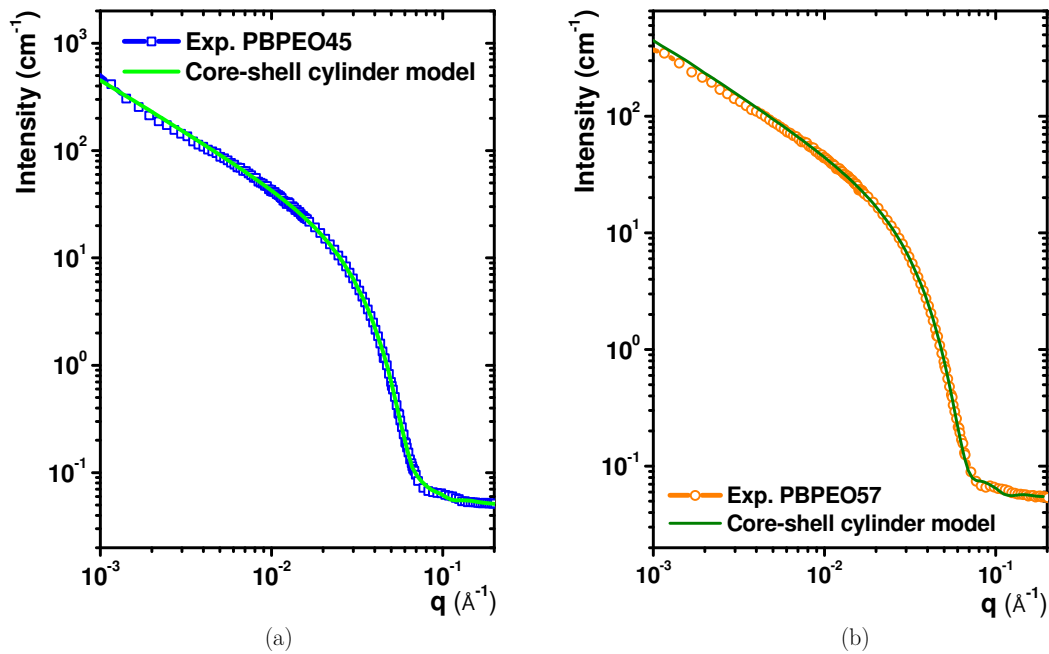


Figure IV.3 Scattering curves and fittings with the core-shell cylinder model with polydispersity in the core radius. (a) For PBPEO45 and (b) PBPEO57. Open symbols represent experimental data. Lines are the fittings to intermediate and large q regions.

WLM flexibility. At $q \sim 0.001 \text{ \AA}^{-1}$, we observe an inflection point for the PBPEO45 WLMs which is an indication of their flexibility, as it was mentioned at the beginning of the section. In contrast, PBPEO57 does not present any change in its slope (Figure IV.1). The contour length of flexible cylinders can be described as a chain of locally stiff segments of persistence length $l_p = b/2$; b is the Kuhn length. This suggests that the lengths of the stiff segments of PBPEO57 are larger than those of PBPEO45. In this low q region, we used a flexible cylinder model to fit the data to get some approximate value of l_p in these systems; see Figure IV.4a and b, and Table IV.1. For the fitting,

the form factor for a flexible cylinder with a circular cross-section and a uniform scattering length density is used [143] [144]. This model excludes volume interactions within the walk of a single cylinder. Intermicellar interactions are not included. Polydispersity is included using a Schulz distribution for the cross-section. To reduce the number of fitting parameters, we used R_{CS} (obtained from Guinier fit) and the scattering length density of D_2O . Our results indicate that WLMs of PBPEO45 are more loosely entangled than those of the PBPEO57 system. Only for the former, it was possible to estimate its persistence length ($l_p \sim 141$ nm). For the later, the flexibility effect cannot be seen in the scattering window, but it seems to be larger than 225 nm. Further studies achieving lower qs are needed to confirm these findings. A relation between the WLM hydrophobic core diameter d_c and l_p has been proposed for a series of PEO-based diblock copolymer amphiphiles [145] which scales as $l_p \sim d_c^{2.8}$. The smallest hydrophobic block used in this case was P(1,2)B45-PEO55 which has a core diameter of 14.2 nm and a persistence length ~ 500 nm. In our case, l_p does not seem to follow this relation.

An accurate comment about the ideal form factors of monodisperse systems is made. It has been known for years that they do not represent real systems as well as expected [146]. Therefore, we expect differences in the parameters obtained with different models. In rod-like systems, we already know that the cross-section form factors produce strong oscillations at high q that have been observed in the WLMs of PBPEO45 with SAXS (Figure II.13i) [52]. However, effects of low contrast, polydispersity, and instrument resolution can contribute to the smearing of the form factors; consequently, the smoothing of the real scattered intensity $I(q)$. In our SANS patterns, the oscillations are missing due to the low contrast and small diameter of the core-shell section. Introducing polydispersity in the core-shell model, we can improve the fitting to the experimental

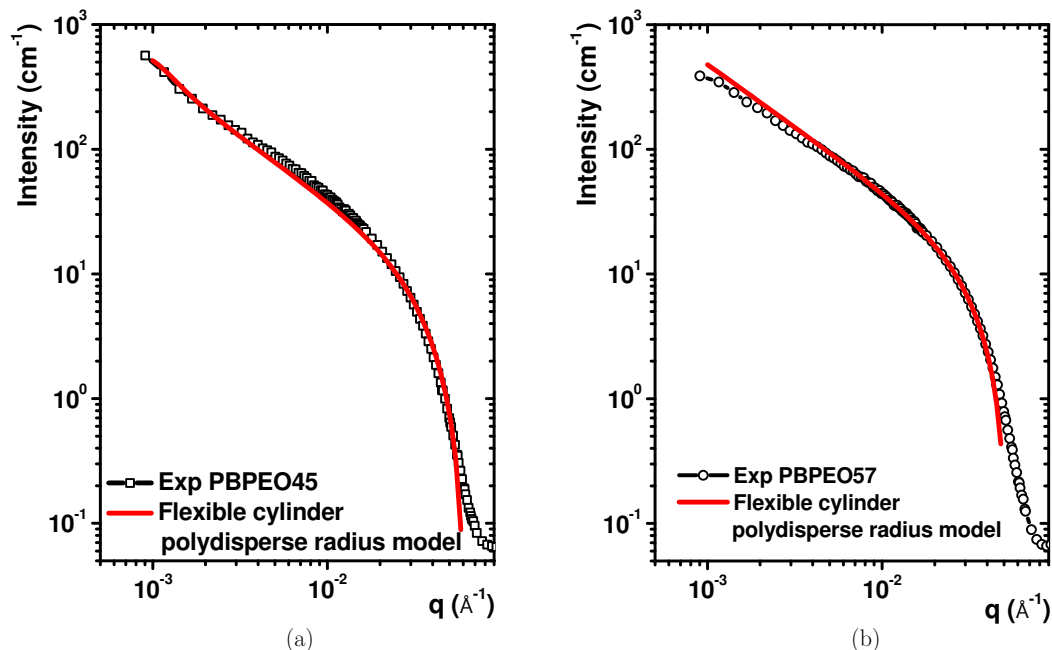


Figure IV.4 Scattering curves and fittings with the flexible cylinder radius model with polydispersity in the core radius. (a) For PBPEO45 and (b) PBPEO57. Open symbols represent experimental data. Lines are the fittings to short q regions.

patterns. The core and total radius obtained from the fitting seems to be acceptable when polydispersity is added.

Is it possible to explain the significant difference in l_p observed for the WLMs of both systems with almost identical core radius and shell thickness? Curiously, the WLMs with the larger PEO block (PBPEO57) present a shell thickness slightly smaller than in the other case. Necessarily, this block is more densely packed than in the case of PBPEO45. According to our SANS data, the hydrophilic PEO side chains are grafted to the hydrophobic PB polymer backbone as in cylindrical polymer brushes. The stiffness in this kind of polymer brushes is usually explained through a balance between repulsive forces originating from steric overcrowding of the side chains and the entropic restoring force of the main chain preferring coiled configurations [147]. In PBPEO57, any bending will harshly increase the steric overcrowding because the PEO block is already more densely packed than PBPEO45. Consequently, the bending energy is more significant for the PBPEO57 WLMs than that for the PBPEO45.

1.4.2. Direct observation with scanning electron microscopy (SEM)

Better surface information of specimens can be obtained when SEM is run at low accelerating voltages due to a more significant surface sensitivity and less beam damage, mainly because charging effects are reduced or even eliminated. Low energy (less than 30 kV) STEM (Scanning Transmission Electron Microscopy)-in-SEM was also employed in addition to the backscattered electrons to survey the samples.

Figure IV.5 presents negatively stained micrographs of dilute samples made of PBPEO57 solutions obtained by SEM; we included an image for the PBPEO45 WLM solutions. In the low energy STEM-in-SEM image of dilute samples made with the PBPEO57 solution (Figure IV.5a), a carpet of tubular structures is observed; no other kinds of structures are detected. We cannot estimate the total contour of the tubular structures, but we observe thread like segments of a length of ~ 100 to 200 nm with an average diameter of ~ 11.4 nm. For the same system, Figure IV.5b shows the same type of microstructure observed with backscattering electrons. For comparison, Figure IV.5c presents an image also obtained with backscattered electrons for the PBPEO45 WLM solution that agrees with the tubular micellar structure obtained with SAXS experiments [52]. This image shows the same kind of microstructure of the PBPEO57 solution, but more entangled. From these results, negative staining in conjunction with SEM and STEM-in-SEM is an easy and fast method to obtain the microstructure in this kind of micellar solutions, simpler than cryo-TEM.

At rest, dilute solutions of both diblock copolymers are not birefringent. However, as seen in Figure IV.6, birefringence appears with shearing which is a typical behavior of WLM solutions. This is another insight that we have WLM aggregates.

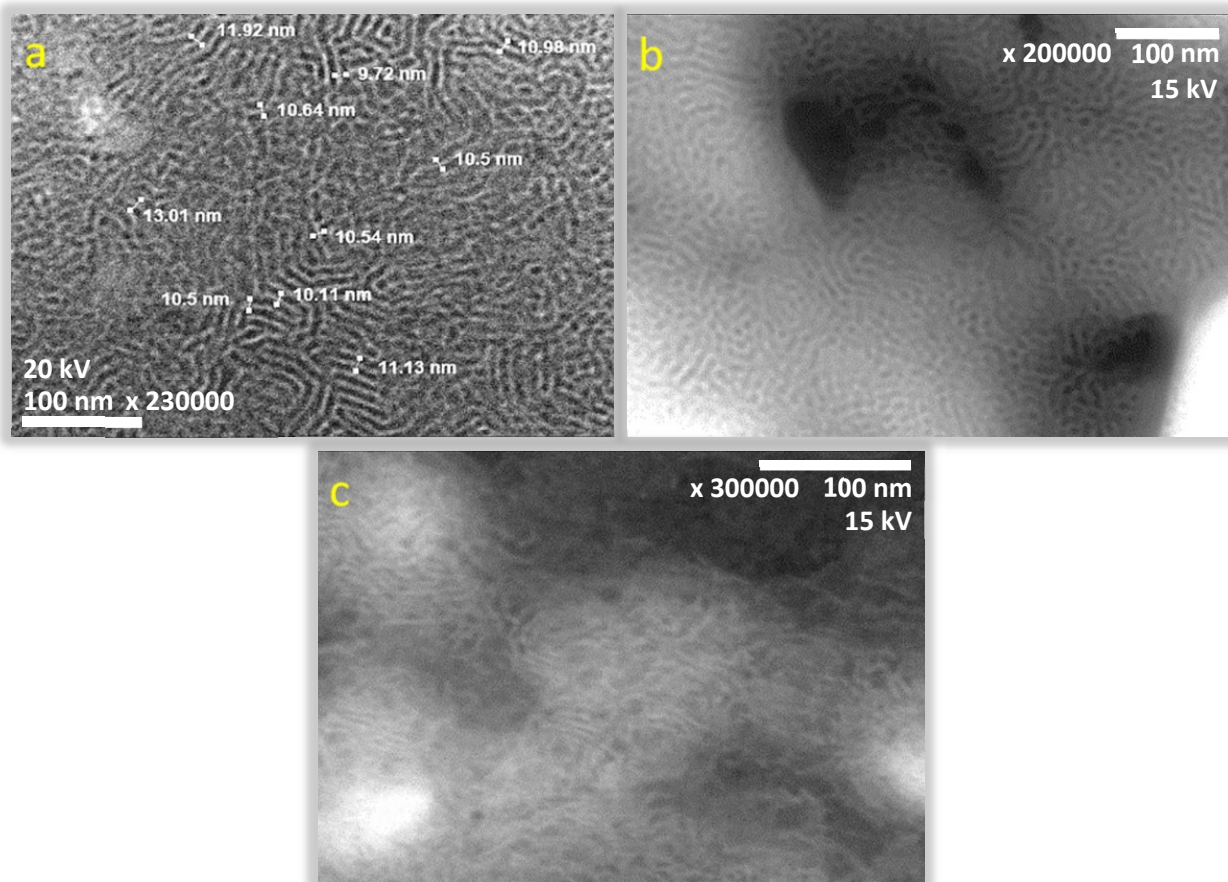


Figure IV.5 Direct observation of WLMs made of PBPEO57 ($C_{\text{PBPEO57}} = 1.1 \text{ wt\%}$): (a) STEM-in-SEM at 20 kV and (b) backscattered electrons at 15 kV, and for comparison (c) backscattered electron images for WLMs made of PBPEO45 at 15 kV ($C_{\text{PBPEO45}} = 0.6 \text{ wt\%}$).

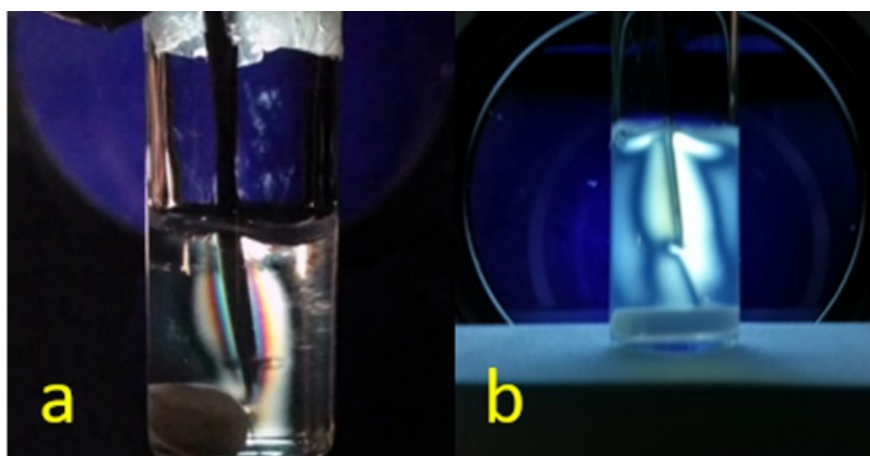


Figure IV.6 Micellar solutions between cross polarizers under shearing when a spatula is slowly dipped into the fluid; (a) PBPEO57 at $C_{\text{PBPEO57}} = 5 \text{ wt\%}$. (b) PBPEO45 at $C_{\text{PBPEO45}} = 2.5 \text{ wt\%}$.

1.5. Rheology results

Flow curves. Figure IV.7a presents flow curves obtained by increasing the applied shear strain rate (logarithmic ramp) to the PBPEO57 micellar solutions, at different concentrations and $T = 20\text{ }^\circ\text{C}$. These sweeps were performed approximately along five orders of magnitude in $\dot{\gamma}$. Shear stress increases in a nonlinear way. Although relatively concentrated PBPEO57 solutions present an important change of curvature in the σ vs. $\dot{\gamma}$ curves at $\dot{\gamma} \sim 1\text{ s}^{-1}$, they do not present a clear plateau zone. For comparison, we included a flow curve for a micellar solution of PBPEO45 at $C_{\text{PBPEO45}} = 2\text{ wt}\%$ which presents a clear plateau-like zone, which is typical of semidilute WLM solutions ($c > c^*$). In contrast with conventional surfactants, before reaching the plateau-like region, in both cases, they do not present a shear thickening peak on the up-shear curve.

Viscosity. Figure IV.7b presents the apparent viscosities $\eta(\dot{\gamma})$ for the PBPEO57 system determined with the measurements shown in Figure IV.7a. The viscosity curves move upward as concentration increases. Viscosity values decrease several orders of magnitude and viscosity shear-thins as $\dot{\gamma}$ increases. At low concentrations ($C_{\text{PBPEO57}} \leq 3\text{ wt}\%$), viscosity shear-thins in two steps. As determined using SANS, the system is made of WLMs; then once the system is sheared, the flow also tends to align the rod-shaped micelles along the fluid flow direction dropping the energy dissipation as in paranematic phases and as a consequence, viscosity decays dramatically. From the analysis of $\log \left[\lim_{\dot{\gamma} \rightarrow 0} \eta(\dot{\gamma}) \right]$ vs. C_{PBPEO57} , a change of behavior is observed at $\sim 0.8\text{ wt}\%$ (not shown), that is $C_{\text{PBPEO57}}^* \sim 0.8\text{ wt}\%$. This value is slightly larger than in the case of the micellar solution of PBPEO45 where $C_{\text{PBPEO45}}^* \sim 0.6\text{ wt}\%$ [148]. Below this concentration, the interaction between micelles is apparently negligible, as in the dilute regime, where viscosity is low and relatively close to the solvent viscosity. Above this concentration, the micelles apparently start to entangle because viscosity increases drastically.

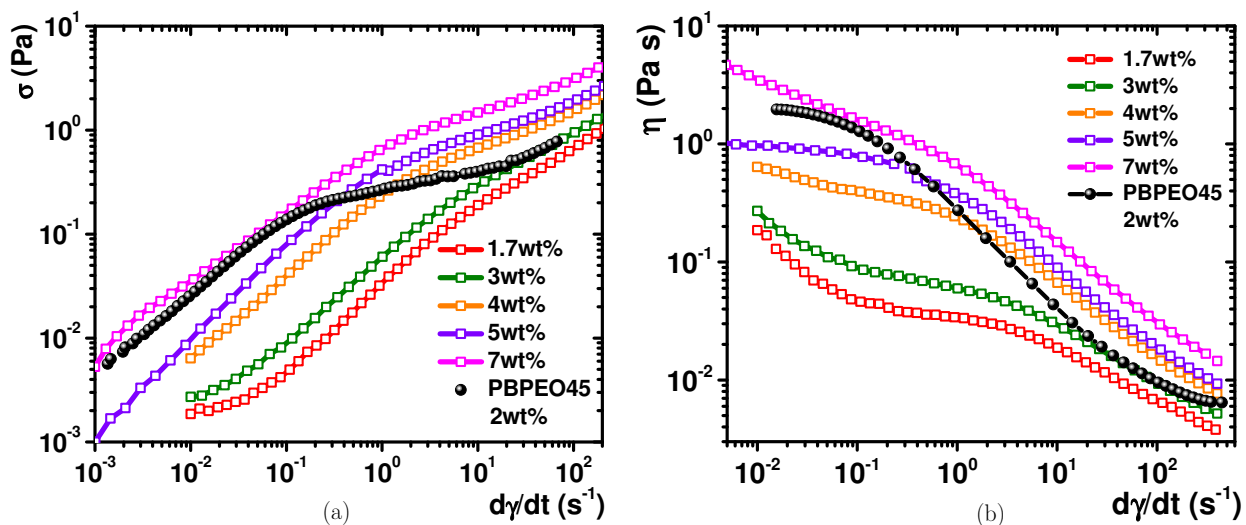


Figure IV.7 (a) σ vs. $\dot{\gamma}$ curves for micellar solutions of PBPEO57 at different concentrations (open symbols). (b) Viscosity curves for micellar solutions of PBPEO57 at different concentrations (open symbols). For comparison, we also included in both figures the micellar solution of PBPEO45 at 2 wt% (full black symbols).

Viscoelastic spectra. In WLM solutions the shear modulus, $G(t)$, exhibits a time or frequency dependence. The latter is expressed through the complex modulus $G^*(\omega) = G'(\omega) + iG''(\omega)$ (equation (III.1.20)) which are related through the Fourier transform (equation (III.1.21)). The real part of the complex modulus is the storage or elastic modulus in phase with the applied shear strain, γ . The imaginary part is the viscous or loss modulus in phase with the shear rate, $\dot{\gamma}$. Figure IV.8a presents the viscoelastic spectra of the micellar solution for different PBPEO57 concentration, at low and intermediate frequencies (for comparison, recall the viscoelastic spectra for PBPEO45, shown in Figure II.13ii). In general, the solutions are more viscous at low frequencies, and at larger frequencies, after the crossing point between $G'(\omega)$ and $G''(\omega)$ curves, the solutions are more elastic. G_0 , defined at the crossing point, (ω_0, G_0) , is relatively constant between 0.4 and 0.7 Pa for all concentrations. This value is larger than for the micelles made of PBPEO45 (~ 0.18 Pa at $C_{\text{PBPEO45}} = 2.5$ wt% and other similar WLMs made of P(1,2)B PEO (~ 0.25 Pa) [149]. Our G_0 values are also lower than those for conventional surfactants where their G_0 is in the range of 1 to 1000 Pa. The crossover frequency, ω_0 , decreases as the concentration increases. Inversely related, the relaxation time $\tau = \omega_0^{-1}$ increases as concentration increases. Figure IV.8b presents a Cole–Cole plot of G''/G_0 vs. G'/G_0 for the solutions. As shown in this figure, there is no way for obtaining a semicircular fitting at low and intermediate frequencies at any concentration; this is a necessary condition for Maxwellian behavior usually followed by WLM solutions. Although this system forms WLMs as shown above, this unusual behavior could be explained because of the impediment of any micellar rearrangement, namely polymer exchange between micelles or breaking and recombination mechanisms, due to the extremely high hydrophobicity of the PB; the system is arrested. As previously reported, this behavior is also found in the PBPEO45 [52]. I mentioned such phenomenon earlier in this work. Maxwellian behavior in WLMs is explained because local stress relaxes through a combination of reptation and breaking/recombination mechanisms (see Chapter II. Section devoted to living polymers) [20]; the characteristic relaxation time of the latter process is quite short with respect to the former, ($\tau_b \lesssim \tau_d$). Therefore, the relaxation modulus is characterized by just one relaxation time (equation (II.6.1)), which is the geometric mean of the relaxation times of both mechanisms (equation (II.6.3)) [20]. $G(t)$ decaying as a single exponential does not describe the system under study. If $G^*(\omega)$ is calculated for the case where $G(t) \sim \exp[-(t/\tau)^{1/2}]$, it corresponds to an intermediate case where the characteristic time τ considers reptation and breaking/recombination of the same order of magnitude. Here, the fitting to the experimental data in the Cole–Cole plot is not good as can be observed in Figure IV.9b. However, if $G^*(\omega)$ is calculated with the corresponding equation (II.5.6), to the power of 1/4 which is the case where stress just relaxes through reptation as in conventional polymers, (limit case when $\tau_b \rightarrow \infty$) the fitting to the experimental $G'(\omega)$ and $G''(\omega)$ curves is quite good for several orders of magnitude as observed in Figure IV.9a and b. This case corresponds to micelles that do not break and reform, in contrast to Maxwellian fluids; they are completely frozen as in the case of chemically bonded polymers.

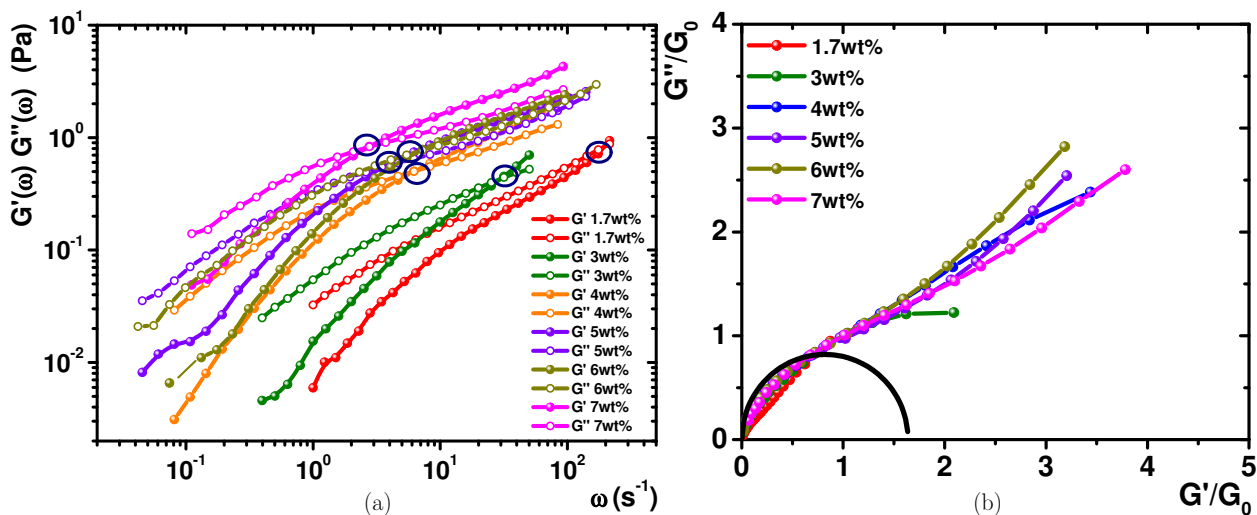


Figure IV.8 (a) Elastic and viscous moduli as given by mechanical rheology for the PBPEO57 micellar solution at different concentrations. Full symbols are the storage moduli and open symbols are the loss moduli. (b) A Cole-Cole plot for the PBPEO57 WLMs solution showing that it is not a Maxwellian fluid (black semi circumference).

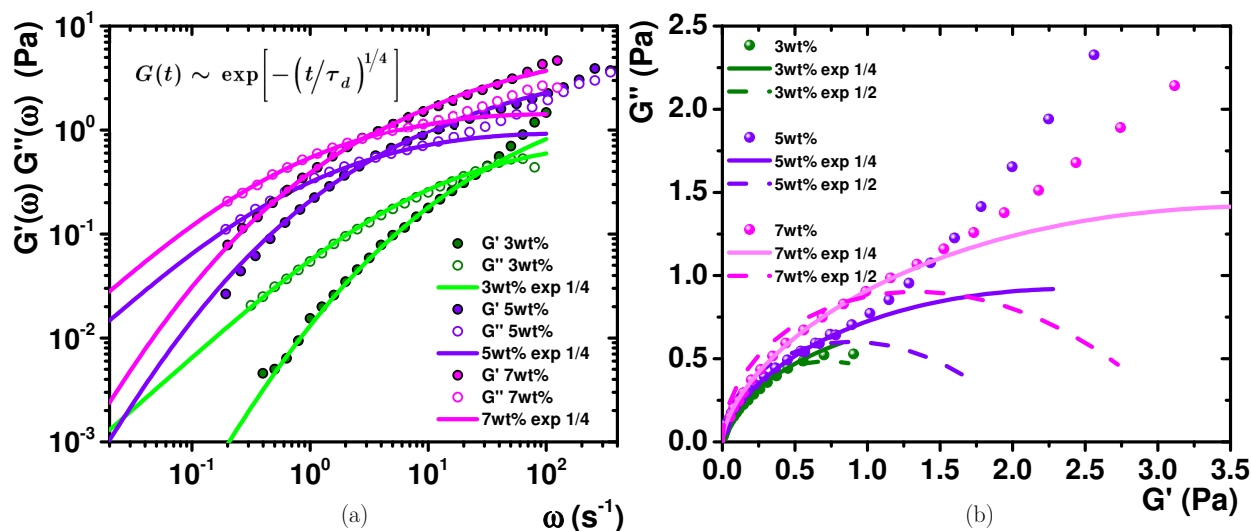


Figure IV.9 Experimental results (dots) are presented for three different concentrations. (a) $G^*(\omega)$ computed with $G(t) \sim \exp[-(t/\tau_d)^{1/4}]$ that corresponds to the case where polymer stress relaxes through reptation (lines). (b) Cole-Cole plot with to different fits. Lines correspond to the case where reptation dominates. Dashed lines are the case where breaking/recombination times are of the same order of reptation times.

1.6. Microrheology results

Some diblock copolymer suspensions present an additional complication because DWS assumes that the system under study is entirely transparent to the incident light beam. Nevertheless, the PBPEO45 and PBPEO57 systems are turbid even at very low concentrations, to overcome this inconvenience, experiments were performed using the inverse adding-doubling method (IAD) [115] [116], which allows us to calculate the optical parameters of the sample, with and without particle tracers (see Table III.4): the transport mean free path l^* , the absorption length l_a , and the anisotropy coefficient, g . The comparison of the calculated parameters with and without tracers allows us to estimate the contribution to the scattered light of the pure diblock copolymer system. The estimation of l_a allows us to use a correction to the DWS correlation function, and hence to the MSD of the tracers for the first time in a turbid complex fluid, using the method developed by Sarmiento-Gómez et al. [111]. Knowing the numerical values of l^* and l_a , and measuring the intensity autocorrelation functions, $g^{(2)}(t)$; the MSD of the microspheres can be obtained when there is light absorption in the fluid of interest that cannot be neglected. The experimental MSD curve is fitted to the model curve proposed by M. Bellour and coworkers (equation (III.3.43)) [125], which predicts an expected behavior of the particles when they are immersed in a typical WLM solution over several decades in time. Finally, each of the components of $G^*(\omega)$ is obtained using the fitted Bellour model curve in equation (III.3.42) [41], although, numerically we used the equation (III.3.47). In a few tests using 0.8 μm microspheres, we confirmed that the particle size does not affect the results [125].

Mean square displacements (MSDs). Figure IV.10 presents the electric field autocorrelation function $|g^{(1)}(t)|^2$ for all concentrations prepared for PBPEO57 (1 – 7 wt%), obtained from experimental results of the scattered light of a DWS experiment due to embedded probe particles (diameter $a = 2 \mu\text{m}$) and after applying the Siegert relation, (III.3.3), which relates $|g^{(1)}(t)|^2$ with $g^{(2)}(t)$, the intensity autocorrelation function. $|g^{(1)}(t)|^2$ can be related to the MSD of the embedded particles, $\langle \Delta r^2(t) \rangle$, through the equation (III.3.35) (corrected for light absorption in samples), using a numerical algorithm proved and used for several systems in our laboratory [40] [41] [111], for experimental total transmission geometry. Figure IV.11a presents typical $\langle \Delta r^2(t) \rangle$ vs. t curves measured for micellar solutions with different C_{PBPEO57} spanning in time over three orders of magnitude. We observe two different regimes of motion. At short times, there is a regime where $\langle \Delta r^2(t) \rangle$ is essentially a linear function of time consistent with $\langle \Delta r^2(t) \rangle = 6Dt$, where D is the diffusion coefficient of the microspheres in the solvent at infinite dilution (as in the case of a free Brownian particle, equations (II.2.7) and (II.2.19)). Our average value is $D = 0.13 \times 10^{-14} \text{ m}^2/\text{s}$ which is close to the particle diffusion in pure water, at the same temperature, $D \sim 0.21 \times 10^{-14} \text{ m}^2/\text{s}$. At intermediate times, the MSD does not reach a constant value as in other complex fluids where a plateau is observed. In this case, we observe just an inflection point around 0.3 ms, from where motion is subdiffusive. At a time above $t \sim 5 \text{ ms}$, we were unable to see a plateau, that is, microspheres are never trapped by the micellar network. Here, our MSDs are quite noisy because we were not able to conduct DWS experiments for a very long time since the viscosity of the suspensions was very low, and the microspheres started to sediment; when l^* started to decline, we ended the experiment (10 min for low concentrations, 15 min for higher concentrations). Instead of the behavior observed in other WLM solutions, in our case at longer times, we never reached the

regime where the MSD is again a linear function of time when particles are released from the trap when the stress relaxed. It is interesting to note that there is a clear difference between the $\langle \Delta r^2(t) \rangle$ curves for WLMs made of PBPEO57 and those made of standard surfactants or PBPEO45 as observed in Figure IV.11a and b. There, we include examples of WLM systems made of: (a) PBPEO45 at 1 wt% and 2 wt% (recall that at ~ 2.5 wt% a phase transition appears). Here, the curves behave like those of PBPEO57, except that at ~ 1 to 2 ms a plateau starts which can be observed where the particles could be trapped in the micellar network; (b) The zwitterionic surfactant N-tetradecyl-N,Ndimethyl-3-ammonio-1-propanesulfonate (TDPS), the cosurfactant sodium dodecyl sulfate (SDS), and salty water [41]. Here, the network is made of WLMs which allows the particles to escape after the stress relaxes through a process of breaking and recombination; therefore, this system follows the Maxwell model at low and intermediate frequencies [41]. (c) Suspensions made of semi-flexible cylinders of fd virus (length $\sim 1 \mu\text{m}$) [150]. Here, the $\langle \Delta r^2(t) \rangle$ curves measured by DWS are more similar to those of PBPEO57.

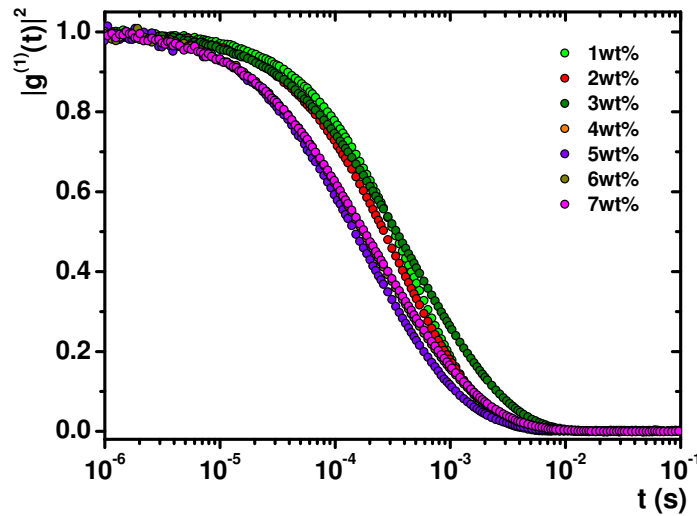


Figure IV.10 Normalized autocorrelation function. The data comes from transformed experimental results by the Siegert relation. Different concentrations for PBPEO57 are analyzed.

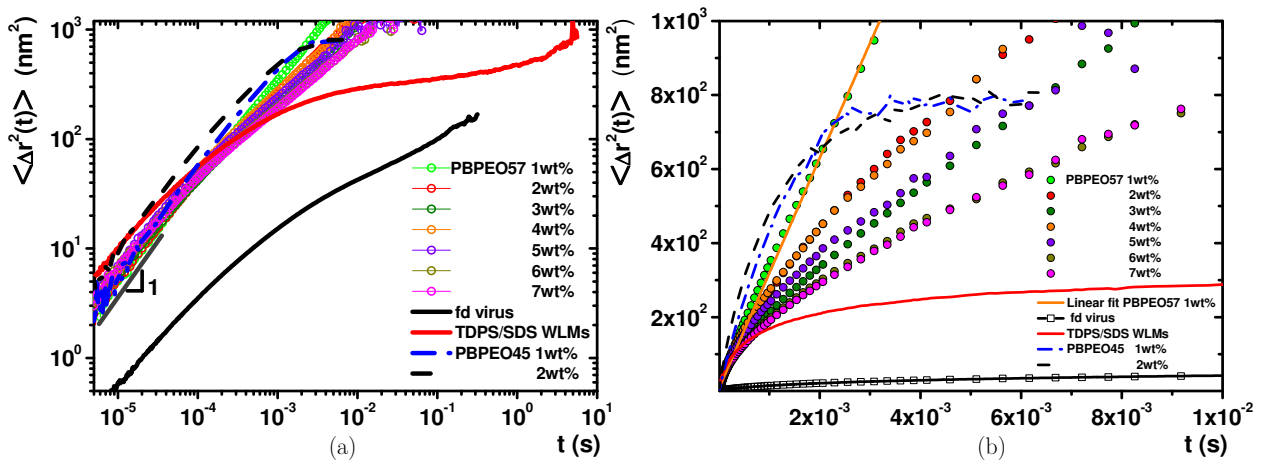


Figure IV.11 $\langle \Delta r^2(t) \rangle$ vs. t for microspheres in PBPEO57 micellar solutions. For comparison, we include data for micellar solutions of PBPEO45 (1 wt% blue dot-dashed line and 2 wt% black dashed line), suspensions of fd virus ($a = 1 \mu\text{m}$, $C_{\text{fd}} = 25 \text{ mg mL}^{-1}$ and $[\text{NaCl}] = 225 \text{ mMol L}^{-1}$, black line), and WLM solutions of TDPS/SDS/brine ($C_{\text{TDPS}} = 46 \text{ mMol L}^{-1}$, $R = 0.45$, $[\text{NaCl}] = 0.5 \text{ Mol L}^{-1}$, red line). (a) Plot in logarithmic scale where different time regimes are observable. (b) Plot in linear scale to observe the nonlinear behavior at short times. Here a diffusive regime is fitted for $C_{\text{PBPEO57}} = 1 \text{ wt\%}$ (orange diagonal line).

Viscoelastic spectra. The $\langle \Delta r^2(t) \rangle$ curves were fitted to the model curve given by M. Bellour et al. [125], as described in Chapter III, to obtain $G^*(\omega)$ at high frequency, using equation (III.3.42). The numerical fitting parameters in the model do not give any physical insight in this case due to the lack of the mentioned plateau, although the overall fitting was excellent and helped to calculate $G^*(\omega)$ with a small error. In Figure IV.12, we present the viscous (imaginary part, Figure IV.12a) and elastic (real part, Figure IV.12c) components, respectively, of the complex modulus $G^*(\omega)$ for the PBPEO57 micellar solutions at $T = 20$ °C. In Figure IV.12a, the lines correspond to measurements using mechanical rheology, and the lies plus squares correspond to the microrheology. For $G''(\omega)$, there is a small tie error between both sets of curves, which is in the range of less than 1 Pa; this is quite reasonable. Figure IV.12b presents the whole spectra for $G''(\omega)$ along eight decades in time for $C_{\text{PBPEO57}} = 4, 5, \text{ and } 6$ wt%. The tie error for $G'(\omega)$ is much larger than for $G''(\omega)$ as observed in Figure IV.12c. The microrheological values of $G'(\omega)$ around $\omega \sim 4$ to 6×10^2 s $^{-1}$ present an unexplained change in curvature. Consequently, there is an unexpected faster decay in the frequency region which comes from the highest measured values of the MSD. These time values correspond to the sector where $g^{(2)}(t) \sim 0$ and that is quite noisy; the numerical error here is large, because it is not clear how the correlation function has to be truncated, and probably this error affects more $G'(\omega)$ than $G''(\omega)$ at these frequencies. Figure IV.13 presents $G'(\omega)$ and $G''(\omega)$ obtained with mechanical rheology (low and intermediate frequencies) and microrheology (high frequencies) for the PBPEO57 micellar system (Figure IV.13a); for comparison, we included the system made of PBPEO45 (Figure IV.13b).

In both cases at high frequency, $G''(\omega)$ is more extensive than $G'(\omega)$. In contrast, as mentioned above, after the first crossing at ω_0 , $G'(\omega) > G''(\omega)$ and before this crossing $G'(\omega) < G''(\omega)$. Therefore, a second crossing point must be observed at some point in the high-frequency range. For PBPEO57, the $G'(\omega)$ and $G''(\omega)$ curves approach each other, but we could not capture the crossing, because $G'(\omega)$ decays faster around $\omega \sim 4$ to 6×10^2 s $^{-1}$, as mentioned before. Therefore, in Figure IV.13a, we included a gray window where the crossing is expected to be found, and we estimate that $G'(\omega)$ values are not accurate. For PBPEO45, the second crossing was captured (Figure IV.13b), but the MSD data never reached the long times needed to obtain the lower values of the microrheological moduli necessary to tie with the mechanical measurements. Hence, we have a gap (dashed lines between 10 s $^{-1} \leq \omega \leq 120$ s $^{-1}$), although the mechanical measurements seem to be the continuation of the microrheological data.

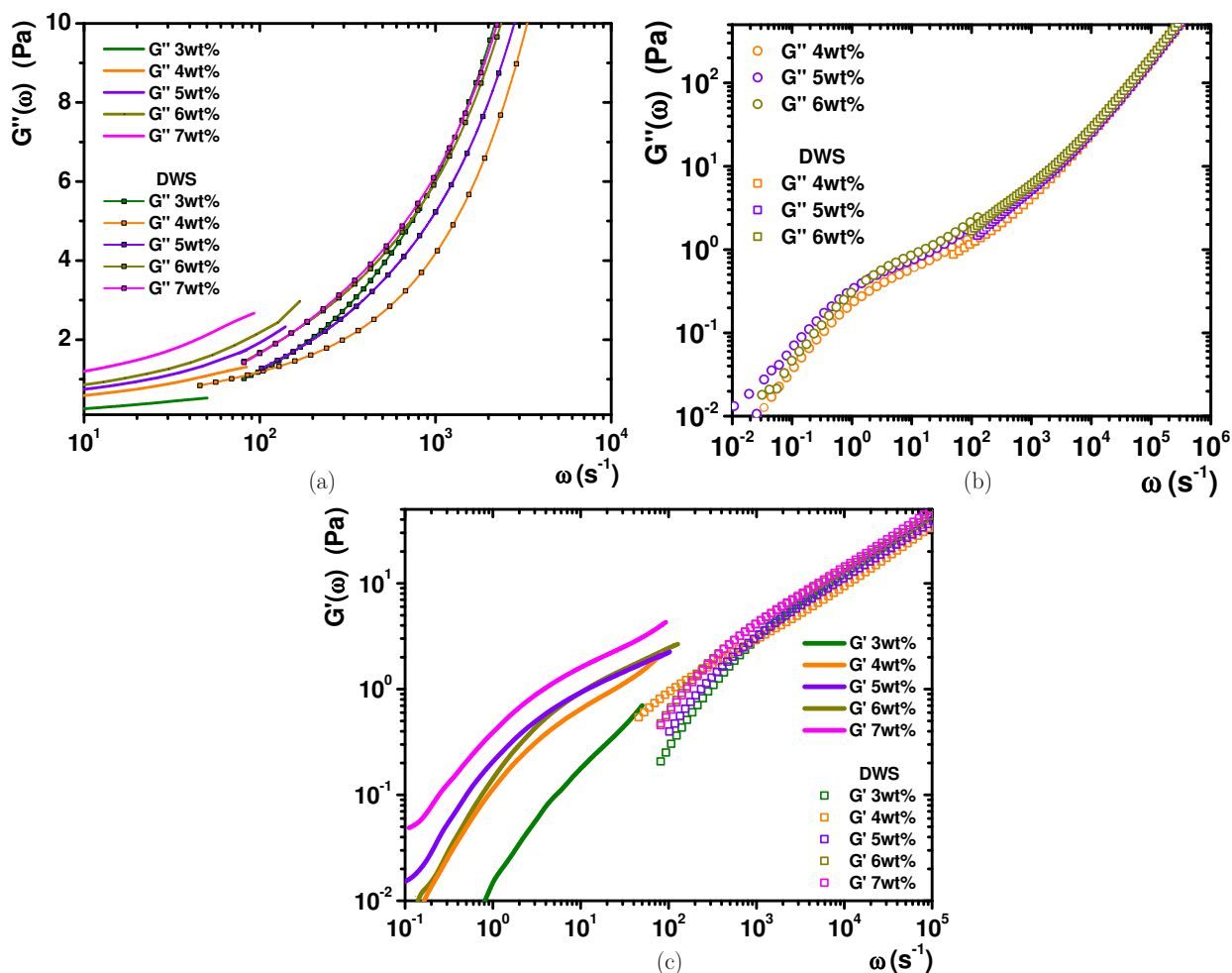


Figure IV.12 Shear moduli vs. ω , for different concentrations of PBPEO57. (a) Viscous modulus. Mechanical rheology (lines) and microrheology (lines + squares). (b) Viscous modulus in the logarithmic scale along eight decades in frequency. Mechanical rheology (circles) and microrheology (squares). (c) Elastic modulus in the logarithmic scale along six decades in frequency. Mechanical rheology (lines) and microrheology (squares).

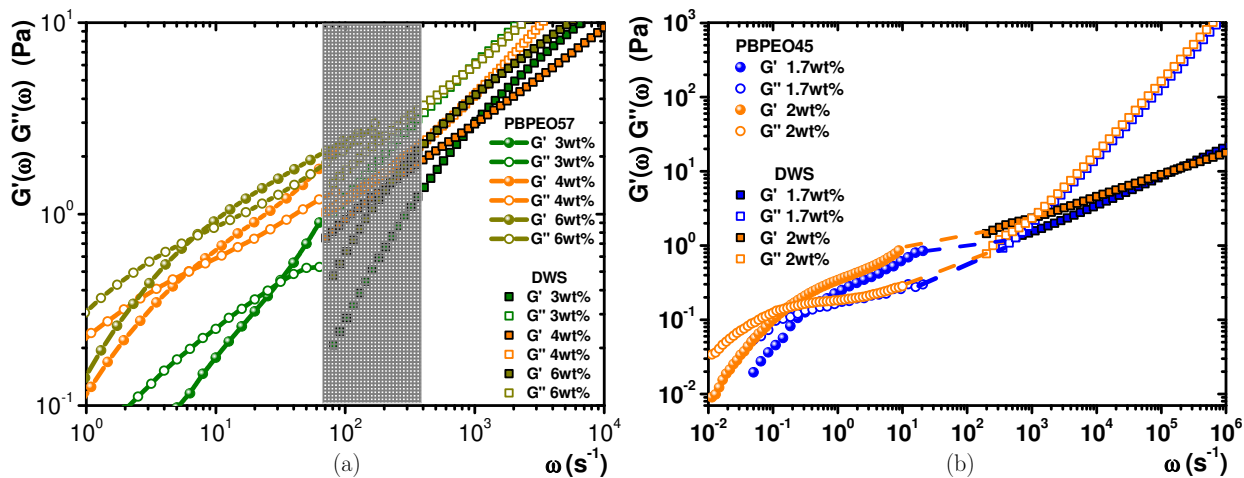


Figure IV.13 $G'(\omega)$ and $G''(\omega)$ obtained by rheology and microrheology for both micellar systems: (a) PBPEO57, here we included a gray window where the crossing is expected to be found and where the measured $G'(\omega)$ values are probably not accurate; (b) PBPEO45, microrheology could not reach the mechanical measurements; the gap is represented by dashed lines. For both cases, different diblock copolymer concentrations are presented.

1.7. An attempt to connect microrheology with mechanical rheology

As we discussed, we can observe in Figure IV.13 that the intermediate frequency region has a lack of the spectrum information. This means that we need more information of the probe particles at longer times, which could be achievable with bigger particles, but with a risk of losing their Brownian behavior and with the possibility of affecting the local structural monitoring within the sample.

1.7.1. DLS experiments

A way to overcome this problem is to obtain the MSD of the particles by conventional dynamic light scattering (DLS) experiments at low angles according to B. R. Dasgupta and coworkers [151]. The application of DLS lies in the local mobility of particles. To get a speckle pattern in DLS, individual particles must exert a long enough displacement to generate a sufficient phase shift of the light waves (half a wavelength of the scattered light) due to the difference in optical path each one has after the individual scattering events, at different times or different positions within the sample, and at very diluted particle concentration. This particle displacements are longer than the ones obtained by DWS experiments, where each particle does not require to exert a long-distance displacement to get an enough phase shift of waves at the detector, due to the several scattering events, each one generating a small phase shift. Each change in phase is summed up with all the others, to generate the interference speckle pattern at the detector, as is showed in the equation (III.3.19).

We used a home-made DLS setup at the laboratory (see Chapter III). Because we performed experiments with particle of sizes 800 nm and 2 μm in DWS, we also used those particles for DLS. Hence, it is necessary to consider the formalism of S. R. Aragón and R. Pecora [104] because the scattering events are in the Rayleigh-Debye regime (see Chapter III). The autocorrelation function we used to analyze the experimental results is the one represented in the equation (III.3.11). Before performing the experiments with the diblock copolymer solutions, we performed some experiments just with the colloidal particles (800 nm and 2 μm) in water at very diluted concentration. The results convinced us to continue with the diblock copolymer experiments. The DLS tests were done just for PBPEO45. Nonetheless, both PBPEO diblock copolymers scatter light due to the sizes of the aggregates in solution; this is not a problem in DWS but represent a complication for DLS. Anyway, we made the proper tests.

Experiments were carried out at the same angles as before for the particles in water to assure a maximum intensity of scattered light. Also, the setup of the experiment included a pair of linear polarizers (one just outside the light source and the other at the entrance of the detector) in vertical-vertical configuration to assure just one scattering event (polarized experiments). However, after some tests with vertical-horizontal configuration (depolarized experiments), at different concentrations of PBPEO45, we were still detecting enough signal to construct an autocorrelation function, that means that there exist bigger aggregates than the colloidal particles, and with non-spherical shape that change the polarizability of light. Further information about polarized and depolarized DLS can be found elsewhere [152] [153] [154].

The experiments were performed for solutions at $C_{\text{PBPEO45}} = 1 \text{ wt}\%$ with a few microliters drop of diluted particles of diameter = $2 \mu\text{m}$ and 800 nm ; and for a solution of $C_{\text{PBPEO45}} = 1.5 \text{ wt}\%$ with particles of $2 \mu\text{m}$. The autocorrelation functions $|g^{(1)}(t)|^2$ are shown in Figure IV.14, for $C_{\text{PBPEO45}} = 1 \text{ wt}\%$ and $2 \mu\text{m}$ particles, just for three different angles, $\theta = 33.6^\circ, 64.4^\circ$ and 85.5° . All plots are compared with the autocorrelation functions of just the particles in water, and with just the PBPEO45. The plots are also accompanied with the respective distribution of decay times of the system PBPEO45 plus particles, obtained with the regularized analysis method [155].

With these results it is evident that there is an overlapping between the natural relaxation times of the aggregate structures of the PBPEO45 and the colloidal particles. For low angles there is a difference between the three plots (particles, PBPEO45, PBPEO45 + particles). The shorter times decay of the PBPEO45 + particles plot, corresponds to the PBPEO45, and the longer times to the particles. For high angles the curves of PBPEO45 + particles plots are more similar to the block copolymer curve, which means that the scattered light by the particles is running low and the contribution to the autocorrelation function is getting just for the PBPEO45. Similarly, the decay times distribution plots show a longer separation between peaks at low angles, than the short separation at high angles; in the same way, the peaks due to the particles' relaxation times are more pronounced at short angles than the corresponding at long angles.

In the autocorrelation functions plots, there are also three different fitting lines. The two gray fitting lines correspond to single exponential functions, each one for the different relaxation times (diblock copolymer and particles respectively). The red fitting lines correspond to a double stretched exponential function,

$$|g^{(1)}(t)|^2 = A_1 \exp(-t/\tau_1)^{b_1} + A_2 \exp(-t/\tau_2)^{b_2}. \quad (\text{IV.1.4})$$

The exponents b_1 and b_2 generate a smoother curve, that permit a better fit at longer times. The value of this fitting is inverted using the equation (III.3.6) to obtain the MSD for each angle. Almost the same results were obtained for the other experiments, with different particle size and concentration of PBPEO45 (not shown). It was even more complicated to discriminate between the particles decay and the PBPEO45 in the case of particle size of 800 nm . The same is presented when the diblock copolymer concentration is increased, even for the bigger particles used.

The MSD obtained for all different angles is not in good agreement with the obtained in DWS (previously shown in Figure IV.11). We got displacements for longer times but with a not so good behavior at short times (the larger times for DWS) (Figure IV.15b). According to the tendency of the behavior of the autocorrelation functions and MSDs, we extrapolated the results of the MSD to $\mathbf{q} = 0$. The extrapolation was made plotting the MSD vs. \mathbf{q} at constant time (constant time cut). For each time a linear extrapolation was done to $\mathbf{q} = 0$, and with the values at the intercept, we constructed the new MSD (Figure IV.15a).

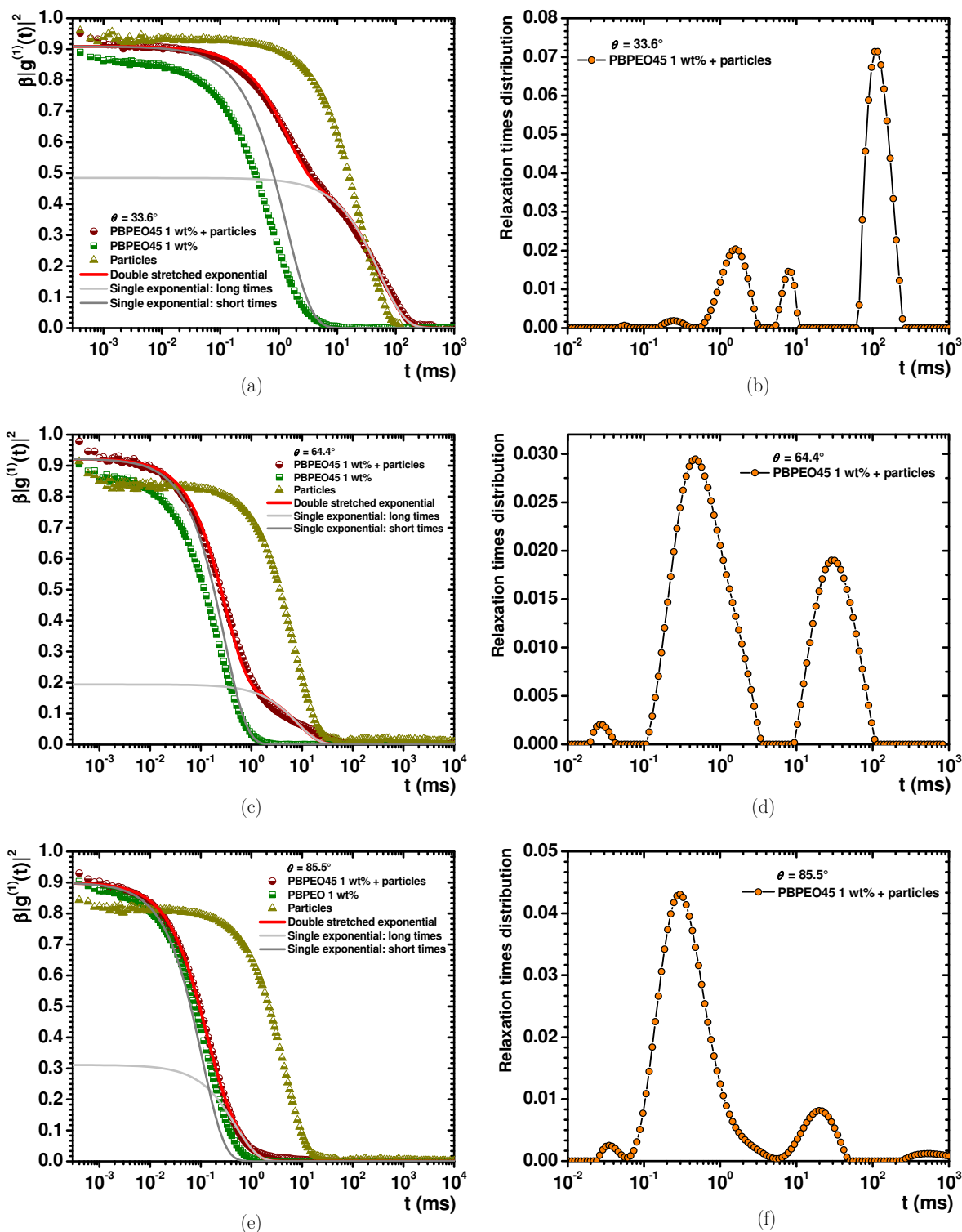


Figure IV.14 (a) (c) (e) Autocorrelation functions for three different scattering angles: 33.6° , 64.4° and 85.5° respectively. Each graph presents the plots for the relaxation of particles of $2 \mu\text{m}$ in water, for the PBPEO45 at 1 wt% and the relaxation for the probe particles embedded within the PBPEO45 solution. (b) (d) (f) These are the relaxation times distribution for each angle. In all plots it is evident that when the angle increases, the response due to the relaxation of the PBPEO45 is more representative than the particles response.

Although the extrapolation considers the information for all angles at all measuring times, the tendency of the MSD is still a bit far away from the DWS MSD. It is in not so good agreement with the tendency followed by DWS experiments (Figure IV.15b). With this shape in the displacement plot, it was very complicated to fit Bellour's equation. Making a direct Fourier transformation of the MSD, we got a bad behaved viscoelastic spectrum, with no connection within the gap we wanted to complete (plot not shown).

In conclusion, with this procedure we could not complete the gap between the mechanical rheological response and the light scattering microrheological response.

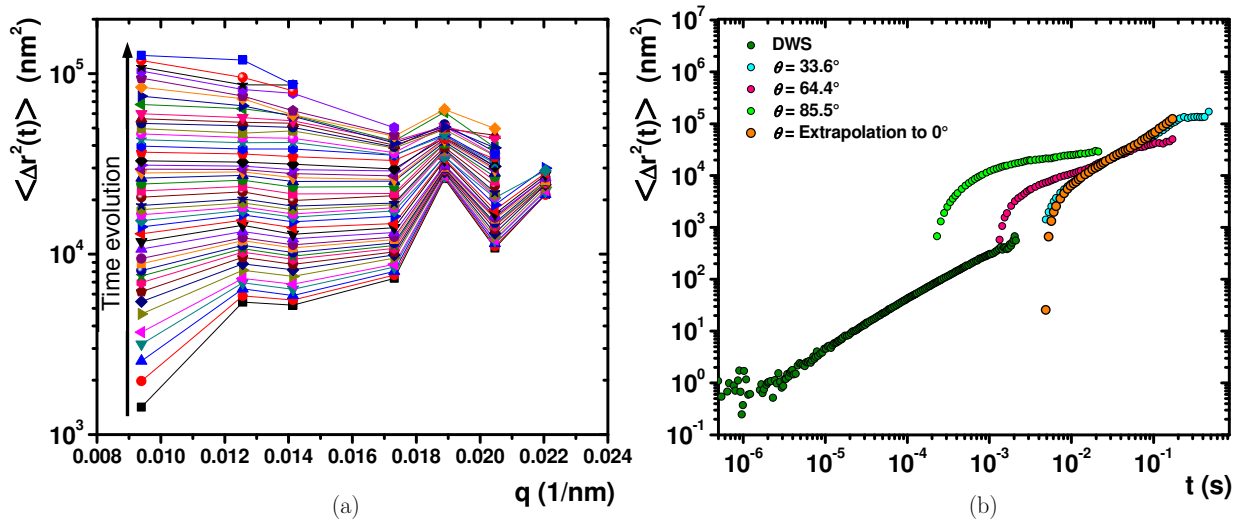


Figure IV.15 (a) MSD construction to extrapolate the values to null angle ($\mathbf{q} = 0$). Each curve with its corresponding figure and color represents a different measurement time, with an evolution towards the direction of the arrow. (b) Comparison of MSDs at different angles: 33.6° , 64.4° and 85.5° . Those are also compared with the MSD obtained extrapolating to $\mathbf{q} = 0$. All of them never have a good agreement with the MSD obtained by DWS experiments. These are experimental results made with PBPEO45 at 1 wt% with embedded particles of diameter = $2 \mu\text{m}$.

1.7.2. Samples with light absorption

Another potential possibility to extent the displacement of the particles to longer times, and consequently to extent the viscoelastic spectrum to shorter frequencies, is adding a light absorption agent to the PBPEO solution with particles, for DWS experiments. When we add this agent artificially, without affecting the mechanical properties of the sample, the scattered light response at the detector change. In particular, in transmission geometry the longer paths of light are attenuated much more than the shorter paths. Therefore, the particles must exert longer displacements to get an enough phase shift of light wave to produce the speckle pattern at the detector. This procedure represents an intermedium between conventional DWS and DLS. To perform these experiments, it is necessary to consider the restrictions imposed by the diffusion approximation of light within the sample. These restrictions have been mentioned earlier in this document (see Chapter III). Finally, with the IAD method it is possible to obtain the optical

parameters of the sample, necessary to compute the numerical inversion of the autocorrelation function, to obtain the MSD.

Because we are using big particles for our experiments (2 μm) to already extent the most possible the response at longer times, these particles have a preferred scattered light direction (Mie scattering regime), hence we could no extent enough the MSD, as could be done by E. Sarmiento-Gómez and coworkers [111], for smaller particles (in the Rayleigh scattering regime). So that, for our purposes the addition of light absorption to the sample was useless. Even though, these experiments permitted us to prove the validity of the IAD method when we add absorption artificially to a real system with internal mesoscopic structure. A further explanation of the experiments was shown in Chapter III. Section 4, where PBPEO45 samples were analyzed after the addition of indian ink.

1.8. Microrheology and structure

At high frequencies, micelles can be regarded as semiflexible chains where the stress relaxation processes, reptation and breaking/recombination, are mostly still. Stress relaxes via intramicellar processes as ω increases; first dominated by the Rouse-Zimm modes and then by the internal relaxation of individual Kuhn segments (recall the formalism of flexible polymers, Chapter II). Thus, at high frequencies, $|G^*(\omega)|$ exhibits a power law behavior, $|G^*| \sim \omega^\nu$, illustrated in Figure IV.16 with an exponent $\nu \sim 5/9$ in the Rouse-Zimm regime [11] that changes at a critical frequency, ω^* , to $\nu \sim 3/4$, where the internal bending modes of Kuhn segments dominate [34]. This change occurs at the shortest relaxation time in the Rouse-Zimm spectrum. At very high frequencies, $|G^*|$ is dominated by the solvent, that is water, $|G^*| = -i\eta\omega$. Using equation (II.7.2), $\omega^* \approx k_B T / 8\eta l_p$ [156] [34] [35], the persistence length of the WLMs is estimated.

We found that ω^* depends on concentration. In Figure IV.17a, we present l_p vs. C_{PBPEO57} . The interaction between WLMs sensibly modifies l_p , since it increases faster as the concentration decreases close to c^* . In this figure, we also included the area (in red) where the experimental l_p value obtained using SANS should be found at 0.5 wt% (> 225 nm). If we extrapolate our concentration-dependent l_p to the concentration where the SANS measurement was done, the agreement is quite reasonable. This behavior of a marked decrease of l_p with concentration increase has been observed in cylindrical polymer brushes in the dilute and semidilute regime using SANS [147] and in polyelectrolyte chains [157] [158]. The explanation for this fact in these systems also seems to be applied here. In the dilute solution ($< c^*$), the macromolecules adopt a worm-like configuration due to the steric interaction between the side chains, in the case of polymer brushes, or due to the electrostatic repulsion, in polyelectrolyte chains. For both systems, the contribution of the intermolecular interactions to the total free energy increases upon increasing the concentration. To reduce this contribution, a reduction in l_p of the thread-like structures occurs because for a flexible macromolecule the excluded volume that is not available for the other macromolecules is smaller than the corresponding one of a rigid macromolecule. In Figure IV.16d, we included an example of the power law behavior of $|G^*|$ for PBPEO45 WLMs at high frequencies. Here with microrheology, the estimated value of l_p is ~ 76 nm at 1.7 wt% which is slightly above c^* . This value

is smaller than that obtained by SANS, $l_p \sim 141$ nm at 0.5 wt%. Observing how fast is the increase of l_p at low concentrations in the case of the PBPEO57, this value could be reasonable. In this case, we do not have enough points to make an accurate estimation because the range of concentrations able to be studied is too small (see Figure IV.17b).

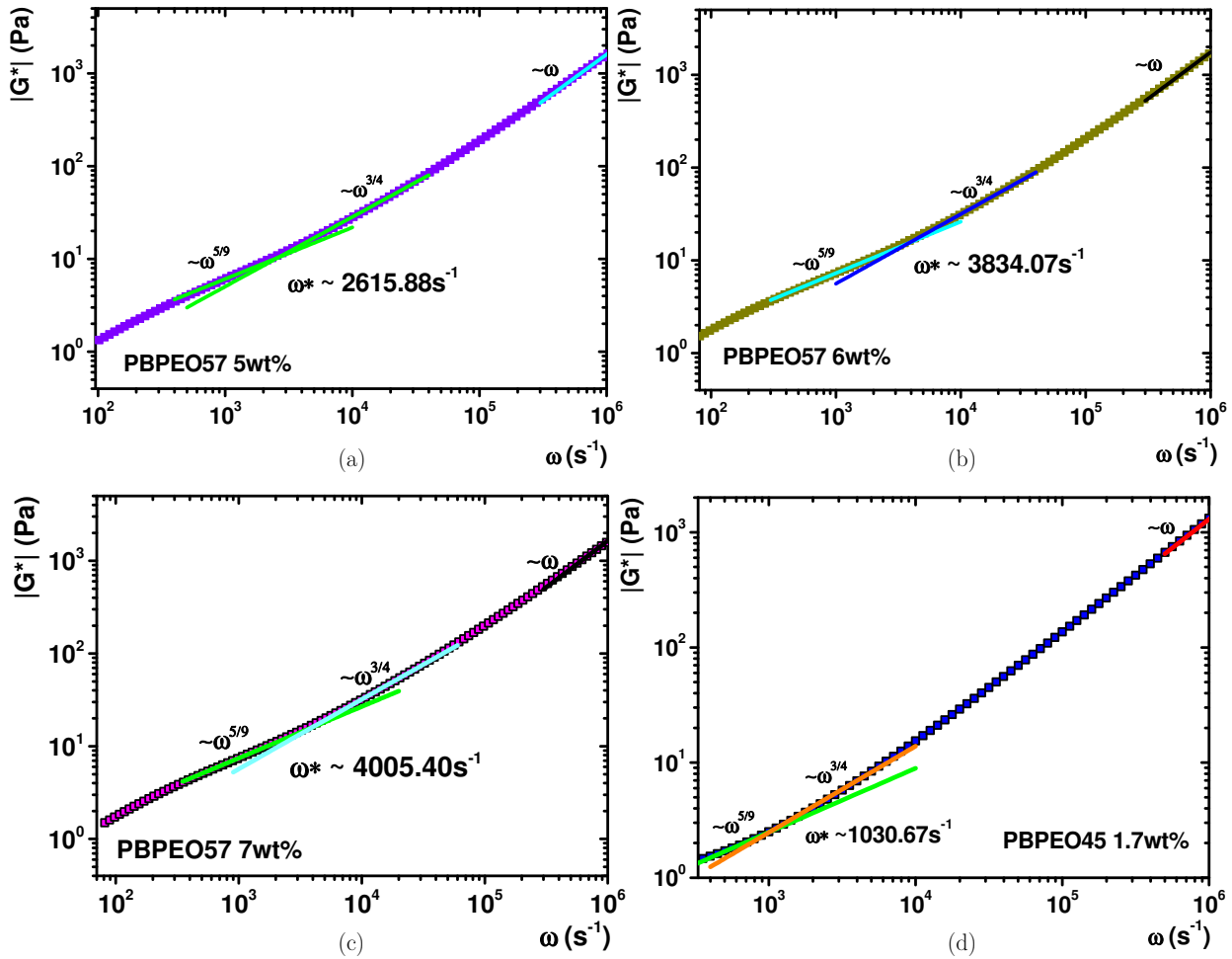


Figure IV.16 Power law behavior of $|G^*| \sim \omega^\nu$ for PBPEO WLMs at high frequencies. First, it is dominated by the Rouse-Zimm modes, then as frequency increases by the internal relaxation of individual Kuhn segments, and finally by the viscous water. (a) $C_{\text{PBPEO57}} = 5$ wt%, (b) $C_{\text{PBPEO57}} = 6$ wt%, (c) $C_{\text{PBPEO57}} = 7$ wt%, and (d) a comparison with $C_{\text{PBPEO45}} = 1.7$ wt%.

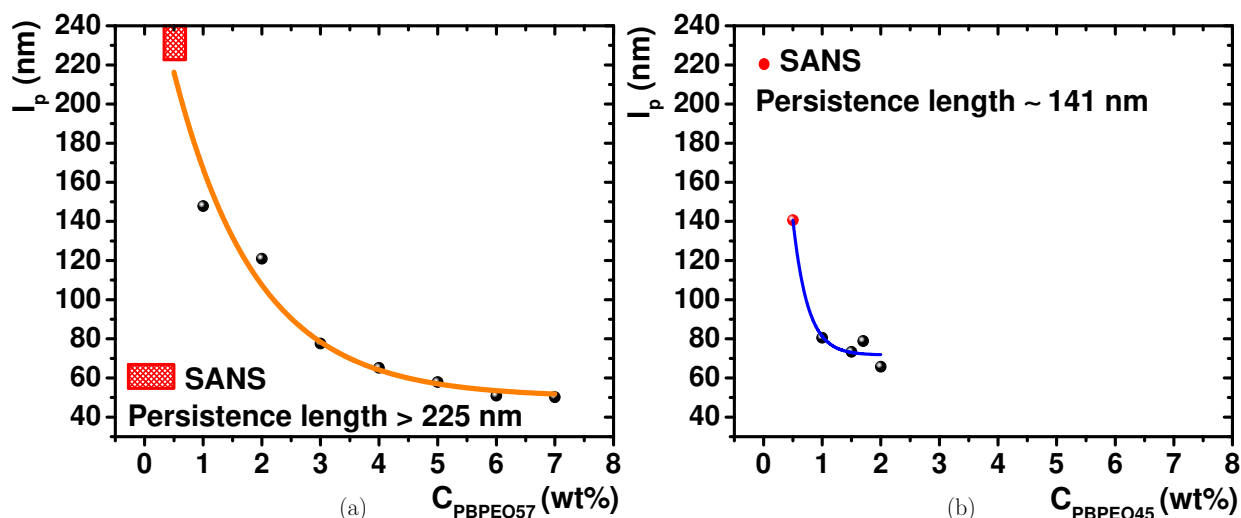


Figure IV.17 (a) Persistence length as a function of concentration for PBPEO57 WLMs obtained with microrheology. A red dashed square was included for the region where the persistence length must be found using SANS. (b) The same plot but for PBPEO45. The red dot corresponds to the persistence length value found by SANS. The concentration range, in this case, is limited because WLMs are found below $C_{\text{PBPEO45}} = 2.5$ wt%, therefore the comparison with (a) is limited.

1.9. PBPEO worm-like micelles' conclusions

It was found that in water solutions PBPEO57 self-assembles into WLMs with a diameter of ~ 12.7 nm, a core radius of ~ 2.7 nm, a shell thickness of ~ 3.0 nm and an estimated persistence length of > 225 nm. The degree of polymerization of PB and PEO blocks is 37 and 57, respectively. We compared this system with another similar system, the PBPEO45 that also forms WLMs in water with the same core as before, but with a PEO block with a degree of polymerization of 45. In the latter, the diameter was ~ 12.8 nm, the core radius was very similar to that of the PBPEO57 ~ 2.6 nm and the shell thickness was ~ 3.1 nm, although with a smaller estimated persistence length of ~ 141 nm. The bending energy is more significant for the PBPEO57 WLMs than that for the PBPEO45. The stiffness difference is because the PEO block is already more densely packed in the WLMs of PBPEO57 than of PBPEO45, any bending will increase this steric overcrowding.

The micelles of PBPEO57 do not follow the rheological behavior of the WLM solutions of conventional surfactants. At low concentration, the micellar solutions steadily shear thins as the shear rate increases reaching low viscosity values at large shear rates; there are no shear thickening peaks. The boundary between dilute and semidilute regimes was estimated according to the behavior of the zero-shear viscosity to be ~ 0.8 wt%. When sheared, the micellar solutions present birefringence. The viscoelastic spectra at low and intermediate frequencies do not follow the Maxwell model. The micelles of PBPEO57 do not break and reform. The same behavior was observed in the case of PBPEO45, which also produces an atypical WLM solution. The slow dynamics of the self-assembly explains this uncommon behavior of a WLMs system; any micellar rearrangement is impeded due to the extremely high hydrophobicity of the PB block.

The mean square displacement of colloidal particles was measured in the micellar solution of PBPEO57 and compared with other fluids with embedded thread-like structures (conventional surfactant WLMs, fd virus, and PBPEO45 WLMs). From the particle mean square displacement, we obtained $G'(\omega)$ and $G''(\omega)$ at high frequencies. $|G^*|$ exhibits a power law behavior. Here, it is evident where the stress relaxation changes from the Rouse-Zimm modes to the bending modes of Kuhn segments at ω^* . From here, l_p was calculated for the PBPEO57 WLMs, which is concentration dependent, but extrapolating our data to the concentration where the SANS measurement was done, the agreement is reasonable. As concentration increases, a reduction in l_p of the thread-like structures occurs to reduce the contribution of the interaction to the total free energy, because for a flexible macromolecule the excluded volume that is not available for the other macromolecules is smaller than the corresponding one of a rigid macromolecule. In summary, we obtained information about the relaxation mechanisms of the system at low (mainly through reptation) and high frequencies (Rouse-Zimm and bending modes), and how they are related to the size of the PEO shell and the diblock copolymer concentration.

2. Photoresponsive worm-like micelles

2.1. Motivation and purpose

The structure and rheology of cetyltrimethylammonium bromide with sodium salicylate (CTAB-NaSal) [40], and N-tetradecyl-N,N-dimethyl-3-ammonio-1-propanesulfonate with the cosurfactant sodium dodecyl sulfate (TDPS-SDS) [159] [41] worm-like micelles systems have been largely studied in the Complex Fluids Group of the Institute of Physics at UNAM. Important results have been found by reproducible mechanical rheology and microrheology experiments. In these cases, worm-like micelles present Maxwellian behavior at low and intermediate frequencies under shear strain within their linear regime. Thus, there was possible to obtain the characteristic lengths of the systems at mesoscopic scale extending the viscoelastic spectrum to high frequencies under diffusing wave spectroscopy (DWS) examinations. It was found that the lengths of the systems are intimately related to the rheological responses, and that it is possible to tune them changing temperature and the ionic strength in the media. The adaptiveness of these systems under environmental changes results in a change of the building blocks assembly to get thermodynamic equilibrium. We wanted to extend the survey of these WLMs systems under external fields stimuli and construct smart materials with different tunable properties. We have decided to add a photo-responsive molecule to the mentioned WLMs systems to identify the adaptiveness of the general structure under shear deformations. Our hypothesis is that the photo-responsive molecule interferes in the mechanisms of breaking and recombination, making possible to break the micelles in smaller segments as implication of the trans-cis isomerization process of the molecule.

Here the results that compare the DWS microrheological experiments with the mechanical rheology experiments for the case of CTAB-NaSal WLMs are presented. The complete study corresponds to the doctoral thesis of Natalia Rincón-Londoño which includes SAXS and nuclear magnetic resonance (NMR) experiments.

Previous studies with photo-responsive molecules which induce bond-cleavage or photo-triggered molecules have been done [9]. A few examples are a mechanical rheology and SANS study with CTAB WLMs and the photo-triggered molecule trans-ortho-methoxycinnamic acid (OMCA) [160], a complete study of WLMs made of CTAB with the photo-triggered molecule sodium (4-phenylazophenoxy)-acetate (AzoNa), in which diverse assemblies at different length scales were obtained varying the UV light irradiation time and analyzed with different experimental techniques to get structural information [161]. A review of spiropyran-based dynamic materials can be found in [162], and also a review that highlights the advances of photo-responsive polymeric micelles, including the design, synthesis and applications, with special emphasizing in the influence of different photo-reaction mechanisms on the morphology, structure and properties of the polymeric micelles is found in [163].

2.2. Specific goals

The questions emerged regarding this investigation are: can we tune the structural conformation of WLMs aggregates with the application of light stimuli? Is it possible to change the behavior of the Maxwellian fluids? How optical properties could be modified adding a photoresponsive molecule? Are we able to perform DWS experiments even when the optical properties can change?

2.3. Materials and sample preparation

Cationic surfactant cetyltrimethylammonium bromide (CTAB; > 99 %) was purchased from Fluka Chemie gmbH (Germany) and sodium salicylate (NaSal; 99.5 %) from Sigma-Aldrich (MO, USA). 4-(phenylazo) benzoic acid (AzoCOOH; > 98 %) was purchased from Tokyo Chemical Industries Co., Ltd. (Japan) and NaOH (\geq 98 %) is from Sigma-Aldrich (Sweden). All of them were used without further purification. 800 nm tracer microspheres for DWS experiments are made of plain polystyrene (Bangs Laboratories, Inc.); they are negatively charged in pure water due to the negatively-charged sulfate groups that populate the surface of the plain polystyrene beads. Because of that, they interact with the CTAB-NaSal-AzoCOO mixture, provoking an evident phase separation, for that reason the acquired particles were functionalized with an amine group since purchasing. The phase separation of samples was avoided. The necessary used water was deionized (Nanopure-UV, USA; resistivity \sim 18.3 M Ω cm).

Sample preparation. Four different WLMs water solutions were prepared by weight. All of them contained constant concentration of CTAB (80 mM) and NaSal (40 mM), but with different concentration of AzoCOO (without, 5 mM, 10 mM and 15 mM). First, the pH of AzoCOOH aqueous solution was adjusted with NaOH to have a basic environment (AzoCOO) in order to get a better affinity with CTAB. CTAB was added to the AzoCOO solution, followed by the addition of NaSal. The solutions were stirred for 2 days at 40 °C before use (mechanical rheology measurements). They were left for 2 additional days to relax at 30 °C. Other four solutions with the same characteristics were prepared with addition of NaCl (0.1 M) to verify possible structural changes in WLMs due to ionic variations in ionic strength. Previous studies determined that better Maxwellian fluids are obtained, with larger WLMs, when NaCl is added.

Rheology. Measurements were carried out in a MCR 702-TwinDrive rheometer (Anton Paar, Austria). Flow curves and oscillatory measurements were performed using a cone-plate geometry (2°; diameter = 40 mm). Samples were allowed to relax before measurements. Experiments were performed at 30 °C.

DWS. Solutions with a concentration slightly above the desired concentration to be measured were prepared. Because micellar solution viscosity is high at room temperature and to avoid colloidal agglomeration, we followed a two-step procedure. In the first step, as pointed out above, AzoCOO aqueous solutions were mixed with CTAB, NaSal, and NaCl for certain cases. Samples were stirred for 2 days at 40 °C. In the second step, the 800 nm functionalized polystyrene microspheres in water

suspension (10.17 wt%) were added while the samples were stirred; the particle weight fraction was $\phi = 0.035$, and subsequently samples were sonicated for 15 minutes to assure a homogeneous dispersion. Due to the high viscosity, samples were kept stirring for 14 days at 40 °C. Finally, samples were left for 2 additional days to relax at 30 °C in rectangular cuvettes of a light path thickness of 2.5 mm, used for DWS experiments, sealed well to avoid water evaporation. Typical acquiring times were about 2 hours for the less AzoCOO concentrated samples, and 3 hours for the samples with 15 mM AzoCOO.

2.4. Microrheology results

The mechanical rheology experiments (not reported here), were carried out in two different ways: in standard conditions without irradiation of sample, and at the same time while the sample is irradiated with UV light. The results have shown that there is no appreciable difference between both experiments. Thus, presumably there is not a structural change of the WLMs, as it is confirmed with NMR experiments (not shown), even when the molecule makes a transition from trans to cis isomerization. The answer to this peculiar behavior is that the presence of NaSal prevents a significative change in the packing factor of micelles. Therefore, all DWS measurements were performed without previous irradiation of samples, and the AzoCOO molecule preserved its native trans isomerization. Future analysis includes the verification of the phenomenon adding another Azo compound, which could force the WLMs to break when isomerization of the molecule changes. The main problem to be faced in the application of DWS is the light absorption nature of AzoCOOH (and AzoCOO). UV-Vis experiments (results not shown here) revealed high absorption at UV wavelengths and also with an important contribution around 514 nm which is the wavelength used in our DWS experiments.

Then, the first step to assure the possibility for doing DWS experiments is to know the power of light absorption of the molecule AzoCOO. We have to remind that there are two necessary values to cover: $l_a/l^* \geq 30$ and $\sim 9 \leq L/l^* \leq 25$ (or a little higher for the more concentrated particle suspensions). Stay within these values can assure the diffusion approximation of light inside the sample. Then, we made an IAD estimation measurement for AzoCOO at 20 mM concentration, with no colloidal particles added. The experiments consisted in varying the optical path length of used cuvettes. For collimated transmittance we got a plot with exponential decay, as shown Figure IV.18.

The exponential decay agrees with the Beer-Lambert law with a value of the inverse of an exponential decay constant of 2.26 ± 0.14 mm. After the application of the IAD method there was no scattering events detected and the only optical property obtained was the absorption length, which results for each different optical path length are summarized in Table IV.2. As expected, the values do not change considerably and are in complete agreement with the decay exponent for collimated transmittance.

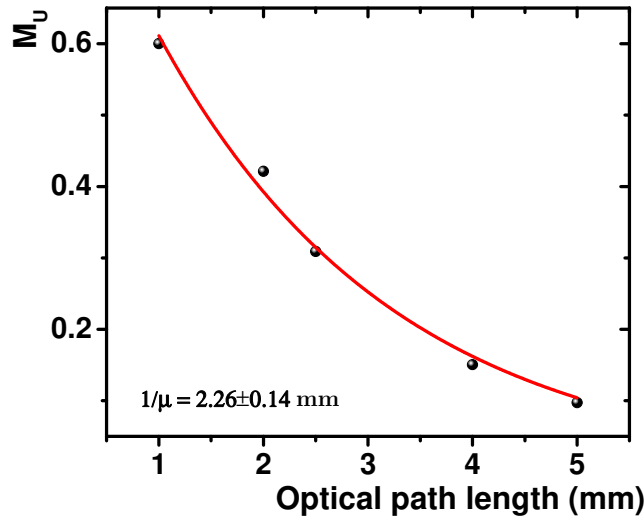


Figure IV.18 Collimated transmittance measurements at constant concentration of AzoCOO (20 mM). Different cuvettes with different optical path lengths were used to perform the experiment.

| Optical path length, L (mm) | l_a (mm) |
|-------------------------------|-------------|
| 1 | 2.41 |
| 2 | 2.60 |
| 2.5 | 2.30 |
| 4 | 2.11 |
| 5 | 2.23 |
| Average | 2.33 |

Table IV.2 Absorption lengths computed for all different surveyed optical path length for AzoCOO aqueous solutions at 20 mM.

To get at least the value $l_a/l^* \approx 30$ once we added probe particles, the light’s transport mean free path value must be shorter than $l^* \approx 77.7 \mu\text{m}$. Using Mie scattering theory, we got a plot of the l^* values in terms of the fill weight fraction of particles within the sample. Figure IV.19 presents this plot. After the survey, we found out that the most possible fill weight fraction of particles to be used is $\phi = 0.035$ which corresponds to $l^* \approx 72.6 \mu\text{m}$. If we use higher particle concentrations we cannot assure the avoiding of interparticle interactions, as well as hydrodynamic correlation. For this value, then $L/l^* \approx 34.44$, which assures that diffusion approximation of light can be used, but with relatively high concentration of particles.

Table IV.3 summarizes the optical parameters obtained for each of the measured samples, which include the contribution of the probe particles added to the samples already. For these samples was impossible to perform collimated transmittance measurements due to the large amount of scattered light by the particles. Then, to apply IAD method we settled the theoretical value of the anisotropy factor for particles of diameter = 800 nm, which is $g = 0.9166$.

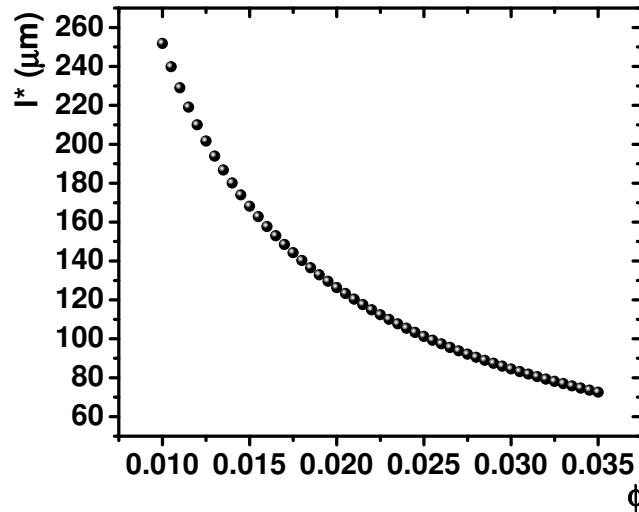


Figure IV.19 Values for the transport mean free path which depend on the weight fill fraction of particles added to the sample. The particles have a diameter of 800 nm.

| AzoCOO | Without | 5 mM | 10 mM | 15 mM |
|---------------------|---------|-------|-------|-------|
| Without NaCl | | | | |
| l_a (mm) | 31.07 | 5.77 | 2.81 | 2.52 |
| L/l^* | 14.78 | 17.25 | 13.25 | 13.18 |
| l_a/l^* | 404.04 | 39.78 | 14.89 | 13.26 |
| With NaCl | | | | |
| l_a (mm) | 144.76 | 6.51 | 3.39 | 2.29 |
| L/l^* | 21.33 | 15.71 | 12.85 | 13.14 |
| l_a/l^* | 1235.15 | 40.89 | 17.69 | 12.04 |

Table IV.3 Optical parameters computed using the IAD method. The values correspond to all different samples studied.

In average, all samples have reached lower values for l_a than the previous obtained for AzoCOO concentration of 20 mM. All the absorption values are almost stable; the significant change is got in the l^* value, which seems that varies due to the real concentration of particles suspended within the samples. Even though, the relations L/l^* are sufficiently good, but with a decrease of around 50 % for the case of value l_a/l^* , when concentration of AzoCOO is 10 mM and 15 mM. We decided to continue with the DWS experiments because several transport mean free paths are followed within all samples, even for the most absorbent cases.

Figure IV.20 shows the normalized autocorrelation function for all concentrations of AzoCOO without NaCl added, and the mean square displacements, corrected for the absorption effects, as well. In the autocorrelation function, which is not corrected for absorption, the decaying times are extended with the increase of AzoCOO concentration, which is a contribution of the absorption conditions of the samples, but also because there exist structural changes within the system. These structural changes are evident in the corrected MSD plot, due to the different behavior of particles at different AzoCOO concentration.

Figure IV.21 shows the same plots that previously but for the case with NaCl added. We could roughly say that there are not important changes compared to the former case. An important point to mention is that in the cases without AzoCOO, the autocorrelation functions present two decays, but the second appears to be much more disengaged or delayed from the first decay than in all other cases. This particularity could be interpreted as a sign of different relaxation time scales due to structures with apparently very different length scales within the sample.

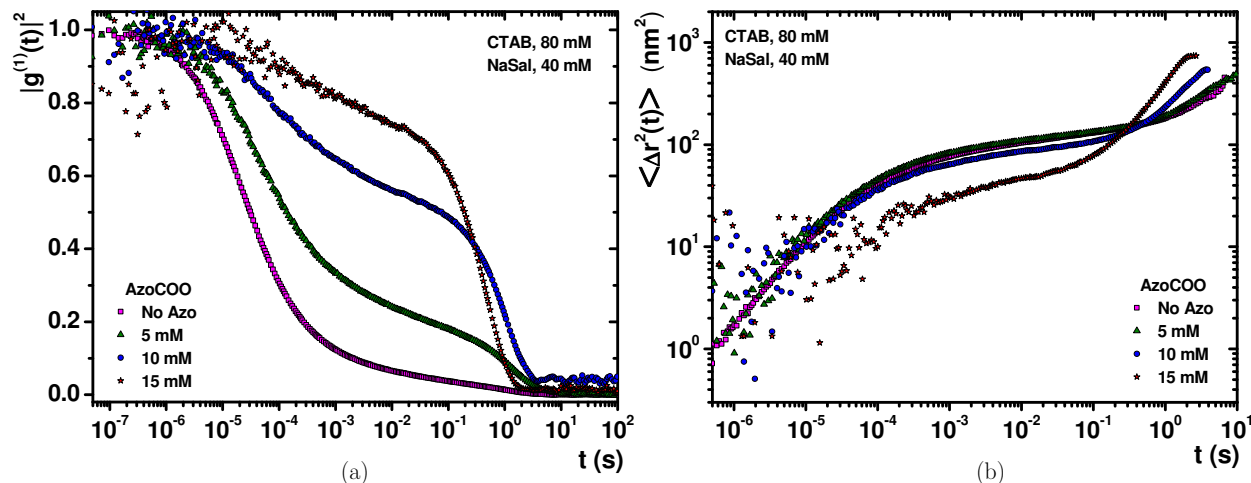


Figure IV.20 (a) Normalized autocorrelation function for all samples analyzed by DWS, before the addition of NaCl. (b) The corresponding MSD plots for the same samples.

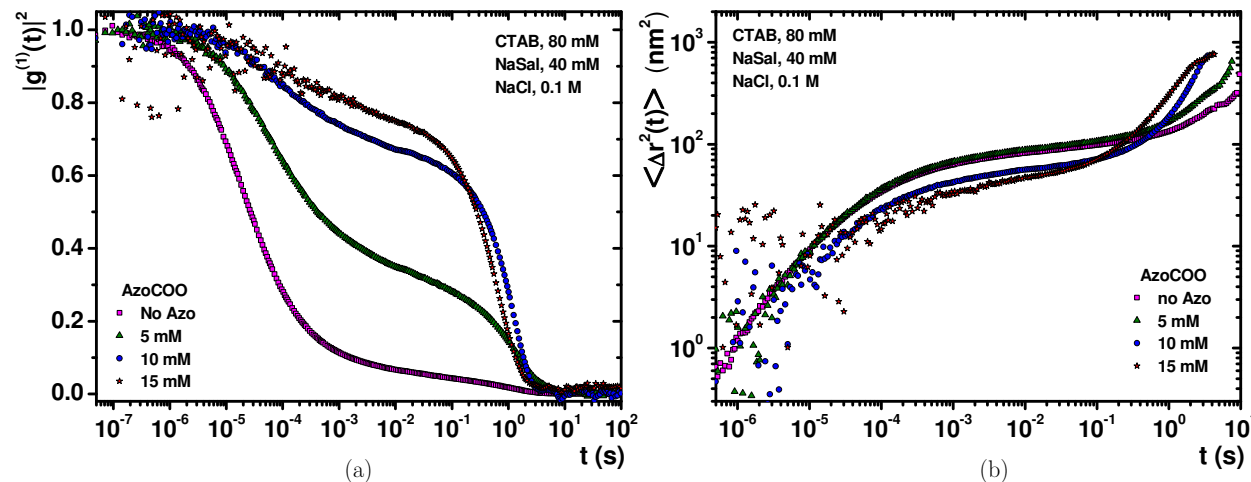


Figure IV.21 (a) Normalized autocorrelation function for all samples analyzed by DWS, with NaCl. (b) The corresponding MSD plots for the same samples.

Figure IV.22 presents the viscoelastic spectra for the four different samples with NaCl. In all of them at low angular frequencies the mechanical responses are presented and at high angular frequencies, the microrheology responses dominate at all. The black lines are adjusted by eye for the ideal cases of a Maxwellian fluid with the same relaxation time and G_0 values as the experimentally obtained. It seems that the addition of AzoCOO enhance the Maxwellian behavior for bit higher frequencies. In all cases the agreement is excellent at low frequencies. In all cases the agreement of mechanical rheology results and microrheology results is enough good as well, with the longer change in the case of AzoCOO at 10 mM, where the $G'(\omega)$ plateau have a little disagree of around 20 Pa. The disagree in relaxation times (crossing points between $G'(\omega)$ and $G''(\omega)$) is always less than an order of magnitude, with the large discrepancy in the case of AzoCOO at 5 mM. The differences are due to the different measurement techniques, where mechanical rheology accounts for bulk measurements, meanwhile microrheology analyze the sample locally.

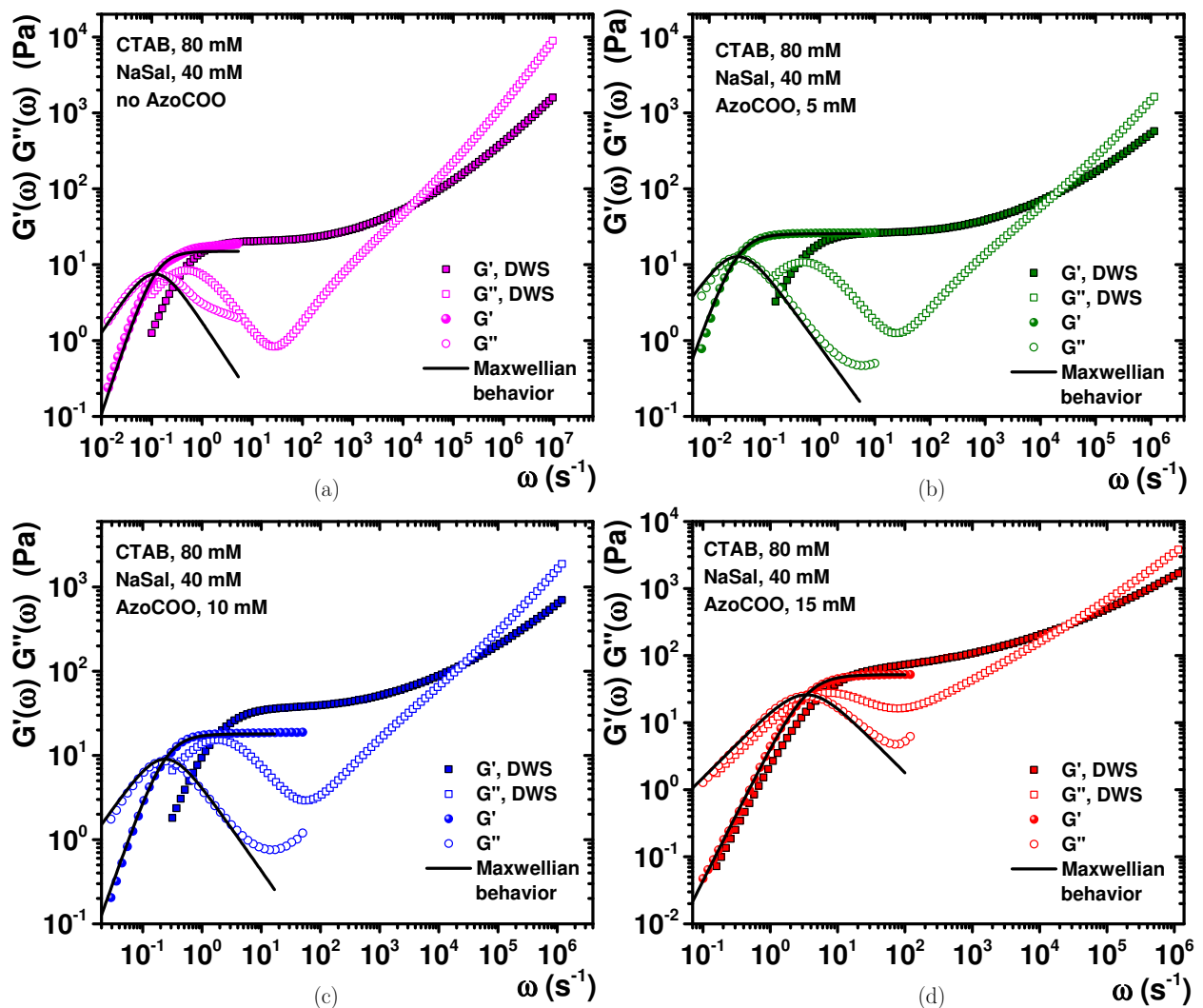


Figure IV.22 Viscoelastic spectra. Circles represent mechanical rheology results; squares are for microrheology results. Full symbols are the storage moduli and open symbols are the loss moduli. Black lines follow the Maxwellian behavior. AzoCOO concentration: (a) without AzoCOO, (b) 5 mM, (c) 10 mM and (d) 15 mM.

Figure IV.23 shows the same results as formerly but for the case of added NaCl. Here in all cases the systems have a Maxwellian behavior at low frequencies. The addition of salt contributes to increase the Maxwellian response for the case without AzoCOO. On the other hand, the discrepancies between mechanical rheology and microrheology essentially are the same as previously, with some differences for different AzoCOO concentrations. Due to the Maxwellian behavior of the samples, it was possible to estimate the characteristic lengths of the WLMs, with the help of equations (II.7.1)-(II.7.4). To have some idea of the relaxation mechanisms depending on AzoCOO concentration, Figure IV.24 presents the relaxation times τ , of the system, with and without addition of NaCl in terms of AzoCOO. A comparison is done between results obtained with mechanical rheology and with DWS microrheology. For the first case, a light increment of relaxation time occurs when AzoCOO is added, followed by a decreasing behavior once the concentration increase. For the case of DWS, the relaxation time decays always with increments of AzoCOO concentration.

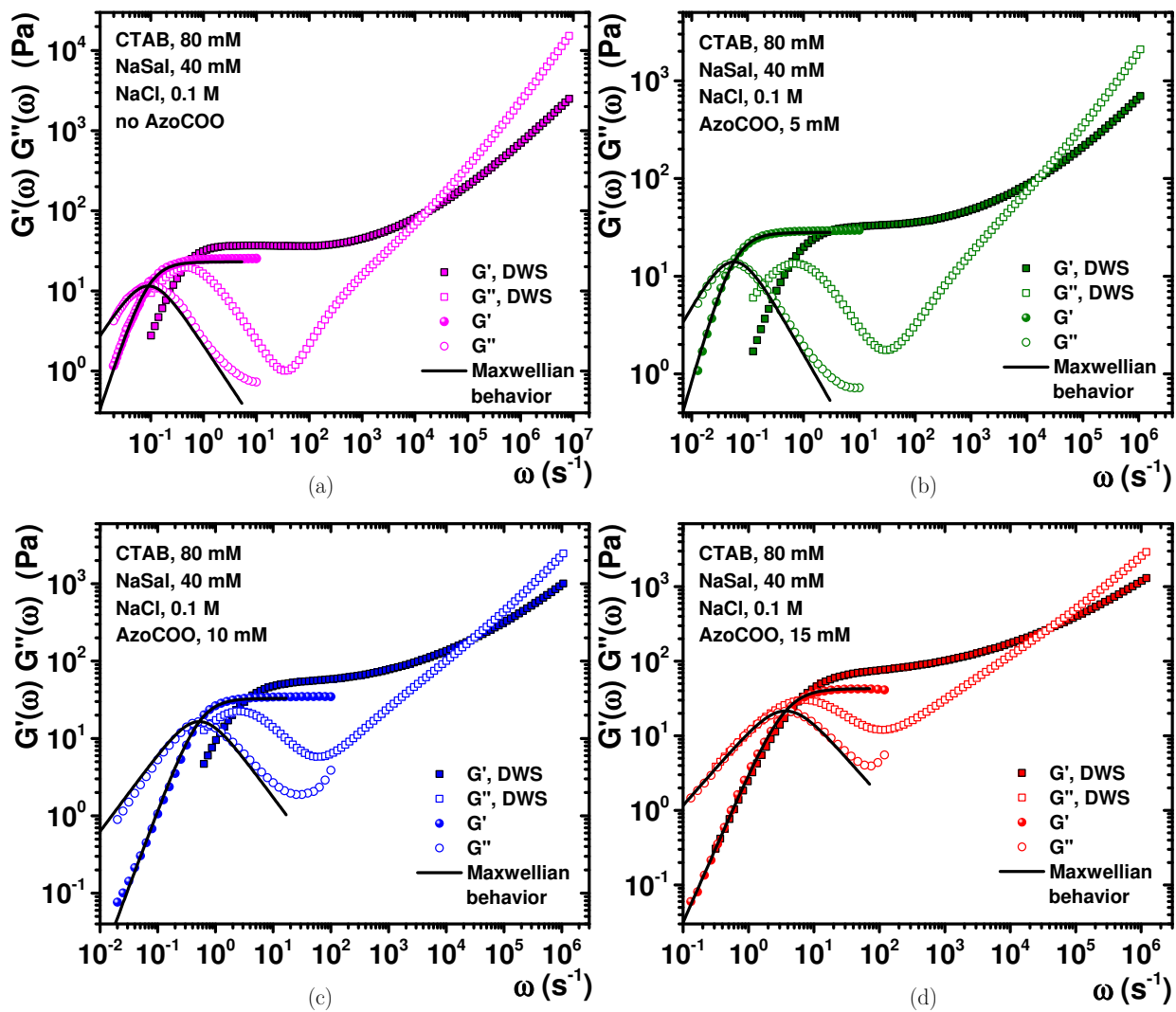


Figure IV.23 Viscoelastic spectra. Circles represent mechanical rheology results; squares are for microrheology results. Full symbols are the storage moduli and open symbols are the loss moduli. Black lines follow the Maxwellian behavior. All samples contain NaCl at concentration 0.1 M. AzoCOO concentration: (a) without AzoCOO, (b) 5 mM, (c) 10 mM and (d) 15 mM.

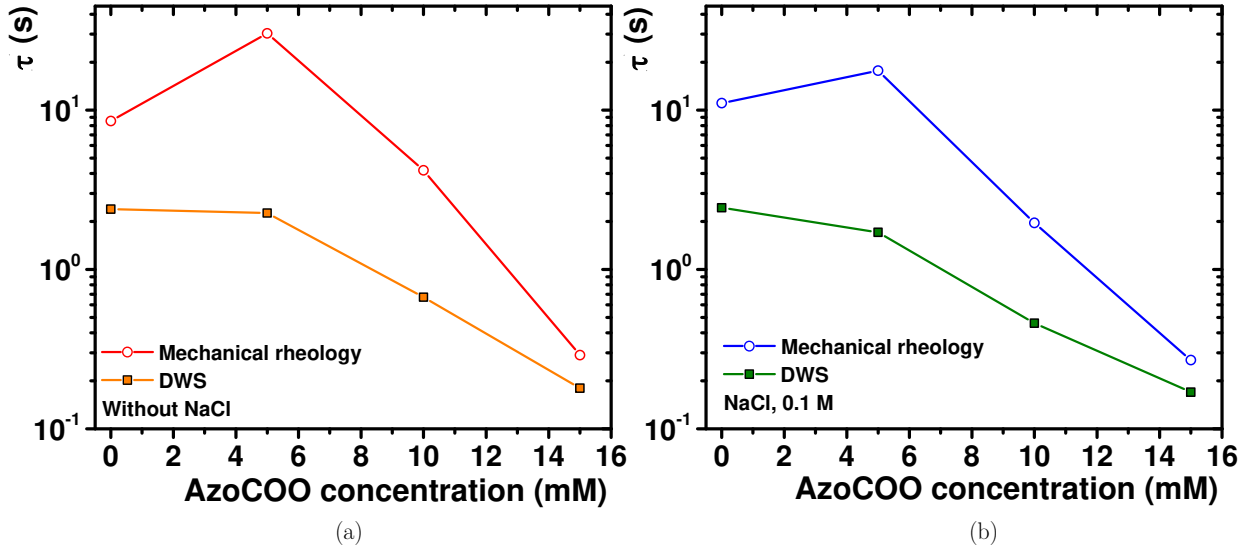


Figure IV.24 Relaxation times of the system of worm-like micelles, in terms of AzoCOO concentration. (a) The cases without addition of NaCl. (b) The cases with NaCl. In both plots the open symbols are the data for mechanical rheology and the full symbols the respective data for DWS microrheology experiments.

Figure IV.25 shows the plot of $|G^*(\omega)|$ for all cases, without (Figure IV.25a) and with (Figure IV.25b) NaCl. These plots help to obtain the stiffness of the WLMs through the calculation of the persistence length. As an example, the slope differences at high frequencies are shown for the cases without AzoCOO, with the frequency value at the point of change. Also, these plots present a different viscoelastic response between species, where the increasing of AzoCOO concentrations leads to an increase of $|G^*(\omega)|$ values.

Table IV.4 summarizes the computed characteristic lengths values for all cases involved in this study, without NaCl, and Table IV.5 reports the same characteristic lengths values for the case with NaCl.

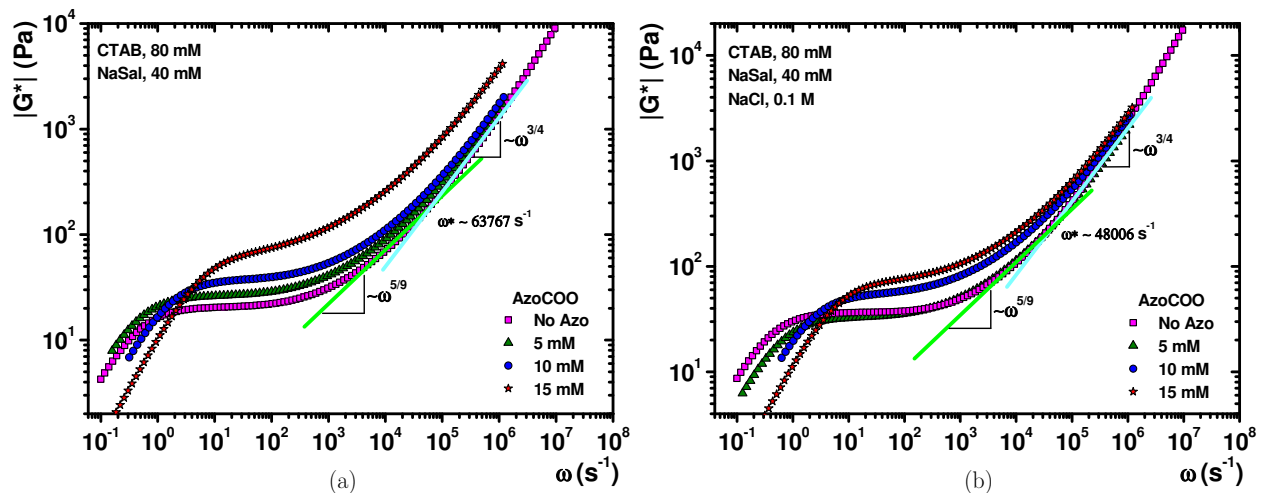


Figure IV.25 Complex viscoelastic spectra for all studied samples at different concentrations of AzoCOO. (a) The cases without addition of NaCl. (b) The cases with NaCl. As an example, the cases without AzoCOO show the slope changes which represent a change of relaxation modes, from Rouse-Zimm to the bending of Kuhn segments.

| Without NaCl | | | | |
|---------------------|------------|------------|------------|------------|
| AzoCOO | L_c (nm) | l_e (nm) | l_p (nm) | ξ (nm) |
| Without | 2663.28 | 128.36 | 21.74 | 63.10 |
| 5 mM | 1398.95 | 81.49 | 34.66 | 57.88 |
| 10 mM | 837.66 | 80.64 | 26.49 | 51.69 |
| 15 mM | 311.51 | 94.87 | 12.65 | 42.38 |

Table IV.4 Characteristic lengths obtained due to the Maxwellian behavior of the samples. Here samples do not contain NaCl.

| With NaCl | | | | |
|------------------|------------|------------|------------|------------|
| AzoCOO | L_c (nm) | l_e (nm) | l_p (nm) | ξ (nm) |
| Without | 2844.84 | 75.13 | 23.91 | 47.52 |
| 5 mM | 1225.59 | 80.40 | 29.65 | 45.15 |
| 10 mM | 519.32 | 69.52 | 24.37 | 45.71 |
| 15 mM | 371.54 | 77.35 | 16.38 | 41.57 |

Table IV.5 Characteristic lengths obtained due to the Maxwellian behavior of the samples. Here samples contain NaCl.

2.5. Photoresponsive worm-like micelles' conclusions

The most important contribution to the experimental procedure was obtaining the optical parameters of the solutions even when the solutions themselves presented light absorption in the region of 514 nm we used for the experiments. The inverse adding doubling method (IAD) was used for the first time in DWS in a structured system at a mesoscopic scale, to correct the experimental autocorrelation function due to adsorption effects.

Microrheology results reveal that the addition of NaCl is more relevant only when there is no presence of AzoCOO in the solution. The most significant difference appears in the entanglement length, l_e , which is much more extended in the case without NaCl, in accordance with a shorter contour length, L_c , when there is not NaCl, and in agreement also with a larger mesh size, ξ , for the same sample. It seems that the addition of AzoCOO contributes similar to the addition of NaCl. A notable feature is that the WLMs become smaller with higher concentration of AzoCOO (L_c). The entanglement length l_e , is preserved in average, equal than the mesh size ξ . The persistence length l_p , is also AzoCOO concentration dependent which decreases as concentration increases and contour length decreases as well. This means that the stiffness is getting lost when the WLMs are shorter. It is worth to notice that this behavior is not monotonic; l_p increases when just 5 mM of AzoCOO are added but decreases subsequently with the addition of more AzoCOO.

3. Suspensions of SWCNTs in a polyelectrolyte

3.1. Motivation and purpose

Preparation of nanocomposites made of Carbon Nanotubes (CNTs) embedded in a polymer matrix could produce materials with properties that might be used for many applications, especially when the nanofiller can provide the polymer matrix with valuable functional properties, as in the case of SWCNTs that exhibit high mechanical strength, high stiffness, and good electrical conductivity [164] [165]. Nevertheless, the poor solubility of carbon nanotubes and the fact that they are not prone to form dispersions lead to their potential applications difficult to be reached. However, some polymers have been used effectively as exfoliation agents of nanotube bundles making possible the incorporation of the nanotubes as individual entities or as very thin bundles.

There is not too much literature available focusing on the dilute regime rheology of CNTs dispersed in a polymer matrix, probably because the viscoelastic response of the polymer would far exceed that of the dispersed CNTs. However, at the percolation concentration, a matrix spanning network must be formed leading to an increase in elasticity because the CNTs are arrested. Around this percolation concentration, the rheological behavior must be dominated by that mesoscale superstructure. The results of rheological experiments for diluted suspensions of SWCNTs in a polyelectrolyte matrix (poly(acrylic) acid, PAA) are presented, which possess an extra degree of freedom; the polymer is sensible to pH. First, it was determined how pH controls the rheological behavior of the PAA polyelectrolyte at different polymer concentrations. Although this rheological behavior is not entirely unknown, it depends on the degree of polymerization. Therefore, this behavior was obtained for our specific case in a way that will be useful for the study when we add SWCNTs to a dilute polymer matrix. In this case, we find out that pH strongly impacts the rheological properties of these composites. We selected pH as main parameter to tune because the direct impact it has in the conformation of PAA, due to charge stabilization in solution, affects the way the PAA interacts with the SWCNTs. Due to the differences in surface area of PAA available (between coil-like and elongated conformation) to be in touch with the surface of individual SWCNTs, the rheological response is different for each case.

3.2. Specific goals

The central question we are motivated to answer is why the rheological behavior of PAA/water solutions at different pH values is so strongly modified, around the overlap concentration, when small quantities of SWCNTs are added to this liquid mixture. As it is reported later, the rheological behavior is dominated by the mesoscale superstructure at concentrations close to the percolation threshold at high pH, where some of its fingerprints are observable with scanning microscopies. This structure behaves as a critical gel described in physical and chemical gelation considered by F. Chambon and H. H. Winter, (equation (II.8.2)) [62] which would be in agreement with the assumption that the dynamic arrest that leads to gelation in our case is mainly due to attractive interactions between SWCNTs. It is shown how we model the rheological behavior of the

SWCNTs/PAA water suspensions using the method developed for describing these physical critical gels [60]. This study allows us to get some physical insight into what is happening in the suspension close to the gel point.

The work has been published in The Journal of Physical Chemistry B [166]: A. Selmani, A. Tavera-Vázquez, C. Garza and R. Castillo, "Tuning the viscoelastic-gel transition of single-wall carbon nanotubes embedded in pH-responsive polyelectrolyte solutions," *J. Phys. Chem. B*, vol. 122, pp. 348-359, 2018. A. Selmani performed some rheology experiments and C. Garza prepared the samples for SEM images and got AFM images.

3.3. Materials and sample preparation

Polyacrylic acid (PAA, $M_w = 450000 \text{ g Mol}^{-1}$, Sigma-Aldrich, USA) was used as received. NaOH ($\geq 98 \%$) is from Sigma-Aldrich (Sweden), HNO_3 (68 %) and HCl (36 %) solutions are from J. T. Baker (USA). All solutions were prepared with Nanopure water (Nanopure-UV, USA; resistivity $\sim 18 \text{ M}\Omega \text{ cm}$). Standard buffers (pH = 4, 7, and 10) from J. T. Baker (Mexico) were used for electrode calibrations, to stabilize pH in suspensions. Single wall carbon nanotubes were purchased from Nano-C Inc. (85 – 90 %, Nano-CPT-100, length $\approx 1 \mu\text{m}$, and diameter $\approx 1 \text{ nm}$, USA) manufactured via combustion method. They contain iron as well as amorphous carbon impurities, so they needed a further purification. We followed this procedure: 300 mg of SWCNTs were suspended in 300 mL of 3 M HNO_3 , stirred with a magnetic stirrer, and sonicated for 10 min using a standard bath sonicator (Cole-Parmer, USA) to disperse large agglomerates and to obtain a homogenous suspension. This suspension was refluxed for 48 hours at 125 °C under magnetic stirring, and then it was neutralized with 3M NaOH. The resulting precipitates were filtered and extensively washed with water until pH was close to the values of the Nanopure water (pH ≈ 6.5) to eliminate remnants of NaNO_3 and NaOH coming from the purification process. The SWCNTs were dried at 80 °C for six hours in air and stored in glass bottles.

Sample preparation. PAA solutions with a different weight fraction ($C_{\text{PAA}} = 1 - 6 \text{ wt } \%$) were prepared by dissolving dry PAA powder in water under magnetic stirring at 40 °C. pH of the PAA solutions (pH = 3, 5, 7 and 9) was adjusted with HCl and NaOH both at 1 M. pH was measured with a pH-meter (Cole-Parmer, USA) equipped with a combined glass electrode (Cole-Parmer, USA) previously calibrated with standard buffers. The polymer solutions were left under magnetic stirring for 24 hours to reach equilibrium. A buffer to stabilize suspension pH was not used in these experiments to avoid screening of the polyacid charges by co-ions.

The SWCNTs suspensions were prepared by suspending purified dry SWCNTs powder in a PAA water solution at a specific weight fraction with the pH previously adjusted (pH = 5, 7, and 9). The concentrations for SWCNTs were $C_{\text{SWCNTs}} = 0.5, 1, \text{ and } 2 \text{ mg/mL}$, and for PAA, $C_{\text{PAA}} = 1 - 6 \text{ wt } \%$. The SWCNTs suspensions were ultrasonicated (43 kHz, QSonica, USA) at 50 W for 3 hours with time cycles, 30 s on and 30 s off, in a water-ice bath to prevent heating of the samples leading to SWCNTs breaking.

Rheology Rheological measurements were carried out in a Kinexus ultra+ rheometer (Malvern Instruments, USA). Flow curves and oscillatory measurements were developed using a cone-plate geometry (4° , diameter = 40 mm) at 20°C . The PAA solutions and SWCNTs/PAA suspensions were allowed to relax at rest for two days before the measurements. The strain was 25 % for the PAA solutions and 5 % for the SWCNTs/PAA suspensions to assure a linear deformation.

Atomic force microscopy (AFM). The SWCNTs/PAA suspensions were prepared at two different concentrations, $C_{\text{SWCNTs}} = 0.01$ and 0.02 mg/mL at three different pH values (5, 7 and 9). $10\ \mu\text{L}$ of these samples were deposited via spin coating onto freshly cleaved mica substrates and then centrifuged at 6000 rpm. The dried specimens were surveyed with a scanning probe microscope (JSTM-4200, JEOL Ltd. Japan) with an $80 \times 80\ \mu\text{m}$ scanner. To obtain topographic images of the samples, we used the non-contact mode with silicon cantilevers (typical force constant of $46\ \text{N/m}$ and a tip radius of $\sim 10\ \text{nm}$, Mickromash, USA).

Electron microscopy (TEM, SEM). We used a Transmission Electron Microscope (TEM; JEM-1200EX11, JEOL Ltd. Japan) working at $100\ \text{kV}$, and an extreme-resolution analytical field-emission Scanning Electron Microscope (SEM; JSM-7800F JEOL Ltd. Japan) working at low electron acceleration voltages [139].

A few microliter drop of SWCNTs/PAA suspension was deposited on a standard copper TEM grid with a carbon covered collodion layer. The excess of sample deposited on the grid was absorbed with paper and dried at ambient conditions to be observed with TEM. In the case of the SEM samples, previous to its introduction in the microscope, the samples were covered with a thin carbon layer to assure that the sample on the grid is conductive. The low energy incident electrons on a specimen produce secondary electrons due to the emission of valence electrons of the constituent atoms, at the top surface of the sample. These emitted electrons form standard topography images using the Lower Electron Detector (LED), or high-resolution topography images using the Upper Electron Detector (UED).

UV-Vis measurements. UV-Vis measurements were performed with an Evolution 300 UV-Vis spectrometer (Thermo Fisher Scientific, USA) in the $200 - 600\ \text{nm}$ wavelength range. UV-Vis experiments were performed for samples with $C_{\text{SWCNTs}} = 0.02\ \text{mg/mL}$ and $\text{pH} = 5, 7, \text{ and } 9$. In all cases, $C_{\text{PAA}} = 2\ \text{wt\%}$.

First, we will present how pH controls the rheological behavior of the PAA solutions at different concentrations for the specific degree of polymerization used here. Next, we will present the results when small quantities of SWCNTs are added to the PAA solutions.

3.4. Rheology results for PAA

Flow curves. Figure IV.26 shows flow curves obtained by increasing the applied shear strain rate (linear ramp). The plot presents an example at $C_{\text{PAA}} = 3\ \text{wt\%}$. There is a variation of the stress response, increasing as the pH increase. The behavior becomes very similar at pH 7 and 9. Non-

linearity is evident, as for viscoelastic systems. A plateau is never found even at a very high shear rate, so the behavior is different from the WMLs behavior.

Viscosity. Figure IV.28 presents the apparent viscosity curves, $\eta(\dot{\gamma})$, for the polyelectrolyte solutions at low concentration and different pH values. These curves are determined by steadily increasing the shear rate. In all cases, the solutions shear thin. Thixotropic loops do not present hysteresis (not shown). In general, the viscosity is small and increases with pH at a fixed concentration, (Figure IV.28a for $C_{\text{PAA}} = 1$ wt%, Figure IV.28b for 3 wt % and Figure IV.28c for 6 wt%). The curves with the lowest values that we measured correspond to $C_{\text{PAA}} = 1$ wt%; here, $\eta \sim 0.2$ Pa s at low $\dot{\gamma}$ and $\text{pH} = 9$. For a fixed pH, viscosity increases with the polymer concentration (Figure IV.28d). In dilute solutions, the contribution from different coils is additive, and solution viscosity increases nearly linear with polymer concentration above the solvent viscosity, and after some concentration, viscosity increases nonlinearly [12]. The behavior of the polyelectrolyte of interest here is consistent with previous studies developed for polyelectrolytes [84] [86]. At high pH, the polymer has a more extended structure that promotes entangling, which also increases as the polyelectrolyte concentration increases. When the system is sheared, the flow forces the polymer to align, dropping the energy dissipation, and as a consequence viscosity decays. This is apparently the reason of shear thinning as pH and polymer concentration increase.

Figure IV.27a presents $\eta_0 = \lim_{\dot{\gamma} \rightarrow 0} \eta(\dot{\gamma})$ as a function of pH for different polymer concentrations. η_0 increases from low values, close to the solvent viscosity, up to more than three units when pH is high (7 – 9), and when the polymer concentration is above 4 wt%. Figure IV.27b presents η_0 vs. C_{PAA} at different pH values, here it is easier to observe that above $\text{pH} = 5$ and at $C_{\text{PAA}} \sim 4$ wt% there is a change of behavior. Below this concentration, the interaction between polymer molecules is not significant as in the dilute regime, i. e., the viscosity is low and relatively close to the solvent viscosity. After this concentration, viscosity increases drastically as in the semidilute regime because polymer molecules begin to entangle with each other. Our estimate for the overlap concentration is $C_{\text{PAA}}^* \sim 4$ wt% for $\text{pH} \geq 5$.

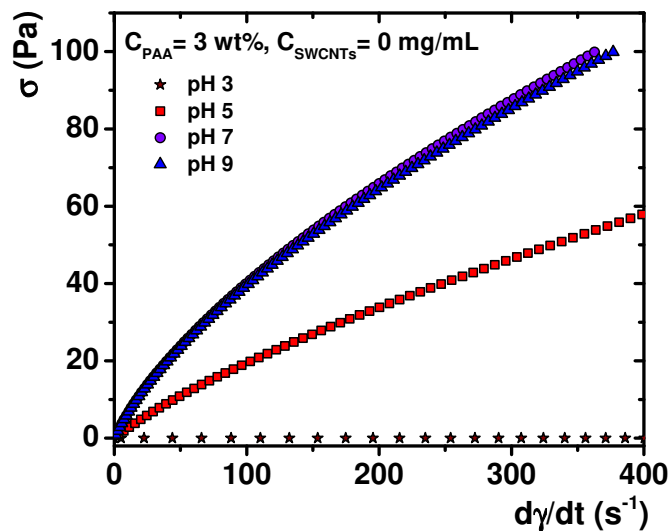


Figure IV.26 Flux curves for a constant concentration $C_{\text{PAA}} = 3$ wt%. There is a notable dependence on the pH. Here the solution of PAA has no SWCNTs added.

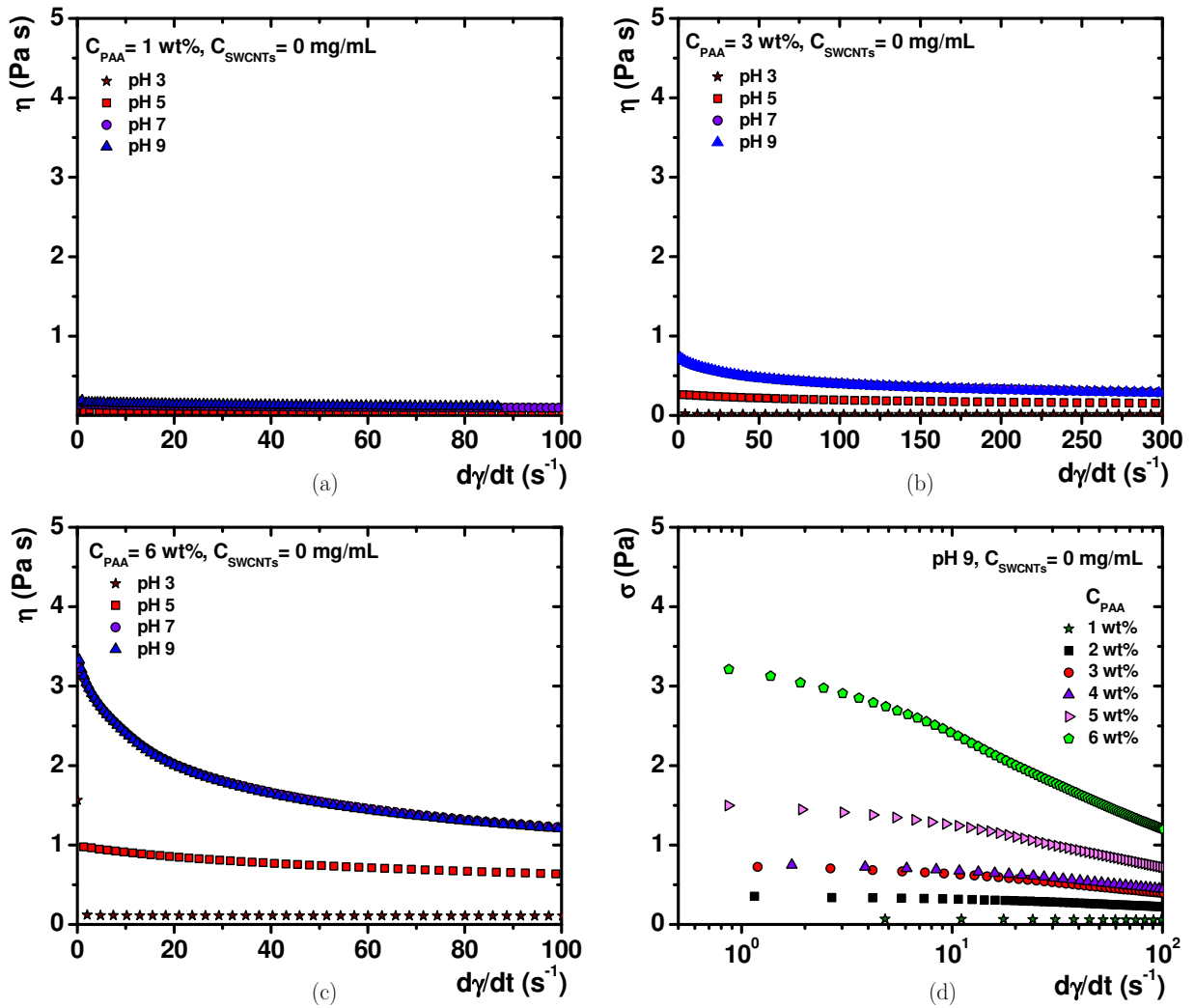


Figure IV.28 Apparent viscosity for the polyelectrolyte solutions at different pH and polymer concentration. (a) Constant concentration, $C_{PAA} = 1 \text{ wt\%}$, (b) constant concentration, $C_{PAA} = 3 \text{ wt\%}$, (c) constant concentration, $C_{PAA} = 6 \text{ wt\%}$. (d) $\eta(\dot{\gamma})$ for different PAA concentration and constant pH = 9.

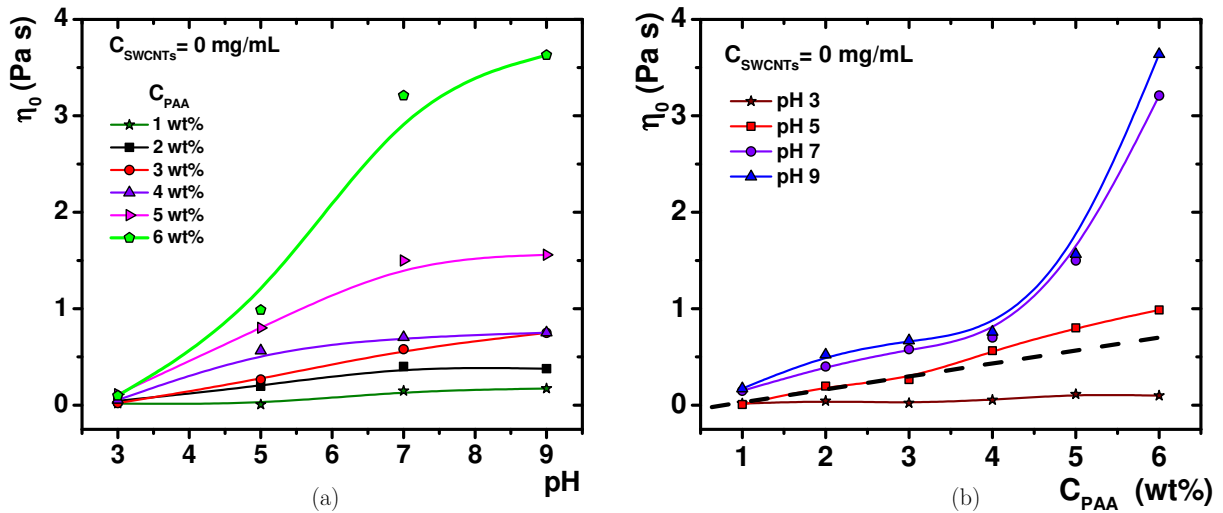


Figure IV.27 (a) η_0 vs. pH for different polymer concentrations. Lines are a guide to the eye. (b) η_0 vs. C_{PAA} at various pH values. The black dash line at pH = 5 shows where η_0 is no longer linearly dependent on C_{PAA} .

Viscoelastic spectra. The shear modulus, $G(t)$, exhibits a significant time or frequency dependence observed in the complex modulus $G^*(\omega) = G'(\omega) + iG''(\omega)$ (equation (III.1.20)). Figure IV.29 presents some examples of the viscoelastic spectra of PAA solutions for different concentrations and pH (1 wt% and 6 wt%). In general, the solutions are more viscous at low frequencies, and after the crossing point, (ω_0, G_0) they are more elastic, as in a typical viscoelastic fluid. Both moduli increase as pH increases, at a constant C_{PAA} as illustrated in Figure IV.29 for pH = 3, 5, 7, and 9. The increment between pH = 3 and pH = 5 can reach an order of magnitude, but this increment decreases between higher pH values. Figure IV.30a presents the variation of $G'(\omega)$ and $G''(\omega)$ as a function of C_{PAA} , at fixed pH = 9. As the concentration increases, both curves move upwards to larger moduli values. The whole behavior of the viscoelastic spectra can be summarized in Figure IV.30b, where G_0 vs. ω_0 is plotted for the PAA solutions measured at different pH and concentrations. All the crossing points collapse in a single exponential curve. For solutions with a low C_{PAA} or low pH, we find their corresponding crossing points in the lower part of the curve, as C_{PAA} or pH increase they move upward along the exponential locus. Surely, this relation between G_0 and ω_0 is far from being an accident and deserves more research to understand its physical origin.

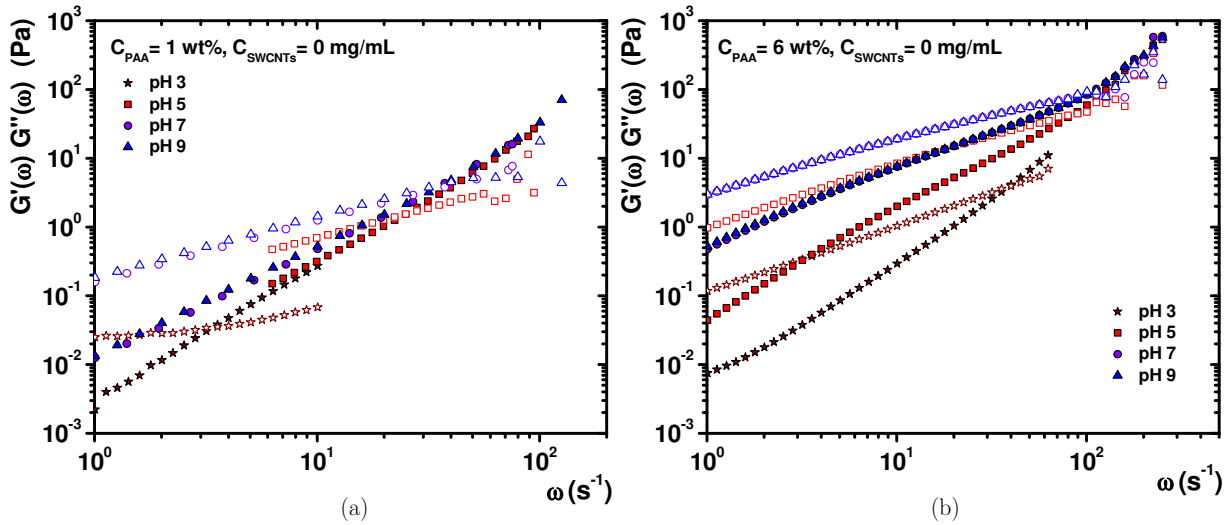


Figure IV.29 Viscoelastic spectra of PAA solutions for different values of concentrations and pH: (a) $C_{PAA} = 1$ wt%, (b) $C_{PAA} = 6$ wt%. Full symbols are for the elastic modulus, open symbols are for the viscous modulus.

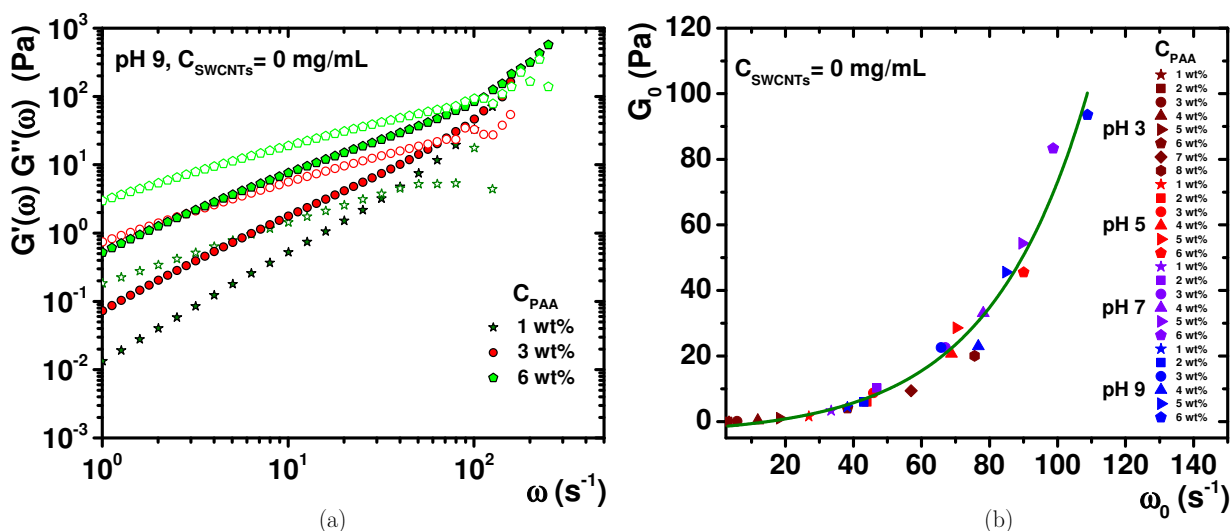


Figure IV.30 Viscoelastic spectra of PAA. (a) $G'(\omega)$ and $G''(\omega)$ as a function of the polyelectrolyte concentration, at constant pH = 9. Full symbols are for the elastic modulus, open symbols are for the viscous modulus. (b) The relation between G_0 vs. ω_0 defined by the crossing points as a function of pH and concentration. Green line is an exponential fitting for all the crossing points.

3.5. Mesoscale structure of SWCNTs/PAA suspensions

Structure and rheology behavior are intimately related. First, we determined how the microstructure of the PAA polyelectrolyte is affected by the addition of SWCNTs at different pH values, performing UV-Vis, SEM, TEM, and AFM experiments. From these experiments, we have shown that the SWCNTs are less exfoliated in suspensions at pH = 9, and apparently, they are forming bundles entangled with PAA molecules. Therefore, the rheological behavior of this system will be dominated by the mesoscale superstructure at concentrations close to the mechanical percolation threshold at high pH.

3.5.1. UV-Vis spectra

UV-Vis has been used to determine the degree of exfoliation of the SWCNTs in a polymer matrix [167] [168]. An absorbance increment corresponds to exfoliation of the SWCNTs bundles in the suspension. Bundles are transformed by the action of a dispersant agent from thick bundles to thin bundles or single nanotubes. UV-Vis experiments were carried out to determine the effect of pH on the degree of exfoliation of SWCNTs in our suspensions, and they will be a useful piece of information to understand the rheological behavior of the suspensions. Figure IV.31a presents our UV-Vis measurements for the SWCNTs/PAA suspensions at three different pH values that are similar to those obtained for PAA in Ref. [167]. They reveal that the SWCNTs are more exfoliated at pH = 5 in comparison to pH = 7 and pH = 9. As we increase pH, the degree of exfoliation decays; visual inspection also confirmed the formation of tiny clusters. This behavior is similar to the case when SWCNTs are exfoliated in water dispersions, using sodium dodecyl sulfate (SDS) as a dispersing agent (Figure IV.31b) [169].

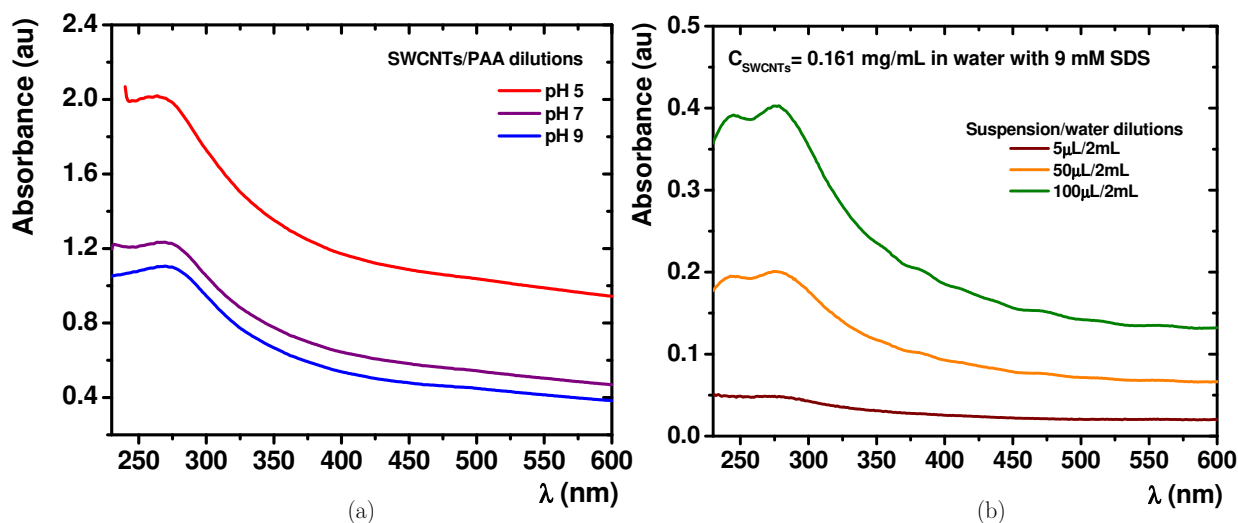


Figure IV.31 (a) UV-vis spectra of SWCNTs/PAA suspensions at different pH values. $C_{\text{SWCNTs}} = 0.02$ mg/mL and $C_{\text{PAA}} = 2$ wt%. (b) The same shape in the spectra for different dilutions of SWCNTs at $C_{\text{SWCNTs}} = 0.161$ mg/mL, suspended in water with 9 mM SDS.

We used it to verify the validity of our preparation in comparison to the results in the literature, which resulted quite similar. Although there is no standard to determine analytically how many exfoliated SWCNTs are in a polymer dispersion to generate a calibration curve (absorbance vs. concentration of exfoliated SWCNTs at $\lambda = 280$ nm) [170], at high dilution, with most of the CNTs exfoliated, we estimated that the number of exfoliated SWCNTs at pH = 5 is around twice those at pH = 9. Previous reports indicate as pH increases, the mechanical percolation point is found first, and at a higher pH the electrical percolation point is reached [168].

3.5.2. Observation with electron microscopy (TEM and SEM)

Figure IV.32a presents a high voltage 100 kV, TEM image of a suspension sample ($C_{\text{SWCNTs}} = 0.05$ mg/mL, $C_{\text{PAA}} = 1$ wt%, pH = 9) where entangled SWCNTs are observed inside the polymer matrix. Here, all planes of the sample are projected on the 2D image since electrons are traversing the whole sample thickness. In this image, we observe SWCNTs forming thick bundles although their concentration is relatively low. In general, secondary electron SEM image (LED) of specimens made of SWCNTs (0.02 mg/mL)/PAA (2 wt%) presents a uniform flat surface covered with globules with elongated protrusions without an apparent structure (not shown). However, using high-resolution low voltage (3 kV) SEM secondary electrons (UED) in samples at pH = 9, the polymer and the SWCNTs seem to interact to form thick rods (length of several micrometers and diameter of ~ 0.5 μm) or surfaces that wind themselves up as shown in Figure IV.32b-d; this does not occur in specimens at low pH. We note that these structures last enough to be observed, notwithstanding the samples were vacuum dried for inspection in the electron microscopes.

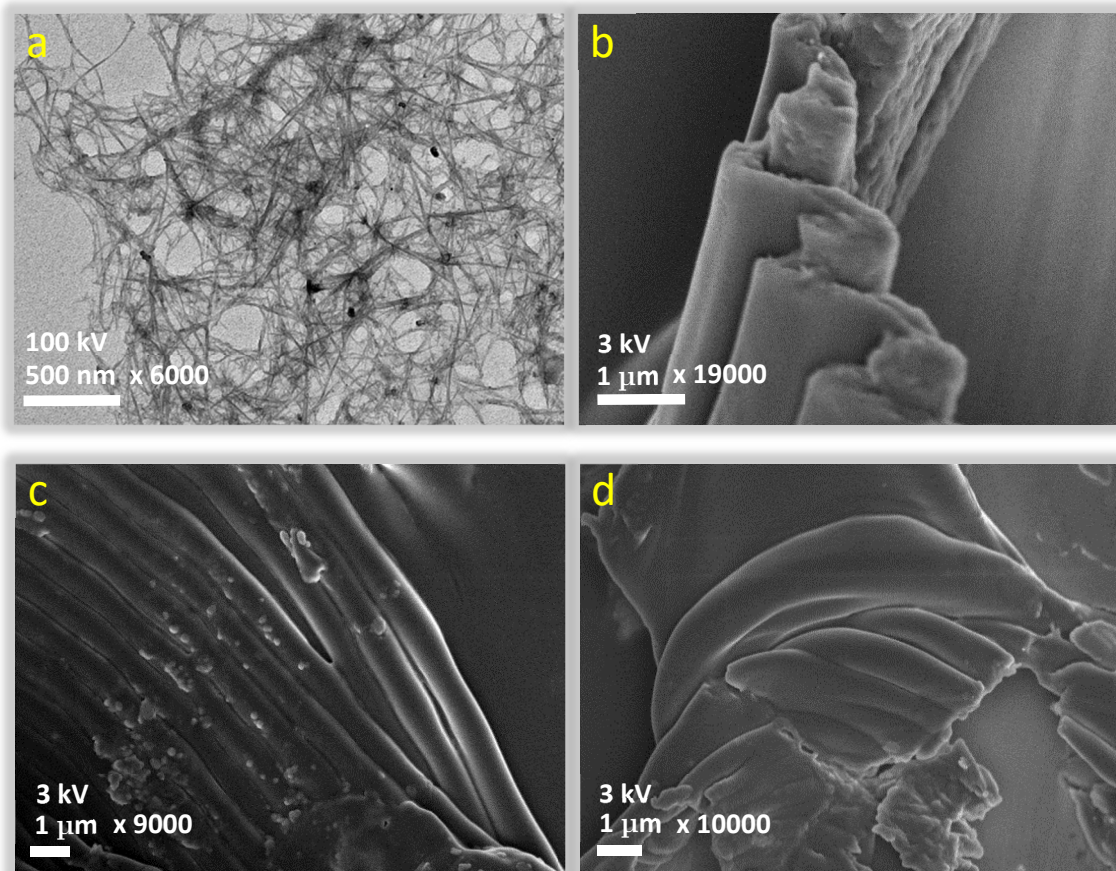


Figure IV.32 Electron microscopy images of SWCNTs/PAA suspensions. (a) TEM image: $C_{\text{SWCNTs}} = 0.05 \text{ mg/mL}$, $C_{\text{PAA}} = 1 \text{ wt\%}$ at $\text{pH} = 9$. (b–d) High-resolution secondary electron SEM images (UED): $C_{\text{SWCNTs}} = 0.02 \text{ mg/mL}$, $C_{\text{PAA}} = 2 \text{ wt\%}$, at $\text{pH} = 9$.

3.5.3. Observation with atomic force microscopy (AFM)

At low pH values ≤ 7 , topographic images do not reveal any structure (not shown), we observe just irregular globular domains over a relatively flat surface. At $\text{pH} = 9$, our observations changed dramatically. Figure IV.33 is a set of amplifications of the same area in the inspected specimen. Figure IV.33a presents a $50 \times 50 \mu\text{m}$ topographic image where linearly oriented bead chains are easily observed. In a further amplification (Figure IV.33b, $15 \times 15 \mu\text{m}$) we observe that the beads forming the chain have a diameter of $\sim 0.5 \mu\text{m}$ and they seem to have some structure that is revealed in Figure IV.33c ($2 \times 2 \mu\text{m}$). Here, the beads apparently are formed by stacks of rods, where these stacks are not all following the same direction. A further amplification shows the rods in a $0.8 \times 0.8 \mu\text{m}$ image, in Figure IV.33d. The thickness of these rods is in the range of $\sim 50 - 70 \text{ nm}$, and the length is difficult of observing because they overlap with other stacks, but they are larger than $0.8 \mu\text{m}$.

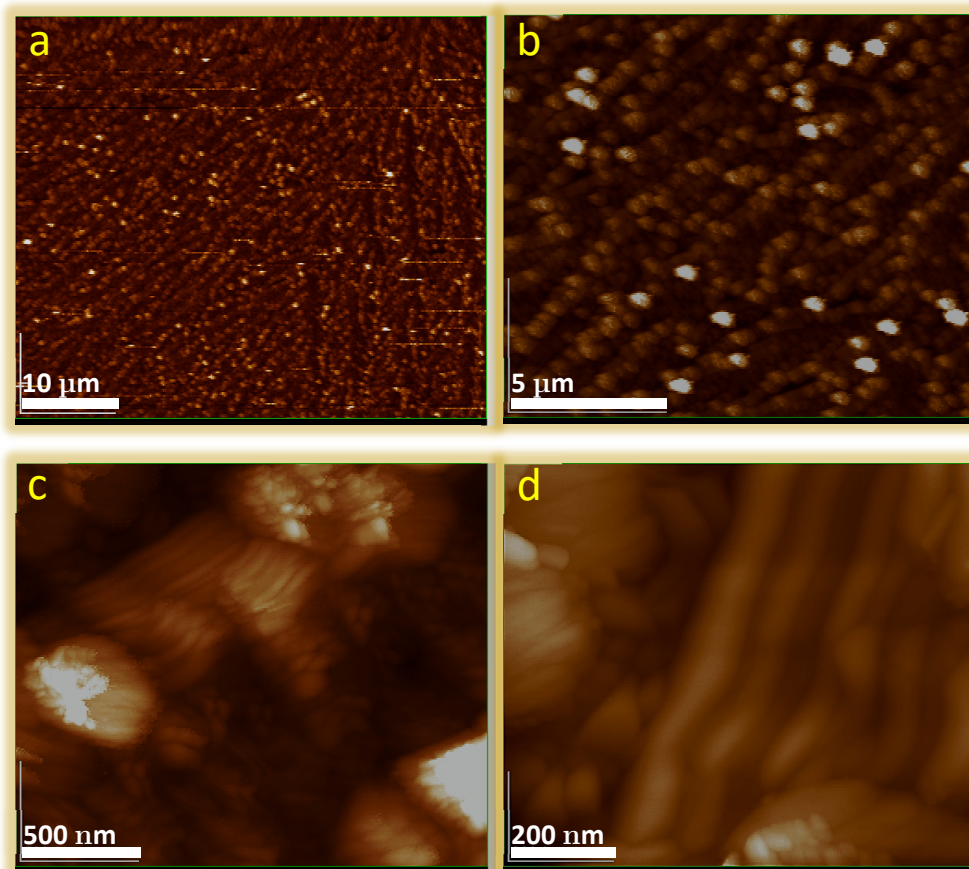


Figure IV.33 Topographic images at successive different amplifications with AFM of a specimen of $C_{\text{SWCNTs}} = 0.01 \text{ mg/mL}$ dispersed in $C_{\text{PAA}} = 2 \text{ wt\%}$ at $\text{pH} = 9$.

3.6. Rheology results for SWCNTs/PAA

Viscosity. Figure IV.34 presents how the flow curves, η vs. $\dot{\gamma}$, are modified varying the quantity of SWCNTs added to the liquid mixtures, at different pH values. All curves were determined by steadily increasing the shear rate. In all the cases, the suspensions shear thin and thixotropic loops do not show hysteresis (not shown). At high shear rates ($\dot{\gamma} \geq 100 \text{ s}^{-1}$), the viscosity of the suspensions is even smaller than those for the pure polymer solutions (Figure IV.28), as observed in Figure IV.34a for $C_{\text{PAA}} = 1 \text{ wt\%}$, and $C_{\text{SWCNTs}} = 2 \text{ mg/mL}$, or Figure IV.34b for $C_{\text{PAA}} = 2 \text{ wt\%}$, and $C_{\text{SWCNTs}} = 1 \text{ mg/mL}$. This behavior can be observed in Figure IV.34c even at the lowest concentrations of CNTs, for $C_{\text{PAA}} = 3 \text{ wt\%}$ and $C_{\text{SWCNTs}} = 0.5 \text{ mg/mL}$. In some cases, there are more than two orders of magnitude difference. When the system is highly sheared, in addition to the polymer alignment, the flow also tends to align rod-shaped colloids along the fluid flow direction dropping, even more, the energy dissipation as in paranematic phases [171]; as a consequence, viscosity decays dramatically. The addition of SWCNTs introduces a significant interaction between the polymer and the SWCNTs, in spite that polymer molecules are far enough to prevent their interaction as in $C_{\text{PAA}} = 3 \text{ wt\%}$; the pure polymer solution is below its c^* . All cases of combination between concentration of PAA and concentration of SWCNTs were obtained, but not all of them

are shown. In the published paper of this work, we show other cases [166]. In many cases, the apparent viscosity increases as pH increases at fixed C_{PAA} and C_{SWCNTs} ; although at large $\dot{\gamma}$, η is slightly larger at pH = 7 than at pH = 9 or they are approximately equal. Figure IV.34d shows how the viscosity increases with the addition of CNTs for $C_{\text{PAA}} = 6 \text{ wt}\%$ and pH = 9. At low $\dot{\gamma}$, the suspensions present a dramatic change in the value of the viscosity for pH = 7 and pH = 9. Viscosity increases several orders of magnitude ($\sim 3 - 4$) with respect to its value at large $\dot{\gamma}$, as shown in Figure IV.35 for some typical examples for pH = 7 (it includes a comparison with two cases without SWCNTs, $C_{\text{PAA}} = 3 \text{ wt}\%$ and $4 \text{ wt}\%$); for pH = 5 the viscosity increases, but in the range of one order of magnitude (not shown). This seems that the system forms a structure when it is quiescent that does not resist deformation.

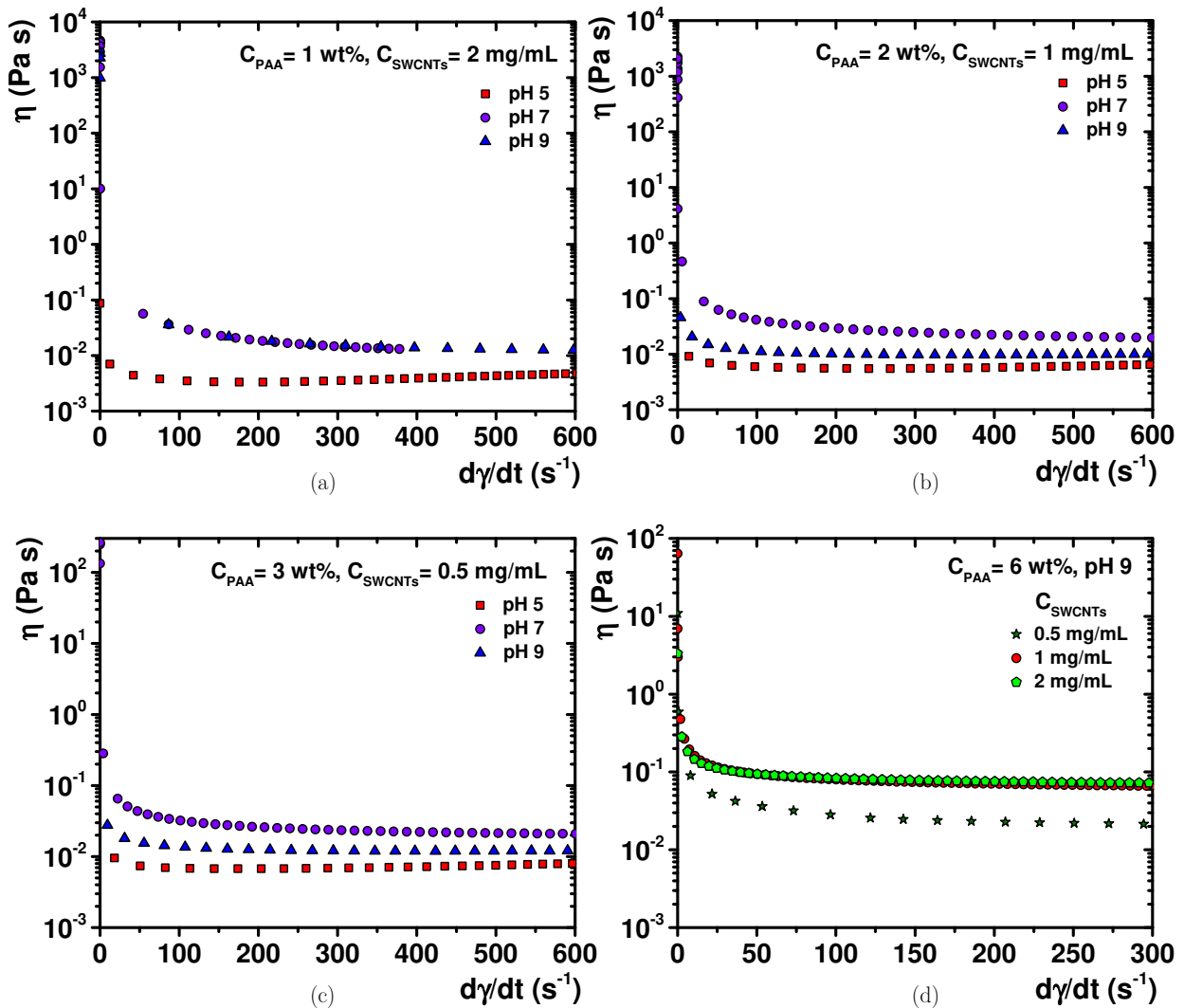


Figure IV.34 Apparent viscosity of the polyelectrolyte solutions at different pH values (5, 7, and 9) where small quantities of SWCNTs have been added. (a) η vs. $\dot{\gamma}$ for a suspension with $C_{\text{PAA}} = 1 \text{ wt}\%$ and $C_{\text{SWCNTs}} = 2 \text{ mg/mL}$. (b) η vs. $\dot{\gamma}$ for $C_{\text{PAA}} = 2 \text{ wt}\%$ and $C_{\text{SWCNTs}} = 1 \text{ mg/mL}$. (c) η vs. $\dot{\gamma}$ for $C_{\text{PAA}} = 3 \text{ wt}\%$ and $C_{\text{SWCNTs}} = 0.5 \text{ mg/mL}$. (d) η vs. $\dot{\gamma}$ varying C_{SWCNTs} at constant $C_{\text{PAA}} = 6 \text{ wt}\%$ and pH = 9.

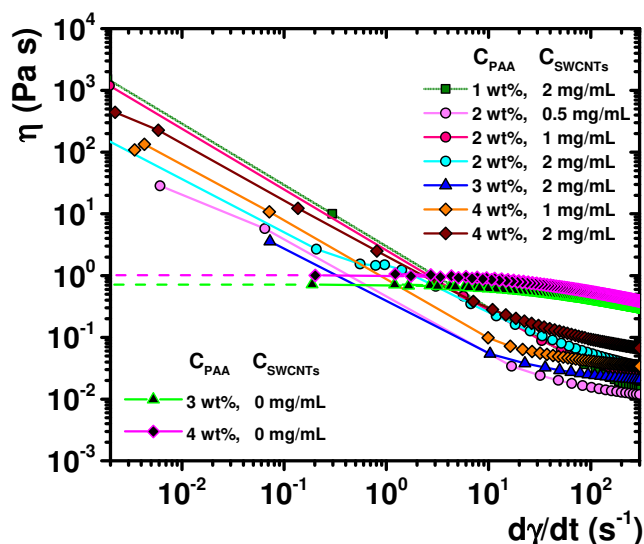


Figure IV.35 Viscosity at low shear rate for some typical examples at pH = 7. A comparison without SWCNTs is shown for the cases of $C_{\text{PAA}} = 3 \text{ wt}\%$ and $4 \text{ wt}\%$. It helps to visualize the differences in viscosity when CNTs are added. Dashed lines are linear extrapolations to zero shear viscosity. All lines are a guide to the eye.

Viscoelastic spectra. Figure IV.37 presents measured viscoelastic spectra of SWCNTs/PAA suspensions for different concentrations in both components and pH. At $C_{\text{PAA}} = 1 \text{ wt}\%$ and $C_{\text{SWCNTs}} = 1 \text{ mg/mL}$, the suspensions are still viscoelastic (Figure IV.37a). G_0 and ω_0 , both increase as the pH increases, but they are smaller, even at these low concentrations than those corresponding to the pure polymer solution (Figure IV.29a). In the Figure IV.37b, we observe a significant change in the rheological behavior at pH = 7 and pH = 9, when more SWCNTs are added to the suspension ($C_{\text{SWCNTs}} = 2 \text{ mg/mL}$). The crossing point disappears, $G'(\omega) > G''(\omega)$ for approximately three decades of ω with a ratio between them of ~ 10 , and the elastic modulus remains essentially constant at low frequencies. Therefore, the suspension behaves like a solid gel [172]. The same loss of viscoelasticity occurs at other low polymer concentrations, as in the case of $C_{\text{PAA}} = 3 \text{ wt}\%$, with $C_{\text{SWCNTs}} = 0.5 \text{ mg/mL}$ or $C_{\text{SWCNTs}} = 2 \text{ mg/mL}$ presented in Figure IV.37c and Figure IV.37d, respectively. In this case, a less amount of added nanotubes is needed to lose the crossing point; at least $C_{\text{SWCNTs}} = 0.5 \text{ mg/mL}$ is enough. However, in all the cases of Figure IV.37, at pH = 5, the suspensions are still viscoelastic. There is a change in the order of the moduli curves as can be noted in Figure IV.37c. In this case, the spectra at pH = 7 present larger values of $G'(\omega)$ and $G''(\omega)$, than those corresponding to pH = 9.

At $C_{\text{PAA}} = 4 \text{ wt}\%$, with a small (Figure IV.36a) or a large (Figure IV.36b) C_{SWCNTs} , the moduli for pH = 7 and pH = 9 goes back to the standard order (curves at pH = 9 \geq pH = 7); in this case, there are no cross points neither. Here, at pH = 5, below the crossover, both $G'(\omega)$ and $G''(\omega)$ approximately coincide. Figure IV.36c presents an example of how the moduli vary as C_{SWCNTs} increases at fixed pH = 7 and $C_{\text{PAA}} = 3 \text{ wt}\%$. In Figure IV.37b and d and Figure IV.36b, we observe that $G'(\omega)$ does not vary too much along two or three orders of magnitude. In a log-log plot, the moduli depend linearly on the frequency with a small slope (almost frequency independent).

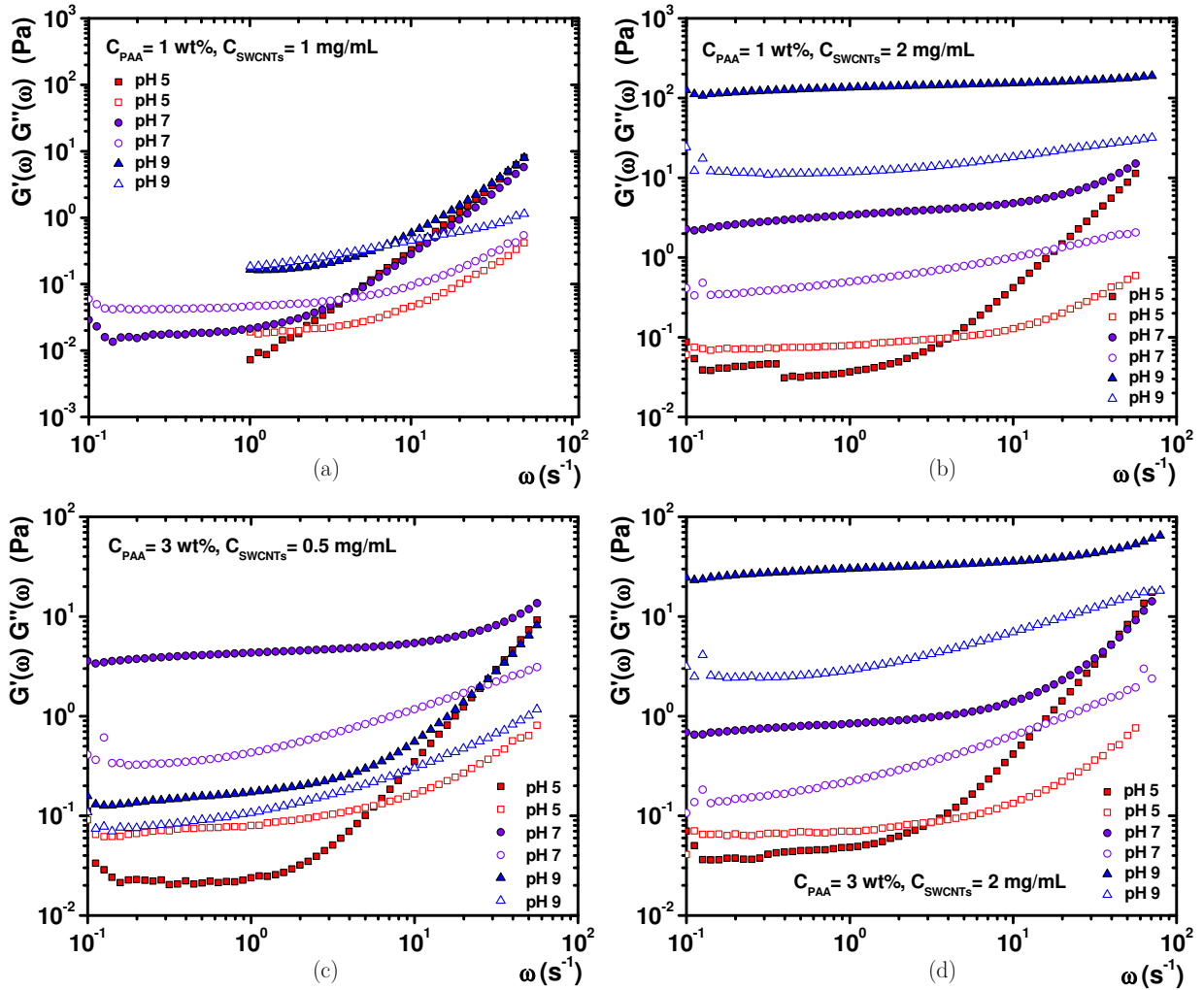


Figure IV.37 Viscoelastic spectra for SWCNTs/PAA water suspensions at different concentrations and pH. Full symbols, $G'(\omega)$; open symbols, $G''(\omega)$. (a) $C_{\text{PAA}} = 1 \text{ wt\%}$ and $C_{\text{SWCNTs}} = 1 \text{ mg/mL}$. (b) $C_{\text{PAA}} = 1 \text{ wt\%}$ and $C_{\text{SWCNTs}} = 2 \text{ mg/mL}$. (c) $C_{\text{PAA}} = 3 \text{ wt\%}$ and $C_{\text{SWCNTs}} = 0.5 \text{ mg/mL}$. (d) $C_{\text{PAA}} = 3 \text{ wt\%}$ and $C_{\text{SWCNTs}} = 2 \text{ mg/mL}$. pH = 5, 7, and 9.

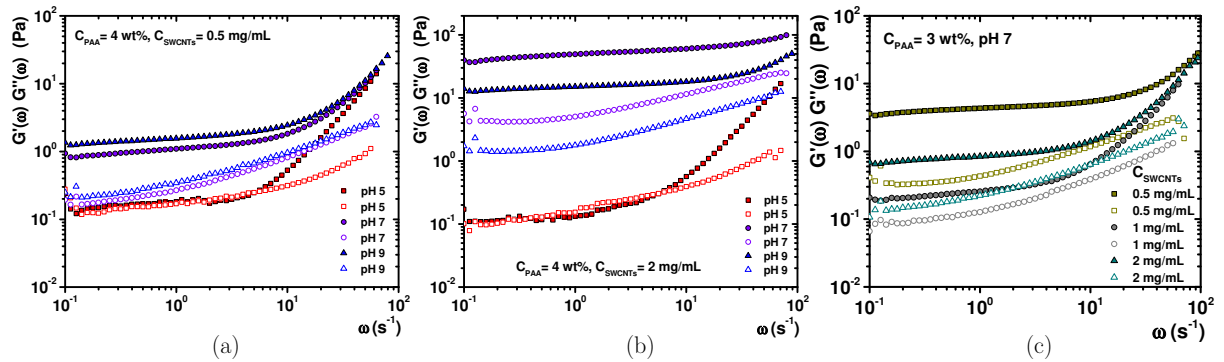


Figure IV.36 Viscoelastic spectra for SWCNTs/PAA water suspensions. Full symbols, $G'(\omega)$; open symbols, $G''(\omega)$. (a) $C_{\text{PAA}} = 4 \text{ wt\%}$ and $C_{\text{SWCNTs}} = 0.5 \text{ mg/mL}$. pH = 5, 7, and 9. (b) $C_{\text{PAA}} = 4 \text{ wt\%}$ and $C_{\text{SWCNTs}} = 2 \text{ mg/mL}$, for all three pH values. (c) $C_{\text{PAA}} = 3 \text{ wt\%}$ and pH = 7 when the C_{SWCNTs} is varied.

3.7. Rheological model for the SWCNTs/PAA suspensions

As mentioned before, the inter-tube attraction in SWCNTs dispersed in polymers yields to the formation of aggregates or bundles even at a modest concentration. At the percolation concentration, a matrix spanning network must be formed that give rise to elasticity, because nanotubes are arrested; as the number of nanotubes increases the elasticity of the composite increases. Around this percolation concentration, the rheological behavior must be dominated by that mesoscale superstructure. SEM and AFM surveys show that the SWCNTs/PAA suspensions presented a mesoscopic structure as pH reached high values. On the other hand, UV-Vis spectra also indicate that exfoliated nanotubes, *i. e.*, individual entities or very thin bundles are present at low pH; but at high pH, they form bundles. Furthermore, viscoelastic spectra also show that the liquid-like viscoelastic behavior is lost in place of a solid-like at high pH values. Here, at $\text{pH} \leq 5$, $G'(\omega) < G''(\omega)$ at $\omega < \omega_0$ and $G'(\omega) > G''(\omega)$ at $\omega > \omega_0$; when pH reaches a value > 5 , $G'(\omega) \gg G''(\omega)$. At high pH, η_0 also grows up to huge numbers as $\dot{\gamma} \rightarrow 0$ similar to what occurs when a weak structure is formed within the fluid, which is quiescent at rest, but it does not resist deformation.

Crosslinking materials form molecular clusters that can grow in size. When the largest cluster diverges in size, at the percolation concentration, a transition from liquid to solid occurs (sol-gel). Materials at this transition or gel point are known as critical gels, as has been mentioned in Chapter II. In general, for critical gels, the long-range connectivity in the material can be reached by different mechanisms. In one named chemical gelation, permanent covalent bonds connect molecular strands into a three-dimensional network. In the other named physical gelation (strong and weak), bonds are temporary, of reversible nature, and the average lifetime of such bonds are long compared with the observation time (see section dedicated to gels in Chapter II). Here, the system under study is behaving like a weak physical gel but presenting some features of strong physical gels; the crosslinking is due to the attractive interaction that is tuned by pH. The overall interaction potential between the suspended CNTs stems from a balance between the van der Waals forces and the pH-sensitive charged moieties of the adsorbed polymeric layer on the tubes. Also, polymers in the polymeric layer can entangle with other polymers free or adsorbed in other polymeric layers. H. H. Winter and co-workers have characterized critical gels where dynamic arrest leads to gelation due to attractive interactions [60]. Since our suspensions apparently are forming a physical gel, we used these arguments to find where they reach the gel point (see equations (II.8.1)-(II.8.4)).

Figure IV.38 shows some examples of how the experimental measured $\tan \delta = G''(\omega)/G'(\omega)$ depends on ω for different PAA and SWCNTs concentrations, when pH is varied. We included the case of pure PAA just for contrasting the results obtained with the suspensions. In Figure IV.38a we see the case where $C_{\text{PAA}} = 1 \text{ wt}\%$ and $C_{\text{SWCNTs}} = 1 \text{ mg/mL}$; here there is a dependence on frequency even when CNTs are added. This is consistent with Figure IV.37a, where the system is viscoelastic for all pH values. In all plots of Figure IV.38, we observe that $\tan \delta$ for pure PAA is not a constant because it is far from forming a gel at these concentrations. However, when we add a small amount of SWCNTs (0.5 mg/mL) to the polymer ($C_{\text{PAA}} = 2 \text{ wt}\%$ or $3 \text{ wt}\%$, Figure IV.38b and c), the behavior of the curve $\tan \delta$ vs. ω turns out to be completely different. For $\text{pH} = 7$ and $\text{pH} = 9$, $\tan \delta$ is small but essentially constant along three orders of magnitude of ω . For $\text{pH} = 5$, $\tan \delta$ is small,

but it is not a constant. Apparently, the system is close to gel point when $\text{pH} \geq 7$, at these concentrations. The same is observed when we increase the concentration of CNTs as seen in Figure IV.38d ($C_{\text{PAA}} = 2 \text{ wt\%}$ and $C_{\text{SWCNTs}} = 1 \text{ mg/mL}$), or Figure IV.38e for the case of $C_{\text{PAA}} = 1 \text{ wt\%}$ and $C_{\text{SWCNTs}} = 2 \text{ mg/mL}$; here it is possible to see that we are close to the gel point when $\text{pH} > 5$. Several combinations of C_{PAA} up to 6 wt% and CNTs present a similar pattern (not shown).

Depending on how good the system behaves with the proposed model, n will be a constant that does not depend on the frequency at the gel point. The suspensions that present less variation in the experimental $\tan \delta$ vs. ω plots were used to calculate the best horizontal line fit along three orders of magnitude in ω to give the exponent n , using $\tan \delta = \tan(n\pi/2)$ (equation (II.8.4)).

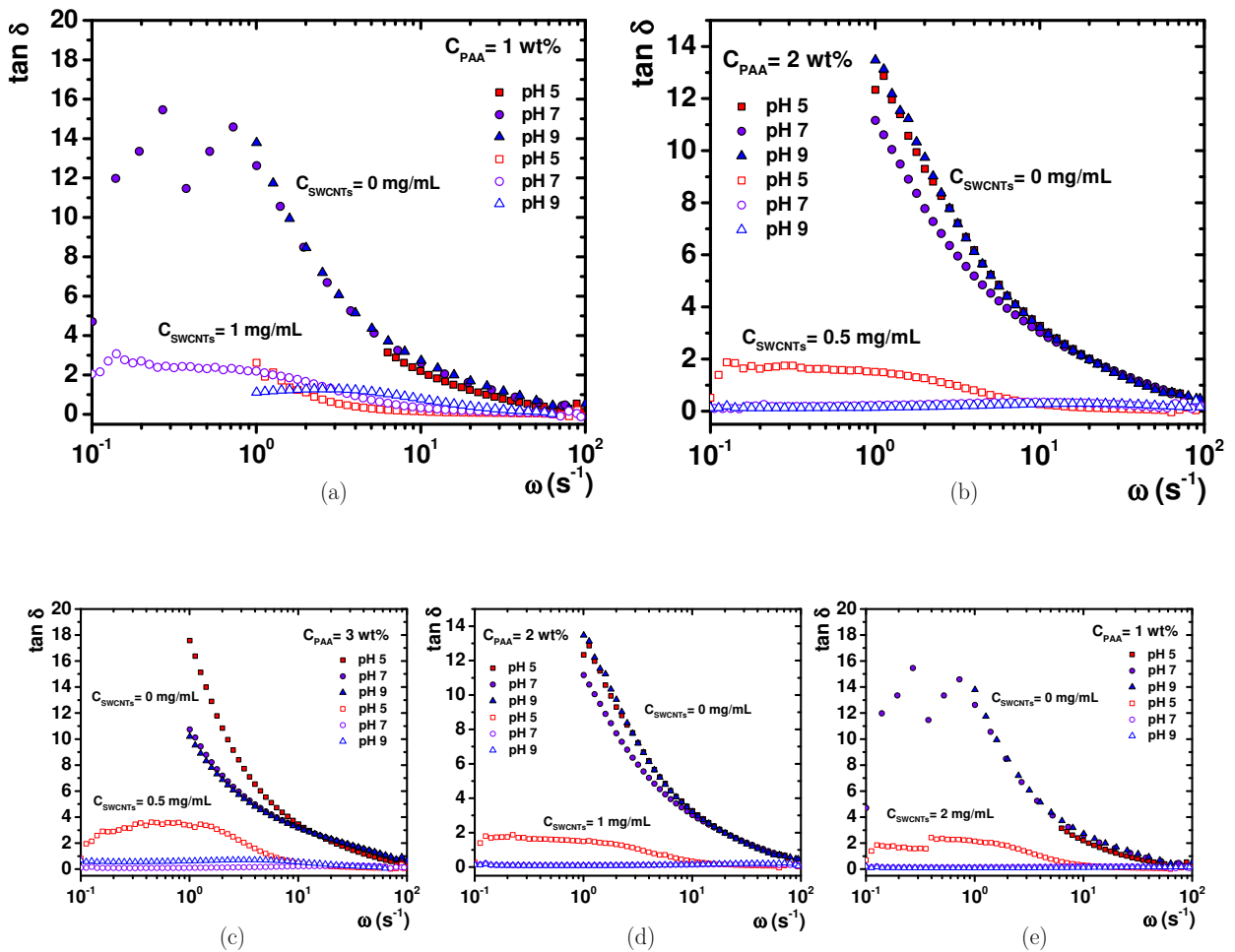


Figure IV.38 $\tan \delta$ vs. ω for pure PAA (full symbols) and SWCNTs/PAA suspensions (open symbols) as a function of pH. (a) $C_{\text{PAA}} = 1 \text{ wt\%}$ and $C_{\text{SWCNTs}} = 1 \text{ mg/mL}$. (b) $C_{\text{PAA}} = 2 \text{ wt\%}$ and $C_{\text{SWCNTs}} = 0.5 \text{ mg/mL}$. (c) $C_{\text{PAA}} = 3 \text{ wt\%}$ and $C_{\text{SWCNTs}} = 0.5 \text{ mg/mL}$. (d) $C_{\text{PAA}} = 2 \text{ wt\%}$ and $C_{\text{SWCNTs}} = 1 \text{ mg/mL}$. (e) $C_{\text{PAA}} = 1 \text{ wt\%}$ and $C_{\text{SWCNTs}} = 2 \text{ mg/mL}$. pH = 5, 7, and 9.

Predictions of the moduli were made using $G'(\omega) = G'_c \omega^n$ and $G''(\omega) = G''_c \omega^n$ (equations (II.8.1)), where the fitting parameters S , G'_c and G''_c were obtained (equation (II.8.2)). Figure IV.39 presents the predicted and experimental moduli for those cases very close to the gel point that turned out to be the suspensions with pH = 9, and in less degree pH = 7. A comparison is also made for the cases with pH = 5, where the system is viscoelastic in all cases. In Figure IV.39a there is the case for $C_{\text{PAA}} = 1$ wt% and $C_{\text{SWCNTs}} = 2$ mg/mL. Here, for pH = 9 the prediction of $G'(\omega)$ is excellent and for $G''(\omega)$ is reasonable for two orders of magnitude in ω ; for pH = 7, the prediction for $G'(\omega)$ goes through two decades, and for $G''(\omega)$ is reasonable for one and a half. The parameters are given in the figure. The same occurs for the case of $C_{\text{PAA}} = 2$ wt%, but here the gel point seems to be closer when $C_{\text{SWCNTs}} = 2$ mg/mL rather than when $C_{\text{SWCNTs}} = 1$ mg/mL, both at pH = 9 and 7 (Figure IV.39b and c). As expected, the S value is higher for $C_{\text{SWCNTs}} = 2$ mg/mL (Figure IV.39c) indicating that the number of contacts between nanotubes is larger, and as a consequence more elastic. On the other hand for $C_{\text{SWCNTs}} = 1$ mg/mL, although S is still large, elasticity is lower than before (Figure IV.39b). For all cases in Figure IV.39, the experimental n values we found are small ($n = 0.07 - 0.08$), but relatively close to those found in other physical gels for instance, thermoplastic elastomeric polypropylene ($n = 0.13 - 0.18$) [173], and fd virus-PNIPAM ($n = 0.08 - 0.130$) [61]. For physical gels, n values are usually much smaller than those for chemical gels that usually are larger than 0.5, revealing that the size distribution of the mesoscale superstructure is not as open as in the chemical gels. Therefore, we consider that our results for the system of interest here are in agreement with those of physical gels close to the gel point.

The gel of SWCNTs/PAA can be visualized by a cartoon given in Figure IV.40 that summarizes all our findings. In the suspension at pH = 5, CNTs are exfoliated and dispersed by the almost neutral coil-like polymer molecules adsorbed on them, as determined by the UV-Vis spectrum. The contacts between CNTs are mainly through polymer entangling, and the suspension is viscoelastic. As pH increases, the polymer is charged, and the solution is not so good solvent for the CNTs (pH > 5). Here, bundles are formed, and at some point, they mechanically percolate along the fluid and become arrested. As a consequence, the rheological behavior must be dominated by the formed mesoscale superstructure. In particular, viscoelasticity is lost, and the suspension becomes more elastic. At even higher pH, the surroundings for CNTs are worst, and bundles grow to a larger extent as determined by UV-Vis, up to the point that they can be observable by SEM and AFM. In particular mixtures, the suspension reaches the gel point, where a power law can model the relaxation moduli in the frequency domain. In this suspension, pH can tune the gel formation because makes the solvent less attractive to the CNTs, so they prefer to form interconnected bundles at low concentration. Presumably, there is a formation of clusters at different concentrations in situations before gelation and up to the gel point when they interconnect and percolate. And there can be also a formation of flocs before and after the gel formation but out of the gel point, provoking sedimentation of aggregates in some cases, but still with the gel response beyond the critical gel formation.

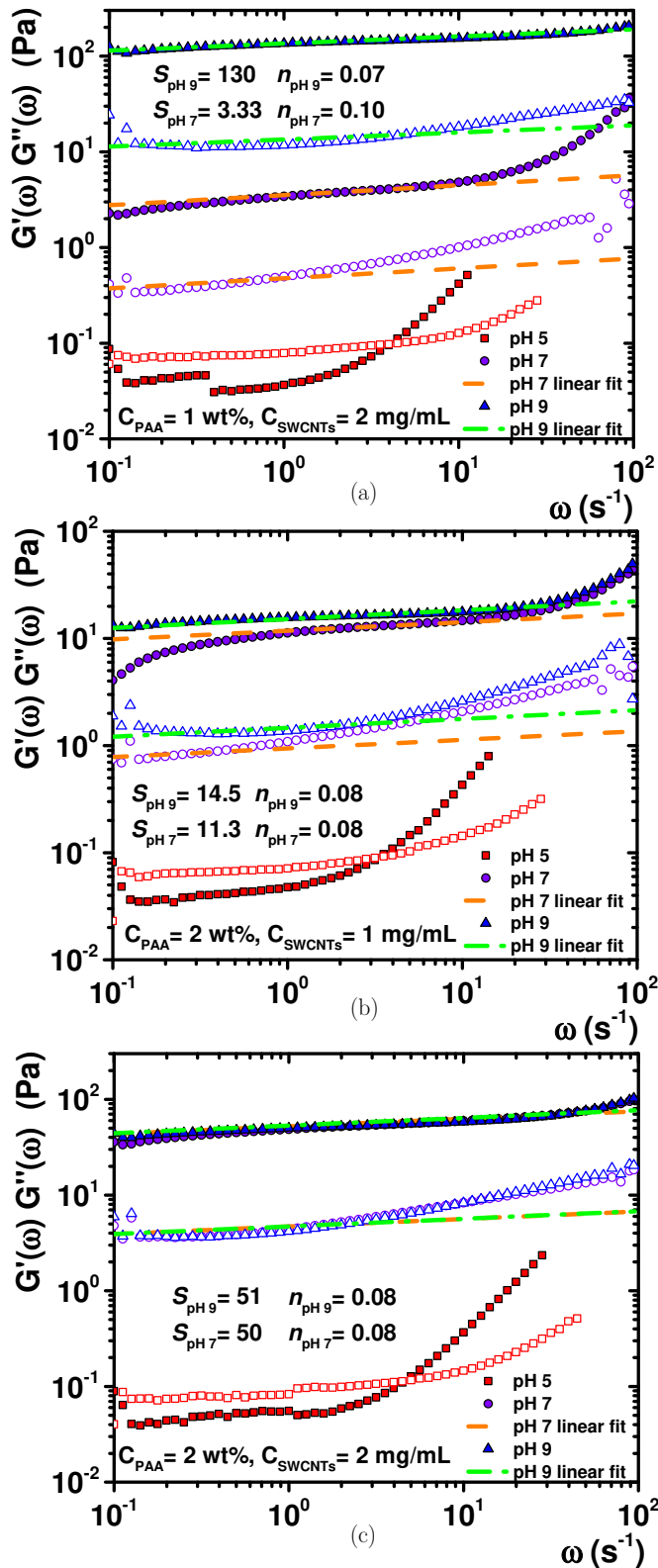


Figure IV.39 Predicted and experimental shear moduli ($G'(\omega)$ full symbols, $G''(\omega)$ open symbols) for three cases closer to the gel point as a function of the frequency that turned out to be at pH = 9. There are presented also the cases for pH 5 and 7. Dash-dotted lines correspond to model $G'(\omega) = G'_c \omega^n$ and $G''(\omega) = G''_c \omega^n$ for pH = 9, and dashed lines for the case of pH = 7.

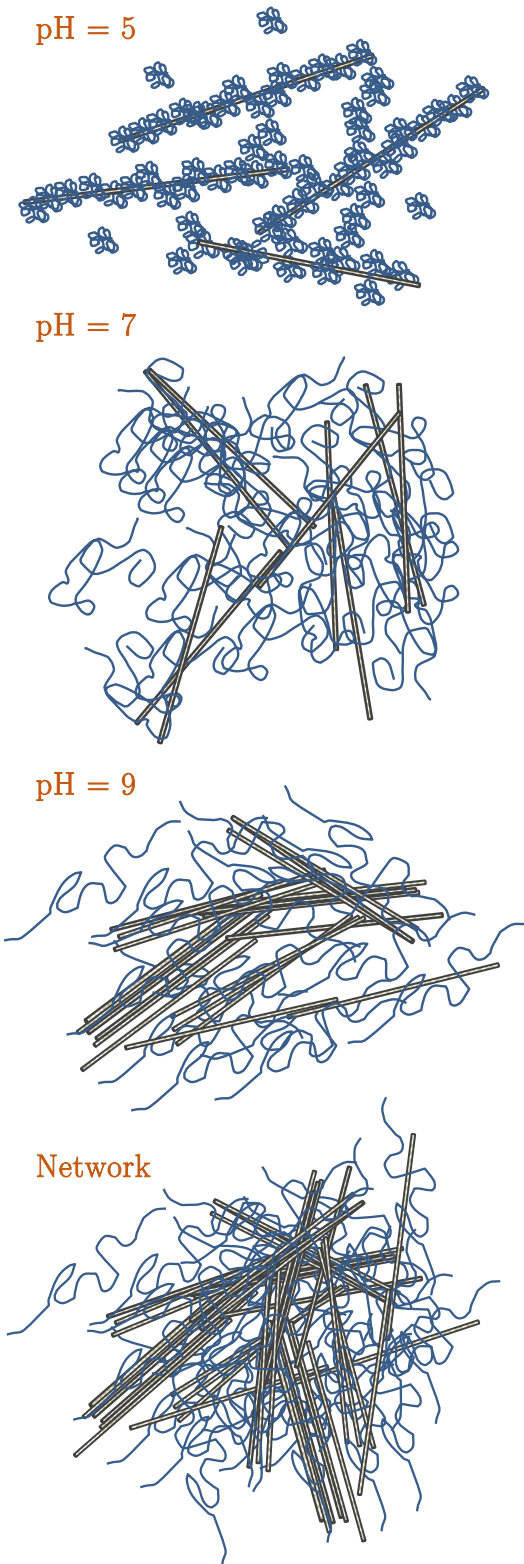


Figure IV.40 Schematics of the structure of SWCNTs/PAA suspensions as pH increases from low pH (top) to high pH (bottom).

If we calculate in our suspensions the volume fraction ($1 \times 10^{-4} - 8 \times 10^{-4}$) and aspect ratio of SWCNTs (10^3), we can localize our system in the reported holistic picture of geometric packing limits given in Figure IV.41, taken from reference [64] for a broad range of rod microstructures for which elasticity has been measured. The suspensions are located in a region where CNTs rods are not sufficiently crowded to arrest due to excluded volume interactions alone, however attractive interactions between them are required to form a connected structure. Then, in this map, the resultant heterogeneous structures may be fractals or bundles. We suspect that our nanotube mesoscale superstructure dispersed in the polymer is made by heterogeneous rod fractal clusters. More research is needed to get more insight of the structure of these dark suspensions, although the size of the SWCNTs has a problem for SANS or SAXS in the range of $qL \sim 1$.

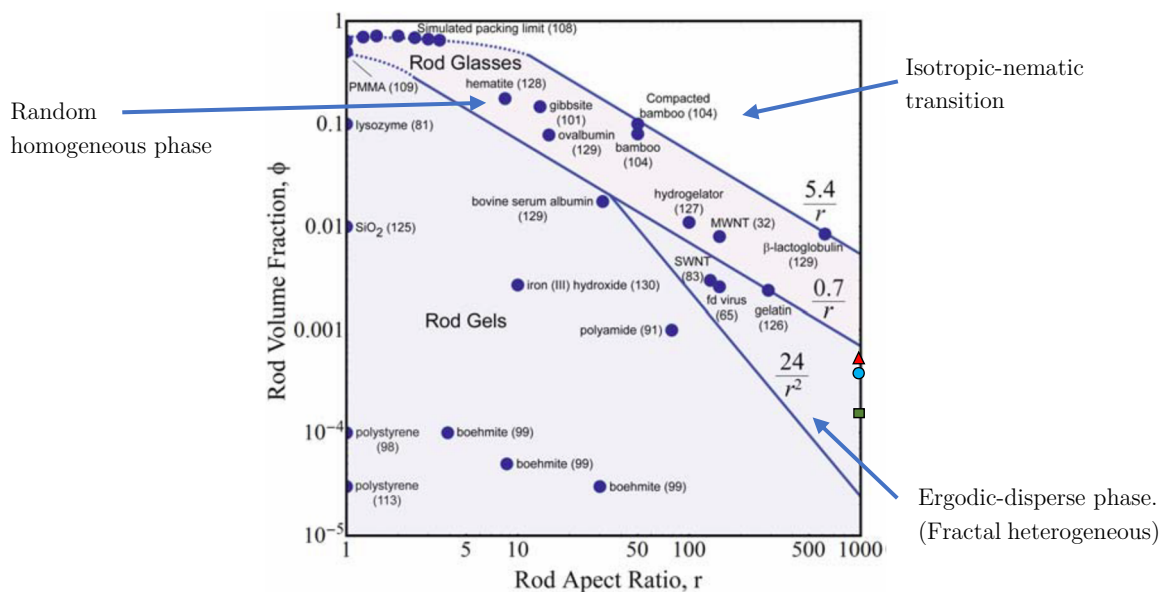


Figure IV.41 Map of the volume fraction vs. aspect ratio for rod suspensions, gels and glasses for which elasticity has been reported. There are data from a wide range of disciplines along with the relevant scaling relationships that bound the physical domains of rod dispersions. The red triangle (2 mg/mL), blue circle (1 mg/mL) and green square (0.5 mg/mL) represents the situated dots for the different SWCNTs concentrations we studied. It is worth to recall that in this map there is considered just one sort of entity for each dot. In our cases, there is a mixture of CNTs and PAA, but the accordance is great. Taken from [64].

3.8. Suspensions of SWCNTs in a polyelectrolyte conclusions

The shear viscosity and viscoelastic spectra were measured for both water solutions of poly(acrylic acid) without and with dispersed single-wall carbon nanotubes, around the overlap concentration of the polymer, at different pH values. In the former case, the polyelectrolyte is charged as pH increases, and due to the electrostatic repulsion between charged not protonated carboxyl groups, extended polymer structures are formed exhibiting a viscoelastic rheological behavior. However, the crossing points collapse in a single exponential curve no matter the concentration and pH as mentioned in Figure IV.30b; as far as we know, it has not been observed before and it deserves further investigation to understand this fact. In the latter case, small quantities of SWCNTs were dispersed in the polyelectrolyte, making this study one of the very few focusing on the dilute regime rheology of

CNTs dispersed in a polymer matrix. At low pH, the nanotube bundles exfoliate making it possible to embed the nanotubes as individual entities or as very thin bundles into the polymer matrix. As pH increases, the added nanotubes apparently form bundles surrounded by a polymer forming a weak mesoscopic network; this occurs at low poly(acrylic acid) and carbon nanotubes concentrations, where the suspensions are highly viscous at very low shear rates and shear thin dramatically at high shear rates. At a very low concentration of carbon nanotubes and for $\text{pH} > 5$, at the percolation concentration, the matrix spanning network increases elasticity because the CNTs are arrested. The suspensions lose their viscoelasticity, up to a point to lose the crossing points between the $G'(\omega)$ and $G''(\omega)$ curves. At a very low concentration of carbon nanotubes and polymer ($\leq c^*$), due to the presence of the mesoscale superstructure formed by nanotubes and polymer, we found that the system behaves as a critical gel. For the first time, as far as we know, it was noticed that close to the gel point these suspensions exhibit a self-similar relaxation modulus ($G(t) = St^{-n}$ or as a power law $G^*(\omega) \propto \omega^n$ in the frequency domain) where pH is the tuning parameter between viscoelasticity and solid gel behavior. The exponent values were evaluated for a couple of suspensions close to their gel points. The power law relaxation moduli description is excellent, for three and two orders of magnitude in ω , in the case of $\text{pH} = 9$ for $G'(\omega)$ and $G''(\omega)$, respectively. For $\text{pH} = 7$ the results are still acceptable but satisfactory for less extension in ω . However, the bonds maintaining the gel structure are soft, as in physically interconnected solid gels, because the system can flow when shear is applied to the suspension. We suspect that our mesoscale superstructure formed by nanotubes in the polymer is made of heterogeneous rod fractal clusters.

V. Summary and conclusions

The dissertation has been focused in the study of anisotropic particles embedded in liquid suspensions. These kind of thread-like structural macromolecules are presented widespread in nature and are widely used in the industry of food, pharmacy, cosmetics, and composite materials.

The results obtained from rheological, microrheological and scattering experiments were shown, which allowed us to understand their mesoscopic structural conformations, related directly with their mechanical properties.

The study was focused in three adaptive systems: a diblock copolymer assembled into worm-like micelles (WLMs) with adaptiveness to polymerization size changes, a system of surfactants assembled with WLM morphologies which presents light absorption and with conformational changes under light exposure, and single wall carbon nanotubes embedded in a polyelectrolyte matrix which presents rheological changes when pH is modified. The cylindrical shapes of these systems lead to interconnections between the components of the liquid suspensions, giving an increase in the rigidity even when the compounds are soft.

1. PBPEO worm-like micelles

The studied diblock copolymer system was (1,4 poly(1,3-butadiene)–polyethylene oxide), with degree of polymerization $m = 37$ for the polybutadiene block and $n = 57$ for the polyethylene oxide block (PBPEO57). The system was studied by different experimental techniques: small angle neutron scattering (SANS), scanning electron microscopy with the implementation of the so-called STEM-in-SEM technique, mechanical rheology and microrheology with diffusing wave spectroscopy (DWS). All techniques together allowed us to interpret the structural conformation of the diblock copolymer aggregates, connecting it with the mechanical properties locally and in bulk.

By SANS experiments it was found that in water solutions PBPEO57 self-assembles into WLMs with a diameter of ~ 12.7 nm (close to the estimated by STEM-in-SEM images), a core radius of ~ 2.7 nm, a shell thickness of ~ 3.0 nm and an estimated persistence length of > 225 nm. To survey the capability of adaptation of these block copolymer WLMs under degree of polymerization changes, the system morphology of PBPEO57 was compared with the morphology of PBPEO45 that also forms WLMs in water with the same core as before, but with a PEO block with a degree of polymerization of 45. In the latter, the found parameters were: a diameter of ~ 12.8 nm, the core radius was very similar to that of the PBPEO57 ~ 2.6 nm and the shell thickness was ~ 3.1 nm, although with a smaller estimated persistence length of ~ 141 nm. It was found that the bending energy is more relevant for the PBPEO57 WLMs than that for the PBPEO45. The PEO block is already more densely packed in the WLMs of PBPEO57 than that of PBPEO45, provoking that any bending increases this steric overcrowding.

In addition, it was found that the PBPEO57 WLMs do not follow the rheological behavior of the WLM solutions of conventional surfactants. The viscoelastic spectra at low and intermediate frequencies (mechanical rheology) do not follow the Maxwell model, resulting that the micelles of PBPEO57 do not break and reform. The same behavior was observed in the case of PBPEO45. The slow dynamics of the self-assembly explains this uncommon behavior of a WLM system; any micellar rearrangement is impeded due to the extremely high hydrophobicity of the PB block.

By diffusing wave spectroscopy experiments (DWS), the mean square displacement of colloidal particles embedded in the micellar solution of PBPEO57 was measured. These displacements were compared with other fluids with embedded thread-like structures (conventional surfactant WLMs, fd virus, and PBPEO45 WLMs). From the particle mean square displacement, we obtained the viscoelastic spectrum at high frequencies. $|G^*|$ exhibits a power law behavior. Here, it is evident where the stress relaxation changes from the Rouse-Zimm modes to the bending modes of Kuhn segments at ω^* . From here, l_p was calculated for the PBPEO57 WLMs, which is concentration dependent, but extrapolating our data to the concentration where the SANS measurement was done, the agreement is reasonable. As concentration increases, a reduction in l_p of the thread-like structures occurs to reduce the contribution of the interaction to the total free energy, because for a flexible macromolecule the excluded volume that is not available for the other macromolecules is smaller than the corresponding one of a rigid macromolecule. In summary, information about the relaxation mechanisms of the system at low (mainly through reptation) and high frequencies was obtained (Rouse-Zimm and bending modes), as well as how they are related to the size of the PEO shell and the diblock copolymer concentration.

2. Photoresponsive worm-like micelles

Preliminary results obtained in the study of aqueous solutions of WLM aggregates done with the cationic surfactant cetyltrimethylammonium bromide with the counterion sodium salicylate (CTAB-NaSal) and with the addition of a photo-responsive molecule 4-(phenylazo) benzoic acid (AzoCOOH, when deprotonated we call it AzoCOO) were presented. The AzoCOOH molecule (and AzoCOO as well) performs conformational structural changes (trans-cis isomerization) when light beams of certain wavelength strike the molecule. It was found by mechanical rheology experiments that the addition of AzoCOOH reinforce the Maxwellian behavior of the systems with no visible modification when trans-cis isomerization occurs after irradiation with UV light. All subsequent experiments were performed then in trans configuration.

Microrheology with DWS experiments was very useful to extract the characteristic lengths of the system with constant concentration of CTAB-NaSal but with different concentration of AzoCOO. Two main cases were revisited: with the addition of NaCl and without it. Different sizes in the characteristic lengths were found. The addition of NaCl was more significant when the AzoCOO molecule was not present. The most significant difference appeared in the entanglement length, l_e , which was much more extended in the case without NaCl, in accordance with a shorter contour length, L_c , when there was not NaCl, and in agreement also with a larger mesh size, ξ , for the same sample. The addition of AzoCOO contributed similar to the addition of NaCl according to results.

WLMs contour lengths L_c , were smaller with higher concentration of AzoCOO. The entanglement length l_e , and the mesh size ξ , were preserved in average. The persistence length l_p , varied with the concentration of AzoCOO. l_p decreases as concentration of AzoCOO increases and also L_c decreases. This means that the stiffness is getting lost when the WLMs are shorter. It is worth to notice that this behavior is not monotonic; l_p increases when just 5 mM of AzoCOO are added but decreases subsequently with the addition of more AzoCOO.

The most valuable contribution to the experimental procedure was obtaining the optical parameters of the solutions even when the solutions themselves presented light absorption in the region of 514 nm that we used for the experiments. The inverse adding doubling method (IAD) was used for the first time in DWS in a structured system at a mesoscopic scale, to correct the experimental autocorrelation function due to the adsorption effects.

3. Suspensions of SWCNTs in a polyelectrolyte

Nanocomposite suspensions of single wall carbon nanotubes (SWCNTs) were prepared. Polyelectrolyte aqueous solutions of poly(acrylic) acid (PAA) were chosen as dispersing media candidates for the SWCNTs, with successful results. It was found that the addition of small quantities of SWCNTs dispersed in low concentrated PAA matrix leads to a transition from viscoelastic response to gelation when the pH change from acidic to basic. The application of UV-Vis spectrometry, transmission and scanning electron microscopy, atomic force microscopy, and mechanical rheology, helped us to understand the implications at a macroscopic level, when a transient mesoscopic superstructure is formed. Tuning the pH was a key property in the formation of gels, which indirectly modified the arrangement of the skeleton-like SWCNTs network.

At $\text{pH} < 5$, the nanotube bundles exfoliate, making it possible to embed the nanotubes as individual entities or as very thin bundles into the polymer matrix. As pH increases, the added nanotubes apparently form bundles surrounded by a polymer forming a weak mesoscopic network. It was found after mechanical rheology experiments, that the suspensions are highly viscous at very low shear rates, as predicted by Flory when a gel is formed. The system shear thins dramatically at high shear rates, due to the elongated geometry of the nanotube bundles. At $\text{pH} > 5$, at a certain percolation concentration, which was reached at low SWCNTs concentration and low PAA concentration, the matrix spanning network is notable elastic because the CNTs are arrested. Electron and atomic force microscopy images showed the formation of thick bundles, and mechanical rheology experiments presented $G'(\omega)$ always above $G''(\omega)$, at low and intermediate frequencies. Due to the presence of a mesoscale superstructure formed by nanotubes and polymer, the system behaves as a critical gel. It was noticed that close to the gel point these suspensions exhibit a self-similar relaxation modulus, $G(t) = St^{-n}$ or $G^*(\omega) \propto \omega^n$ in the frequency domain, where pH is the tuning parameter between viscoelasticity and solid gel behavior. The power law relaxation moduli description was excellent, for three and two orders of magnitude in ω , in the case of $\text{pH} = 9$. For $\text{pH} = 7$ the results were acceptable but satisfactory for less extension in ω . However, the bonds maintaining the gel structure were soft, as in physically interconnected weak gels, because the system can flow when shear is applied to the suspension. We suspect that our mesoscale superstructure formed by nanotubes in the polymer is

made of heterogeneous rod fractal clusters, in accordance with former results found in the literature for thread-like systems.

4. Concluding remarks and future perspectives

The model thread-like structures we chose to study brought an extra degree of complication to the investigation, but at the same time, these morphologies permitted us to visualize the behavior found among different systems with anisotropic structures, from biological systems to the ones used in industry.

The general goals were reached satisfactorily. Every small achieved step in the investigation process, using different experimental techniques and in accordance with the theoretical framework, permitted us to interpret the physical phenomena presented in every system. The most valuable teaching was that a better understanding of physical phenomena is achieved when the research is done in communication with colleagues. Sharing different points of view and performing different kind of experiments lead us to conform an adequate investigation.

Dynamic light scattering techniques are a good complement to interpret the local rheological behavior. In some cases, the agreement is perfect with the bulk surveys, but even when this is not the case, the information provided about the relaxation processes of the systems is valuable and can be connected to the structural information obtained with static scattering experiments. For a first time, we applied the IAD method to extract the optical properties of mesoscale-structured systems necessary for the implementation of DWS. This method permitted us to extend the study for systems which present light absorption due to their intrinsic internal optical properties. Future research in this direction includes the comparison of backscattering DWS experiments with the results obtained in transmission geometry when a light absorption agent is added artificially. With backscattering experiments, it is possible to discriminate between light beams that have traveled the long paths within the sample and the ones with have traveled the shortest paths. The addition of absorption to the system attenuates the longest paths of light, meaning that the light incoming to the detector must have presented a phase shift with less scattering events, which imply that every particle presented a longer displacement in time. Then, without the necessity of performing backscattering experiments, adding absorption to the systems and performing DWS experiments in transmission geometry can help us to extent the achievable mean square displacement of the particles to longer times, what is the same to extend the survey of relaxation mechanisms of the systems to longer times as well, or shorter frequencies in the Fourier domain. The implementation and efficiency of these experiments might vary depending on the size of the probe particles used, due to the different regimes for scattering phenomena (Rayleigh, Rayleigh-Debye or Mie).

For the point of view of the structural properties of the diblock copolymers studied here, a future analysis can be the implementation of USANS experiments to reach the region where contour length of WLMs is found. In addition, the implementation of computational simulations could provide a better understanding of the interactions between polymeric chains at the shell of the micelles. And also, simulations could give us an idea of the dynamics of the polymer located within the core of the

WLMs, which plays an important role in the stiffness of the micelles. With these studies, it is possible to complete the picture which connects the mechanical properties of the system with its structural conformation, directed by the different interactions within all components.

For the case of photo-responsive WLMs, further similar analyses are performed currently for a system of WLMs made of the surfactant N-tetradecyl-N,N-dimethyl-3-ammonio-1-propanesulfonate with the cosurfactant sodium dodecyl sulfate (TDPS-SDS), adding AzoCOO. The research is part of the main doctoral project of Natalia Rincón-Londoño, member of the Complex Fluids Group of the Institute of Physics at UNAM. She also plans to analyze the systems using another Azo component, which might influence more the rheological properties of the micelles tuned by changes in light.

Finally, it is desirable to implement static scattering experiments to go beyond in understanding the structural conformation of the system of SWCNTs embedded in the PAA matrix. However, due to the very high aspect ratio of the nanotubes (1000), and the presumably smaller structures formed, it is complicated to span over all necessary scattering vector values with SANS and SAXS. An alternative could be an experiment with visible light, but the system attenuates high quantities of light. Computational simulations are also a challenge due to the geometric constrains of the system, but an approximation to our system can be done for particles with aspect ratios of ~ 100 .

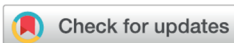
VI. Published works



Soft Matter

PAPER

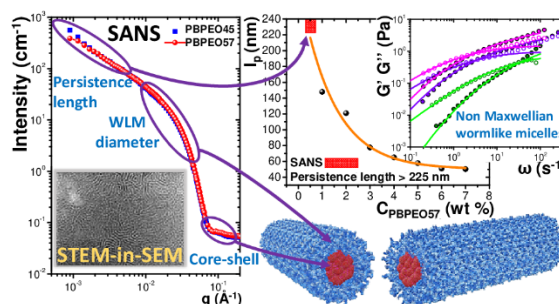
[View Article Online](#)
[View Journal](#)



Cite this: DOI: 10.1039/c8sm01530a

Structure, rheology, and microrheology of wormlike micelles made of PB–PEO diblock copolymers[†]

Antonio Tavera-Vázquez,^a Brisa Arenas-Gómez,^{bc} Cristina Garza,^{id}^a Yun Liu,^{cd} and Rolando Castillo^{id}^{*a}



THE JOURNAL OF
PHYSICAL CHEMISTRY B

Article

Cite This: *J. Phys. Chem. B* 2018, 122, 348–359

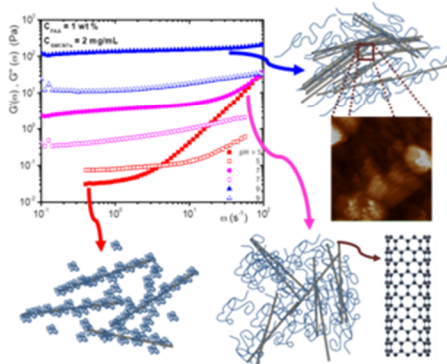
pubs.acs.org/JPCB

Tuning the Viscoelastic-Gel Transition of Single-Wall Carbon Nanotubes Embedded in pH-Responsive Polyelectrolyte Solutions

Atida Selmani,^{†,‡,‡#} Antonio Tavera-Vázquez,^{‡,‡#} Cristina Garza,[‡] and Rolando Castillo^{*,‡,‡}

[†]Laboratory for Biocolloids and Surface Chemistry, Division of Physical Chemistry, Ruder Bošković Institute, Bijenička cesta, 54, 10000 Zagreb, Croatia

[‡]Instituto de Física, Universidad Nacional Autónoma de México, P.O. Box 20-364, 01000, México City, México



References

- [1] M. Kleman and O. D. Lavrentovich, *Soft matter physics. An introduction*, New York: Springer-Verlag Inc., 2003.
- [2] M. Daoud and C. E. Williams, *Soft matter physics*, Berlin, Heidelberg: Springer-Verlag, 1999.
- [3] W. M. Gelbart and A. Ben-Shaul, "The "new" science of "complex fluids"," *J. Phys. Chem.*, no. 100, p. 13169–13189, 1996.
- [4] E. Sarmiento-Gómez, "Tesis para obtener el grado de Doctor en Ciencias Físicas: El movimiento Browniano en fluidos complejos embebidos con estructuras filiformes," Posgrado en Ciencias Físicas, Instituto de Física, UNAM, Ciudad Universitaria, México D.F., 2012.
- [5] C. Creton, "50th Anniversary Perspective: networks and gels: soft but dynamic and tough," *Macromolecules*, vol. 50, pp. 8297-8316, 2017.
- [6] S. Bauer, S. Bauer-Gogonea, I. Graz, M. Kaltenbrunner, C. Keplinger and R. Schwödiauer, "25th Anniversary Article: A soft future: from robots and sensor skin to energy harvesters," *Adv. Mater.*, vol. 26, pp. 149-162, 2014.
- [7] M. Fialkowski, K. J. M. Bishop, S. K. Smoukov, C. J. Campbell and B. A. Grzybowski, "Principles and implementations of dissipative (dynamic) self-assembly," *J. Phys. Chem. B, Feature Article*, vol. 110, pp. 2482-2496, 2006.
- [8] S. R. Nagel, "Experimental soft-matter science," *Rev. Mod. Phys.*, vol. 89, no. 2, p. 025002, 2017.
- [9] A. Wang, W. Shi, J. Huang and Y. Yan, "Adaptive soft molecular self-assemblies," *Soft Matter*, vol. 12, pp. 337-357, 2016.
- [10] G. Gompper, J. K. G. Dhont and D. Richter, "A unified view of soft matter systems?," *Eur. Phys. J. E*, vol. 26, pp. 1-2, 2008.
- [11] M. Doi and S. F. Edwards, *The theory of polymer dynamics*, Oxford University Press, 1986.
- [12] M. Rubinstein and R. H. Colby, *Polymer physics*, Oxford University Press, 2003.
- [13] A. Einstein, "Über die von der molekularkinetischen Theorie der Wärme geforderte Bewegung von in ruhenden Flüssigkeiten suspendierten Teilchen," *Ann. Phys.*, vol. 17, pp. 549-560, 1905.
- [14] A. Einstein, "Zur Theorie der brownshen Bewegung," *Ann. Phys.*, vol. 19, pp. 371-381, 1906.
- [15] F. Reif, *Fundamentals of statistical and thermal physics*, Waveland Press, Inc., 2009.
- [16] C. W. Macosko, *Rheology principles, measurements, and applications*, New York: Wiley-VCH, Inc., 1993.
- [17] P. E. Rouse, "A theory of the linear viscoelastic properties of dilute solutions of coiling polymers," *J. Chem. Phys.*, vol. 21, pp. 1272-1289, 1953.
- [18] B. H. Zimm, "Dynamics of polymers molecules of dilute solution: Viscoelasciticy, flow," *J. Chem. Phys.*, vol. 24, pp. 269-278, 1956.
- [19] P. G. de Gennes, "Reptation of a polymer chain in the presence of fixed obstacles," *J. Chem. Phys.*, vol. 55, p. 571, 1971.

REFERENCES

- [20] M. E. Cates, "Reptation of living polymers: dynamics of entangled polymers in the presence of reversible chain scission reactions," *Macromolecules*, vol. 20, pp. 2289-2296, 1987.
- [21] M. E. Cates and S. J. Candau, "Statics and dynamics of worm-like surfactant micelles," *J. Phys.: Condens. Matter*, vol. 2, pp. 6869-6892, 1990.
- [22] M. S. Turner and M. E. Cates, "Linear viscoelasticity in living polymers: a quantitative probe of chemical relaxation times," *Langmuir*, vol. 7, no. 8, pp. 1590-1594, 1991.
- [23] R. Granek and M. E. Cates, "Stress relaxation in living polymers: Results from a Poisson renewal model," *J. Chem. Phys.*, vol. 96, no. 6, 1992.
- [24] S. A. Safran, L. A. Turkevich and P. A. Pincus, "Cylindrical microemulsions: a polymer-like phase?," *J. Phys. Lett.*, vol. 45, no. 2, pp. 69-74, 1984.
- [25] J. N. Israelachvili, D. J. Mitchell and B. W. Ninham, "Theory of self-assembly of hydrocarbon amphiphiles into micelles and bilayers," *J. Chem. Soc., Faraday Trans.*, vol. 1525, p. 72, 1976.
- [26] P. Pimenta and E. E. Pashkovski, "Rheology of viscoelastic mixed surfactant solutions: effect of scission on nonlinear flow and rheochaos," *Langmuir*, vol. 22, pp. 3980-3987, 2006.
- [27] J. N. Israelachvili, *Intermolecular & surface forces*, San Diego: Academic Press, 1991.
- [28] V. J. Anderson, J. R. A. Pearson and E. S. Boek, "The rheology of worm-like micellar fluids," *Rheol. Reviews*, pp. 217-253, 2006.
- [29] M. E. Cates and M. R. Evans, Eds., *Soft and fragile matter*, Edinburgh, U.K.: SUSSP Publications, 1999.
- [30] N. Dan and S. A. Safran, "Junctions and end-caps in self-assembled non-ionic cylindrical micelles," *Adv. Colloid Interface Sci.*, vol. 123-126, pp. 323-331, 2006.
- [31] "<http://www.ifnh.ethz.ch/vt/research/projects/vivianel/>," [Online].
- [32] J. -F. Berret, "Rheology of wormlike micelles: equilibrium properties and shear banding transitions," in *Molecular Gels. Materials with Self-Assembled Fibrillar Networks*, R. G. Weiss and P. Terech, Eds., Netherlands, Springer, 2005, pp. 663-716.
- [33] S. Lerouge and J. -F. Berret, "Shear induced transitions and instabilities in surfactant wormlike micelles," *Adv. Polym. Sci.*, no. 203, pp. 1-71, 2010.
- [34] F. Gittes and F. C. MacKintosh, "Dynamic shear modulus of a semiflexible polymer network," *Phys. Rev. E*, vol. 58, no. 2, pp. R1241-R1244, 1998.
- [35] N. Willenbacher, C. Oelschlaeger, M. Schopferer, P. Fischer, F. Cardinaux and F. Scheffold, "Broad bandwidth optical and mechanical rheometry of wormlike micelle solutions," *Phys. Rev. Lett.*, vol. 99, p. 068302, 2007.
- [36] B. A. Schubert, E. W. Kaler and N. J. Wagner, "The microstructure and rheology of mixed cationic/anionic wormlike micelles," *Langmuir*, vol. 19, pp. 4079-4089, 2003.
- [37] P. G. de Gennes, *Scaling concepts in polymer physics*, Ithaca, NY: Cornell University Press, 1979.
- [38] C. A. Dreiss, "Wormlike micelles: where do we stand? Recent developments, linear rheology and scattering techniques," *Soft Matter*, no. 3, pp. 956-970, 2007.
- [39] D. López-Díaz and R. Castillo, "Microrheology of solutions embedded with thread-like supramolecular structures," *Soft Matter*, vol. 7, p. 5926, 2011.

-
- [40] J. M. Galvan-Miyoshi, J. Delgado and R. Castillo, "Diffusing wave spectroscopy in Maxwellian fluids," *Eur. Phys. J. E*, vol. 26, pp. 369-377, 2008.
- [41] E. Sarmiento-Gómez, D. López-Díaz and R. Castillo, "Microrheology and characteristic lengths in wormlike micelles made of a zwitterionic surfactant and SDS in brine," *J. Phys. Chem. B*, vol. 114, p. 12193-12202, 2010.
- [42] F. S. Bates and G. H. Fredrickson, "Block copolymers—Designer soft materials," *Phys. Today*, vol. 52, no. 2, p. 32, 1999.
- [43] E. B. Zhulina, M. Adam, I. LaRue, S. S. Sheiko and M. Rubinstein, "Diblock copolymer micelles in a dilute solution," *Macromolecules*, vol. 38, pp. 5330-5351, 2005.
- [44] B. Lonetti, A. Tsigkri, P. R. Lang, J. Stellbrink, L. Willner, J. Kohlbrecher and M. P. Lettinga, "Full characterization of PB-PEO wormlike micelles at varying solvent selectivity," *Macromolecules*, vol. 44, p. 3583-3593, 2011.
- [45] Y. -Y. Won, H. T. Davis and F. S. Bates, "Giant wormlike rubber micelles," *Science*, vol. 283, p. 960, 1999.
- [46] Y. -Y. Won, K. Paso, H. T. Davis and F. S. Bates, "Comparison of original and cross-linked wormlike micelles of poly(ethylene oxide-b-butadiene) in water: rheological properties and effects of poly(ethylene oxide) addition," *J. Phys. Chem. B*, vol. 105, pp. 8302-8311, 2001.
- [47] S. Jain and F. S. Bates, "On the origins of morphological complexity in block copolymer surfactants," *Science*, vol. 300, p. 460, 2003.
- [48] S. Jain and F. S. Bates, "Consequences of nonergodicity in aqueous binary PEO-PB micellar dispersions," *Macromolecules*, vol. 37, pp. 1511-1523, 2004.
- [49] S. Jain, X. Gong, L. E. Scriven and F. S. Bates, "Disordered network state in hydrated block-copolymer surfactants," *Phys. Rev. Lett.*, vol. 96, p. 138304, 2006.
- [50] S. Förster, B. Berton, H. -P. Hentze, E. Krämer, M. Antonietti and P. Lindner, "Lyotropic phase morphologies of amphiphilic block copolymers," *Macromolecules*, vol. 34, pp. 4610-4623, 2001.
- [51] Y. -Y. Won, H. T. Davis, F. S. Bates, M. Agamalian and G. D. Wignall, "Segment distribution of the micellar brushes of poly(ethylene oxide) via small-angle neutron scattering," *J. Phys. Chem. B*, vol. 104, pp. 7134-7143, 2000.
- [52] B. Arenas-Gómez, M. Vincekovic, C. Garza and R. Castillo, "Worm-like micelles in water solutions of 1, 4 poly (1, 3-butadiene)-polyethylene oxide diblock copolymer," *Eur. Phys. J. E*, vol. 37, no. 51, 2014.
- [53] Y. -Y. Won, H. T. Davis and F. S. Bates, "Molecular exchange in PEO-PB micelles in water," *Macromolecules*, vol. 36, pp. 953-955, 2003.
- [54] E. Zaccarelli, "Colloidal gels: equilibrium and non-equilibrium routes," *J. Phys.: Condens. Matter*, vol. 19, p. 323101, 2007.
- [55] P. J. Flory, "Molecular size distribution in three dimensional polymers. I. Gelation," *J. Am. Chem. Soc.*, vol. 63, p. 3083, 1941.
- [56] W. H. Stockmayer, "Theory of molecular size distribution and gel formation in branched-chain polymers," *J. Chem. Phys.*, vol. 11, no. 2, p. 45, 1943.
-

REFERENCES

- [57] W. H. Stockmayer, "Theory of molecular size distribution and gel formation in branched polymers II. General cross linking," *J. Chem. Phys.*, vol. 12, no. 4, p. 125, 1944.
- [58] P. D. Godfrin, N. E. Valadez-Pérez, R. Castañeda-Priego, N. J. Wagner and Y. Liu, "Generalized phase behavior of cluster formation in colloidal dispersions with competing interactions," *Soft Matter*, vol. 10, pp. 5061-5071, 2014.
- [59] R. P. Murphy, "A dissertation submitted to the Faculty of the University of Delaware in partial fulfillment of the requirements for the degree of Doctor of Philosophy in Chemical Engineering: The nature of anisotropic particles with short range interactions," Department of Chemical and Biomolecular Engineering. University of Delaware, Newark, DE, 2017.
- [60] C. Schwittay, M. Mours and H. H. Winter, "Rheological expression of physical gelation in polymers," *Faraday Discuss.*, vol. 101, pp. 93-104, 1995.
- [61] N. K. Reddy, Z. Zhang, M. P. Lettinga, J. K. G. Dhont and J. Vermant, "Probing structure in colloidal gels of thermoreversible rodlike virus particles: rheology and scattering," *J. Rheol.*, vol. 56, pp. 1153-1174, 2012.
- [62] F. Chambon and H. H. Winter, "Linear viscoelasticity at the gel point of a crosslinking PDMS with imbalanced stoichiometry," *J. Rheol.*, vol. 31, pp. 683-697, 1987.
- [63] P. J. Flory, Principles of polymer chemistry, Ithaca, NY: Cornell University Press, 1953.
- [64] M. J. Solomon and P. T. Spice, "Microstructural regimes of colloidal rod suspensions, gels, and glasses," *Soft Matter*, vol. 6, pp. 1391-1400, 2010.
- [65] S. Manivannan, I. O. Jeong, J. H. Ryu, C. S. Lee, K. S. Kim, J. Jang and K. C. Park, "Dispersion of single-walled carbon nanotubes in aqueous and organic solvents through a polymer wrapping functionalization," *J. Mater. Sci. Mater. Electron.*, vol. 20, pp. 223-229, 2009.
- [66] Y. Y. Huang and E. M. Terentjev, "Dispersion of carbon nanotubes: mixing, sonication, stabilization, and composite properties," *Polymers*, vol. 4, pp. 275-295, 2012.
- [67] D. O. O. Ayewah, D. C. Davis, R. Krishnamoorti, C. D. Lagoudas, H. J. Sue and M. Willson, "A surfactant dispersed SWCNT-polystyrene composite characterized for electrical and mechanical properties," *Composites*, vol. Part A 41, pp. 842-849, 2010.
- [68] M. J. O'Connell, P. Boul, L. M. Ericson, C. Huffman, Y. Wang, E. Haroz, C. Kuper, J. Tour, K. D. Ausman and R. E. Smalley, "Reversible water-solubilization of single-walled carbon nanotubes by polymer wrapping," *Chem. Phys. Lett.*, vol. 342, pp. 265-271, 2001.
- [69] T. Chatterjee, K. Yurekli, V. G. Hadjiev and R. Krishnamoorti, "Single-walled carbon nanotube dispersion in poly(ethylene oxide)," *Adv. Funct. Mater.*, vol. 15, pp. 1832-1838, 2015.
- [70] J. H. Rouse and P. T. Lillehei, "Electrostatic assembly of polymer/single walled carbon nanotube multilayer films," *Nano Lett.*, vol. 3, pp. 59-62, 2003.
- [71] R. J. Chen, Y. Zhang, D. Wang and H. Dai, "Noncovalent sidewall functionalization of single-walled carbon nanotubes for protein immobilization," *J. Am. Chem. Soc.*, vol. 123, pp. 3838-3839, 2001.
- [72] J. L. Bahr, J. P. Yang, D. V. Kosynkin, M. J. Bronikowski, R. E. Smalley and J. M. Tour, "Functionalization of carbon nanotubes by electrochemical reduction of aryl diazonium salts: a bucky paper electrode," *J. Am. Chem. Soc.*, vol. 123, pp. 6536-6542, 2001.

-
- [73] Y. Sun, S. R. Wilson and D. I. Schuster, "High resolution and strong light emission of carbon nanotubes in aromatic amine solvents," *J. Am. Chem. Soc.*, vol. 123, pp. 5348-5349, 2001.
- [74] E. T. Mickelson, C. B. Huffman, A. G. Rinzler, R. E. Smalley, R. H. Hauge and J. L. Margrave, "Fluorination of single-wall carbon nanotubes.," *Chem. Phys. Lett.*, vol. 296, pp. 188-194, 1998.
- [75] V. Georgakilas, K. Kordatos, M. Prato, D. M. Guldi, M. Holzinger and A. Hirsch, "Organic functionalization of carbon nanotubes," *J. Am. Chem. Soc.*, vol. 124, pp. 760-761, 2002.
- [76] B. Sohrabi, N. Poorgholami-Bejarpasiand and N. Nayeri, "Dispersion of carbon nanotubes using mixed surfactants: experimental and molecular dynamics simulation studies," *J. Phys. Chem. B*, vol. 118, pp. 3094-3103, 2014.
- [77] D. T. N. Chen, K. Chen, L. A. Hough, M. F. Islam and A. G. Yodh, "Rheology of carbon nanotube networks during gelation," *Macromolecules*, vol. 43, pp. 2048-2053, 2010.
- [78] J. Y. Shin, T. Premkumar and K. E. Geckeler, "Dispersion of single-walled carbon nanotubes by using surfactants: are the type and concentration important?," *Chem. Eur. J.*, vol. 14, pp. 6044-6048, 2008.
- [79] F. K. Brunecker, F. Schöppler and T. Hertel, "Interaction of polymers with single-wall carbon nanotubes," *J. Phys. Chem. C*, vol. 120, pp. 10094-10103, 2016.
- [80] Y. Lin, L. F. Allard and Y. P. Sun, "Protein-affinity of single-walled carbon nanotubes in water," *J. Phys. Chem. B*, vol. 108, pp. 3760-3764, 2004.
- [81] T. Chatterjee and R. Krishnamoorti, "Rheology of polymer carbon nanotubes composites," *Soft Matter*, vol. 9, pp. 9515-9529, 2013.
- [82] V. A. Davis, A. N. Parra-Vasquez, M. J. Green, P. K. Rai, N. Behabtu, V. Prieto, R. D. Booker, J. Schmidt, E. Kesselman, W. Zhou and e. al., "True solutions of single-walled carbon nanotubes for assembly into macroscopic materials," *Nat. Nanotechnol.*, vol. 4, pp. 830-834, 2009.
- [83] F. Du, R. C. Scogna, W. Zhou, S. Brand, J. E. Fischer and K. I. Winey, "Nanotube networks in polymer nanocomposites: rheology and electrical conductivity," *Macromolecules*, vol. 37, pp. 9048-9055, 2004.
- [84] A. Sharma, J. D. Smith, K. B. Walters and S. W. Rick, "Constant pH simulations of pH responsive polymers," *J. Chem. Phys.*, vol. 145, p. 234906, 2016.
- [85] A. V. Dobrynin and M. Rubinstein, "Theory of polyelectrolytes in solutions and at surfaces," *Progress Polymer Sci.*, vol. 30, pp. 1049-1118, 2005.
- [86] T. Swift, L. Swanson, M. Geoghegan and S. Rimmer, "The pH-responsive behaviour of poly(acrylic acid) in aqueous solution is dependent on molar mass," *Soft Matter*, vol. 12, pp. 2542-2549, 2016.
- [87] H. A. Barnes, J. F. Hutton and K. Walters, *An introduction to rheology*, Elsevier, 1989.
- [88] H. A. Barnes, *A handbook of elementary rheology*, University of Wales. Institute of Non-Newtonian Fluid Mechanics: Aberystwyth, 2000.
- [89] L. Rogers, "Operators and fractional derivatives for viscoelastic constitutive equations," *J. Rheol.*, vol. 27, p. 351, 1983.
-

REFERENCES

- [90] C. Friedrich, "Relaxation and retardation functions of the Maxwell model with fractional derivatives," *Rheol. Acta*, vol. 30, pp. 151-158, 1991.
- [91] F. Mainardi, *Fractional calculus and waves in linear viscoelasticity. An introduction to mathematical models*, London: Imperial College Press, 2010.
- [92] F. Mainardi and G. Spada, "Creep, relaxation and viscosity properties for basic fractional models in rheology," *Eur. Phys. J. Special Topics*, vol. 193, pp. 133-160, 2011.
- [93] L. Boltzmann, "Zur Theorie des elastischen Nachwirkung," *Ann. Phys. Chem.*, vol. 7, pp. 624-654, 1876.
- [94] R. Kubo, "Statistical-mechanical theory of irreversible processes," *J. Phys. Soc. Jap.*, vol. 12, pp. 570-586, 1957.
- [95] N. J. Wagner and J. F. Brady, "Shear thickening in colloidal dispersions," *Physics Today*, vol. 62, no. 10, p. 27, 2009.
- [96] T. Pritz, "Verification of local Kramers-Kronig relations for complex modulus by means of fractional derivative model," *J. Sound and Vib.*, vol. 228, no. 5, pp. 1145-1165, 1999.
- [97] T. Pritz, "Unbounded complex modulus of viscoelastic materials and the Kramers-Kronig relations," *J. Sound and Vib.*, vol. 279, pp. 687-697, 2005.
- [98] S. John, "Localization of light," *Physics Today*, vol. 44, no. 5, p. 32, 1991.
- [99] P. Lindner and T. Zemb, *Neutron, X-rays and light: scattering methods applied to soft condensed matter*, Amsterdam: North-Holland, 2002.
- [100] R. Pecora, *Dynamic light scattering: applications of photon correlation spectroscopy*, Plenum Press, 1985.
- [101] B. Chu, *Laser light scattering: basic principles and practice*, New York: Academic Press Inc, 1974.
- [102] K. S. Schmitz, *An introduction to dynamic light scattering by macromolecules*, San Diego, CA: Academic Press, Inc., 1990.
- [103] P. N. Pusey and J. A. Tough, "Particle Interactions," in *Dynamic Light Scattering: applications of photon correccorrelation*, R. Pecora, Ed., New York, Plenum Press, 1981.
- [104] S. R. Aragón and R. Pecora, "Theory of dynamic light scattering from large anisotropic particles," *J. Chem. Phys.*, vol. 66, no. 6, 1977.
- [105] D. J. Pine, D. A. Weitz, J. X. Zhu and E. Herbolzheimer, "Diffusing-wave spectroscopy: dynamic light scattering in the multiple scattering limit," *J. Phys. France*, no. 51, pp. 2101-2127, 1990.
- [106] D. A. Weitz and D. J. Pine, "Diffusing-wave spectroscopy," in *Dynamic light scattering: the method and some applications*, W. Brown, Ed., New York, Oxford University Press, 1993, pp. 652-721.
- [107] J. L. Harden and V. Viasnoff, "Recent advances in DWS-based micro-rheology," *Curr. Opin. Colloid Interface Sci.*, vol. 6, no. 438, 2001.
- [108] E. Sarmiento-Gómez, J. M. Galvan-Miyoshi and R. Castillo, "A dynamical light scattering technique and its application in viscoelastic networks in soft matter," *Proc. of SPIE*, vol. 8011, p. 801178, 2011.

-
- [109] H. S. Carslaw and J. C. Jaeger, *Conduction of heat in solids*, Oxford: Clarendon Press, 1990.
- [110] F. Scheffold, "Particle sizing with diffusing wave spectroscopy," *J. Dispersion Sci. and Technol.*, vol. 23, pp. 591-599, 2002.
- [111] E. Sarmiento-Gómez, B. Morales-Cruzado and R. Castillo, "Absorption effects in diffusing wave spectroscopy," *Applied Optics*, vol. 53, no. 21, 2014.
- [112] T. Durduran, A. G. Yodh, B. Chance and D. A. Boas, "Does the photon diffusion coefficient depend of absorption?," *J. Opt. Soc. Am. A*, vol. 14, p. 3358, 1997.
- [113] A. Ishimaru, *Wave propagation and scattering in random media: single scattering and transport theory*, vol. 1, Academic Press, Inc., 1978.
- [114] L. V. Wang and H. Wu, *Biomedical optics: principles and imaging*, New Jersey: John Wiley & Sons, 2007.
- [115] S. A. Prahl, M. J. C. van Gemert and A. J. Welch, "Determining the optical properties of turbid media by using the adding-doubling method," *Applied Optics*, vol. 32, no. 4, 1993.
- [116] S. A. Prahl, "Inverse Adding Doubling," [Online]. Available: <http://omlc.orgi.edu/software/iad/index.html>.
- [117] S. Prahl, "Everything I think you should know about inverse adding-doubling (IAD manual)," Wilsonville OR, 2011.
- [118] H. C. van de Hulst, *Multiple light scattering*, vol. 1, New York: Academic Press, 1980.
- [119] H. C. van de Hulst, *Multiple light scattering*, vol. 2, New York: Academic Press, 1980.
- [120] J. E. Sader and et al., "Rheological measurements using microcantilevers," *J. Rheol.*, vol. 46, no. 4, pp. 891-899, 2002.
- [121] A. Darwiche, F. Ingremeau, Y. Amarouchene, A. Maali, I. Dufour and H. Kellay, "Rheology of polymer solutions using colloidal-probe atomic force microscopy," *Phys. Rev. E*, vol. 87, p. 062601, 2013.
- [122] I. Dufour, A. Maali, Y. Amarouchene, C. Ayela, B. Caillard, A. Darwiche, M. Guirardel, H. Kellay, E. Lemaire, F. Mathieu, C. Pellet, D. Saya, M. Youssry, L. Nicu and A. Colin, "The microcantilever: a versatile tool for measuring the rheological properties of complex fluids," *J. of Sensors*, vol. 2012, 2011.
- [123] T. G. Mason, H. Gang and D. A. Weitz, "Diffusing-wave-spectroscopy measurements of viscoelasticity of complex fluids," *J. Opt. Soc. Am. A*, vol. 14, no. 1, pp. 139-149, 1997.
- [124] T. G. Mason, "Estimating the viscoelastic moduli of complex fluids using the generalized Stokes-Einstein equation," *Rheol Acta*, no. 39, pp. 371-378, 2000.
- [125] M. Bellour, M. Skouri, J. -P. Munch and P. Hébraud, "Brownian motion of particles embedded in a solution of giant micelles," *Eur. Phys. J. E*, vol. 8, no. 4, pp. 431-436, 2002.
- [126] O. Glatter, "Evaluation of small-angle scattering data from lamellar and cylindrical particles by the indirect transformation method," *J. Appl. Cryst.*, vol. 13, pp. 577-584, 1980.
- [127] O. Glatter, "Convolution square root of band-limited symmetrical functions and its application to small-angle scattering data," *J. Appl. Cryst.*, vol. 14, pp. 101-108, 1981.
- [128] B. Hammouda, "Probing nanoscale structures - The SANS toolbox," National Institute of Standards and Technology, Center for Neutron Research, 2016. [Online]. Available:
-

- https://www.ncnr.nist.gov/staff/hammouda/the_SANS_toolbox.pdf. [Accessed 27 October 2018].
- [129] P. D. Kaplan, M. H. Kao and A. G. Yodh, "Geometric constraints for the design of diffusing-wave spectroscopy experiments," *Appl. Opt.*, vol. 32, no. 21, 1993.
- [130] P. Zakharov, F. Cardinaux and F. Scheffold, "Multispeckle diffusing-wave spectroscopy with single-mode detection scheme," *Phys. Rev. E*, vol. 73, p. 011413, 2006.
- [131] F. Scheffold, S. E. Skipetrov, S. Romer and P. Schurtenberger, "Diffusing-wave spectroscopy of nonergodic media," *Phys. Rev. E*, no. 63, p. 061404, 2001.
- [132] V. Viasnoff, S. Jurine and F. Lequeux, "How are colloidal suspensions that age rejuvenated by strain application?," *Faraday Discuss.*, no. 123, pp. 253-266, 2003.
- [133] J. M. Galvan-Miyoshi and R. Castillo, "Absolute values of transport mean free path of light in non-absorbing media using transmission and reflectance measurements," *Rev. Mex. Fis.*, vol. 54, no. 3, pp. 257-264, 2008.
- [134] B. Morales-Cruzado, J. A. Delgado-Atencio, S. Vazquez y Montiel and E. Sarmiento-Gómez, "Hybrid algorithm for simulating the collimated transmittance of homogeneous stratified turbid media," *Biomed. Opt. Express*, vol. 6, no. 5, pp. 1726-1737, 2015.
- [135] E. Hecht, *Optics*, Fourth ed., New York: Addison Wesley, 2002.
- [136] M. Kerker, *The scattering of light and electromagnetic radiation*, Academic Press, Inc., 1969.
- [137] S. R. Kline, "Reduction and analysis of SANS and USANS data using IGOR Pro," *J. Appl. Cryst.*, vol. 39, pp. 895-900, 2006.
- [138] A. Tavera-Vázquez, B. Arenas-Gómez, C. Garza, Y. Liu and R. Castillo, "Structure, rheology, and microrheology of wormlike micelles made of PB-PEO diblock copolymers," *Soft Matter*, vol. 14, pp. 7264-7276, 2018.
- [139] S. Asahina, T. Togashi, O. Terasaki, S. Takami, T. Adschiri, M. Shibata and N. Erdman, "High-resolution low-voltage scanning electron microscope study of nanostructured materials," *Microsc. Anal.*, vol. 26, no. 7, pp. S12-S14, 2012.
- [140] Y. Zhao, A. M. Jamieson, B. G. Olson, N. Yao, S. Dong, S. Nazarenko, X. Hu and J. Lal, "Conformation of comb-like liquid crystal polymers in isotropic solution probed by small-angle neutron scattering," *J. Polym. Sci. B*, vol. 44, no. 17, pp. 2412-2424, 2006.
- [141] B. Hammouda, "A new Guinier-Porod model," *J. Appl. Cryst.*, vol. 43, pp. 716-719, 2010.
- [142] A. Guinier and G. Fournet, *Small-angle scattering of x-rays*, New York: John Wiley & Sons, Inc., 1955.
- [143] J. S. Pedersen and P. Schurtenberger, "Scattering functions of semiflexible polymers with and without excluded volume effects," *Macromolecules*, vol. 29, no. 23, pp. 7602-7612, 1996.
- [144] W. -R. Chen, P. D. Butler and L. J. Magid, "Incorporating intermicellar interactions in the fitting of SANS data from cationic wormlike micelles," *Langmuir*, vol. 22, no. 15, pp. 6539-6548, 2006.
- [145] P. Dalhaimer, H. Bermudez and D. E. Discher, "Biopolymer mimicry with polymeric wormlike micelles: Molecular weight scaled flexibility, locked-in curvature, and coexisting microphases," *J. Polym. Sci. B*, vol. 42, no. 1, pp. 168-176, 2004.

-
- [146] J. S. Pedersen, "Analysis of small-angle scattering data from colloids and polymer solutions: modeling and least-squares fitting," *Adv. Colloid Interface Sci.*, vol. 70, pp. 171-210, 1997.
- [147] S. Bolisetty, S. Rosenfeldt, C. N. Rochette, L. Harnau, P. Lindner, Y. Xu, A. H. E. Müller and M. Ballauff, "Interaction of cylindrical polymer brushes in dilute and semi-dilute solution," *Colloid Polym. Sci.*, vol. 287, no. 2, pp. 129-138, 2009.
- [148] S. Förster, M. Konrad and P. Lindner, "Shear thinning and orientational ordering of wormlike micelles," *Phys. Rev. Lett.*, vol. 94, p. 017803, 2005.
- [149] Y. -Y. Won, A. K. Brannan, H. T. Davis and F. S. Bates, "Cryogenic transmission electron microscopy (Cryo-TEM) of micelles and vesicles formed in water by poly(ethylene oxide)-based block copolymers," *J. Phys. Chem. B*, vol. 106, no. 13, pp. 3354-3364, 2002.
- [150] E. Sarmiento-Gómez, D. Montalván-Sorrosa, C. Garza, J. Mas-Oliva and R. Castillo, "Rheology and DWS microrheology of concentrated suspensions of the semiflexible filamentous fd virus," *Eur. Phys. J. E*, vol. 35, no. 35, 2012.
- [151] B. R. Dasgupta, S. -Y. Tee, J. C. Crocker, B. J. Frisken and D. A. Weitz, "Microrheology of polyethylene oxide using diffusing wave spectroscopy and single scattering," *Phys. Rev. E*, vol. 65, p. 051505, 2002.
- [152] C. Haro-Pérez, E. Andablo-Reyes, P. Díaz-Leyva and J. L. Arauz-Lara, "Microrheology of viscoelastic fluids containing light-scattering inclusions," *Phys. Rev. E*, vol. 75, p. 041505, 2007.
- [153] P. Díaz-Leyva, E. Pérez and J. L. Arauz-Lara, "Dynamic light scattering by optically anisotropic colloidal particles in polyacrylamide gels," *J. Chem. Phys.*, vol. 121, no. 18, pp. 9103-9110, 2004.
- [154] E. Andablo-Reyes, P. Díaz-Leyva and J. L. Arauz-Lara, "Microrheology from rotational diffusion of colloidal particles," *Phys. Rev. Lett.*, vol. 94, p. 106001, 2005.
- [155] R. T. C. Ju, C. W. Frank and A. P. Gast, "CONTIN analysis of colloidal aggregates," *Langmuir*, vol. 8, no. 9, pp. 2165-2171, 1992.
- [156] S. J. Holder and N. A. J. M. Sommerdijk, "New micellar morphologies from amphiphilic block copolymers: disks, toroids and bicontinuous micelles," *Polym. Chem.*, vol. 2, pp. 1018-1028, 2011.
- [157] M. J. Stevens and K. Kremer, "Structure of salt-free linear polyelectrolytes," *Phys. Rev. Lett.*, vol. 71, p. 2228, 1993.
- [158] A. Yethiraj, "Conformational properties and static structure factor of polyelectrolyte solutions," *Phys. Rev. Lett.*, vol. 78, p. 3789, 1997.
- [159] D. López-Díaz and R. Castillo, "The wormlike micellar solution made of a zwitterionic surfactant (TDPS), an anionic surfactant (SDS), and brine in the semidilute regime," *J. Phys. Chem. B*, vol. 114, p. 8917-8925, 2010.
- [160] A. M. Ketner, R. Kumar, T. S. Davies, P. W. Elder and S. R. Raghavan, "A simple class of photorheological fluids: surfactant solutions with viscosity tunable by light," *J. Am. Chem. Soc.*, vol. 129, pp. 1553-1559, 2007.
-

REFERENCES

- [161] Y. Lin, X. Cheng, Y. Qiao, C. Yu, Z. Li, Y. Yan and J. Huang, "Creation of photo-modulated multi-state and multi-scale molecular assemblies via binary-state molecular switch," *Soft Matter*, vol. 6, p. 902–908, 2010.
- [162] R. Klajn, "Spiropyran-based dynamic materials," *Chem. Soc. Rev.*, vol. 43, pp. 148-184, 2014.
- [163] Y. Huang, R. Dong, X. Zhu and D. Yan, "Photo-responsive polymeric micelles," *Soft Matter*, vol. 10, p. 6121–6138, 2014.
- [164] M. S. Dresselhaus, G. Dresselhaus and P. Avouris, Eds., Carbon nanotubes: synthesis, structure, properties and applications, Heidelberg: Springer-Verlag, 2001.
- [165] R. H. Baughman, A. A. Zakhidov and W. A. de Heer, "Carbon nanotubes. The route toward applications," *Science*, vol. 297, pp. 787-792, 2017.
- [166] A. Selmani, A. Tavera-Vázquez, C. Garza and R. Castillo, "Tuning the viscoelastic-gel transition of single-wall carbon nanotubes embedded in pH-responsive polyelectrolyte solutions," *J. Phys. Chem. B*, vol. 122, pp. 348-359, 2018.
- [167] K. Saint-Aubin, P. Poulin, H. Saadaoui, M. Maugey and C. Z. Zakri., "Dispersion and film-forming properties of poly(acrylic acid)-stabilized carbon nanotubes," *Langmuir*, vol. 25, pp. 13206-13211, 2009.
- [168] K. C. Etika, M. A. Cox and J. C. Grunlan, "Tailored dispersion of carbon nanotubes in water with pH-responsive polymers," *Polymer*, vol. 51, pp. 1761-1770, 2010.
- [169] N. Grossiord, J. Loos, J. Meuldijk, O. Regev, H. E. Miltner, B. V. Mele and C. E. Koning, "Conductive carbon-nanotube/polymer composites: spectroscopic monitoring of the exfoliation process in water," *Compos. Sci. Technol.*, vol. 67, pp. 778-782, 2007.
- [170] S. Kuwahara, T. Sugai and H. Shinohara, "Determining exact molar absorbance coefficients of single-wall carbon nanotubes," *Phys. Chem. Chem. Phys.*, vol. 11, pp. 1091-1097, 2009.
- [171] T. A. J. Lenstra, Z. Dogic and J. K. G. Dhont, "Shear-induced displacement of isotropic-nematic spinodals," *J. Chem. Phys.*, vol. 114, pp. 10151-10162, 2001.
- [172] S. R. Raghavan and J. F. Douglas, "The conundrum of gel formation by molecular nanofibers, wormlike micelles, and filamentous proteins: gelation without cross-links?," *Soft Matter*, vol. 8, pp. 8539-8546, 2012.
- [173] Y. G. Lin, D. T. Mallin, J. C. W. Chien and H. H. Winter, "Dynamic mechanical measurement of crystallization-induced gelation in thermoplastic elastomeric poly(propylene)," *Macromolecules*, vol. 24, pp. 850-854, 1991.
-